Constraining the North Atlantic Circulation with Transient Tracer Observations

by

Xingwen Li

Submitted to the Joint Program in Physical Oceanography
in partial fulfillment of the requirements for the degree of

Doctor of Philosophy

at the

MASSACHUSETTS INSTITUTE OF TECHNOLOGY

and the

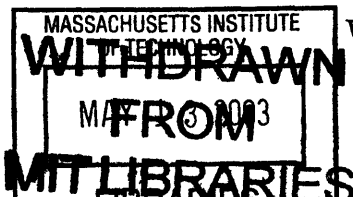WOODS HOLE OCEANOGRAPHIC INSTITUTION

February 2003

©Xingwen Li, 2002

Author ....

Joint Program in Physical Oceanography
Massachusetts Institute of Technology
Woods Hole Oceanographic Institution
October 30, 2002

Certified by...........

Carl Wunsch
Cecil and Ida Green Professor of Physical Oceanography
Massachusetts Institute of Technology
Thesis Supervisor

Accepted by ...

Carl Wunsch
Chairman, Joint Committee for Physical Oceanography
Massachusetts Institute of Technology
Woods Hole Oceanographic Institution

Constraining the North Atlantic Circulation with Transient Tracer Observations

by

Xingwen Li

Abstract

The capability of transient tracers to constrain the ocean circulation in the North Atlantic is explored. Study of an idealized tracer shows that inferences of circulation properties from transient state distributions are impacted by uncertainties in the time-varying boundary conditions and sparse data coverage. Comparison of CFC, tritium, temperature and salinity (T-S) observations with model results in the North Atlantic shows that regions of important model-data disagreements in the transient tracer fields can also be readily identified in the T-S distributions. In the model, excessive vertical penetration of convective adjustment, leads to problematic production and outflow of the NADW, again appearing in both transient tracer and T-S fields.

Sensitivities of the model fields are determined using the adjoint model. In the dual solutions, CFC-11, CFC-11/CFC-12 ratio age, and $T - (\beta/\alpha)S$ (α and β are thermal and haline expansion coefficients, respectively) exhibit the major ventilation pathways and the associated timescales, in the model. High sensitivity fields are candidates for providing the most powerful constraints in the corresponding inverse problems. Assimilation of both CFC and tritium data, with different input histories, sampling distributions, and radioactive decay constants, shows that by adjusting only initial-boundary conditions of CFCs and tritium, a $1^o \times 1^o$ offline model and the transient tracer data can be brought into near-consistency, in the domain between 4.5^oS and 39.5^oN of the North Atlantic.

Constraining a GCM with transient tracers is thus fully practical. However, the large uncertainties in the time-varying boundary conditions of transient tracer concentrations, and in their interior distributions, renders the transient tracers less-effective in determining the circulation than are more conventional steady tracers, and known oceanic dynamics.

Thesis Supervisor: Carl Wunsch

Title: Cecil and Ida Green Professor of Physical Oceanography
Massachusetts Institute of Technology

Acknowledgments

I would like to extend my sincere appreciation for all the assistance and support that I got throughout this thesis and my years at both MIT and WHOI.

First and foremost, I would like to thank my supervisor, Carl Wunsch, who provided me with invaluable time, resources, advice and financial support. His insight, integrity, enthusiasm and disposition are good sources to benefit my whole life. I felt incredibly fortunate to have a prominent advisor, who responded to my questions and results in time, who patiently read numerous drafts of this work, which made working on this thesis an enjoyable and exciting experience. His constructive comments and suggestions were essential to this thesis.

I thank the other members of my committee, Nelson Hogg, Glenn Flierl, Michael Follows and David Glover. Their doors were always open for questions and discussions. They carefully read many drafts of this thesis, made valuable comments, and helped me go through theoretical and technical problems at various stages of this work. Michael Follows explained the essential details of the adjoint modeling to me. Thanks also go to the other members of the physical oceanographic group at MIT and WHOI who provided me assistance.

I am grateful to all the investigators who allowed me to use their data, either directly or through the WHPO. Thanks in particular to Scott Doney, Thomas Haine, John Bullister, Bill Smethie, Wolfgang Roether, Martin Gould, Laurent Mémery, Peter Schlosser, and Samar Khatiwala. Scott Doney also provided necessary data and associated scripts for computing the CFC age and tritium distributions.

I felt very lucky that I studied among very nice classmates. I thank Geoffrey Gebbie for his valuable discussions with me about study and research problems, and for being my sincere counselor about cultural and academic problems. Much gratitude

Contents

List of Figures

11

13

List of Tables

Chapter 1

Introduction

1.1   Transient tracers in the ocean

Transient tracers are a variety of man-made chemical species that have been introduced into the earth system, as a result of either industrial production or nuclear bomb tests. These anthropogenic tracers have made their way to the ocean through its surface. Because of their time-varying concentrations in the atmosphere, these man-made chemicals in the ocean are called transient tracers. Neither the oceanic distributions of these tracers nor their inputs are steady.

The most commonly studied transient tracers in oceanography are chlorofluorocarbons (CFCs) such as CCl_3F (CFC-11) and CCl_2F_2 (CFC-12), tritium, helium (^{3}He), and bomb radiocarbon (^{14}C). CFCs are entirely man-made gases having been used by refrigerators and manufacturing processes since the 1930s. Their concentrations in the atmosphere continuously increased with time from the 1930s to the early 1990s [e.g., Walker et al., 2000]. The decomposition products of CFCs in the stratosphere cause the destruction of ozone [Anderson et al., 1991]. As a consequence of the Montreal Protocol, which limited the amount of CFCs emitted, the CFC increase rates dropped in the 1990s. Politicians and scientists continue working hard to decrease the amount of CFCs released into the atmosphere. CFCs enter the ocean through air-sea gas exchange.

Tritium is a radioactive isotope of hydrogen ^{3}H. It is found in the ocean as tritiated

water (HTO). The decay product of tritium is ^{3}He. Oceanic ^{3}He is composed of two parts: terrigenic ^{3}He released from the ocean floor and tritiugenic ^{3}He from tritium decay.

Major amounts of both tritium and ^{14}C were produced as the result of atmospheric nuclear bomb tests in the early 1960s. Both isotopes were injected into the stratosphere of the northern hemisphere, where the tritium atoms were quickly incorporated into H_2O molecules and ^{14}C atoms into CO_2 molecules. After being transferred to the troposphere, bomb tritium and ^{14}C followed quite different routes to the sea. Tritium entered the ocean through direct precipitation, water vapor exchange between the atmosphere and ocean, and river outflows [e.g., Weiss et al., 1980; Doney et al., 1993]. As the tritiated water molecules were quickly absorbed into raindrops or wet surfaces, tritium entered the ocean preferentially in the high-latitude northern hemisphere as a pulse in the 1960s. On the other hand, bomb ^{14}C entered the ocean through gas exchange of CO_2 at the air-sea interface, and thereby was nearly uniformly spread in the atmosphere before entering the sea [Nydal et al., 1983].

Once in the ocean, these chemicals are mixed and advected by the ocean circulation. A major motivation for studying the transient tracers in the ocean is to infer the ocean circulation, especially the exchange processes between the ocean surface and interior. These exchange processes are critical in redistributing not only heat and fresh water but also climatically important greenhouse gases such as CO_2 globally. Another objective for the study of the transient tracers in the ocean is to investigate the CO_2 budget of the world ocean. Both CFCs and CO_2 enter the ocean through air-sea gas exchange. Because the biogeochemical carbon cycle is very complicated, we might hope that understanding the distributions of CFCs, which are chemically and biologically inert in the ocean, is a first step toward a better evaluation of the ocean's role in the global carbon cycle.

As described previously, the processes through which these tracers enter the ocean surface are very complex. To quantitatively infer ocean circulation from transient tracer distributions, reconstruction of the time-varying boundary conditions is essential. This reconstruction requires extrapolation from a restricted amount of historical

data. For example, estimates of tritium concentration at the ocean surface are based on very sparse observations obtained by a few weather ships and research cruises, notably in the 1960s when the major amount of tritium entered the ocean [Dreisigacker et al., 1978]. Estimates of the surface CFC and CO_2 fluxes are based on limited knowledge about the complex air-sea gas exchange process. The relationship between the gas transfer velocity and wind speed is not yet totally understood [Wanninkhof, 1992]; the effects of boundary layer stability, turbulence and bubbles in the air-sea tracer exchange are still uncertain. Inevitably, large uncertainties exist in the estimates of the transient tracer input functions. One focus of this study is interpreting the transient tracer distributions with uncertain input histories. There is another catalog of tracers that are released into the ocean under control, to investigate the circulation and dispersion in the ocean [Ledwell et al., 1993 etc.]. These tracers with accurately known input sources are not discussed here.

With great effort and big investments, a large amount of transient tracer data has been obtained from the world oceans. The Geochemical Ocean Sections Study (GEOSECS) program in the early 1970s systematically sampled a number of natural and anthropogenic tracers, such as tritium, ^{3}He and ^{14}C, for the first time. In the early 1980s, the Transient Tracers in the Ocean (TTO) program was carried out. The measurement of CFCs was introduced during the TTO North and Tropical Atlantic expeditions. Surveys of transient tracers continued with the South Atlantic Ventilation Experiment (SAVE) in the late 1980s. Recently, more transient tracer observations were made along hydrographic sections of the World Ocean Circulation Experiment (WOCE). Despite these efforts, the transient tracer data are sparse when compared with measurements of traditional tracers, such as temperature and salinity (T-S). This sparseness makes practical problems for the extraction of ocean circulation information from the transient tracer data, that are very different from purely theoretical ones. Understanding the information content of transient tracers must account for practical reality: the sparseness of data coverage and the large uncertainties in the transient tracer input histories.

Observations of the transient tracers in the ocean attracted some earlier attention.

A major application is to use these tracers as dyes to scrutinize the thermohaline circulation, driven by the renewal of dense North Atlantic Deep Water (NADW) in the northern North Atlantic and by a smaller input of Antarctic Bottom Water (AABW) formed principally at the Weddell Sea [e.g., Schmitz, 1995; Haine et al., 1998; Schlosser et al., 1991].

A synthesis of CFC observations is used to survey the large-scale circulation pathways and timescales for the spreading of NADW components, i.e, the Upper Labrador Sea Water (ULSW), the Classic Labrador Sea Water (CLSW), Iceland-Scotland Overflow Water (ISOW), and Denmark Strait Overflow Water (DSOW), by Smethie at el. [2000]. It is found that these water masses coincide with high CFC concentrations and have characteristic potential temperature, salinity and density. The pathways of these water masses are exhibited by CFC distributions, which are mapped from data of different cruises taken at different times. As Smethie et al. [2000] point out, a problem is presented when using transient tracers: their inputs vary with time and their distributions are not in steady states. To obtain the basin-scale distribution pattern from transient tracer data, corrections must be made to normalize concentrations sampled at different times. This has been done by using the CFC-11/CFC-12 ratio.

It is generally assumed that the CFC-11/CFC-12 ratio is conserved once a water parcel leaves the surface. This assumption is true if mixing is negligible or CFC-tagged water mixes only with CFC-free water. Based on this assumption, the CFC-11/CFC-12 ratio age is derived according to the atmospheric CFC-11/CFC-12 ratio, which increased steadily with time until the late 1970s. First, the CFC concentrations in sea water are converted to the corresponding dry air atmospheric mixing ratios, using Henry's law [e.g., Warner et al., 1985]. Here it is assumed that the potential temperature and salinity in a water mass are conserved. The dry air mixing ratio of CFC-11/CFC-12 is then compared to the appropriate historical atmospheric ratio of CFC-11/CFC-12 to determine the time when the water parcel was last at the ocean surface [Doney et al., 1997]. Smethie et al. [2000] use the CFC-11/CFC-12 ratio age to infer the timescales for the spreading of NADW components. Because there are

23

recirculation, mixing, and entrainment of CFC-tagged water in both upper and deep ocean, inferences based on the CFC age are biased.

Smethie et al. [2000] assume the oceanic CFC concentrations at a specific observational location change at the same rates as the atmospheric CFCs at the year when the observed water parcel left its source region. Using this assumption, Smethie et al. [2000] normalize the CFC concentrations sampled at different years to the same year. Large errors are introduced in the normalization and mapping processes to obtain the basin-scale distributions of CFCs. Inferences from the spatial distributions of CFCs have large uncertainties.

A review of the application of transient tracers as well as other natural tracers in studies of the Weddell Sea is given by Schlosser et al. [1991]. Tritium and CFC concentrations are used to qualitatively interpret channels where newly formed young waters leave the shelves of the Weddell Sea and flow down the continental slope into the deep basin. The CFC-11/CFC-12 ratio together with CFC-11/tritium ratio is used to estimate the transit times of young waters, because the CFC-11/tritium ratio increased monotonically between 1975 - 1987 when the CFC-11/CFC-12 ratio was nearly constant. Again, the effect of mixing among CFC-enriched waters is neglected. Schlosser et al. [1991] also discuss the use of steady tracers ^{18}O and Helium isotopes to distinguish deep waters and their pathways from different surface source regions, because the concentrations of these steady tracers are different in glacial meltwater and seawater.

The export of AABW from the Weddell Sea into the southwest Indian Ocean is estimated by Haine et al. [1998], using CFC data. The routes of AABW leaving the Weddell Sea have been described by Mantyla et al. [1995], according to traditional hydrographic structures, i.e., distributions of potential density anomaly, potential temperature, salinity, dissolved oxygen and silicate. In Haine et al. [1998], the transient tracer fields confirm the pathway of AABW established by the analysis of steady tracer distributions. An along-stream advection and cross-stream mixing model is established by Haine et al. [1998]. Using this simple kinematic model and assuming that the surrounding water of AABW is CFC-free, Haine et al. [1998]

24

estimate the outflow speed and mixing rates for the AABW transport.

The pathways of water between the Pacific and Indian oceans in the Indonesian seas are investigated by Gordon and Fine [1996]. T-S and CFC-11 distributions at different locations of Indonesian Sea are combined together to infer the pathways of the Indonesian through-flow (ITF). Water with similar T-S and CFC properties is attributed to the same origin. Gordon and Fine [1996] conclude that the ITF is dominated by two components: one of low-salinity, well ventilated North Pacific water through the upper thermocline of the Makassar Strait, and the other of more saline South Pacific water through the lower thermocline of the eastern Indonesian seas.

There are published papers about studies of deep water formation processes at the Ross Sea [Trumbore et al., 1991], Red Sea [Mecking et al., 1999], and Arctic Ocean [Anderson et al., 1999], using transient tracer observations. But we should notice that, in the oceanographic literature (including some of the studies mentioned above), formations and pathways of the upper ocean central waters (e.g., 18° mode water), intermediate waters (e.g., Antarctic Intermediate Water), deep waters (e.g., NADW), and bottom waters (e.g., AABW), have been successfully explored and depicted by employing approximately steady tracers (e.g., T-S, oxygen, silicate). See Pickard and Emery [1990] for a summary. The roles of both transient and steady tracers need further examination.

Besides qualitative interpretations of flow paths, quantitative inferences about water mass formation rates, mixing rates and ventilation timescales are made from the transient tracer data. Smethie et al. [2001] estimate the formation rates of the NADW components, using CFC observations and the equation,

$$I = \sum RC_s \delta t. \tag{1.1}$$

Here I is the total CFC-11 inventory, R is the rate of water mass formation, C_s is the CFC-11 concentration in the source water as a function of time, and δt is the time step. First, vertical profiles of CFC-11 are segmented into components of NADW. The profile within each segment is then integrated vertically to obtain the

25

water column inventory. The water column inventories are normalized to year 1990 and mapped, using the method in Smethie et al. [2000], which has been described previously. The total inventory I is obtained by integrating the map of the water column inventory. The summation is carried out over the time period of CFC input, 1945 - 1990. C_s is estimated from the atmospheric history of CFC-11 concentration, the CFC-11 solubility, and the saturation at the source region of a specific water mass. The saturation is assumed to vary among different source regions but remain constant with time. The formation rate R of each water mass is also assumed to be constant in time.

During these processes to obtain the formation rate R, a large error is introduced by constructing the map of CFC-11 water column inventory from sparse data. There are errors in the source water concentration C_s, arising from the uncertainty in the saturation of CFC-11 in the source water, uncertainty in the T-S of the source water which determine the CFC solubility, and uncertainty in the atmospheric CFC history. The total NADW rate given by Smethie et al. [2001] is 17 Sv with 30% uncertainty, as compared to 14 Sv estimated from hydrography and current measurements (see Schmitz, 1995 for a review).

Jenkins [1991] calculates the isopycnal eddy diffusivity in the Sargasso Sea, using the tritium-^{3}He age equation

$$\frac{\partial \tau}{\partial t} = \kappa \nabla^2 \tau - \mathbf{V} \cdot \nabla \tau + 1 + \kappa \left(\frac{\nabla \zeta}{\zeta} + \frac{\nabla \theta}{\theta} \right) \cdot \nabla \tau. \tag{1.2}$$

Here τ is the tritium-^{3}He age, κ is the isopycnal diffusivity, $\mathbf{V}$ is the isopycnal velocity, ζ is the sum of tritium and ^{3}He, and θ is tritium. The tritium-^{3}He age [Clarke et al., 1976] is defined as

$$\tau = 17.93 \ln \left(\frac{^3H + ^3He}{^3H} \right). \tag{1.3}$$

Jenkins [1991] estimates the spatial and temporal derivatives of τ, ζ, and θ directly from observations. The isopycnal diffusivity is calculated as

$$\kappa = \frac{\frac{\partial \tau}{\partial t} + \mathbf{V} \cdot \nabla \tau - 1}{\left(\nabla^2 \tau + \left(\frac{\nabla \zeta}{\zeta} + \frac{\nabla \theta}{\theta} \right) \cdot \nabla \tau \right)}. \tag{1.4}$$

26

Generally, the transient tracer observations are made at different times in different areas. The transient tracer data are sparse in most of the ocean regions. Therefore, the spatial and temporal derivatives of τ, ζ, or θ obtained directly from observations are inaccurate.

A common approach to infer mixing rates is by fitting data to simple models [e.g., Haine et al. 1998]. Using observed tritium profiles and a one-dimensional advection-diffusion model, Kelley et al. [1999] estimate the vertical diffusivity κ_v in the upper subtropical North Pacific and give $\kappa_v = (1.5 \pm 0.7) \times 10^{-5} m^2/s$. By fitting a one-dimensional advection-diffusion model to CFC data in the upper North Pacific at 50°N, Matear et al. [1997] obtain $\kappa_v = (4 \pm 0.1) \times 10^{-5} m^2/s$. As the inferences from the transient tracer data are based on very simple models and assumptions, those inferences should be regarded as rough first-order approximations which need to be improved using more realistic models [Schlosser et al., 1991].

Quantitative inferences of timescales of ocean circulation from the transient tracer data are based on tracer ages. The derived tracer ages are treated as proxies for the ideal age, defined as the elapsed time since a water parcel was last exposed to the atmosphere [e.g., Doney et al., 1997]. Intuitively, it is believed that tracer age simplifies interpretation of the transient tracer distributions mainly due to its simple surface boundary condition, which is zero. On the other hand, as Wunsch [2002] points out, the simplification of the boundary condition of the tracer age is at the sacrifice of losing the linearity of the governing equation, in the geophysical fluid system. Analytical solutions show that the expression of the tracer age is more complicated than that of the tracer concentration. Interpretation of the tracer age is very difficult.

Holzer and Hall [2000] argue that a water mass comprises a distribution of times [e.g., Hall and Plumb, 1994] since it made contact with the surface, via a multiplicity of pathways. The mean age is the first moment of the transit time probability density function (pdf), i.e., the mean transit time. The ideal age converges to the mean age when it reaches a steady state [e.g., Holzer and Hall, 2000; Haine and Hall, 2001]. Any tracer measurement, steady or transient, provides integrated information about

transit times. The water mass composition of steady tracers includes a distribution of transit times for tracer originating from each surface source point [Haine and Hall, 2001]. On the other hand, the transient tracer ages have no simple relation to the mean transit time, because not all pathways from the surface have been sampled by the transient tracers. For example, a CFC sample contains no information about transit times exceeding 80 years. In the presence of turbulent mixing, the transient tracer ages are biased estimates of the true ocean ventilation age.

The pdf of transit times can be represented as a boundary Green function [e.g., Holzer and Hall, 2000; Haine and Hall, 2001]

$$\frac{\partial G}{\partial t} + \vec{u} \cdot \nabla G - \nabla \cdot (\mathbf{K} \nabla G) = 0, \tag{1.5}$$

with the concentration boundary $G = \delta(t - t')$ defined in a region Ω of the ocean surface. Here $\vec{u}$ and $\mathbf{K}$ represent the flow field and mixing tensor, respectively. The boundary Green functions serve as diagnostics in a numerical model. No inference of boundary Green function has been obtained from transient tracer observations. Because the boundary Green function itself depends on the flow field and mixing rates, improvements of the model circulation are fundamentally important for us to understand the transport processes and their timescales.

There is a growing literature about the use of transient tracers to improve model performances. Commonly, the transient tracer observations are compared with model predictions to evaluate ocean models [e.g., Craig et al., 1998; England, 1995; Sarmiento, 1983]. A comprehensive review of using chemical tracers in ocean models is given by England and Maier-Reimer [2001]. In these papers, it is reported that the model predictions and observations agree reasonably well. Noticeable differences, however, remain. Comparisons between model results and observations show disagreements on issues such as the deep water formation in the high latitudes. For example, England and Hirst [1997] find excessive downward penetration of CFC-11 in the high latitude Southern Ocean, which is related to excessive vertical convection at these latitudes. In the North Atlantic, most model simulations [e.g., England and Hirst, 1997; Craig

et al., 1998] capture only a single core, corresponding to the upper NADW. The lack of a deeper core is due to the absence of Overflow Water (OW) in the models [e.g., England, 1998]. As Craig et al. [1998] point out, problems with deep water mass formation lead to the model-data disagreements in CFC pathways downstream. Model-data misfits of tracer distributions in the Antarctic Intermediate Water (AAIW) are also reported by Craig et al. [1998]. Modeled CFC penetration in the AAIW is too weak, associated with erroneous water mass structure; the modeled AAIW is too warm and its volume is too small. In general, model-data discrepancies of transient tracer fields appear in regions where the modeled and observed water mass structures are different.

One technique to nudge modeled T-S fields towards observations is restoring three-dimensional T-S but not transient tracer fields in the model. This restoring changes the evolution dynamics of T-S. Because the governing physics of T-S and transient tracers are no longer the same after restoring, their signatures of model-data misfits are different sometimes; the modeled T-S might be in good agreement with the observations while the transient tracers might not. The restoring technique is useful for forward simulations. When we want to evaluate and improve the model physics and thus the model performance, we should, however, let the model physics play their roles freely without any purposeful forcing.

In a model of the real ocean, both transient and steady tracers are governed by the same physics. All characteristic properties of a water mass, the transient tracer concentrations as well as its T-S, will be imprinted along its trajectory. A water mass can be identified by its traditional hydrographic structure, such as T-S, oxygen and silicate. For example, Talley et al. [1982] successfully exhibit the pathway of the newly ventilated Labrador Sea Water (LSW) from salinity distribution. T-S can also be used to locate rapid mixing processes where vertical homogeneity is present. The under-saturation associated with deep convection can be demonstrated by oxygen field. A systematic investigation of the roles of both transient and steady tracers in helping us to evaluate model performances is needed.

There are few published papers about direct combination of a model and the

29

transient tracer observations, that is, incorporating the transient tracer observations as constraints on an ocean circulation model. This is another approach to extract information from sparse transient tracer data. The pioneering work of Mémery and Wunsch [1990], using a geostrophic coarse box model and a Green function approach, shows that uncertainty in the transient tracer boundary conditions and sparse data coverage greatly weaken the ability of tritium to constrain the model.

Almost 10 years later, Gray and Haine [2001] combined a North Atlantic ocean general circulation model (OGCM) with CFC observations. They give 23 smeared impulsive sources on the North Atlantic surface and solve for the corresponding boundary Green function components. Given that the CFC concentration is zero at the initial time, the CFC concentration at location $\mathbf{r}$ and time t is represented by these Green function components

$$C(\mathbf{r}, t) = \sum_{i} \int_0^t G(\mathbf{r}, t; i, t_0) B_N(i, t_0) dt_0. \tag{1.6}$$

Here $G(\mathbf{r}, t; i, t_0)$ represents the boundary Green function at location $\mathbf{r}$ and time t, forced by the ith smeared impulse at time t_0; $B_N(i, t_0)$ is the CFC surface flux at the location of the ith impulse at time t_0. In Gray and Haine [2001], the ocean circulation is assumed to be steady. This assumption leads to $G(\mathbf{r}, t; i, t_0) = G(\mathbf{r}, t-t_0; i, 0)$, which greatly reduces the computational expense. The CFC surface flux B_N is constrained by minimizing model-data differences of CFC-11 and CFC-12. The boundary Green function components are stored annually at the end of August and observations are adjusted to late summer values. The result of Gray and Haine [2001] shows that after optimization of the surface fluxes, the model and data are marginally consistent.

Some issues arise in the above application of the Green function theory. When a tracer distribution is represented in terms of Green function components, they should include all components due to impulse sources at all points and all times. When the impulses are smeared and the integrations are discretized as summations over large steps, uncertainties are introduced. Within the surface region of each smeared impulse, the CFC flux B_N has to be constant in space. Because the gas-exchange rates

30

of CFCs depend on wind speed, for which the spatial variability is large, the assumption of constant CFC flux in space within a large-scale region certainly introduces errors. As the sources are all located on the ocean surface, lateral fluxes of CFCs are totally ignored in Gray and Haine [2001]. An inverse study that allows more realistic transient tracer boundary conditions is needed.

1.2   The transient tracer problem

While the oceanic transient tracer data are now common, there are difficulties with their quantitative use. As Wunsch [1988] points out, direct inferences of ocean circulation parameters from the transient data are not straightforward. Considering any passive tracer C, its concentration satisfies an equation like

$$\frac{\partial C}{\partial t} + \vec{u} \cdot \nabla C - \nabla \cdot (\mathbf{K} \nabla C) = -\lambda C + S, \tag{1.7}$$

where S represents sinks/sources, λ is a decay constant, $\vec{u}$ is velocity, and $\mathbf{K}$ is the mixing tensor. Inferences from transient tracer distributions require our knowledge about the initial-boundary conditions and the derivatives of C. There inevitably exist large degree of uncertainties in the time history of the transient tracer boundary conditions. Given the difficulties and expense of collecting transient tracer data, it is impractical to obtain accurate temporal and spatial derivatives of C from the sparsely distributed transient tracer data.

These difficulties can be overcome by the use of approximately steady tracers (simply called steady tracers hereafter). If we want to infer the first order large-scale mean ocean circulation from steady tracer observations, we can combine measurements made at similar climatological conditions together to yield a complete spatial picture, in a way that is impossible with the transient tracers [Wunsch, 1987]. In addition, the traditional steady tracer observations are far more abundant than the transient observations.

Nowadays, more and more accurate inferences about mixing rates, flow fields, heat

and fresh water transports in the ocean are made from measurements of steady tracers, such as T-S, oxygen, silica and phosphate [e.g., Ganachaud and Wunsch, 2000]. With OGCMs, estimation of the daily-evolving large-scale ocean circulation is made possible through a combination of traditional hydrography, expendable bathythermograph (XBT), surface drifters and deep floats, altimetric data sets and dynamics [Stammer et al., 2002]. The existence of these competing data sets leads to a question: how much additional information about the ocean circulation can the transient tracers provide us, given our current knowledge?

Incorporation of real transient tracer data in a model requires a long-term transport integration, because the transient tracer distributions at observational times depend on their previous histories. The large degree of uncertainty in the transient tracer input histories is one of the major difficulties in obtaining quantitative information about ocean circulation from the transient tracer data. For some tracers, such as helium, it is very difficult to quantify the mantle sources. Separating natural and bomb-produced distributions of ^{14}C is still a challenge [Toggweiler et al., 1989]. Practically, whether the inherent temporal variabilities of the sparse transient tracer data can be used to provide unique information about ocean circulation, or on the contrary, the complexity of the temporal variabilities actually undermines the systematic and quantitative inferences, is still unknown. Efficiently constraining the surface and lateral boundary conditions is a prerequisite to evaluate the extent to which the transient tracer observations can constrain the ocean circulation, and thereby enhance our present estimation of the ocean state. In addition, the long term integration requirement puts a great computational burden on the assimilation of transient tracer data into a comprehensive OGCM.

1.3 Objectives

This thesis is directed at understanding, evaluating, and using the information content of the transient tracers. Specifically, this study will explore the potential capabilities of both transient and steady tracers in the contexts of model evaluation and data

assimilation, and quantitatively access the extent to which the current transient tracer data can constrain the large-scale ocean circulation properties. The results of this study can provide useful information for designing future observational strategies.

Our area of interest here is the North Atlantic, because its circulation contains a range of physical processes, including deep water formation. It is also one of the regions best covered by transient tracer observations. This study investigates not only the roles of both transient and steady tracers in tracking the formation of the NADW and its pathway in a forward model, but also analyzes and compares amplitudes, propagation timescales and pathways of the sensitivities of transient and steady tracer properties in an adjoint model (see Appendix A). In doing so, we try to understand the information content of transient tracers relative to steady tracers.

Because the transient tracer data are sparse, a direct combination of a numerical model with the data is one of the major techniques to quantitatively use the transient tracer data. There are many published papers about assimilation of T-S observations in OGCMs [e.g, Stammer et al, 2002; Yu et al., 1996; Schlitzer, 1993], yet studies of assimilation of transient tracer data in an OGCM are few. A study is needed to explore whether the transient tracer data can provide additional information, using realistic transient tracer boundary conditions. A major objective for the study of transient tracers in the ocean is the possibility that they can improve the estimates of surface CO_2 flux. Therefore, investigation of the extent to which the gas exchange rates at the air-sea interface can be constrained by CFC observations is important.

As recommended by Mémery and Wunsch [1990], this study continues to explore the capability of the present transient tracer observations to constrain ocean circulation properties in an OGCM. Unlike the work of Gray and Haine [2001], in which assumptions of constant inter-annual saturation rate in the mixed layer and smeared impulse surface sources in space are made, we use realistic CFC surface fluxes at each model-grid point with temporally and spatially varying saturation in the mixed layer. Compared to the model used by Gray and Haine [2001], our model has a higher resolution and allows tracer fluxes across open boundaries. More important, in this study, we seek to evaluate the extent to which the transient tracer data can constrain

33

the circulation properties quantitatively, which is not addressed fully by Gray and Haine [2001].

This study uses the so-called adjoint method [e.g., Wunsch , 1996; Marotzke et al., 1999] to assimilate the transient tracer data in an offline version of the MIT GCM [Marshall et al., 1997a,b]. In the assimilation process, the estimates of the model parameters (control variables) will be optimized with regard to minimizing the misfit between observations and model predictions. Misfits come from both the model and the data. All data contain noise from instrumental errors and other sources. The models used are never exact. (1) Although the boundary conditions that drive the tracer fields have been largely explored, the details are not completely understood. The uncertainties of the transient tracer boundary histories at surface and open ocean still need to be reduced as much as possible. (2) The sub-grid scale parameterizations are represented as empirical coefficients of uncertain values. For example, the imperfect mixing parameters and convective schemes will have impacts on the tracer fields. (3) The numerical schemes and model resolution will influence the model results. There are numerical errors in computational processes. A discretized model cannot resolve the sub-grid scale variabilities in the real ocean. (4) Approximations are made to the Navier-Stokes equations which cause a model to deviate from reality.

For transient tracers, the number of reasons for the model-data misfit is very large. Any variations in the transient tracer input histories over a few decades will imprint their signatures along the tracer evolution trajectories [Wunsch, 2002]. Therefore, it is unclear at the beginning of this study whether the transient tracer observations can provide any additional information about the ocean circulation and whether the final, optimal estimates of the ocean circulation properties will be reasonable. Sorting out these issues is the goal of this thesis.

This study aims at understanding the transient tracer distributions in the background of the large-scale mean ocean circulation of the North Atlantic. As the ocean is full of variabilities, e.g., small-scale turbulence, meso-scale eddies, interannual to decadal climatic changes, the information content of transient tracers is inevitably complex and rich [Wunsch, 2002], and differs from one region to another. With the

development of an eddy-resolving model together with its adjoint [Geoffrey Gebbie, personal communication], an outlook for continued investigation, such as a detailed study over regions (e.g., the deep convective regions) where the variabilities of both surface boundary conditions of all tracers and the interior ocean are strong, is necessary. Therefore, this study should be regarded as a step toward understanding a difficult synthesis of transient tracers in the ocean.

1.4 Thesis outline

This thesis can be divided into three parts. The first part (Chapter 2) establishes a conceptual context for understanding the mathematical and physical structures of transient tracers, especially in the aspect of doing inversions. The second part compares the capabilities of transient and steady tracers in the contexts of model evaluation (Chapter 3) and data assimilation (Chapter 4) in the North Atlantic. The third part (Chapter 5) uses the currently available CFC and tritium data to constrain an offline model of the North Atlantic.

Chapter 2 introduces an idealized passive tracer forced by a unit step surface concentration. Structures of the tracer distributions and the associated implications for inverse studies are investigated in simple one-dimensional cases, both analytically and numerically. In three-dimensional cases, model-generated "observations", with different spatial and temporal coverage, and noise level, are used to infer a simple model parameter and to adjust noise-contaminated surface tracer concentration. This simplified and idealized tracer study will serve as a reference for the later study: the full inversion of comprehensive model parameters from real data.

Chapter 3 compares the CFC, tritium, helium and T-S observations in the North Atlantic with model predictions. Capabilities of both transient and steady tracers in helping us to evaluate model performance, such as indicating problematic representations of deep convection, deep water masses and the associated ventilation pathways, are exhibited and compared qualitatively.

Chapter 4 investigates the potential capabilities of transient and steady tracers in

35

constraining an OGCM, according to their adjoint sensitivities. It analyzes and compares the timescales and pathways of the most important physical processes provided by the sensitivities of different tracer properties. Sensitivities of CFC-11 concentration, CFC-11/CFC-12 ratio age, and $T - (\beta/\alpha)S$ (β and α are thermal and haline expansion coefficients respectively) [e.g., Veronis et al, 1972; Munk, 1981] in the NADW and lower subtropical thermocline are exhibited as examples.

Chapter 5 continues to explore the capability of the present transient tracer observations to constrain ocean circulation properties by directly incorporating the CFC-11, CFC-12, and tritium observations as constraints on the offline model, using the adjoint method. This assimilation study focuses on the large uncertainties in the temporally varying surface and open boundary conditions. Model-data misfits after optimization of the boundary and initial conditions are shown. Limitations due to model resolution are discussed.

Chapter 6 summarizes the results of this thesis. This chapter also outlines the limitations of this study and suggests directions for future work.

Chapter 2

Theoretical and Numerical Study of an Idealized Tracer

The objective of this chapter is to establish a simple scenario for understanding transient tracers, especially as an inverse problem of constraining the ocean circulation properties with transient tracer observations. Because the distributions of transient tracers in the ocean are governed by their uncertain input histories and physical processes on a vast range of space and time scales, understanding the information content of the transient tracers is very difficult. Before simulating real transient tracers in a comprehensive model, we investigate their basic mathematical and physical structures, using an idealized tracer. Some simple examples are provided to familiarize readers with the inverse problem of transient tracers.

In this chapter, an idealized passive tracer forced by a unit step surface concentration is introduced into a one-dimensional (1-D) and a three-dimensional (3-D) ocean model. In 1-D cases, the temporal and spatial evolution patterns of this idealized tracer are investigated both analytically and numerically. Model-generated "observations", with different spatial and temporal coverage, and noise level, are used to constrain the vertical background mixing rate and surface tracer concentrations, in both 1-D and 3-D cases. The inverse solutions can be evaluated by comparing these solutions with the parameters used to produce the artificial "observations". This simplified and idealized tracer study will be a reference for the later study: the full

inversion of comprehensive model parameters from real data.

2.1 One-dimensional advection-diffusion experiments

2.1.1 An analytical solution

A governing equation for a passive tracer in 1-D is

$$\frac{\partial C}{\partial t} + w\frac{\partial C}{\partial z} - \frac{\partial}{\partial z}(\kappa\frac{\partial C}{\partial z}) = -\lambda C + q, \tag{2.1}$$

where C is the tracer concentration, w is the vertical speed (positive sign indicates upward movement), λ is a decay constant, q is a generalized source/sink, and κ is the vertical mixing coefficient. Equation (2.1) can be solved given initial and boundary conditions.

Analytical solutions of Eq. (2.1) with typical sources q have been given by Wunsch [2002], with an emphasis on a qualitative description of anticipated transient tracer behavior in forward time evolution. With a different focus, this study explores the discrepancies between time-dependent and steady tracers, particularly in the context of doing inversions. We begin with examining an idealized tracer distribution in a simple 1-D pipe flow.

Suppose we have a tracer that is forced by a unit step surface concentration, with zero concentration at initial time,

$C(z,t) = 0$ at $t = 0$; $C(z,t) = H(t)$ at $z = 0$; $C \to 0$ as $z \to -\infty$.

Here we can regard $z = 0$ as the point from which the tracer enters the interior, such as the bottom of the Ekman layer where w does not necessarily vanish. If w, κ, and λ are constant, taking the Laplace transform of (2.1), we get

$$s\hat{C} + w\frac{\partial \hat{C}}{\partial z} - \kappa\frac{\partial^2 \hat{C}}{\partial z^2} = -\lambda\hat{C}. \tag{2.2}$$

Here $\hat{C}$ is the Laplace transform of C, and the initial condition $C(z,0) = 0$ has been used. The boundary conditions are changed to

$\hat{C}(s, 0) = 1/s$ at $z = 0$; $\hat{C} \to 0$ as $z \to -\infty$.

We can rewrite (2.2) as

$$\kappa \frac{\partial^2 \hat{C}}{\partial z^2} - w \frac{\partial \hat{C}}{\partial z} - (s + \lambda)\hat{C} = 0. \tag{2.3}$$

Its solution is

$$\hat{C} = A e^{\frac{w + \sqrt{w^2 + 4\kappa(s+\lambda)}}{2\kappa} z} + B e^{\frac{w - \sqrt{w^2 + 4\kappa(s+\lambda)}}{2\kappa} z}. \tag{2.4}$$

Using the boundary conditions, we get

$A = 1/s$, $B = 0$.

Therefore,

$$\begin{aligned} \hat{C} &= \frac{1}{s} e^{\frac{w + \sqrt{w^2 + 4\kappa(s+\lambda)}}{2\kappa} z} \\ &= \frac{c}{s} e^{-a(s+b^2)^{\frac{1}{2}}}, \end{aligned} \tag{2.5}$$

where $a = -z/\sqrt{\kappa}$, $b = \sqrt{\lambda + w^2/4\kappa}$, and $c(z) = e^{(w/2\kappa)z}$.

Taking an inverse Laplace transform, we get [Roberts et al., 1966]

$$C_t(z, t) = e^{\frac{w}{2\kappa} z} \cdot \left[\frac{e^{-ab}}{2} erfc \left(\frac{a}{2\sqrt{t}} - b\sqrt{t} \right) + \frac{e^{ab}}{2} erfc \left(\frac{a}{2\sqrt{t}} + b\sqrt{t} \right) \right]. \tag{2.6}$$

Here $erfc$ is the complementary error function, defined as

$$erfc(x) = \frac{2}{\sqrt{\pi}} \int_x^\infty e^{-t^2} dt. \tag{2.7}$$

The structures of transient tracers based on analytical solutions have been discussed in detail by Wunsch [2002]. In Eq. (2.6), $a/(2\sqrt{t})$ and $b\sqrt{t}$ dominate the temporal evolution. For a very short time t, $a/(2\sqrt{t})$ is the governing term; for a very long time t, $b\sqrt{t}$ is dominant. Which one is more important depends on the time scale $t \sim (a/2\sqrt{t})/(b\sqrt{t}) \times t \sim a/b \sim O(z/w)$, for a non-decaying tracer. Between the infinitesimal t and infinitely large t, there are two timescales, $a^2 = z^2/\kappa$ determined by mixing, and $1/b^2 = 1/(\lambda + w^2/4\kappa)$ determined by the ratio of advection effect to

mixing effect, or decay rate λ. Even in this simple case, the tracer distribution at its transient stage is a very complicated function of the flow field and mixing rate. For the real ocean, the temporally and spatially varying horizontal advection and mixing rates will lead to more complex expressions. This, as Wunsch [2002] points out, tends to undermine any simple interpretation of observed distributions.

When $t \to \infty$, then $a/(2\sqrt{t}) \ll 1$ and $b\sqrt{t} \gg 1$, the tracer will reach a steady state, which can be represented as

$$
\begin{aligned}
C_d(z) &= e^{\left(\frac{w}{2\kappa} + \frac{\sqrt{\lambda + w^2/4\kappa}}{\sqrt{\kappa}}\right)z} \\
&= e^{\left(\frac{w}{2\kappa} + \frac{\sqrt{4\kappa\lambda + w^2}}{2\kappa}\right)z},
\end{aligned}
\tag{2.8}
$$

by substituting $erfc\,(-\infty) = 2$ and $erfc\,(\infty) = 0$ into Eq. (2.6). For a stable tracer $(\lambda = 0$), Eq. (2.8) becomes

$$
C_s(z) = e^{(w/\kappa)z}.
\tag{2.9}
$$
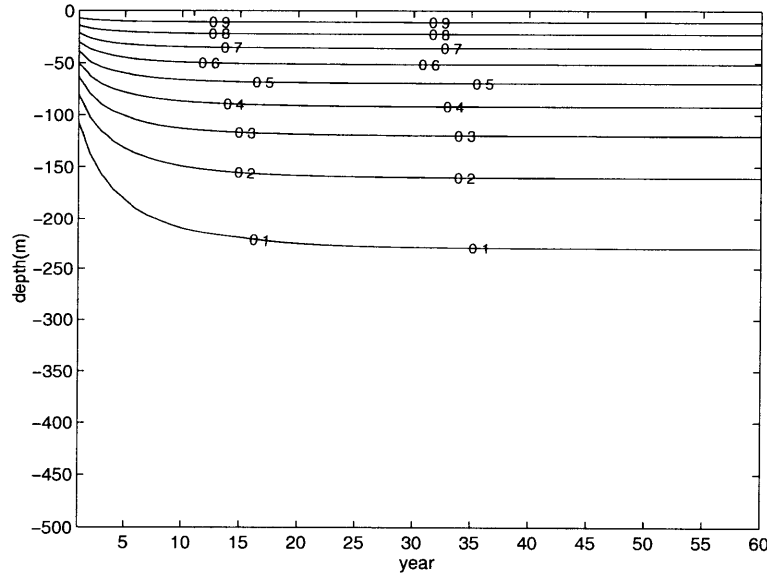
Figure 2-1: Evolution of the idealized tracer concentration with $w = 10^{-6}$ m/s, $\kappa = 10^{-4}$ m^2/s, and $\lambda = 0$.

Take $w = 10^{-6} m/s$, $\kappa = 10^{-4} m^2/s$ [e.g., Munk and Wunsch, 1998], and $\lambda = 0$ in the above equations. The tracer distribution represented by Eq. (2.6) is shown in

Fig. 2-1. Thirty years later, a steady state is reached. The downward diffusion is balanced by the upwelling. The vertical penetration scale is given by k/w, with this information clearly exhibited by the steady state.

A clear difference between the steady states of a stable tracer and a decaying tracer is that the latter contains information about $b = \sqrt{\lambda + w^2/4\kappa}$ and $1/\sqrt{\kappa}$ (Eq. (2.8)), mathematically. Take $\lambda = 3.836 \times 10^{-12}$ s^{-1}, corresponding to a half-life of 5730 years for natural radiocarbon. Figure 2-2 shows the concentration difference between the decaying (Eq. (2.8)) and the stable (Eq. (2.9)) tracer at year 6000 in the same 1-D pipe flow. The maximum difference is less than 0.1% of the tracer concentration, which is uncomfortably small and cannot be distinguished from a data error of 1% uncertainty, in this simplified 1-D case. We refer to the idealized tracer as the one that does not decay hereafter.
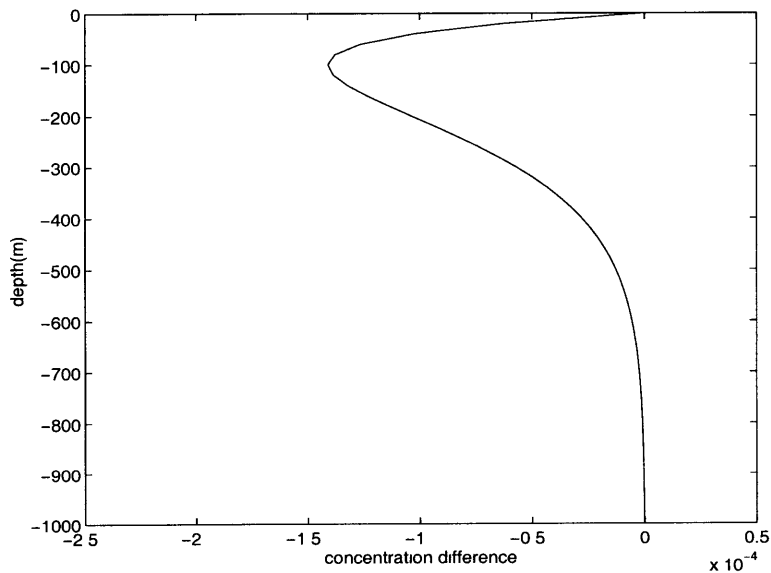
Figure 2-2: Concentration difference between a decaying tracer ($\lambda = 3.836 \times 10^{-12}$ s^{-1}) and a stable tracer at year 6000 in a pipe flow with $w = 10^{-6} m/s$ and $\kappa = 10^{-4} m^2/s$. Both tracers are forced by a unit step surface concentration.

Extracting information about $b = \sqrt{\lambda + w^2/4\kappa}$ and $1/\sqrt{\kappa}$ from the tracer distributions in the transient stage (Eq. (2.6)) might be even harder than from the steady state distribution of the decaying tracer (Eq. (2.8)), because the information is entan-

41

gled with various complicated timescales. In the real ocean, the boundary histories of transient tracers are generally not well known. Adding any transient tracer measurement at time t_0 in an inverse calculation will introduce additional variables of boundary conditions at t_0. This makes extracting circulation information from the transient tracer measurements more difficult. Numerically, we can do some inversions to infer flow properties from the idealized tracer distributions. This will be presented in the next section.

2.1.2 Numerical results

For a more general case, following Wunsch [1987], Eq. (2.1) is discretized with a centered-in-space scheme as

$$
\begin{aligned}
\frac{\partial C_i}{\partial t} &= C_{i-1}\left[\frac{wT}{2\triangle z} + \frac{\kappa T}{(\triangle z)^2}\right] + C_i\left[-\lambda T - \frac{2\kappa T}{(\triangle z)^2}\right] + C_{i+1}\left[-\frac{wT}{2\triangle z} + \frac{\kappa T}{(\triangle z)^2}\right] + Tq_i \\
&= C_{i-1}\left[\frac{\bar{c}}{2} + d\right] + C_i\left[l - 2d\right] + C_{i+1}\left[-\frac{\bar{c}}{2} + d\right] + Tq_i.
\end{aligned}
\tag{2.10}
$$

Here T is a dimensional timescale, t is now dimensionless, $\bar{c} = wT/\triangle z$, $d = \kappa T/(\triangle z)^2$, and $l = -\lambda T$. The above equation can be written as

$$
\frac{\partial \mathbf{X}(t)}{\partial t} = \mathbf{A}\mathbf{X}(t) + \mathbf{q},
\tag{2.11}
$$

where the state vector $\mathbf{X} = \{C_i(t)\}$, and the state transition matrix is

$$
\mathbf{A} = \begin{pmatrix}
0 & 0 & 0 & \dots & 0 & 0 & 0 \\
\gamma & \alpha & \beta & \dots & 0 & 0 & 0 \\
0 & \gamma & \alpha & \beta & 0 & \dots & 0 \\
& & \dots & & & \dots & \\
0 & 0 & \dots & 0 & \gamma & \alpha & \beta \\
0 & 0 & 0 & \dots & 0 & 0 & 0
\end{pmatrix},
$$

with $\gamma = \bar{c}/2$, $\alpha = l - 2d$, and $\beta = -\bar{c}/2 + d$. The first and last rows are fixed by boundary conditions which are imposed through q.

If w, κ, and λ are constant, **A** will be a constant matrix. The solution for (2.11) will be

$$\mathbf{X} = e^{\mathbf{A}t} + \int_0^t e^{\mathbf{A}(t-t')}\mathbf{q}dt'. \tag{2.12}$$

A steady state will be reached if all eigenvalues of **A** are negative for continuous time, or all eigenvalues of $\mathbf{A_1}$ are less than 1 for discrete time [e.g., Levine, 1996].

Equation (2.11) is discretized in time for computational convenience

$$\mathbf{X}(t + \triangle t) = \mathbf{A_1}\mathbf{X}(t) + \mathbf{q}', \tag{2.13}$$

where $\mathbf{A_1} = \mathbf{I} + \triangle t\mathbf{A}$, $\mathbf{q}' = \triangle t\mathbf{q}$.

First, let us examine the responses of the idealized tracer distribution to variations of κ, the most common circulation property inferred from transient tracer distributions. Figure 2-3 shows the evolution of the idealized tracer distribution in flows with different κ, with a fixed $w = 10^{-6}$ m/s. Obviously, the depth at which the tracer penetrates changes dramatically with different κ. When κ is 10^{-3} m^2/s, the diffusion process is strong and the tracer penetrates deeply. When κ becomes very small, say 10^{-5} m^2/s, tracer concentration is confined to the surface.

The inverse problem is to infer flow properties, such as the mixing rate, from tracer distributions. The flow velocity is usually not our primary interest, because it can be obtained from dynamic theories and direct measurements. Kelley et al. [1999] estimate the vertical diffusivity κ_v in the upper subtropical North Pacific, by fitting tritium profiles to a reflected-Gaussian profile, a solution to a 1-D advection-diffusion equation. The reflected-Gaussian profile is expressed as

$$C \propto exp\left(-\frac{1}{2}\frac{(z - z_0 + wt)^2}{D^2} \right) + exp\left(-\frac{1}{2}\frac{(z + z_0 + wt)^2}{D^2} \right), \tag{2.14}$$

where $D = \sqrt{2\kappa t}$. Unfortunately, this solution does not satisfy the surface boundary condition prescribed by Kelley et al. [1999]. Using this wrong solution, Kelley et al.

43
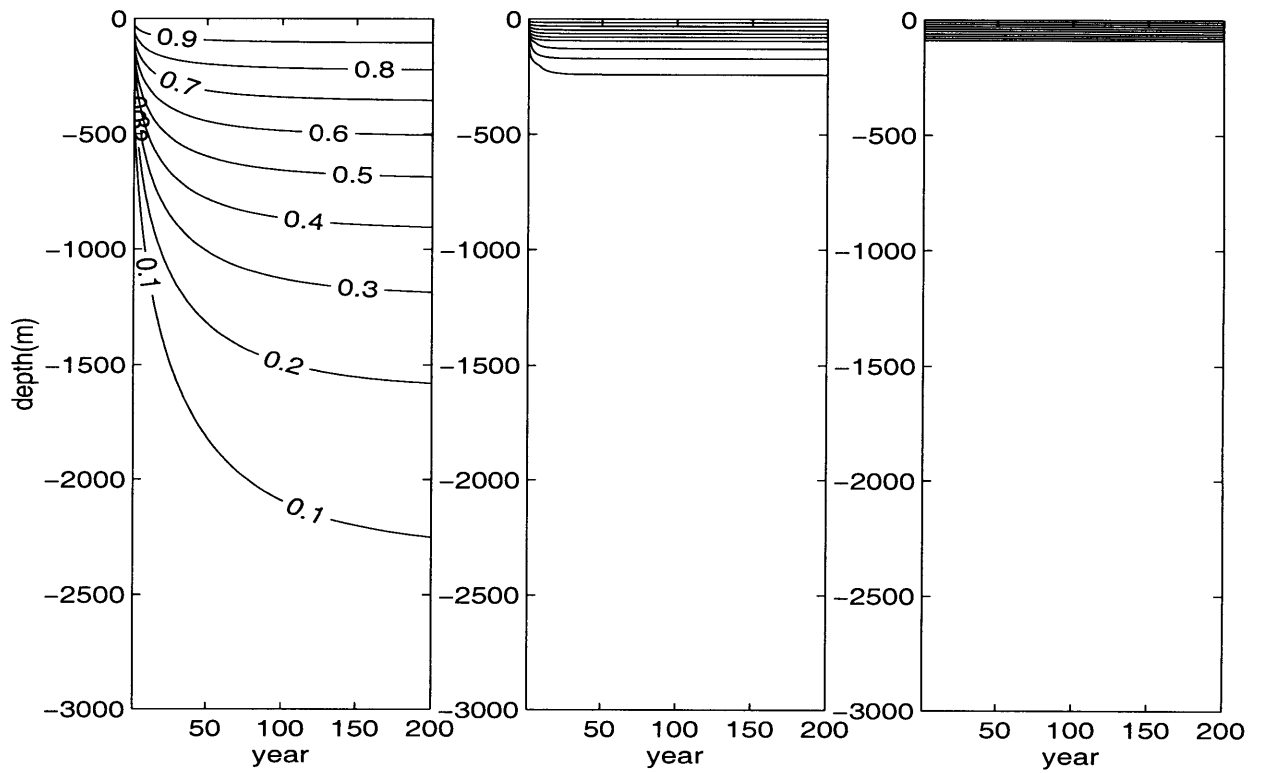
Figure 2-3: Evolution of tracer distribution with different κ (m^2/s): 10^{-3} (left), 10^{-4} (middle), and 10^{-5} (right). w and λ are 10^{-6} m/s and 0 s^{-1}, respectively. Note the different depths at which the tracer penetrates in the steady states.

44

[1999] obtained a vertical diffusivity of $(1.5\pm0.7)\times10^{-5}$ m^2/s in the upper subtropical North Pacific, whose significance is unclear.

Haine et al. [1998] give a vertical diffusivity of 3 - $7\times10^{-4}m^2/s$ for the transport of Antarctic Bottom Water (AABW) into the southwest Indian Ocean, using CFC observations. In Haine et al. [1998], CFC data are fitted to plume-shape CFC distributions, based on an along-stream advection and cross-stream mixing model. These two inferences of κ_v for two different regions differ in an order of magnitude. In both Kelley et al. [1999] and Haine et al. [1998], uncertainties in the transient tracer boundary conditions are ignored.

Equation (2.6) shows that the transient distribution of the idealized tracer with a simple boundary condition, in a simple pipe flow, is very complicated. Distributions of real transient tracers, with uncertain time-varying boundary histories, are governed by the complex ocean circulation. Representing oceanic transient tracer distributions as simple patterns introduces large uncertainties. Microstructure data [e.g., Polzin et al., 1997] and purposefully released tracer measurements [e.g., Ledwell, 1993 etc.] show that vertical mixing in the interior ocean varies from $O(1.0 \times 10^{-5})$ m²/s to $O(1.0 \times 10^{-4})$ m²/s. Accurate inferences of vertical mixing rates are fundamentally important for understanding and interpreting the associated physical mechanisms. The inverse study of the idealized tracer in the following will examine how the uncertainty in the transient tracer boundary conditions influences the accuracy of inferences.

Given perfect tracer distributions, the inverse problem can be solved by searching for the global minimum of the cost function,

$$J = \sum_{i=1}^{n}(C_m^i - C_{obs}^i)^2. \tag{2.15}$$

Here C_m and C_{obs} are the modeled and observed tracer concentrations, respectively.

In an ideal case, suppose we have perfect "observations" sampled every 20 m in a water column of 4000 m every year during years 1 to 20, in the model with $w = 10^{-6}$ m/s, $\kappa = 10^{-4}m^2/s$, and $\lambda = 0$. Figure 2-4 shows J as a function of w and κ, with the surface boundary condition perfectly known. By searching for the global minimum of
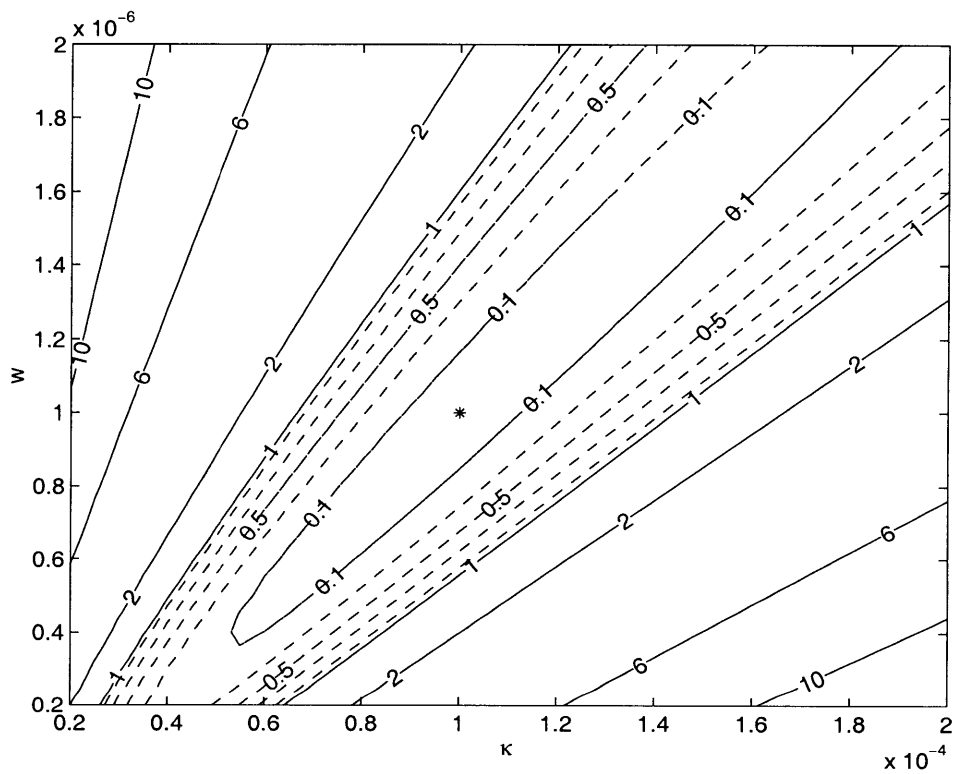
Figure 2-4: J as a function of w and κ . The minimum point J=0 is indicated by the star. Near the line $w/\kappa = 10^{-2}$, J is small (if J=0.1, the root-mean square difference of model-data misfit will be 0.005).

J with expected minimal value of 0, the inversion gives $w = 10^{-6}$ m/s and $\kappa = 10^{-4}$ m^2/s. We should note that, however, near the line $w/\kappa = 10^{-2}$, the cost function is sufficiently small. For example, if J=0.1, the root-mean square difference of model-data misfit will be 0.005, about two orders less than the tracer concentration. This means it is the ratio w/κ that mostly determines where the cost function is the smallest. The steady state can clearly indicate this ratio, from the depth at which the tracer penetrates. In a real data-assimilation experiment, we cannot expect that the cost function drops to zero due to data errors and uncertainties in transient tracer boundary conditions. Once model-data misfits fall within the errorbars of data and model, the data cannot provide any new information to the model.

Inevitably, both data and boundary conditions contain noise. We have to reconstruct the noise contaminated boundary values to infer κ. The inverse calculation uses the adjoint method, which adjusts boundary conditions and circulation parameters in the meantime. The cost function is expressed as

$$J(\mathbf{X}, \mathbf{U}) = (\mathbf{X} - \mathbf{X}_{obs})^T \mathbf{R}^{-1} (\mathbf{X} - \mathbf{X}_{obs}) + (\mathbf{U} - \mathbf{U}')^T \mathbf{Q}^{-1} (\mathbf{U} - \mathbf{U}'). \qquad (2.16)$$

Here $\mathbf{U}$ is the control vector, comprising the model parameters to be constrained by observations $\mathbf{X}_{obs}$. $\mathbf{R}$ and $\mathbf{Q}$ are error covariance matrixes of observations and controls, respectively. For more details, see Appendix A.

Suppose we have "observations" sampled each year at different locations (Fig. 2-5). A white noise with a standard deviation of 0.1 is added to these "observations". We can imagine that the noise corresponds to instrumental errors and subgrid scale variabilities that the model cannot resolve. Also suppose our initial estimates of the surface concentrations are biased and are 30% lower than the true, i.e., the unit step surface concentration. We now use these "observations" to constrain κ and the surface tracer concentrations, which are allowed to vary independently each year.

The inversion gives $\kappa = 1.97 \times 10^{-4}$ m^2/s, which is about 100% larger than the correct value, i.e., 1.00×10^{-4} m^2/s. Figure 2-6 shows the constrained tracer distribution. Obvious adjustments of the surface values appear only at locations
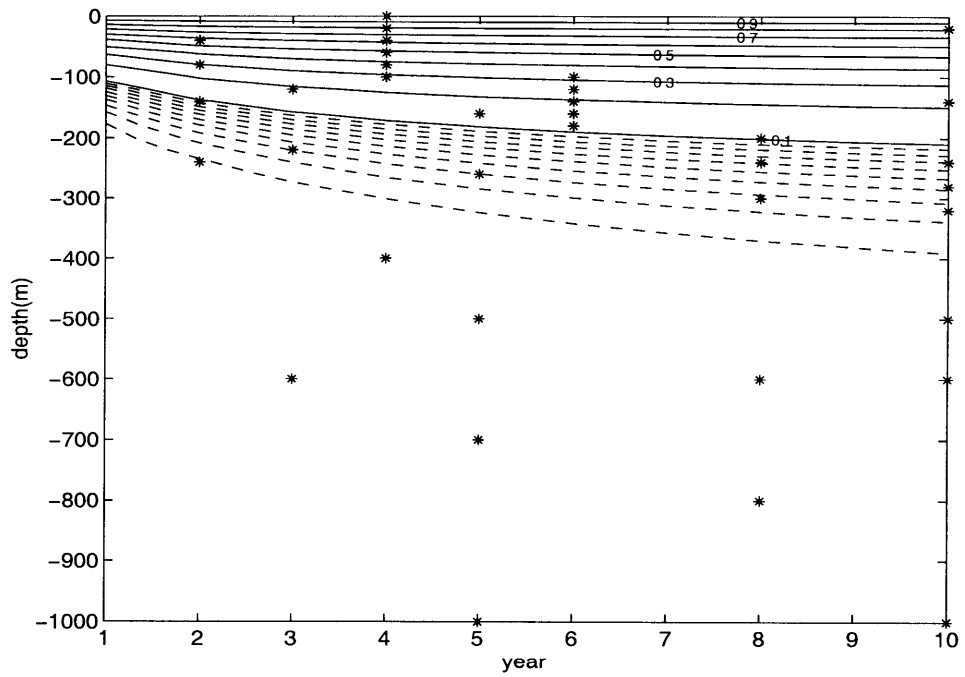
Figure 2-5: Locations (denoted by stars) of model-produced "observations". The background is the evolution of the idealized tracer concentration in a pipe flow with $w = 10^{-6}$ m/s and $\kappa = 10^{-4}$ m^2/s. Contour intervals are 0.01 and 0.1 for concentration below 0.1 (dashed lines) and above 0.1 (solid lines), respectively.

where observations are available near the surface. After the "data" are assimilated, most surface concentrations are still about 0.7, 30% lower than the true. Even though the tracer distribution given by the inversion does not totally agree with the true one, the model and the "data" are consistent at observational locations. The model-data misfits fall within the errorbars, as shown in Fig. 2-7. Since there still exists 30% uncertainty in the surface tracer concentration estimates after optimization, κ is not accurately constrained to the correct value by the transient state observations.
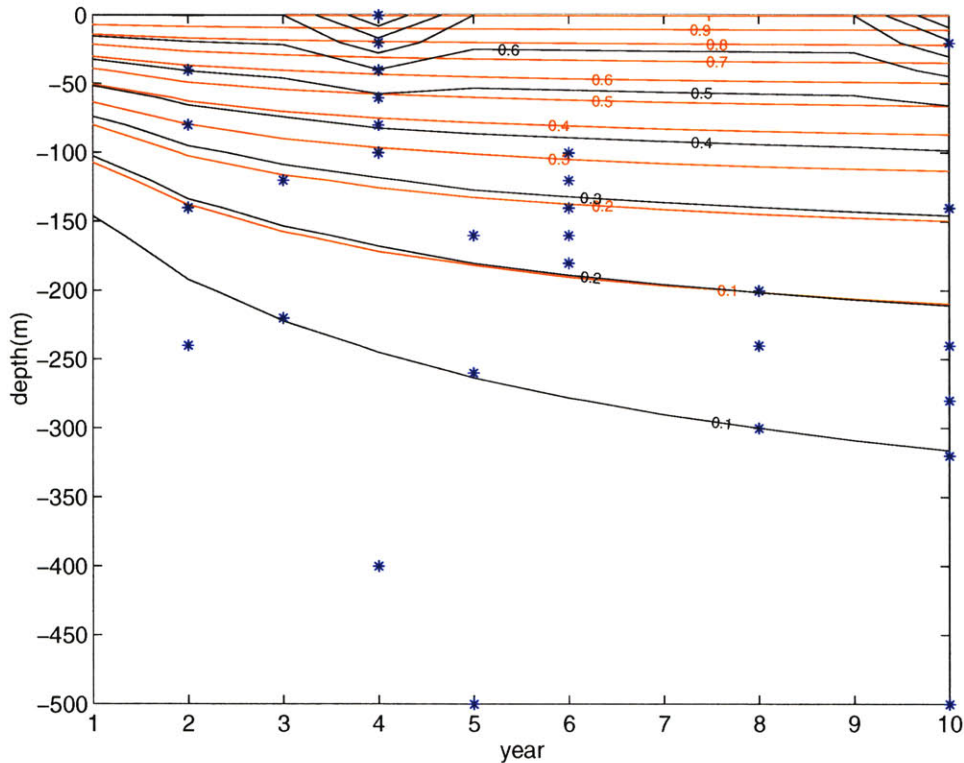
Figure 2-6: Distribution of the tracer concentration (black lines) given by the inversion and the distribution of the idealized tracer concentration (red lines) in the pipe flow with $w = 10^{-6} \ m/s$ and $\kappa = 10^{-4} \ m^2/s$. Locations of "observations" are denoted by stars.

For steady tracers, we can combine observations sampled at different times to form a complete vertical profile. From this vertical profile we can easily obtain w/κ. If w is relatively well known, we can infer κ from w/κ. Suppose we have steady state "observations" as shown in Fig. 2-8, distributed similarly to transient state "observations" in Fig. 2-5. The true state is the steady distribution of the idealized

49
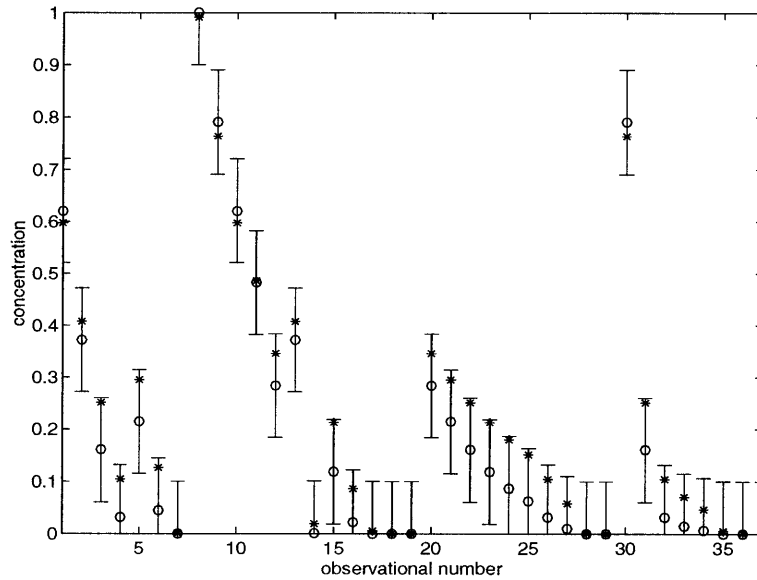
Figure 2-7: Constrained model (star) and observational (circle) tracer concentrations. Errorbars represent a white noise with standard deviation of 0.1. Notice that the model-data misfits fall within the errorbars. The "observations" in Fig. 2-5 are numbered from the top to the bottom and from early to late years. This numbering method leads to the chains of tracer concentration in the figure.

tracer in the flow with $w = 10^{-6}$ m/s and $\kappa = 10^{-4}$ m^2/s. The same white noise with a standard deviation of 0.1 embedded in the transient state "observations" is added to the steady state "observations". Our initial estimate of the steady state surface concentration is also biased, 30% lower than the true value. In this steady tracer inverse problem, we only have two control variables, κ and the steady surface tracer concentration. The inversion first adjusts κ (Fig. 2-9), to which the 1-D tracer distribution pattern is very sensitive. At iteration 8, κ is adjusted to 1.10×10^{-4} m^2/s and the surface concentration is adjusted to $C_{z=0} = 0.97$, very close to the true values. Finally, the inversion gives $\kappa = 1.05 \times 10^{-4}$ m^2/s and $C_{z=0} = 1.00$.

With the same noise in the "data" and uncertainty in the first estimates of boundary conditions, the steady state "observations" successfully constrain κ and the steady surface tracer concentration to the correct values; the transient state "observations", however, cannot effectively constrain the large number of yearly-varying surface concentrations. Consequently, κ is not constrained to the correct value by the transient
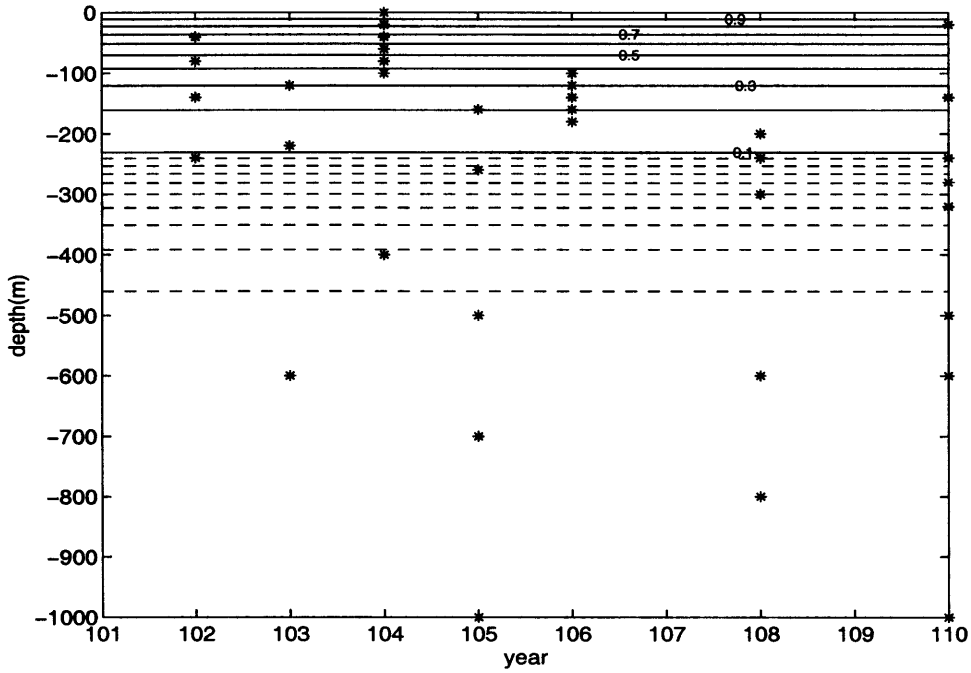
Figure 2-8: Locations (denoted by stars) of steady state "observations". The background is the steady state of the idealized tracer in a pipe flow with $w = 10^{-6}$ m/s and $\kappa = 10^{-4}$ m^2/s. Contour intervals are 0.01 and 0.1 for concentration below 0.1 (dashed lines) and above 0.1 (solid lines), respectively.
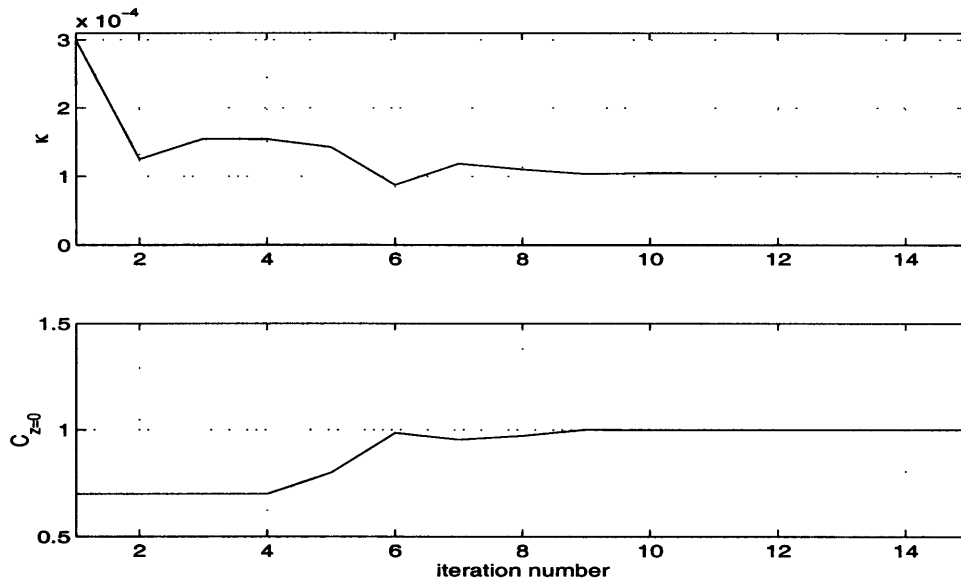
Figure 2-9: Values of κ and the surface tracer concentration during the inversion using steady state "observations".

state "observations". This raises a warning flag: a biased estimate of one parameter will lead to a biased estimate of another. For the transient tracer inverse problem, a physically acceptable estimate of the boundary conditions is a prerequisite for reasonable inferences of circulation properties.

Equation (2.6) mathematically shows that the transient distribution is a function of w/κ, $1/\sqrt{\kappa}$ and w^2/κ. The information concerning $1/\sqrt{\kappa}$ and w^2/κ, however, is entangled in time in a complicated fashion. A practical problem is whether we can really take advantage of this information to infer the circulation. With the same transient stage "observations" in Fig. 2-5 and biased surface concentration estimates of 30% uncertainty, we now try to infer w and κ. Starting at different initial guesses, the inversion gives different solutions. The following table lists some of the solutions, all of which can bring the "data" and model into consistency. The existence of these

Table 2.1: Inverse solutions for w and κ, using transient stage "observations".

flow property	inverse solutions			
w (10^{-6} m/s)	3.09	2.20	0.6	0.34
κ (10^{-4} m^2/s)	4.10	2.81	1.19	0.81

different solutions is consistent with the fact that the model-data misfits near the line $w/\kappa = 10^{-2}$ are significantly smaller than the starting values. Inferring both w and κ from the transient tracer "observations" without other physical constraints can easily lead to erroneous solutions that are an order of magnitude far from the true values.

The next step is to examine whether a decaying transient tracer with accurately known λ has some advantages in providing information about the circulation. Take $\lambda = 1.768 \times 10^{-9}$ s^{-1}, corresponding to a half life of 12.43 years for tritium. We sample this decaying tracer concentration in a flow with $w = 1.0 \times 10^{-6}$ m/s and $\kappa = 1.0 \times 10^{-4}$ m^2/s at different locations and times from year 1 to 20, shown in Fig. 2-10. A unit step surface concentration is used to produce the true state. These "observations" are used to infer w and κ. Again suppose the first estimates of the surface tracer values are 30% lower than the true ones. Three pairs of solutions are shown in Table 2.2. There still exist several different solutions, some of which are
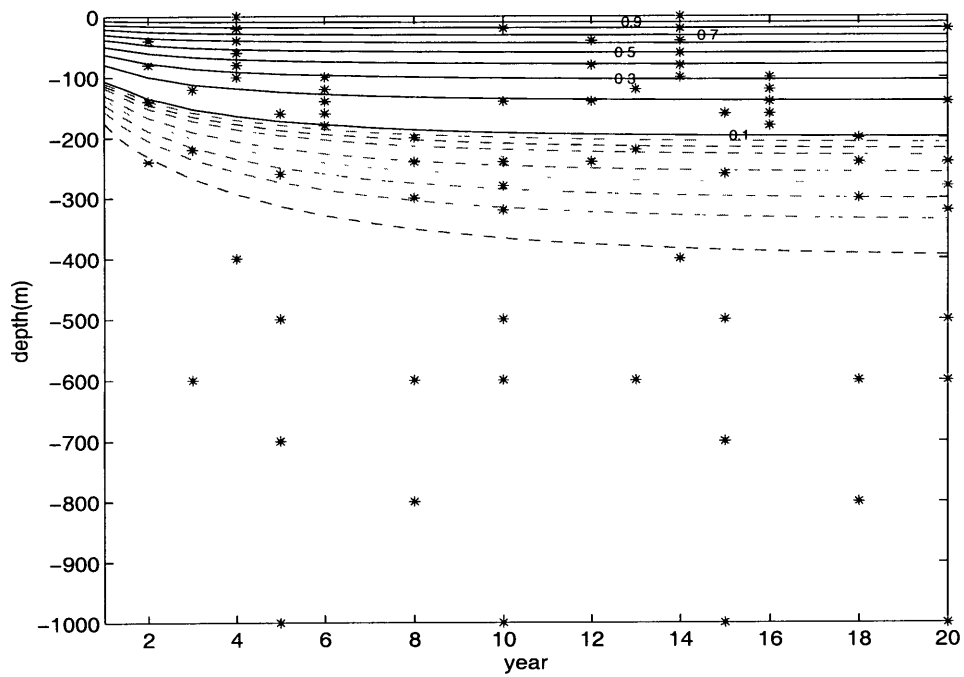
Figure 2-10: Locations (denoted by stars) of the decaying ($\lambda = 1.768 \times 10^{-9}$) tracer "observations". The background is the tracer distribution in a pipe flow with $w = 10^{-6}$ m/s, $\kappa = 10^{-4}$ m^2/s, forced by a unit step surface concentration. Contour intervals are 0.01 and 0.1 for concentration below 0.1 (dashed lines) and above 0.1 (solid lines), respectively.

Table 2.2: Inverse solutions for w and κ, using the decaying tracer "observations".

flow property	inverse solutions		
w (10^{-6} m/s)	3.27	1.46	0.27
κ (10^{-4} m^2/s)	4.11	1.82	0.66

far from the true values. Without an accurate estimate of the flow field, inferring both flow field and mixing rate from the sparse transient stage "observations" with uncertain boundary history is not successful, in the above idealized experiments.

As a transient tracer measurement provides integrated information about the ocean circulation, we often study the transient tracers in the background of large scale mean circulation. Generally, there are many variabilities in the ocean. How does short timescale variability influence the tracer fields? Figure 2-11 shows the evolution of the tracer concentration in a purely periodic flow $w = (10^{-6}/\sqrt{2})cos(\sigma t)$ m/s with a period of 30 days. The evolution pattern is constructed from vertical profiles sampled every year. Experienced eyes will see immediately that this evolution pattern represents a purely diffusive case. The steady inverse solution for this oscillating flow is its mean, i.e., zero. If w is changed to $10^{-6} + (10^{-6}/\sqrt{2})cos(\sigma t)$ m/s with σ the same, the tracer distribution (not show here) is the same as that in Fig. 2-1. The steady inverse solution of this w is its mean: 10^{-6} m/s. The impact of fast fluctuations whose timescales are far less than the timescale of transient tracer input history and sampling period can be ignored.

Figure 2-12 shows evolution of the idealized tracer in an oscillating flow $w = 10^{-6} + (10^{-6}/\sqrt{2})cos(\sigma t)$ m/s with a period of 2 years. The yearly fluctuation has clear signatures, in both transient and steady states. Obvious variability appears in the upper 100 m. To capture this fluctuation, the tracer field should be sampled at an adequate frequency [e.g., Wunsch, 1996].

If the period of flow oscillation is a decade, a timescale comparable to the transient time, the fluctuation becomes obvious in the deep ocean (Fig. 2-13). The variability is still observable in the transient stage distribution, which does not periodically vary with time. When the tracer distribution approaches its equilibrium, the distribution
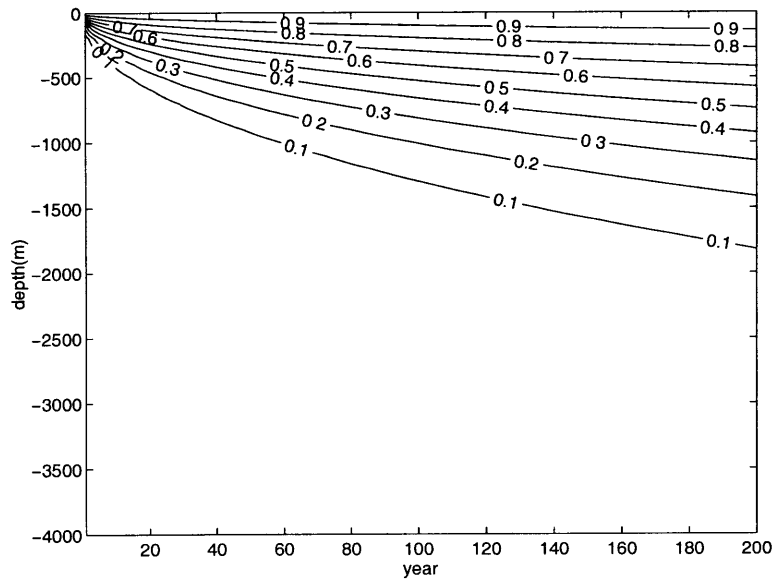
Figure 2-11: Evolution of the idealized tracer concentration in an oscillating pipe flow. $w = (10^{-6}/\sqrt{2})cos(\sigma t)$ m/s, with a period $T = 2\pi/\sigma = 30$ days. κ is the same as in Fig. 2-1.
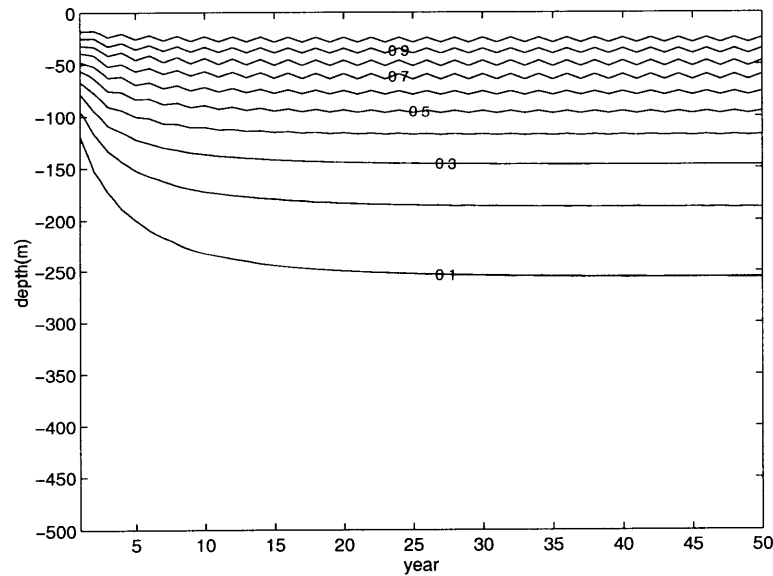
Figure 2-12: Evolution of the idealized tracer concentration in an oscillating pipe flow. $w = 10^{-6} + (10^{-6}/\sqrt{2})cos(\sigma t)$ m/s, with a period $T = 2\pi/\sigma = 2$ years. κ is the same as in Fig. 2-1.

55

oscillates periodically. We can easily infer the oscillating period from the steady state distribution.
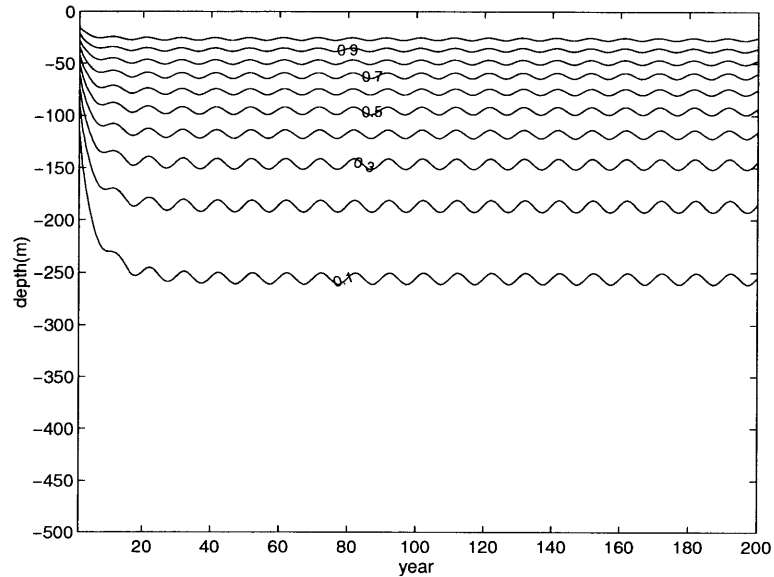
Figure 2-13: Evolution of the idealized tracer concentration in an oscillating pipe flow. $w = 10^{-6} + (10^{-6}/10)cos(\sigma t)$ m/s, with a period $T = 2\pi/\sigma = 10$ years. κ is the same as in Fig. 2-1.

If the flow oscillates on a timescale much longer than the transient time, the variability is not clear in the transient state distribution (Fig.2-14). Only the steady state can capture this fluctuation of the flow field. Using tracer fields to investigate temporal variabilities in the ocean is not an emphasis of this study. This 1-D study shows that, however, variabilities in the flow field have clearer signatures in the steady tracer fields.

This 1-D study of the idealized tracer is highly simplified. Transient tracer distributions in the real ocean are far more complicated than those in the 1-D cases. Next we go to the 3-D modeling of this idealized tracer.

56
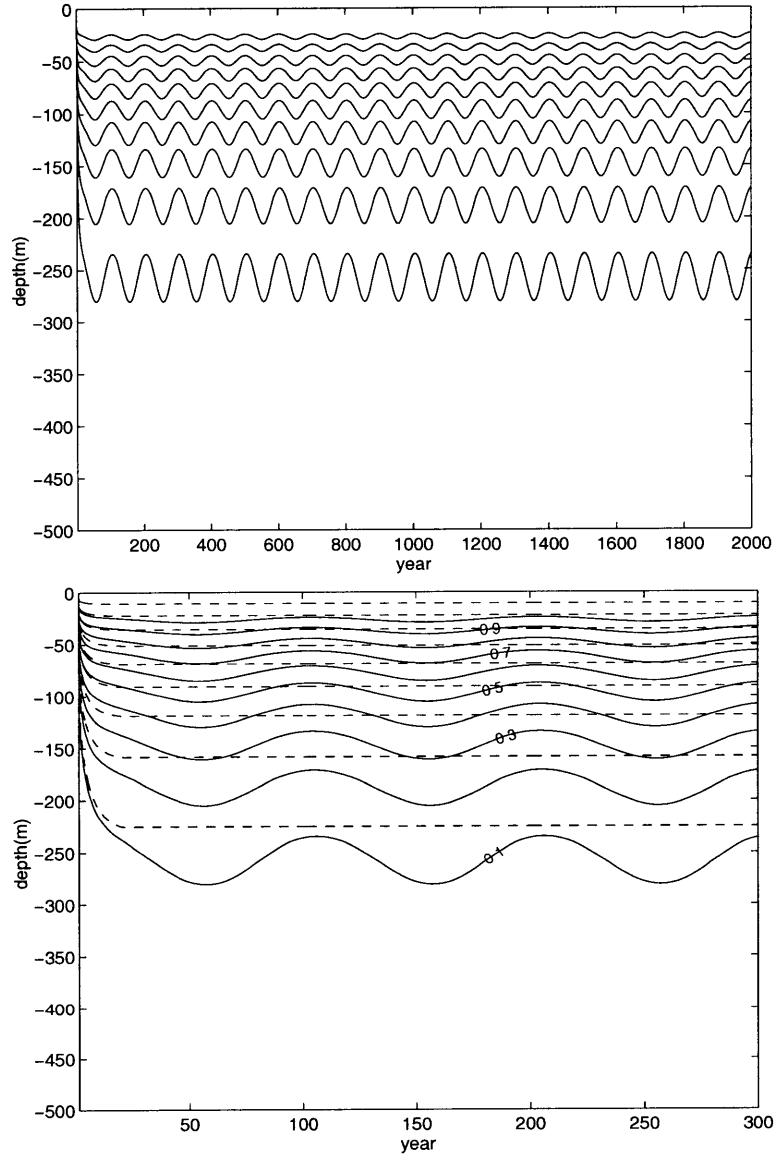
Figure 2-14: Evolution of the idealized tracer concentration in an oscillating pipe flow. $w = 10^{-6} + (10^{-6}/10)cos(\sigma t)$ m/s, with a period $T = 2\pi/\sigma = 100$ years. The lower panel shows the tracer evolution in the first 300 years. Dashed lines represent tracer distribution in a steady pipe low with $w = 10^{-6}$ m/s. κ is the same as in Fig. 2-1.

2.2　Three-dimensional model experiments

Evolution of the same idealized tracer is simulated in an offline version of MIT GCM of the North Atlantic. In this section, the offline model is introduced first. Then the propagation of the idealized tracer is presented to show the ventilation processes in the model. Simple examples of inversion are shown last, to familiarize readers with the 3-D adjoint calculation.

2.2.1　Description of the model

The offline model is based on the equation,

$$\frac{\partial C}{\partial t} = -\nabla \cdot (\vec{u}C) + \nabla \cdot (\mathbf{K}\nabla C) + S + Con, \tag{2.17}$$

where C is the tracer concentration, $\mathbf{K}$ is the mixing tensor, S is sources/sinks, and Con represents vertical mixing due to convection.

The Gent and McWilliams mixing scheme [Gent et al., 1990, 1995] is used to parameterize the eddy-induced tracer transport. In both the offline and the online model, the mixing coefficient is a function of the large scale Richardson number as recommended by Visbeck et al. [1997]. The 3-D flow fields $\vec{u}$ are the monthly mean circulation fields in the MIT GCM from 1987 to 1995. In the offline version, convective mixing is carried out by allowing vertically adjacent grid cells to homogenize tracer concentration when a hydrodynamically unstable condition appears. The monthly statistics of convective mixing in the GCM uses a diagnostic convective index, the frequency of the convection in the MIT GCM. The deep mixed layers are formed only by convection of vertically unstable waters.

Spatial coordinates of the offline model are longitude, latitude, and height. The offline model extends from 99.5°W to 21.5°E, 4.5°S to 79.5°N at $1^o \times 1^o$ horizontal resolution with an entirely closed wall at the northern boundary. There are 21 vertical levels in the model with nonuniform vertical resolution ranging from 25 m at the surface to 500 m near the ocean bottom. Realistic topography is employed. The

tracer concentration at each surface point is specified to be a unit step function in time. The tracer fluxes at lateral boundaries are set to zero.

The MIT GCM is documented in detail by Marshall et al. [1997a,b]. The model is based on the primitive equations on a sphere with hydrostatic, non-hydrostatic, and quasi-hydrostatic versions. The hydrostatic version under the Boussinesq approximation is used to simulate the large-scale ocean circulation here. The condition of no normal flow is applied to all solid boundaries, the coasts and the bottom. The model is initialized with the Levitus climatology and driven by climatological winds for a "spin-up" period of 40 years. The global ocean is then driven by 12-hourly analyzed winds and surface fluxes of heat and fresh water (obtained from the National Meteorological Center reanalysis) from January 1987 to January 1995.

2.2.2 The idealized tracer distributions in the offline model

One of the reasons for interest in transient tracers is the information they carry about the pathways and rates of surface properties into the ocean interior. Through a combination of advection and mixing, the interior ocean is ventilated. In the ocean, it was found a long time ago that surface water invaded the oceanic thermocline mainly along isopycnal surfaces [Montgomery, 1938; Iselin, 1939]. The fact that the diapycnal mixing process is weak has been confirmed by direct tracer observations [e.g., Ledwell et al., 1993]. The notion that ventilating flows follow isopycnals has served as a foundation for theories explaining the dynamics of the oceanic thermocline [Luyten et al., 1983]. The subduction is a transformation process converting mixed-layer fluid into the thermocline. Only at the end of the winter, can fluid pass from mixed layer into the main thermocline [Stommel, 1979]. Whether transient tracers will provide new information about ventilation will be investigated later. The general pictures of the transport trajectories of surface properties in the unconstrained model will be shown first.

Fig. 2-15 presents the evolution of the idealized tracer concentration in the model at 360 m. The early tracer distribution at this depth shows a strikingly similar pattern to the observed winter mixed-layer-depth (Fig. 2-16). The mixed-layer-depth
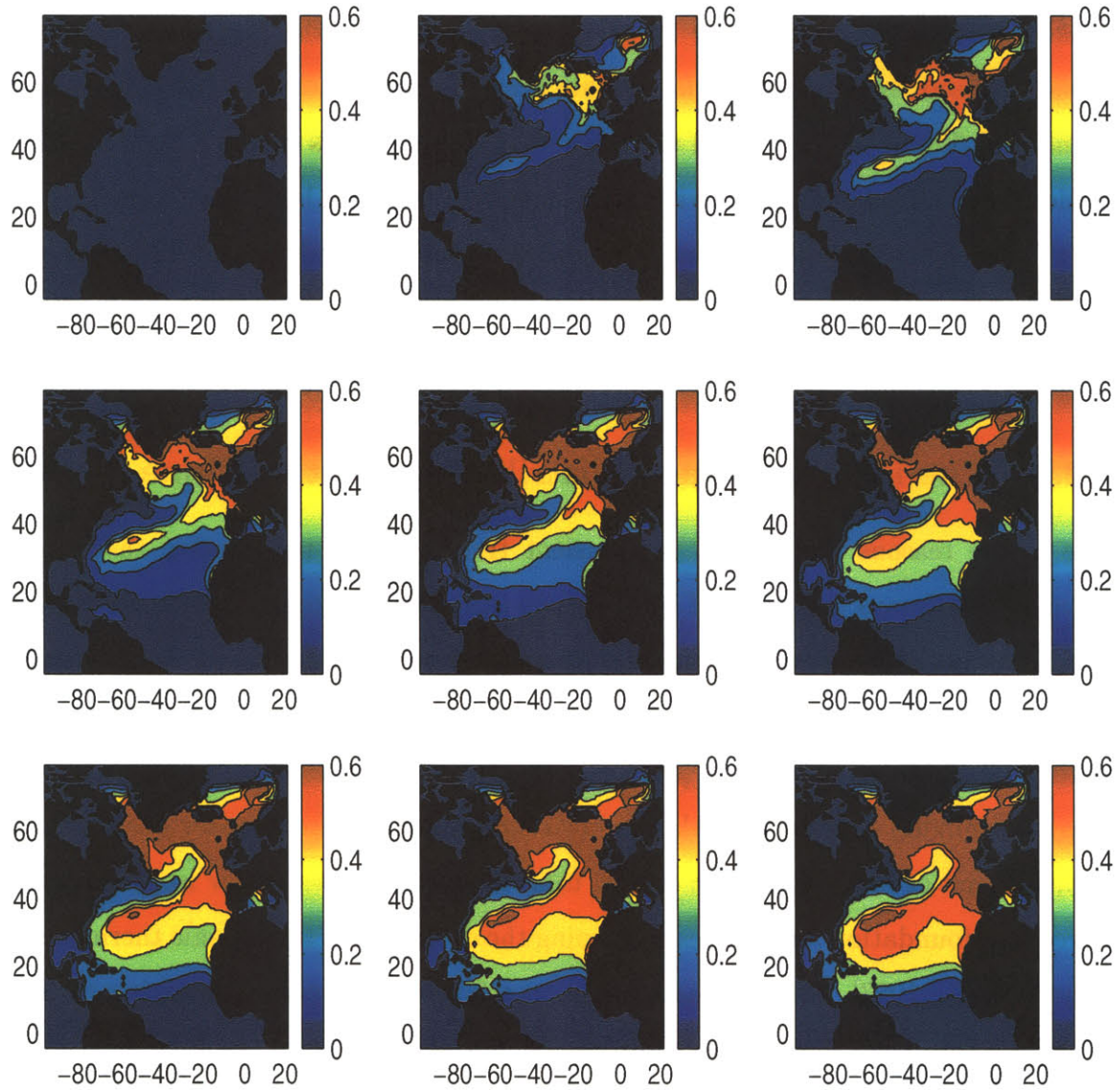
Figure 2-15: Snapshots of the idealized tracer concentration at 360 m depth in the model, from the beginning of year 1 to year 9. A unit step concentration in time is prescribed at each surface grid. The time of the panels increases from left to right, then from the top to the bottom. Land areas are shaded.
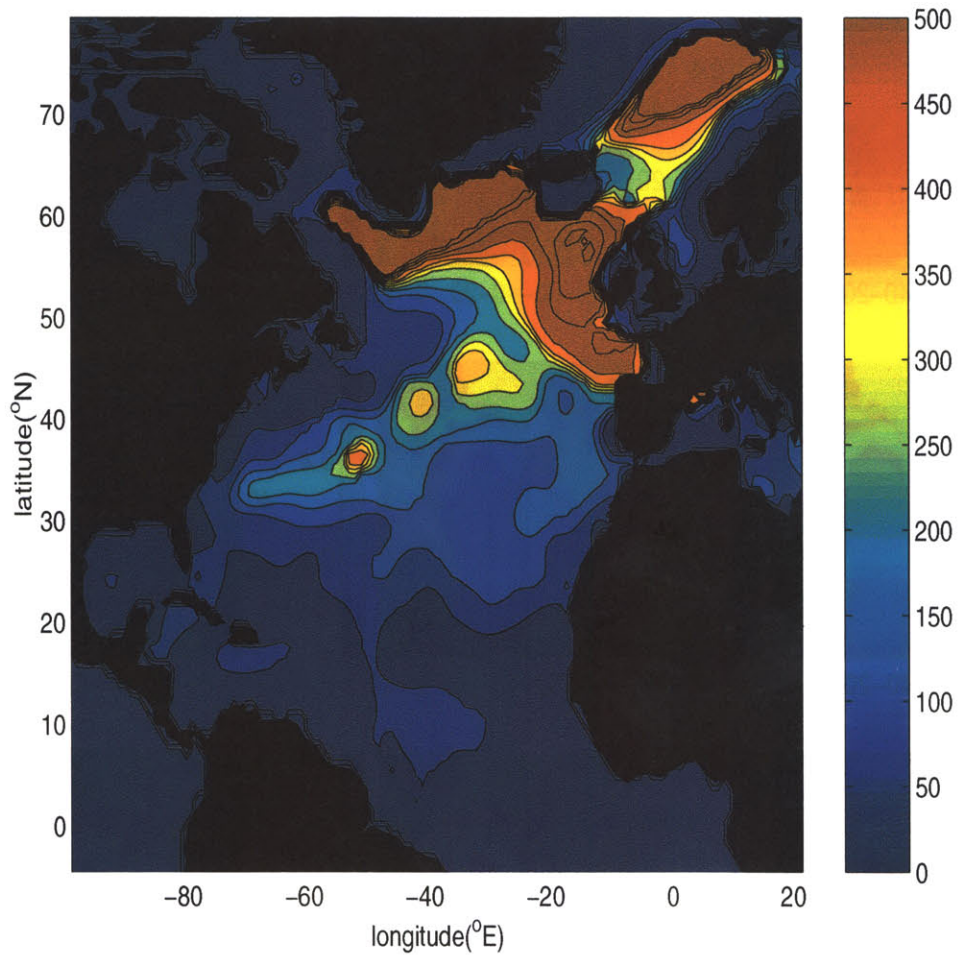
Figure 2-16: Climatological mixed-layer-depth (meter) in March from Monterey et al. [1997]. The contour intervals are 50 m and 200 m for values below and above 400 m, respectively.
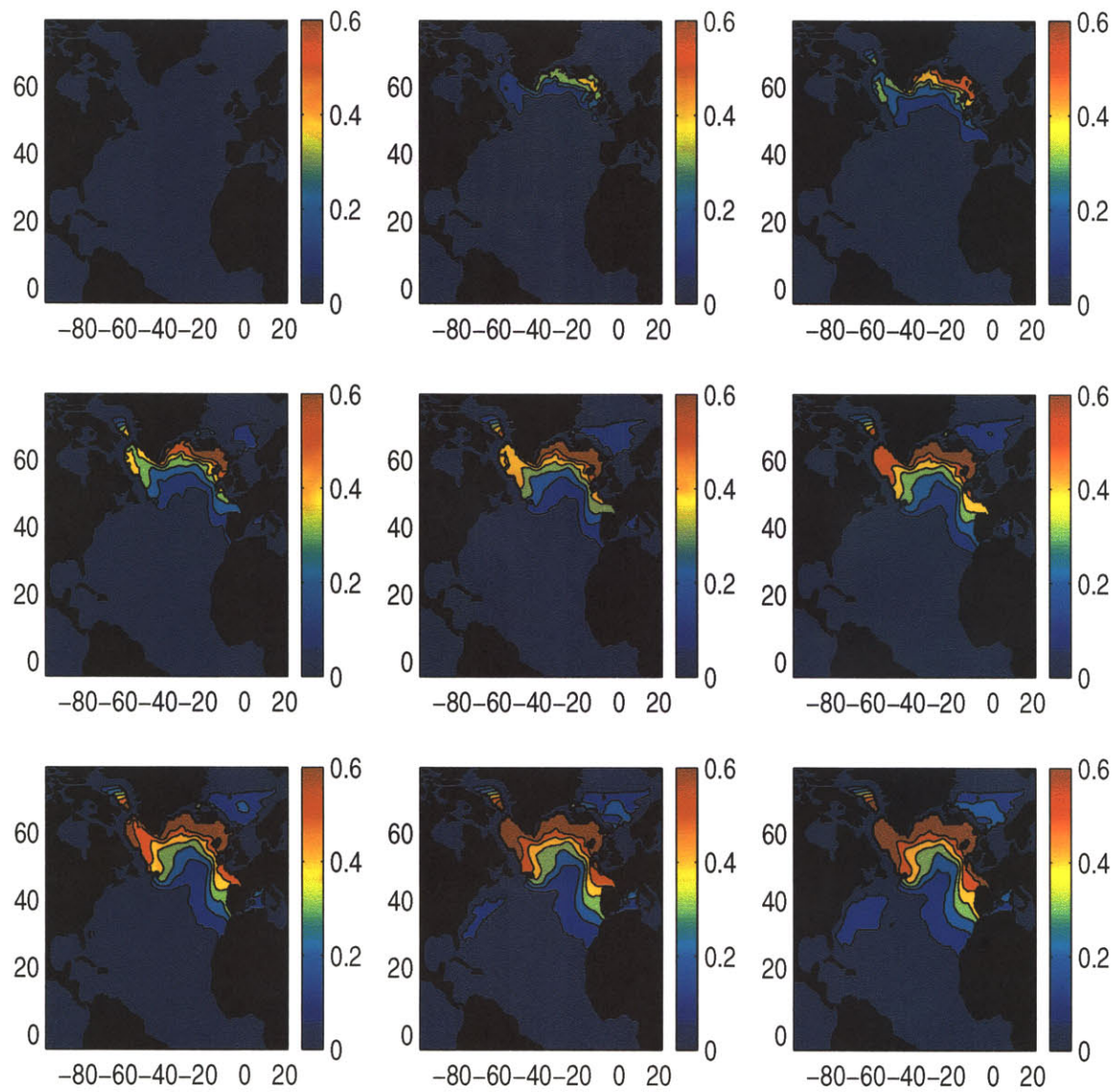
Figure 2-17: Same as Fig. 2-15 but for 710 m depth.

in March, approximately the time of extreme winter convective penetration, exceeds 360 m in some areas of the high and middle latitudes. Therefore, at this depth, the areas where the mixed-layer-depth is greater than 360 m are directly ventilated in late winter. At high latitudes, deep winter convection quickly brings the surface water with high tracer concentration down. In the subtropical gyre, through the interaction of downward pumping by wind-stress and seasonal mixing in late winter, the tracer-enriched surface water can escape irreversibly into the main thermocline. Once the tracer enters the thermocline in the subtropical gyre, it is carried around by the recirculation.

In the lower thermocline, at 710 m depth, the invasion of the idealized tracer into the subtropical gyre is much slower (Fig. 2-17). At this depth, the tracer is introduced to the subtropical gyre from the northeast corner of the gyre, where isopycnals outcrop. Due to the general decrease of current speed with depth, the rate at which the tracer circulates around the gyre is much smaller than that at 360 m depth. The interior flow speed in the eastern basin is less than 1 cm/s, and the diffusive process might play an important role for ventilating the subtropical area at this depth. This will be discussed in detail in Chapter 4.

Figure 2-18 shows the idealized tracer distributions in meridional cross sections. The isolines of the tracer concentration are consistent with typical features of isopycnals. The upward bulge of contours in the equatorial zone and the rise of the isopleths toward the surface between latitudes 40°N and 50°N are prominent. This indicates that water carrying the tracer information spreads almost along isopycnals. Cross-isopycnal diffusion and mixing are secondarily important. In the high latitudes, deep convection can carry the tracer to more than 1000 m deep within a month. The vigorous convection and subduction are the dominant processes responsible for the communication between surface conditions and the subsurface interior in the model.

The modeled tracer concentration at 1750 m depth is shown in Fig. 2-19. The deep water formation region in the high latitudes is marked by high tracer concentration. From there, the NADW carries the tracer southward, with strong signals near the western boundary.
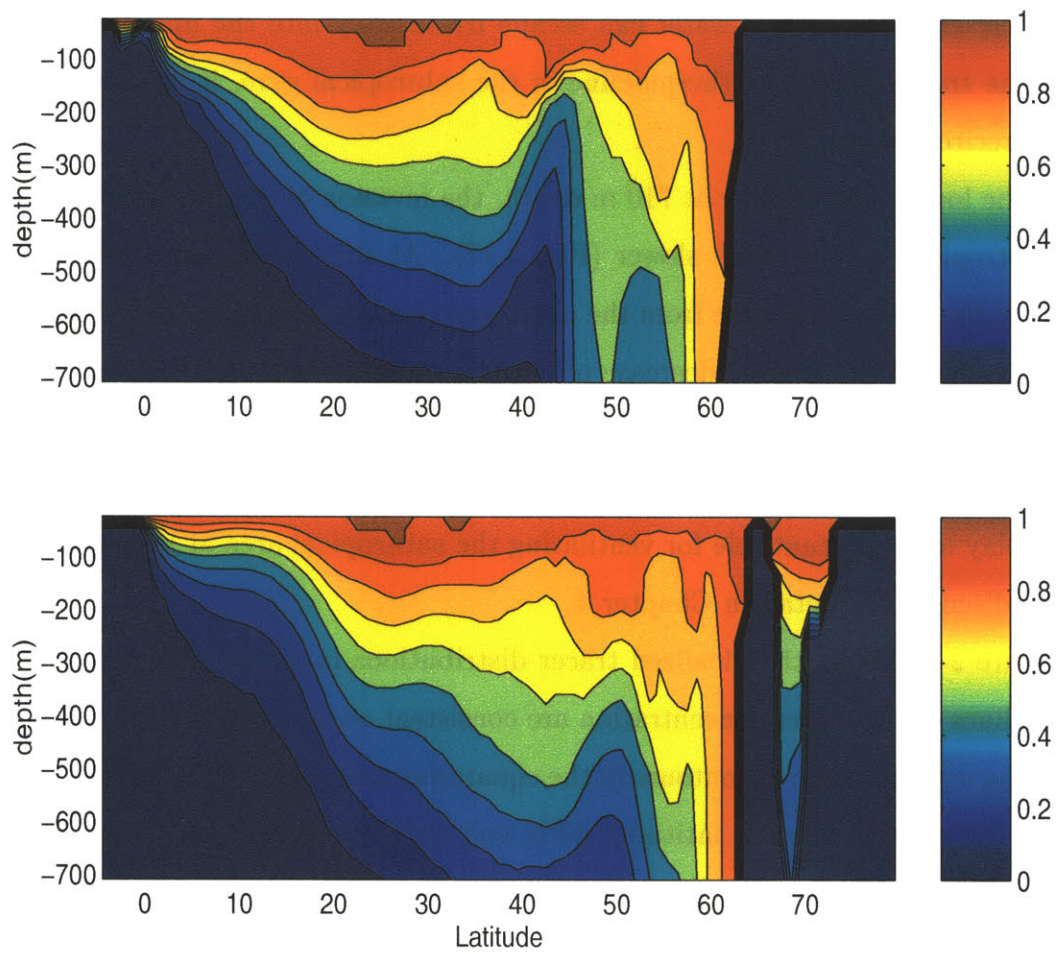
Figure 2-18: The idealized tracer distributions at meridional sections 40.5^{o}W (upper) and 20.5^{o}W (lower) at the beginning of year 9 in the model.
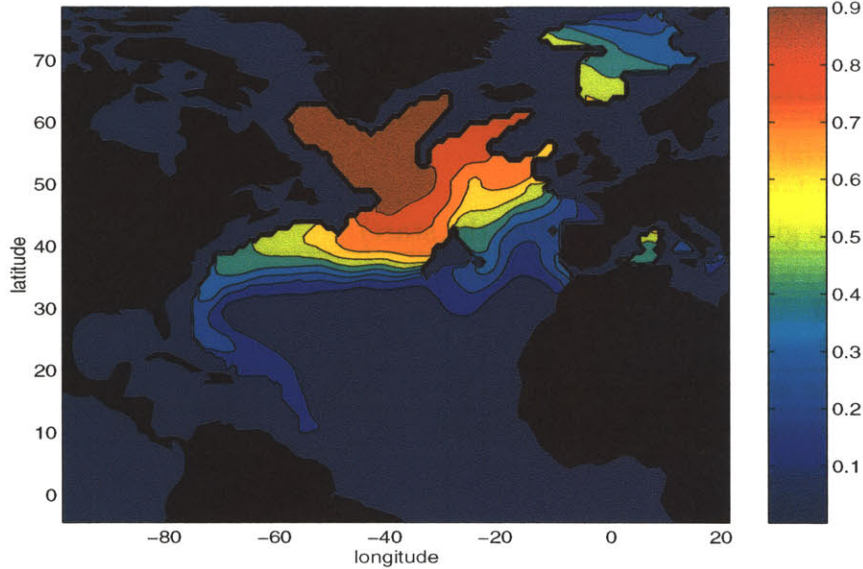
Figure 2-19: Snapshot of the idealized tracer concentration at 1750 m depth at the beginning of year 20 in the model.

2.2.3   Examples of inverse calculations

The inverse calculations in 3-D cases make use of the offline model together with its "adjoint". The adjoint model is obtained from the forward code in a semi-automatic way using the Tangent Linear and Adjoint Model Compiler (TAMC), which is described in Appendix A. Due to the computational limit of a work station in this preliminary exploration, we integrated the adjoint model only over a time interval of 60 days, beginning from the first day of the 10th year. The idealized tracer distribution in the forward model at this time is treated as the initial condition. The purpose of the following examples over this short integration period is to present simple and idealized pictures for inversions of transient tracer data, using the adjoint method.

We start with a very simple case. Suppose the only parameter that needs to be adjusted is the background vertical diffusivity κ_v, with the boundary conditions perfectly known. The "observations" are sampled from the idealized tracer concentrations in the offline model, in which $\kappa_v = 6 \times 10^{-5} m^2/s$. Table 2.3 shows the inverse solutions of κ_v, with "observations" of different spatial coverage and noise, and sampled at different time. These "observations", with or without noise, can con-

Table 2.3: The inverse solutions for κ_v. Note that the correct value should be $6.00 \times 10^{-5} m^2/s$.

Exp.	Characteristics of the observations: spatial coverage standard deviation(d) time given(t=nth day after the start)	$\kappa_v(\times 10^{-5} m^2/s)$
1	everywhere in the model domain d=0 t=2	5.85
2	same as in Exp. 1 except t=30	6.01
3	everywhere in the model domain d=0.33 t=30 & t=60	7.7
4	at cross sections(31.5°N, 59.5°N, 20.5°W, 40.5°W) d=0 t=30 & t=60	6.10
5	same as in Exp. 4 except d=0.1	6.45

strain κ_v to the right order, if the boundary conditions are perfectly known. We add larger noise to the uniformly distributed data, corresponding to the error introduced by mapping. The inverse solution is sensitive to integration time and data coverage. The longer we integrate the model, the more sensitive the model-data misfit is to κ_v; therefore Exp. 2 gives a much more accurate solution than Exp. 1. The sparsity of the data reduces the accuracy of the solution, according to the results of Exp. 4 and Exp. 2.

Generally, the boundary conditions of real transient tracers are not perfectly known and have uncertainties. Now we try to constrain κ_v and the surface tracer values at the same time. Suppose we have uniformly distributed perfect "observations" as used in Exp. 2 in Table 2.3. The surface boundary concentration is known to be a step function in time and its amplitude varies independently at each surface point. A white noise in space with a standard deviation of 0.33 (Fig. 2-20) is embedded in the first estimate of the surface tracer concentration.

The inversion starts at $\kappa_v = 5.00 \times 10^{-5}\ m^2/s$. The adjoint model calculates the gradients (called sensitivities) of the cost function to control variables. These sensi-

tivities determine the search direction for the global minimum of the cost function. During the first five iterations, the cost function drops dramatically (Fig. 2-21) with a rapid adjustment of the surface concentration, to which the cost function is very sensitive initially. At iteration 5, the surface concentration is within the range 0.9—1.0. As the sensitivities to the surface values drop after a few iterations, the adjoint model adjusts the surface concentration slowly while seeking an optimal solution for κ_v. At iteration 20, κ_v =6.02$\times 10^{-5}$m^2/s and $C_{z=0}$= $(1 \pm 0.06)H(t)$, which is within a few percent accuracy of the correct values. The sensitivity to surface tracer concentration at iteration 20 is two orders less than that at iteration 1, as shown in Fig. 2-21.

Now we add noise to both the uniformly distributed "observations" and surface tracer concentration with standard deviations of 0.33 and 0.5, respectively. At iteration 20, the standard deviation of the surface concentration is 0.2, which is less than that of the initial guess (Fig. 2-22). There are, however, obvious errors in the surface boundary condition after optimization. The optimal value of κ_v is $(11.5 \pm 5) \times 10^{-5}m^2/s$.

The third case is one where we have very accurate sectional data along 31.5^{o}N, 59.5^{o}N, 20.5 ^{o}W, and 40.5^{o}W, the same as those in Exp.4 in Table 2.3. The sensitivities to the surface values (Fig. 2-23) are always concentrated near those sections during iterations. This is so because the observational information has not propagated far away over the short period of model integration. Without any information about other areas, the adjoint model adjusts the surface values only near those sections. Consequently, κ_v is not well constrained. The sparse data in space cannot effectively constrain the spatially varying surface tracer concentration and κ_v in this short time integration. Also, this result could imply that sparse transient tracer data in time might not well constrain their time-varying boundary conditions, and hence model parameters, which has been shown by the 1-D inverse study.

Even though the 3-D experiments are done over a very short time period, they do reflect problems in the inversion of transient tracer data. First, the real transient tracer data are sparse in both space and time. Second, as mentioned in Chapter 1, our current estimates of the time-varying boundary conditions of the transient tracers
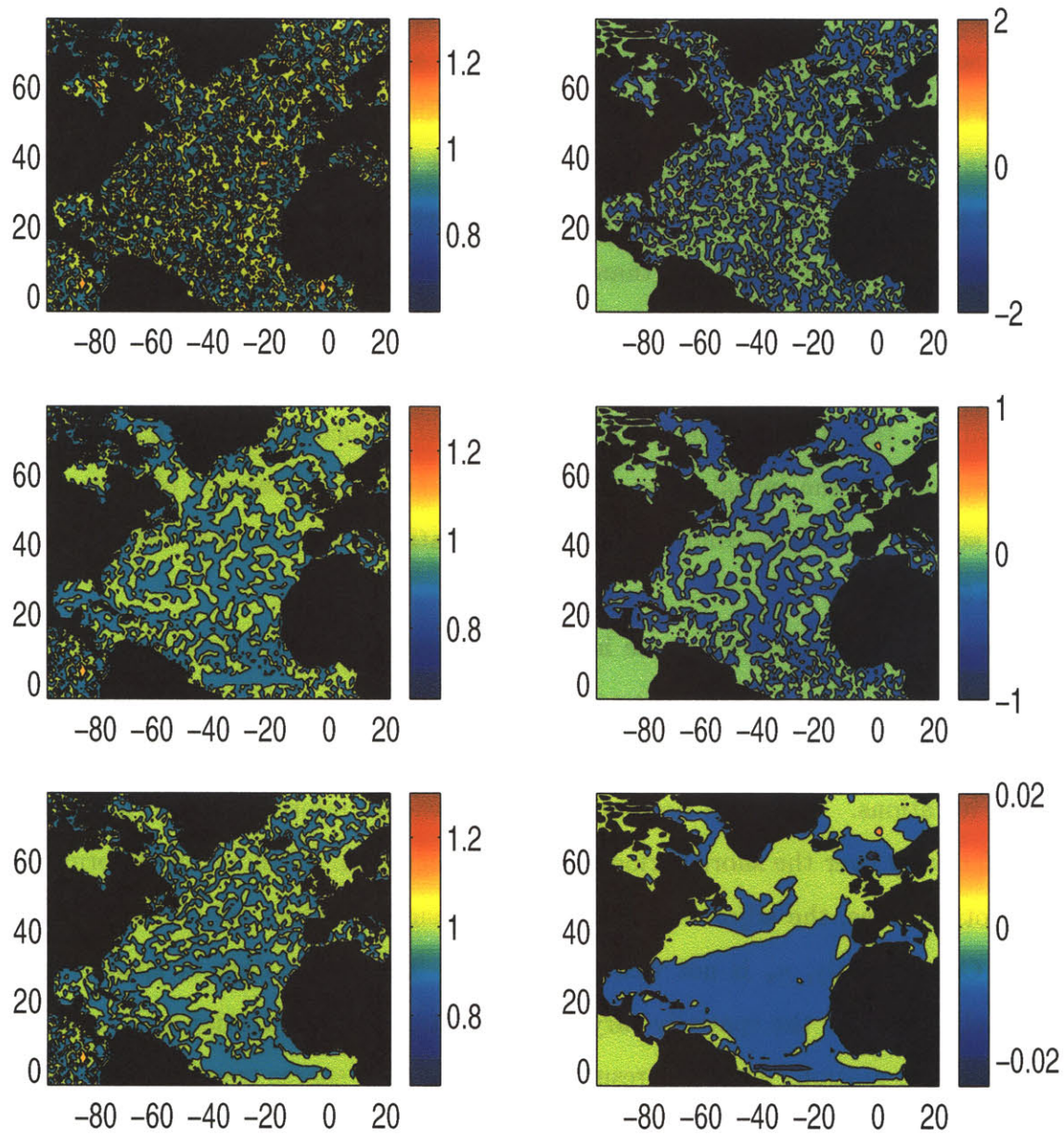
Figure 2-20: Surface tracer concentrations (left panels) and the corresponding gradients of the cost function (right panels) at iteration 1 (upper panels), 5 (middle panels), and 20 (lower panels). The "observations" are uniform in space and perfect.
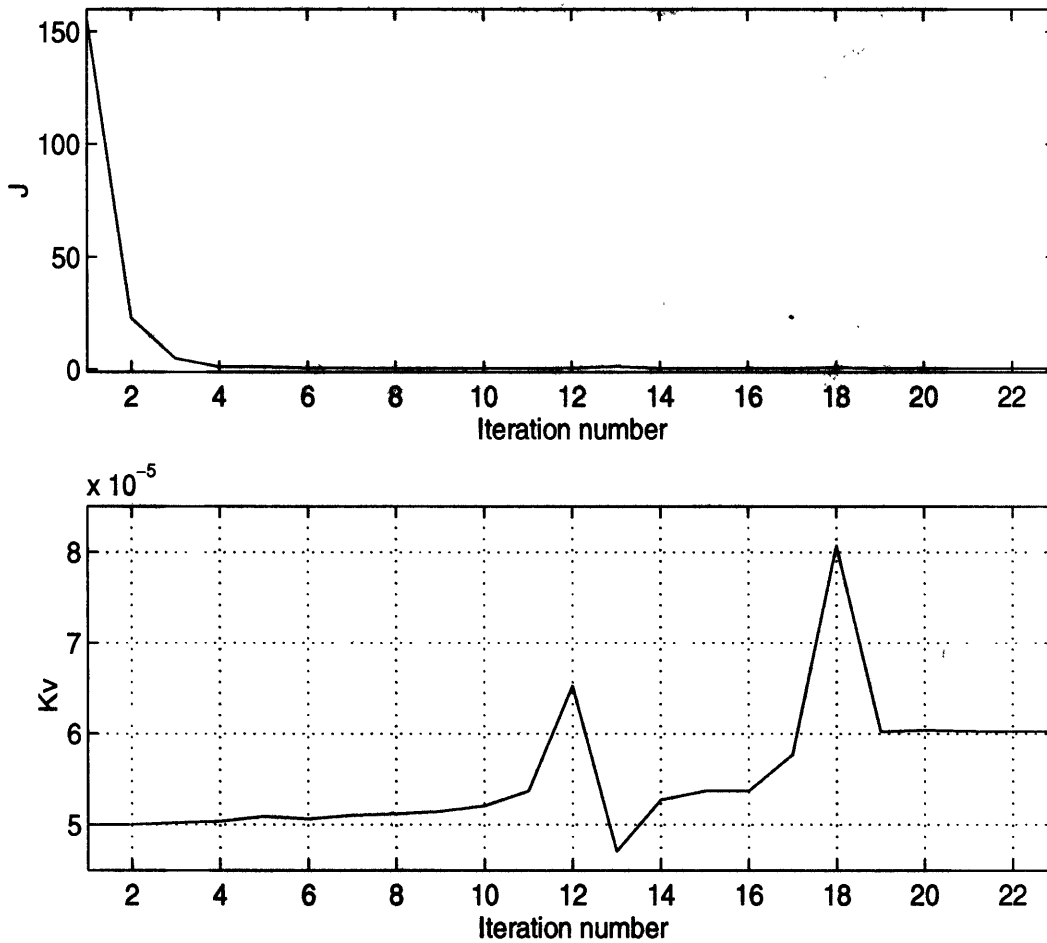
Figure 2-21: Value of the cost function and vertical background diffusivity during iterations. The "observations" are uniform in space and perfect.
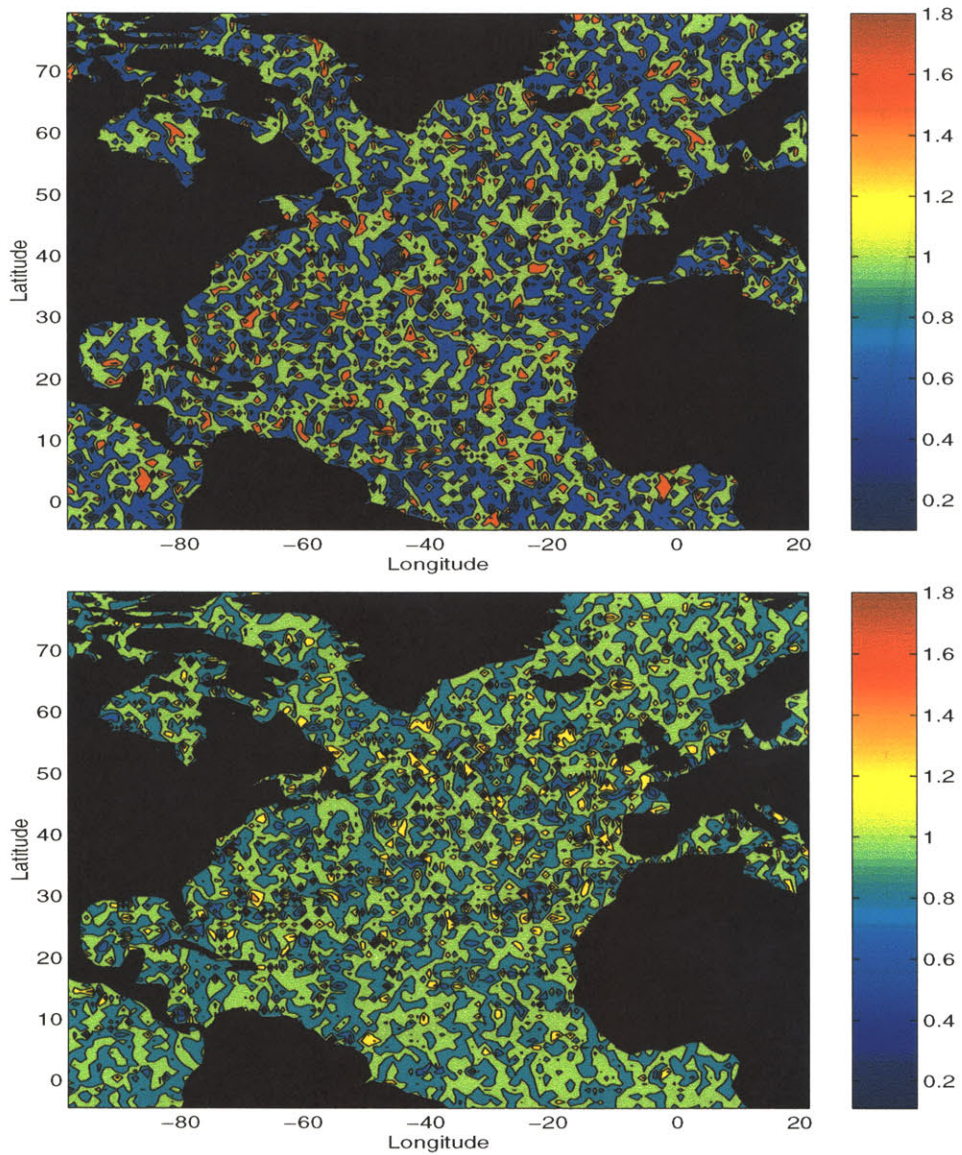
Figure 2-22: Surface tracer concentrations at iteration 1 (upper) and iteration 20 (lower). The "observations" are uniform in space with a standard deviation of 0.33.

have large uncertainties. Our experiments show that the goodness of the optimal estimate of a circulation property, e.g, the vertical mixing rate, depends on the estimates of the boundary conditions. The sparse transient tracer data cannot effectively and accurately constrain the model circulation if their boundary conditions are not accurately known. For the transient tracer inverse problem, improving the estimate of the boundary conditions is a prerequisite for accurate inferences of circulation properties.
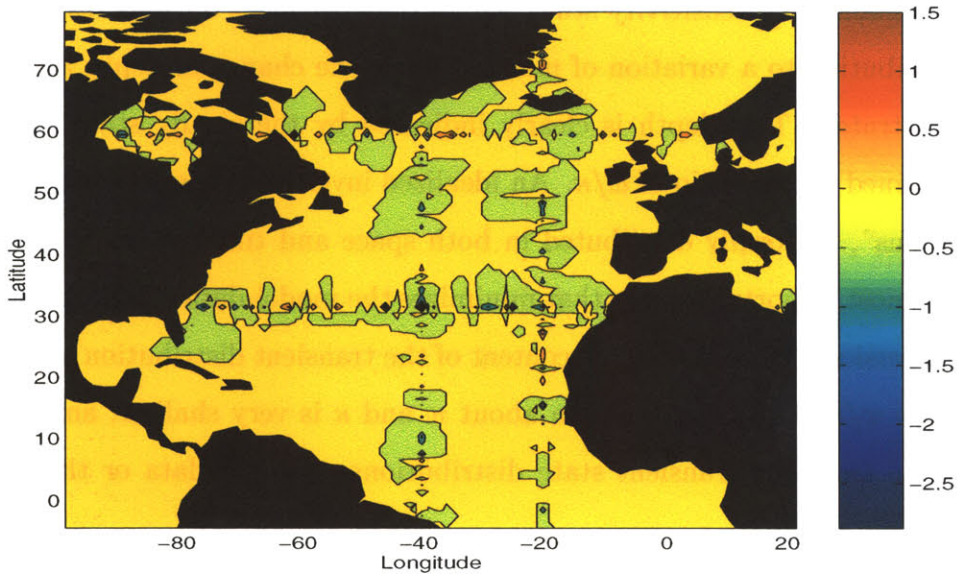
Figure 2-23: Sensitivity distribution of the cost function to surface tracer concentration. The "observations" are perfect at cross sections 31.5^oN, 59.5^oN, 20.5^oW, and 40.5^oW. Note that sensitivity is concentrated along those cross sections.

2.3 Summary

An idealized passive tracer forced by a unit step surface concentration in time is introduced in this chapter. Analytical study of this idealized tracer shows that its transient distribution is a very complex function of advective and mixing rates entangled with various timescales, while its steady state distribution is very simple. Interpretation of the transient distribution is difficult.

A one-dimensional sensitivity study shows that the most obvious response of the tracer distribution to a variation of mixing rate is the change of depth at which the tracer penetrates. This depth is clearly indicated by the steady state distribution and determined by the ratio of w/κ. An idealized inversion of perfect transient stage "observations", uniformly distributed in both space and time, shows that the ratio w/κ is the most important factor that minimizes the model-data misfit. In the aspect of doing inversions, the information content of the transient distribution is dominated by the ratio w/κ. Other information about w and κ is very shallow, and is hard to be extracted from the transient state distributions once the data or the boundary conditions contain noise.

Model-produced "observations" with same spatial and temporal coverage, are sampled in both steady and transient states at different locations in different years. The same data noise is added to these transient and steady state "observations", respectively. Inverse studies show that the temporally and spatially sparse transient state "data" cannot effectively constrain the time-varying surface tracer concentrations in the transient state, and thus the mixing rate. On the other hand, the steady state "observations" quickly constrain the steady surface tracer concentration and mixing rate to the expected correct values within a few percent accuracy.

1-D numerical experiments show that the impact of fast fluctuations whose timescales are far less than the timescale of transient tracer input history and sampling period can be ignored. This result is important for the later study. For example, if the surface uptake rate of CFC-11 can be regarded as constant within a month, the observational CFC-11 distribution at a synoptic section cannot distinguish a monthly

mean flow field from a daily-varying flow field in that month.

Evolution of the idealized tracer distribution in the offline model in the North Atlantic shows that the deep winter convection and subduction are the important processes for the surface tracer information to reach the ocean interior in the model. Simple inversions over short time span are presented to familiarize readers with the inverse problem of tracers, using the adjoint method. The results show that only "observations" uniformly distributed in space can adjust the spatially varying boundary condition and κ_v to the right order. High accuracy sectional "data" adjusts the surface concentration only near "data" locations. Consequently, the model parameter, in our case κ_v, is not well constrained.

Even though the examples of inversion in this chapter are highly simplified and idealized, and are over short time span in the 3-D cases, they do give us some basic information easily understandable. All examples show that the goodness of the final optimal estimate of one control variable depends on the optimal estimates of the others. For example, if the model cannot adjust the surface boundary condition well, as in the 1-D inversion with temporally sparse transient state "data" and the 3-D inversion with the spatially sparse cross-sectional "data", it will not adjust κ_v well. This raises a warning flag: the bad estimate of one parameter will lead to a bad solution of another. Therefore, we must make sure that the optimal estimate of every control variable falls within a reasonable range. For the transient tracer inverse problem, a physically acceptable estimate of the boundary conditions is a prerequisite for reasonable inferences of circulation properties.

Chapter 3

Comparison of Transient Tracer, Temperature, and Salinity Observations with Model Results in the North Atlantic

3.1 Introduction

In this chapter, CFC-11, CFC-12, tritium and helium (^{3}He), the commonly studied transient tracers with typically different oceanic input histories, are simulated in the offline model of the North Atlantic. Model predictions of transient tracers, temperature and salinity (T-S) in the North Atlantic are compared with observations. Testing model results against observations can help us to evaluate the transient tracer source functions and the ocean circulation in the model. Another motivation arises from preparations for future data-assimilation. A reasonable simulation is a prerequisite of the assimilation.

A global comparison of modeled tracer distributions with observations has been done by Craig et al. [1998] with limited details in the North Atlantic, which is our area of interest. In Craig et al. [1998], one of the most conspicuous shortcomings is

the small volume of Antarctic Intermediate Water (AAIW) in the model results. This leads to errors in the general water mass structure and in CFC concentrations in the model in other regions. Craig et al. [1998] find that the model-data disagreements in CFC fields appear in regions where water mass structures are incorrectly modeled, notably in deep water formation regions. As the transient tracers and T-S are governed by the same physics, all characteristic properties of a water mass, the transient tracer concentrations as well as its T-S, will be imprinted along its trajectory. It will be interesting to see that not only transient tracers but also T-S can help us to evaluate model performance, especially the model representations of the deep water masses, their ventilation pathways, and deep convection.

The same offline model introduced in Chapter 2 is used to predict the time-varying transient tracer distributions. Some modifications are made in order to simulate real tracers. First, the entirely closed wall at the northern boundary is discarded. The northern boundary is opened corresponding to the realistic topography and is located 78.5^oN, as shown in Fig. 3-1. Second, convective adjustment is replaced by enhanced vertical diffusivity, which can be expressed as $\kappa_{cov} = h^2/t_{mix}$ [Klinger et al. 1996]. Here t_{mix} is estimated from the monthly mean convective frequency and h is the total height of the vertical adjacent cells within which water properties are homogenized. Unlike convective adjustment, this implicit vertical mixing scheme produces a tracer distribution that is a continuous function of the enhanced mixing rates.

3.2 Boundary conditions

The time histories of atmospheric CFC-11 and CFC-12 come from Walker et al., [2000], as shown in Fig. 3-2. CFC atmospheric concentrations are reconstructed from direct measurements and, prior to the early 1980s, from industry production estimates and atmospheric chemical lifetimes. CFCs enter the ocean through air-sea gas exchange at the sea surface.

The fluxes of CFC-11, CFC-12, and ^{3}He at the ocean surface are computed using
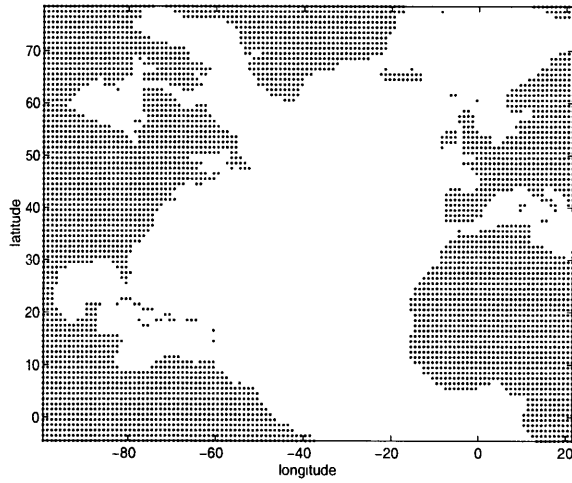
Figure 3-1: The new model surface geometry with land areas dotted. Note that parts of the northern and southern boundaries are open.
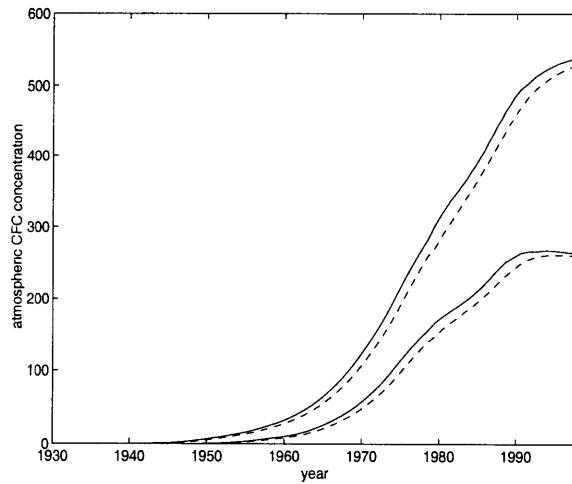
Figure 3-2: Estimates of atmospheric CFC-11 and CFC-12 concentrations (parts per trillion) as a function of time and hemisphere, following Walker et al., [2000]. Values in the southern hemisphere are dashed.

a piston velocity flux parameterization

$$F = K_w(C_{eq} - C_{sur}). \tag{3.1}$$

Here K_w represents piston velocity, the velocity with which gas diffuses across the air-sea interface [Najjar, 1991]. C_{sur} is the modeled sea surface tracer concentration. The oceanic surface equilibrium C_{eq} of CFC-11 or CFC-12 depends on sea surface temperature and salinity [Warner and Weiss, 1985]. For ^{3}He, it is set to zero, which is a good approximation to the low solubility of ^{3}He. The error introduced by this approximation is small compared to uncertainties in the components due to modeled tritium decay and mantle outgassing. As the solubility properties and the atmospheric concentrations of CFCs are well known, the uncertainties of the CFC fluxes are mainly due to the uncertainties in the piston velocities K_w. All right hand terms in Eq. (3.1) are different for CFC-11, CFC-12, and ^{3}He.

The monthly climatology of K_w, taken from Ocean Carbon-Cycle Model Intercomparison Project (OCMIP), is computed with the equation adapted from Wanninkhof [1992]

$$K_w = a < u^2 > (Sc/660)^{-1/2}. \tag{3.2}$$

Here a is a constant coefficient; Sc is the Schmidt number, a dimensionless parameter used for mass transfer [Najjar, 1991]. The $<>$ denotes time average. Let $u = <u> +u'$, Eq. (3.2) becomes

$$
\begin{aligned}
K_w &= a < (<u> +u')^2 > (Sc/660)^{-1/2} \\
&= a(<<u>^2> + <u'^2 >)(Sc/660)^{-1/2}.
\end{aligned} \tag{3.3}
$$

Taking the effect of sea ice into account, we get

$$K_w = (1 - F_{ice})[a(<<u>^2> +v)](Sc/660)^{-1/2}. \tag{3.4}$$

Here F_{ice} is the fraction of the sea surface covered with ice, which varies from 0.0 to

1.0; $<< u >^2>$ is the instantaneous satellite wind speed, averaged for each month, then squared, and subsequently averaged over the same month of all years to give the monthly climatology; v is the variance of u; a is the coefficient of 0.337, when using the satellite wind information; Sc is calculated as $Sc = a_1 + a_2\theta + a_3\theta^3 + a_4\theta^4$, with θ the sea surface temperature in degree Celsius. For ^{3}He, the coefficients a_1 to a_4 are 410.14, -20.503, 0.53175, and -0.0060111, respectively. For CFCs, the formulation from Zheng et al. [1998] is used. This formulation yields an estimate of K_w for CFC-12 that is 1-5% lower than that of CFC-11. More detailed information about the piston velocity can be found on the web page *http://www.ipsl.jussieu.fr/OCMIP*.

The lateral boundary concentrations of CFCs are from a global run of the MIT GCM [Dutay et al., 2002]. The CFCs are simulated in the model from a zero background at the beginning of 1940.

Most tritium was produced as the result of the atmospheric nuclear bomb tests in the early 1960s. The tritium distribution in the ocean can be regarded as the reflection of the recent transient input history because its natural background before 1952 is negligible. Tritium is measured in "Tritium Units", TU, the HTO to H_2O ratio of 10^{-18}. TU81 refers to the tritium concentration that is decay corrected to the date of January 1, 1981, with a half-life of 12.43 years [e.g., Östlund and Rooth, 1990].

The concentration of tritium is imposed at the ocean surface. Following the results of Dreisigacker et al. [1978] and Doney et al. [1992], the tritium surface concentration is supposed to be separable in time and space. The time history for years 1950 - 1986 comes from the data of Doney et al. [1993] (Fig. 3-3). After 1986, the tritium surface concentration is extended by assuming an exponential (radioactive) decay. The spatial distribution of surface tritium, in Fig. 3-4, is based on Dreisigacker et al. [1978] and Doney et al. [1992]. The absolute value of tritium surface concentration is obtained by multiplying the temporal part with the corresponding spatial part.

The tritium flux across the southern boundary is set to zero, which is minor in comparison with other inputs according to Doney et al. [1993]. A source flux at the northern boundary is set equal to the amount of Arctic inflow in Doney et al. [1993],

and the flux is carried to the North Atlantic via the East Greenland Current and the Baffin Island Current in the model.
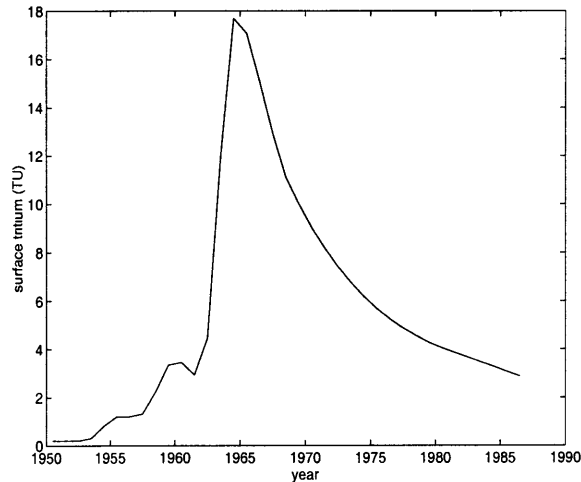
Figure 3-3: Temporal distribution of tritium concentration in the North Atlantic surface water, following Dreisigacker et al. [1978] and Doney et al. [1993].

3.3 Observations

The CFC-11 and CFC-12 data in the North Atlantic from WOCE and pre-WOCE have been collated. The tritium and ^{3}He data mainly consist of the dataset used by Khatiwala [2001]. Table 3.1 and 3.2 list the cruise names and cite references for each dataset. There are over 40,000 CFC-11/CFC-12 samples and 10,000 tritium/^{3}He samples. The data span is 1972 - 1999. We are grateful to all colleagues who provided these measurements for our analysis. The locations of observations are shown in Fig. 3-5, covering much of the North Atlantic at various times.
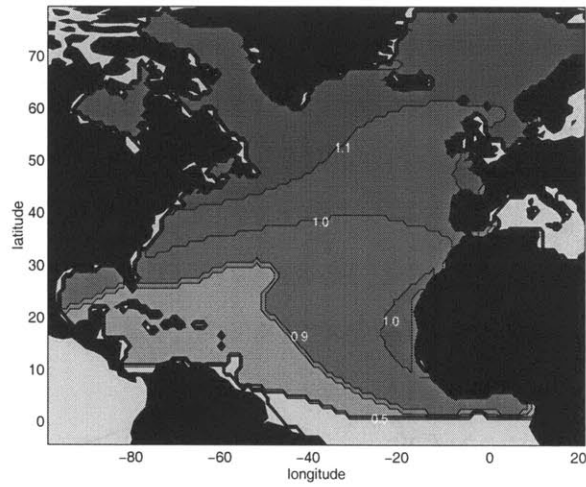
Figure 3-4: Estimated spatial coefficient of tritium concentration in the North Atlantic surface water; to obtain absolute tritium concentration, the value in this figure has to be multiplied by the temporal distribution in Fig. 3-3.
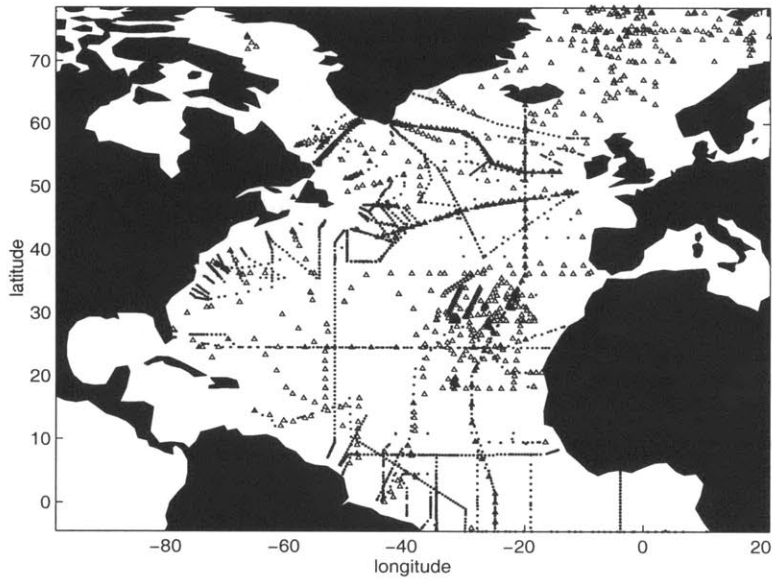
Figure 3-5: Map of tracer stations used in this study. Dots represent CFC-11/CFC-12 stations; triangles represent tritium stations.

Table 3.1: CFC-11 and CFC-12 data sources.

Cruise	Reference
WOCE section A01EW, A01W, A05, A06, A07, A15, A17, A22, A24, AR04A-E, AR07EH,AR07WC, AR07WD, AR12B, AR13A-D	WOCE hydrographic Program, 2000
WOCE section AR21,AR01, Transient Tracer in the Ocean expedition Endeavor214, 223, Knorr 134, Oceanus134,	John Bullister, pers. comm., 2000
WOCE section A20	Bill Smethie, pers. comm., 2000
Charles Darwin62	Martin Gould, pers. comm., 2000
Oceanus202	Doney and Bullister [1992]
WOCE section A01E, A02A, METEOR393	Wolfgang Roether, pers. comm., 2000

Table 3.2: Tritium and helium data sources except that from Khatiwala [2000].

Cruise	Reference
Oceanus202	Scott Doney, pers. comm., 2000
WOCE section A01E, A02A, METEOR393	Wolfgang Roether, pers. comm., 2000
GEOSECS, Transient Tracer in the Ocean, North Atlantic Tracer Sections expedition, Pilot Subduction study,	H.G.Östlund, pers. comm., 2000
1991-1993 Subduction study	WHOI Helium Isotope Lab

3.4 Comparison of CFC-11, temperature, and salinity observations with model results

First, monthly means of the model outputs are compared with the observations at individual cruise tracks. Two meridional sections nominally at 20°W along the track of the Oceanus Cruise No. 202 (WOCE A16N) and 52°W (WOCE A20) are chosen to show the tracer distributions in the eastern and western basins. Three longitudinal sections are chosen. Two are nominally along 46°N (WOCE A02A) and 56°N (WOCE A01E), respectively. Another one is in the subtropical gyre, about 24°N (WOCE AR01). One section across the Labrador Sea (WOCE AR07WD) is chosen to study deep convection in the model. The data usually provides higher resolution along cruise tracks than the model, both vertically and horizontally. Therefore, the observations are interpolated onto the model grids.

Our comparison focuses on the roles of CFCs and T-S in evaluating the model performance, especially in tracking the reproduction of the deep water masses and their ventilation pathways. Since the offline model does not generate T-S fields, their monthly climatological means in the online GCM are compared with those at synoptic sections. Given the fact that on large scales, monthly mean T-S should not be very different from those at a synoptic section (e.g., the thermocline depth and thickness on scales of hundreds to thousands of kilometers do not change from year to year), we can compare their large scale differences.

3.4.1 20°W (WOCE A16N)

Figure 3-6 shows the observed and modeled CFC-11 distributions along the meridional section nominally 20°W (see Fig. 3-5 for detailed section location), July - August, 1988. Their overall patterns are similar. Isolines of CFC-11 concentration shoal toward low latitudes. CFC-enriched water fills the entire water column of the subpolar basin. In the upper 1000 m, the modeled and observed CFC-11 distributions agree well. CFC-11 concentration is high in the high latitudes and gradually decreases

towards low latitudes. In the deep ocean, 40° north, both model and observations show a southward spreading tongue with high CFC-11 concentration. This is the signature of the Labrador Sea Water (LSW), since the northern part of this section cuts across the eastern margin of the LSW outlined by Talley et al. [1982].

Obvious model-data discrepancies appear in the high latitudes. Near 60^oN, isolines of the modeled CFC-11 concentration are very steep. Water with very high CFC-11 concentration (above 3 pmol/kg) penetrates down to about 2000 m, while observations show that this water mass extends less than 800 m. Comparisons of modeled and observed T-S distributions yield a similar result: modeled T-S surfaces are very steep in the high latitudes. This permits a quick vertical invasion of the surface water properties along the steep isopycnals.

Down deep, observations show a clear plume of the CFC-enriched LSW. This water mass has a salinity between 34.9 and 34.94 along this section (Fig. 3-7). The high CFC concentration centered at about 2000 m (Fig. 3-6) between 40^oN and 60^oN corresponds to a salinity minimum at the same location. In the model, the tongue of high CFC concentration appears very thick vertically. This spuriously thick LSW can be identified in the modeled salinity field as well. The modeled LSW with salinity lower than 34.94 occupies the water column from 2000 m down deep to 4000 m. Both salinity and CFC distributions show that the volume of the modeled LSW is too large at this meridional section.

The pathway of the newly ventilated LSW in the model is shown very clearly in the horizontal tracer fields at 2200 m. Figure 3-8 shows that both CFC-11 and salinity fields exhibit a strikingly similar pattern of the ventilation pathway of the LSW, although some details are different due to their different boundary conditions. Formed in the deep convective region in the Labrador Sea, the modeled LSW spreads southeast-ward with the Labrador Sea Current. After it passes the Grand Banks of Newfoundland, a large part of it turns southward with the Deep Western Boundary Current (DWBC) along the American coast. The rest enters the eastern basin via the Charlie-Gibbs Fracture Zone. Both CFC-11 and salinity are carried by the LSW along its trajectory, distributed by the same physical processes. Steady tracers, here
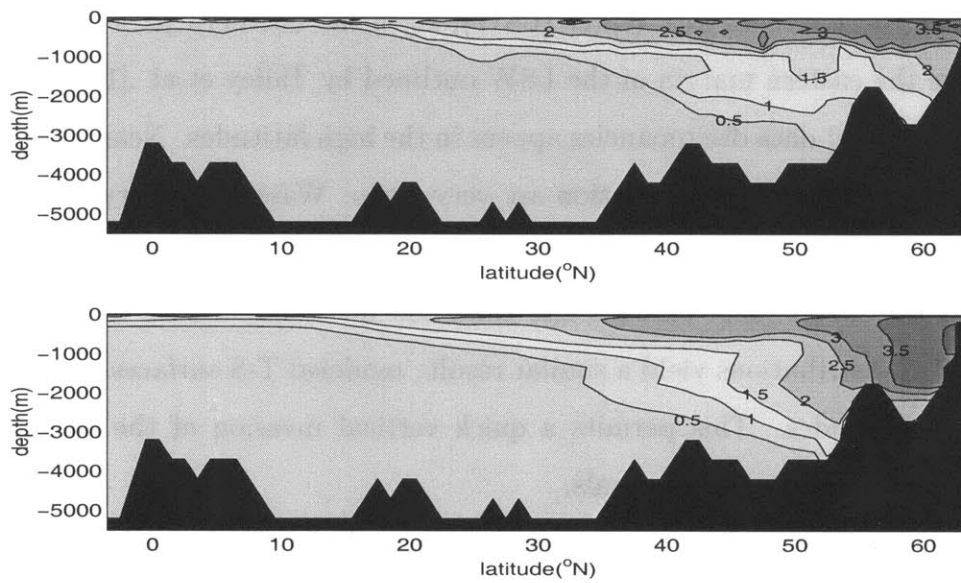
Figure 3-6: Observational (upper) and modeled (lower) CFC-11 distributions nominally along 20°W (WOCE A16N), July-Aug., 1988. Unit of CFC concentration is pmol/kg and hereafter.
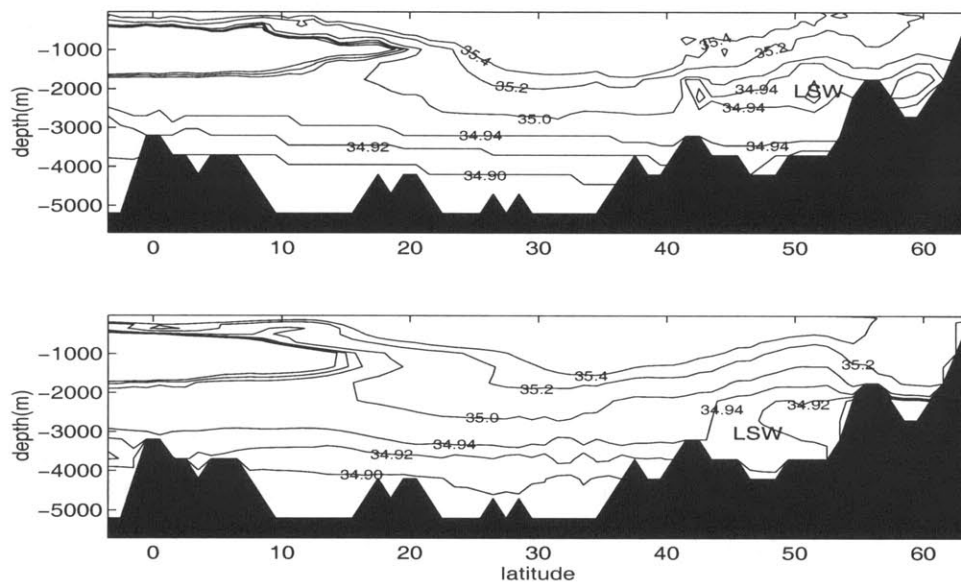
Figure 3-7: Observational (upper) and modeled (lower) salinity distributions at the same section in Fig. 3-6. The salinity of the LSW is less than 34.94.

salinity, can track the ventilation pathways in the model as well.
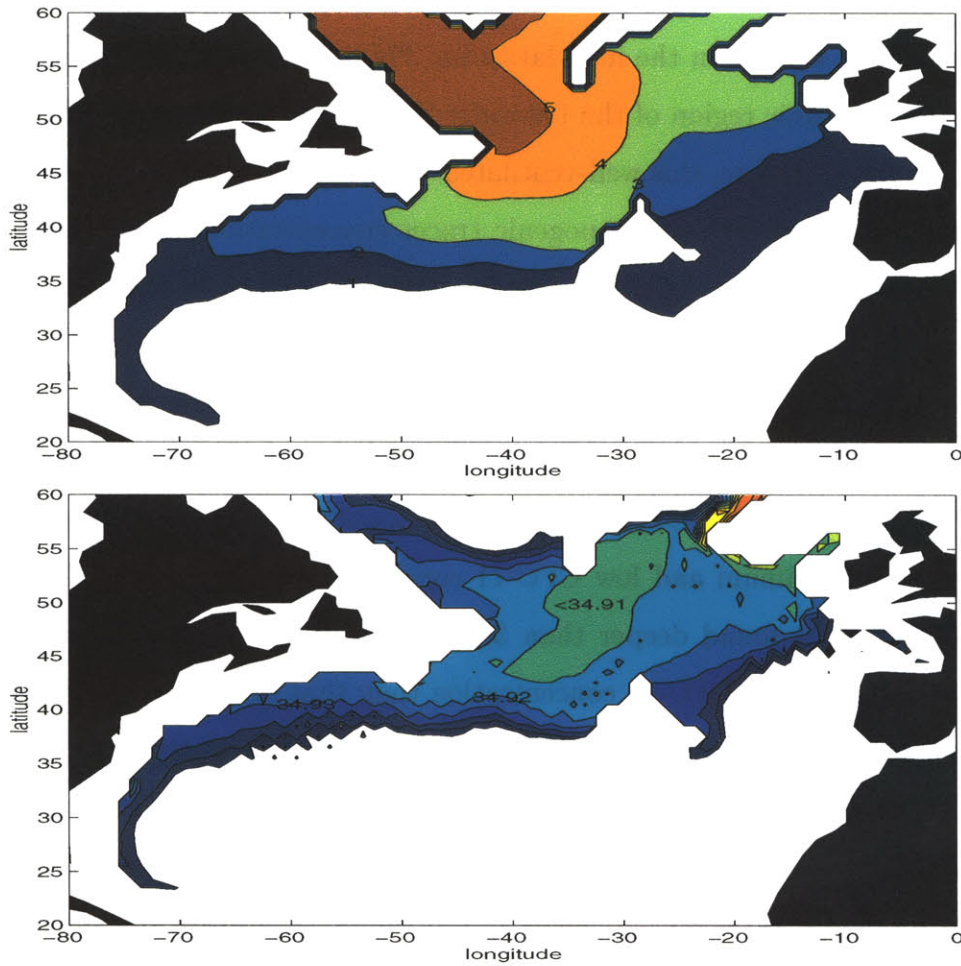
Figure 3-8: Modeled CFC-11 (upper) and salinity (lower) distributions at 2200 m depth, Jan. - Feb., 1998. Values of CFC-11 concentration higher than 1 pmol/kg and salinity lower than 34.95 are plotted out respectively to show the pathway of the LSW.

3.4.2 High latitudes (WOCE AR07WD and A01E)

The differences between the modeled and observed deep waters can be traced back to the formation regions in the high latitudes. Following the trajectory of the LSW, we go to the dynamic region of the Labrador Sea. Here the prototype of the LSW is formed. As shown before, this well-ventilated water mass, characterized by low salinity, temperature and high anthropogenic tracer concentrations, has heavy imprints in the transport processes of ocean tracers. Observations show that, in the central Labrador Sea (WOCE AR07WD), three deep water masses are clearly identifiable (Fig. 3-9). From depths 100 m to 2000 m is the large volume of LSW. Below it are the North East Atlantic Deep Water (NEADW) and Denmark Strait Overflow Water (DSOW). The NEADW has its core at about 2800 m. It is characterized by a temperature maximum and low CFC-11 concentration. Underlying the NEADW is the DSOW. It is found deeper than 3000 m in the central Labrador Sea and is characterized by higher CFC-11 concentration than that in the NEADW. Above 100 m is the cold, fresh, and high CFC-11 concentration surface water.

Unfortunately, the model fails to reproduce these water masses. The surface values of CFC-11, temperature, and salinity go downward to the ocean bottom. Water properties in the model are overly homogenized in the vertical direction. The enhanced vertical mixing is indicated by both T-S and CFC fields: the vertical homogenization of the tracer properties.

While the offline model uses the monthly climatological mean fields of velocities and T-S, deep water formation varies from year to year. This contributes to the model-data mismatch to some degree. The climatic changes of enhanced vertical mixing in winter and their impacts on the tracer distributions need further quantification. Nevertheless, comparison of observational and modeled tracer distributions indicates that the modeled vertical penetration of surface values is too strong. This leads to the excessive uptake of the surface values, the transient tracer concentrations as well as T-S. Therefore, the largest model-data misfits are along the trajectory of the LSW and provide information about the model performance.
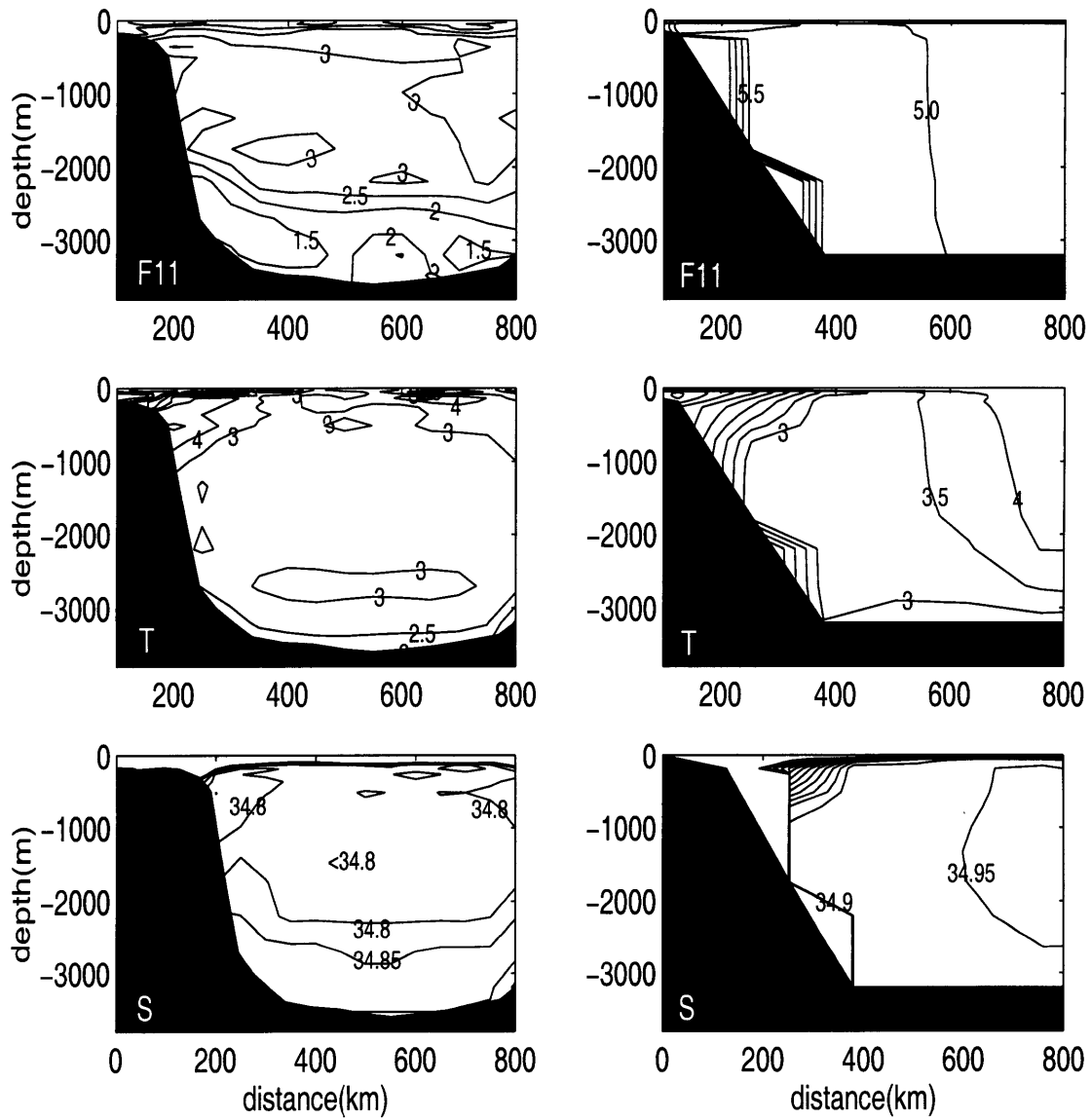
Figure 3-9: Observational (left) and modeled (right) tracer distributions along a section cross the Labrador Sea (WOCE AR07WD), June, 1993.

Farther north, nominally along 56°N (WOCE A01E), the observational and modeled CFC-11 and temperature distributions show the model-data differences of the lower North Atlantic Deep Water (NADW) (Fig. 3-10). In the eastern basin, surface CFC-11 concentration and subsurface maximum at about 400 m depth are well reproduced by the model. High CFC-11 concentration appears in the western basin, due to the entrainment of the newly formed LSW. Unlike the observations, the entrained LSW occupies the entire western basin in the model, with very steep temperature and CFC-11 isolines. Modeled CFC-11 concentrations in the Irminger Sea are thus higher than those in the observations, especially in the deep ocean. The observed DSOW, with CFC-11 concentration of about 2.5 pmol/kg, temperature of 2°C, and salinity of 34.85, is characterized by CFC-11 maximum 200 m off the bottom in the western basin. In the model, the DSOW does not exist. In our case, the model topography is partly responsible for it. The shallowest part of the Denmark Strait, which in reality is about 600 m, is less than 400 m in the model. The shallow topography in the model blocks the DSOW behind the Greenland-Iceland ridge. Therefore, the only component of the NADW in the model is the LSW. As the offline model uses the flow field in the online GCM, changing the model topography will lead to the change of the flow field. For the consistency of the model topography and the flow field, the model topography remains as it is given. The absence of the Overflow Waters (OW) is a general feature typical of a coarse resolution model [e.g., England, 1998]. Modeling the OW is not explored in this study.

3.4.3   46°N (WOCE A02A)

The excessive vertical penetration of convective adjustment in the Labrador Sea leads to an erroneously voluminous water mass a little downstream along the pathway of the LSW, at 46°N (WOCE A02A), as shown in Fig. 3-11. In the model, the CFC-enriched LSW water occupies almost the whole deep western basin along this section. This large water mass at depth in the model is also exhibited by the T-S fields with values of 2.5 - 4 °C and 34.9 - 35.0, respectively. Near the ocean bottom, the observed OW with a maximum of CFC-11 concentration above 1.5 pmol/kg off the bottom of
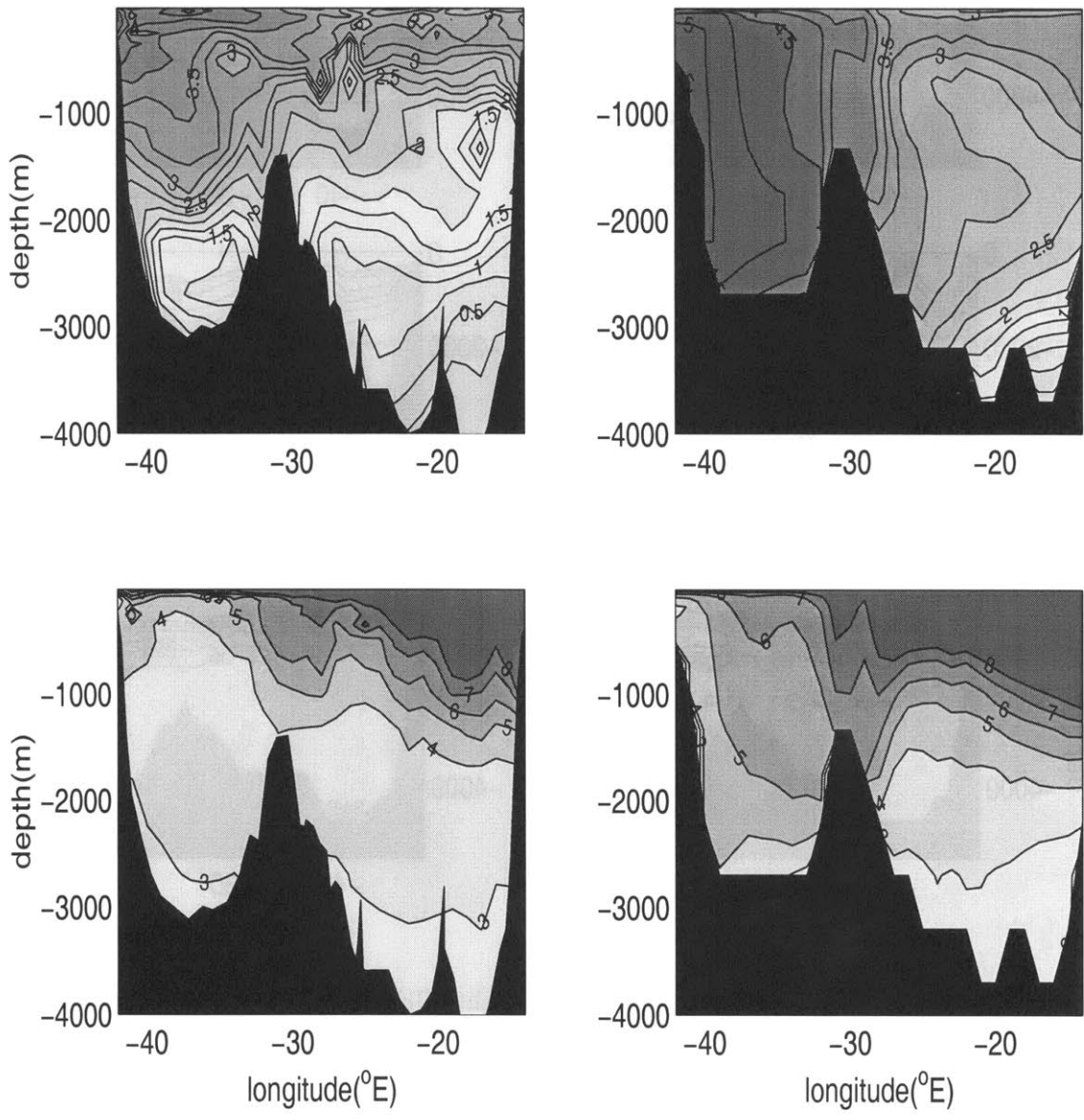
Figure 3-10: Observational (left) and modeled (right) CFC-11 (upper) and temperature (lower) distributions along a section nominally 56°N (WOCE A01E), Sep., 1991.

the western basin is not reproduced by the model.
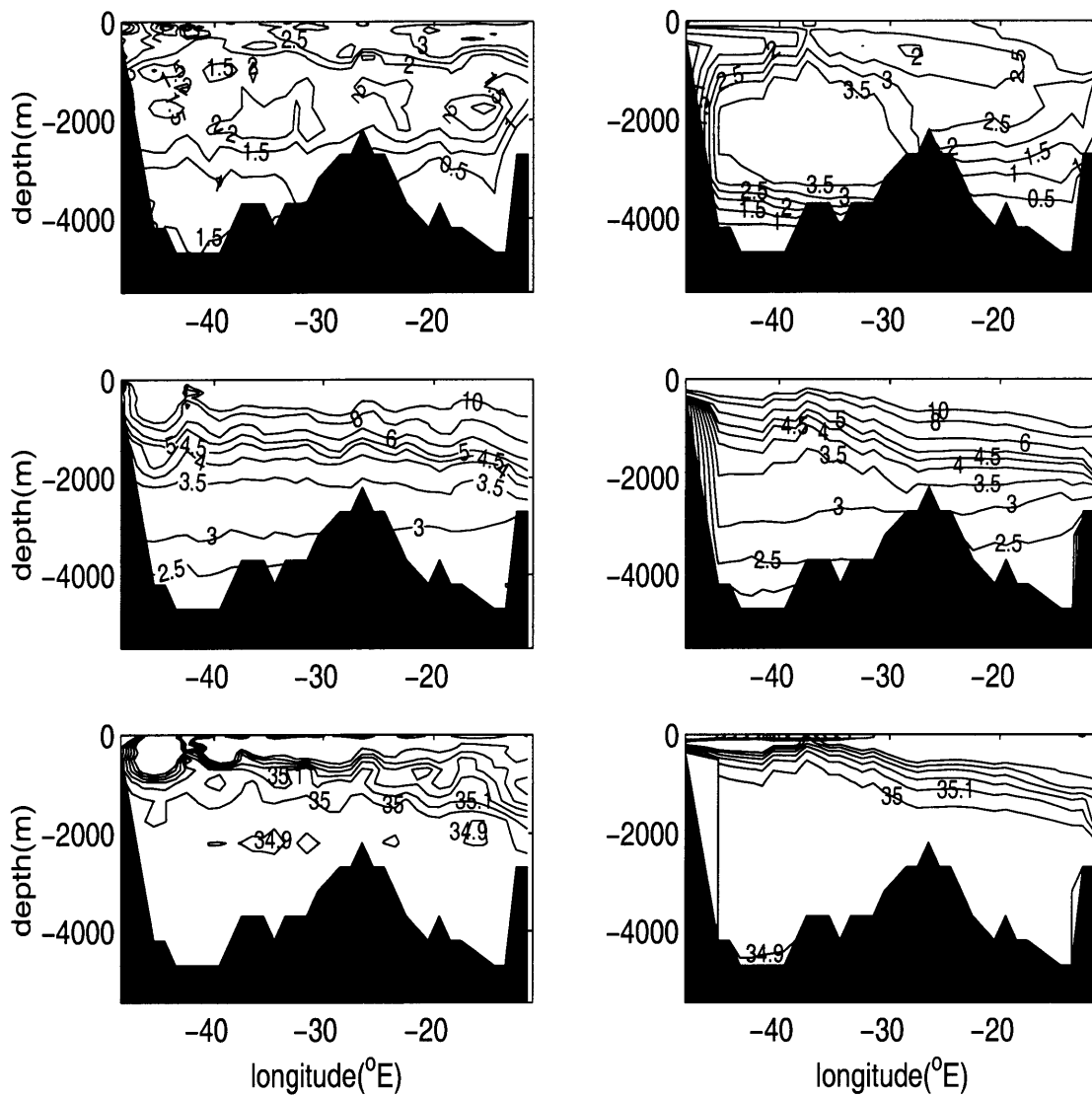
Figure 3-11: Observational (left) and modeled (right) CFC-11 (upper), temperature (middle), and salinity (lower) distributions at 46°N (WOCE A02A), Nov., 1994. Note the similar shape of the contours of CFC-11=3 pmol/kg, T=4°C, and S= 35.

3.4.4   24°N (WOCE AR01)

As the LSW is mixed with the surrounding water, the model-data misfits of the tracer properties in the LSW become smaller farther downstream. Figure 3-12 shows the modeled and observational CFC-11 distributions along a section nominally at 24°N. Ignoring the meso-scale variabilities in the observations that cannot be reproduced by our non-eddy resolving model, we can see the simulated CFC-11 concentration at this section agree much better with observations, as compared to the model-data disagreements in the high latitudes. Both model prediction and observations show a subsurface maximum centered at about 300 m, with relatively uniform CFC-11 concentration. It is the subtropical mode water, with temperature of 18°C and CFC-11 concentration of 2.25 pmol/kg, in both model and data.

Deep in the ocean, observations show two CFC-11 maxima near the western boundary. Both maxima represent the recently formed components of the NADW that are transported equatorward via the DWBC. The core of the upper one is centered at 1800 m depth with temperature about 4.0°C and salinity about 35.0. This is identified as the upper NADW originating from the Labrador Sea. The other one, centered about 4000 m depth with temperature of 2.4°C and salinity of 34.9, is the OW. In the model, however, there is only a spuriously thick and broad deep maximum centered at about 2000 m depth near the western boundary. The modeled T-S fields show the same deep water distribution (Fig. 3-13): there is a large water mass with relatively uniform T-S near the deep western boundary (notice the pinching of the modeled T-S isopleths towards the east between 2000 - 4000 m). Due to the absence of the OW water, the modeled deep water off the bottom near the western boundary is colder than that in the observations. Examination of the initial state (which is the Levitus climatology) shows that initial T-S distributions are similar to those in the observations along this section. This demonstrates that the model-data differences in the T-S fields in the deep ocean are not due to the impact of the initial state.
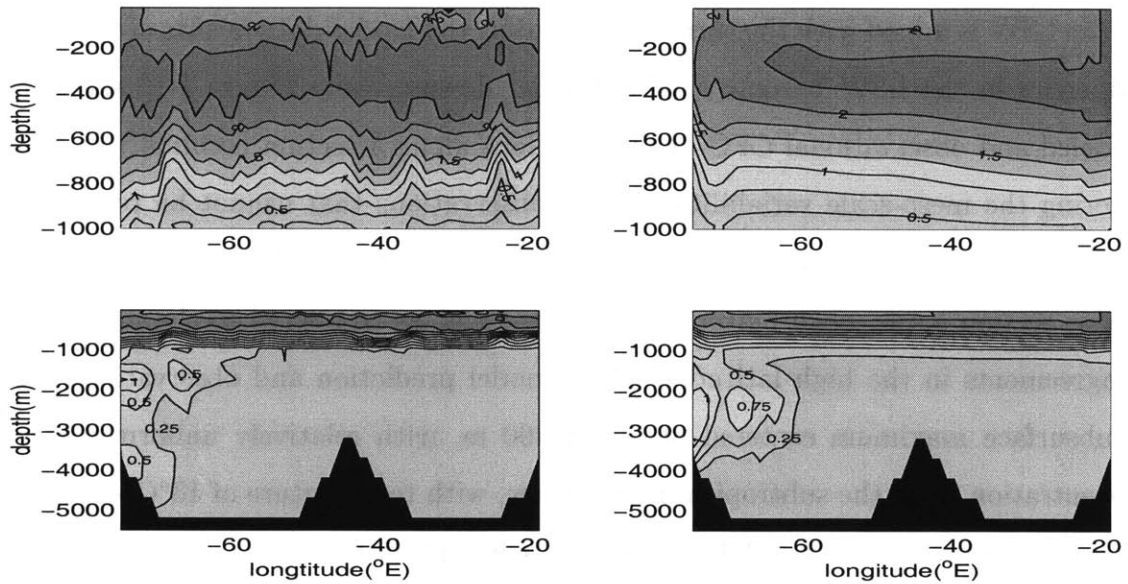
Figure 3-12: Observational (left) and modeled (right) CFC-11 distributions nominally along 24°N (WOCE AR01), Jan. - Feb., 1998. The upper panels show the top 1000 m expanded.
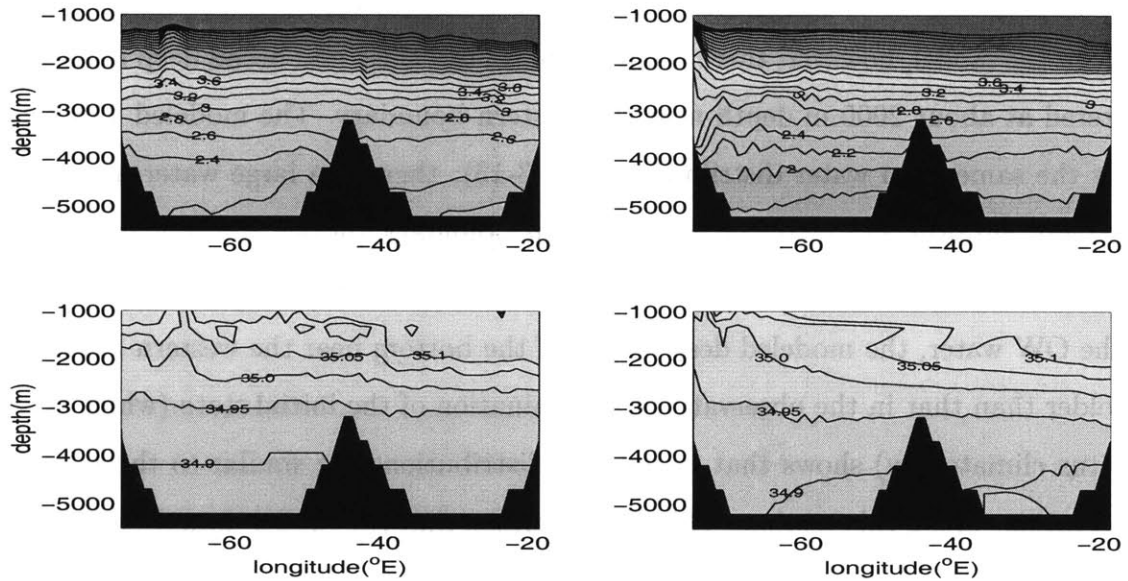
Figure 3-13: Observational (left) and modeled (right) temperature (upper) and salinity (lower) distributions at ~24°N.

3.4.5 52°W (WOCE A20)

Last, let us compare the modeled and observed CFC-11 distributions along a meridional section in the western basin, nominally 52°W. Figure 3-14 shows that the modeled and observational CFC-11 concentrations at the sea surface agree with each other, with warm water having lower CFC-11 level compared with cold surface water. The sub-surface maximum at upper thermocline shows a similar distribution pattern. At the middle depth, about 1000 m, the minimum is indicative of AAIW. Down deep, there are two deep CFC-11 maxima in the observations. They represent two sources of the NADW, the LSW and the OW. Separate signatures of these two sources extend from the northern edge to 23°N. In the model, however, there is only a broad single maximum that extends from 1500 m to more than 4000 m deep, indicating the modeled NADW originating from the Labrador Sea. North of 35°N, modeled CFC-11 concentrations in the NADW far exceed those of the observations, owing to the excessive surface value uptake in the deep convective regions.

3.4.6 Temperature gradients: implication for flow fields

The model-data misfits shown above might lead to a doubt about the goodness of the modeled flow fields. It is worth mentioning here that the flow fields are determined by the gradients of T-S, but not by T-S themselves. In large scales, the flow fields are geostrophic. According to the differences between the modeled and observed T-S gradients, we can estimate the rough uncertainty in the modeled flow fields.

Supposing there exists a model-data misfit of temperature gradient, according to the geostrophic and hydrostatic balance, we have

$$\mathbf{U} = \frac{1}{f\rho_o}\hat{k} \times \nabla_H P, \qquad (3.5)$$

$$\frac{\partial P}{\partial z} = -\rho g, \qquad (3.6)$$
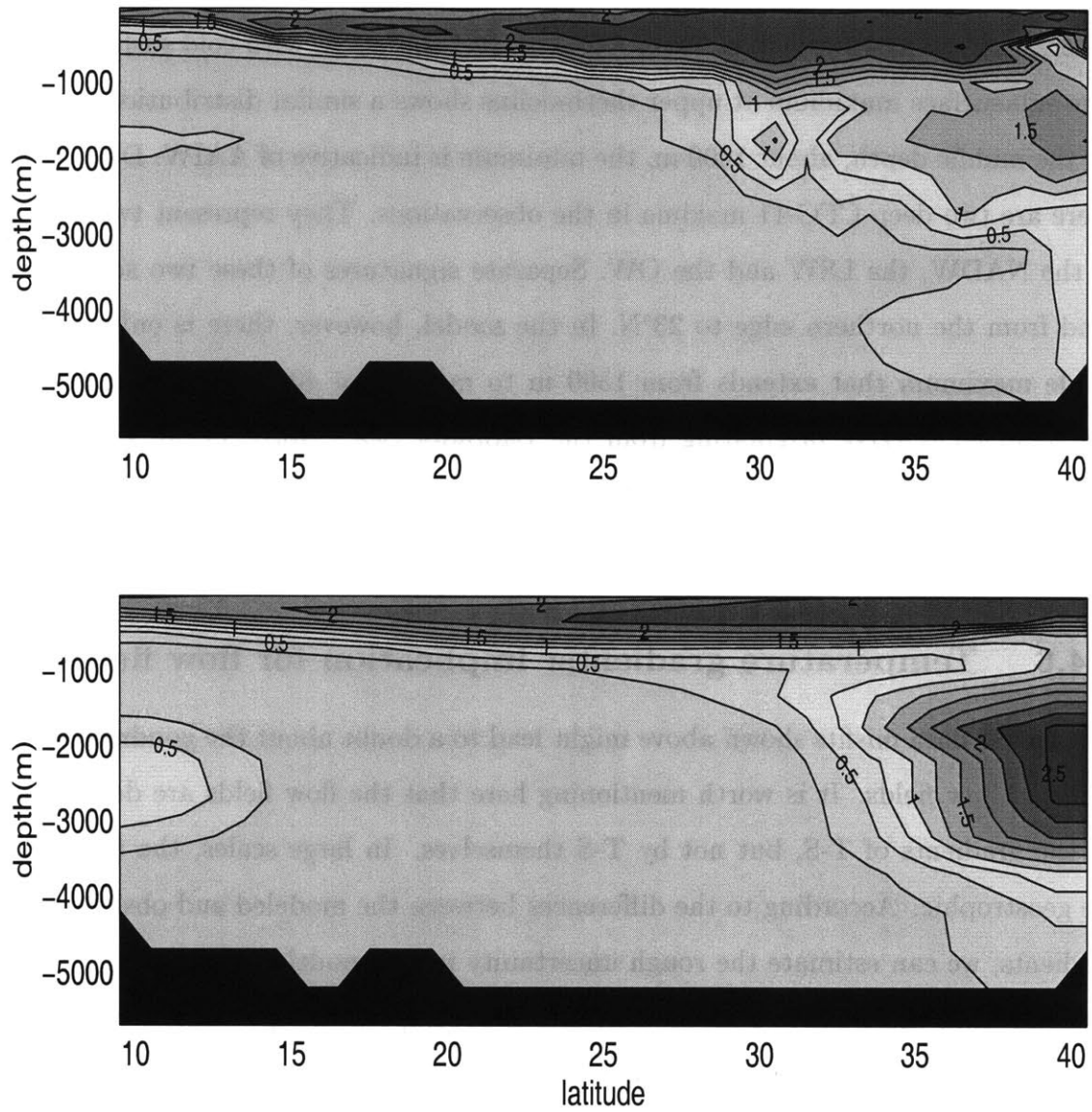
Figure 3-14: Observational (upper) and modeled (lower) CFC-11 distributions along 52°W (WOCE A20), July-August, 1997.

where f is the Coriolis parameter. Scale analysis of the above equations gives us

$$\delta U \sim \frac{gH}{f\rho_o}\delta(\nabla\rho),$$

(3.7)

where H is the vertical scale, typically $O(10^3)$ m. In addition, the equation of state tells us,

$$\nabla\rho \sim \alpha\rho_o\nabla T,$$

(3.8)

where α is the thermal expansion coefficient. Substituting (3.8) into (3.7), we get

$$\delta U \sim \frac{gH\alpha}{f}\delta(\nabla T).$$

(3.9)

Equation (3.9) tells us a model-data misfit of ∇T with $O(10^{-3})$ ^oC/km will lead to an error of $O(1)$ cm/s in the modeled flow field.

In calculating the temperature gradients, the data are first interpolated onto the model grids. Then the gradients are obtained using a center difference scheme

$$\frac{\partial T}{\partial r} = \frac{T_{i+1} - T_{i-1}}{2\delta r}.$$

(3.10)

Here δr is the distance between two model grid points, i.e., the distance in kilometers of 1° in longitude or latitude.

The distributions of latitudinal temperature gradient $\partial T/\partial y$ along $\sim$52°W show that, at the northern edge at the depth where the NADW is located, the model-data misfit of $\partial T/\partial y$ is about $O(10^{-3})$ ^oC/km (Fig. 3-15). This value corresponds to an error of 1 cm/s in the modeled longitudinal flow field. Comparison of modeled and observed longitudinal temperature gradients along $\sim$24°N, in Fig. 3-16, tells us that the problematic temperature distribution in the NADW leads to 1 cm/s error in the modeled DWBC. Figure 3-17 shows the flow field at 2200 m depth in February in the offline model. The modeled DWBC at 24.5^{o}N has a value of 4 cm/s. Taking a 1 cm/s error into account, we regard the modeled flow field as consistent with observations to first order.
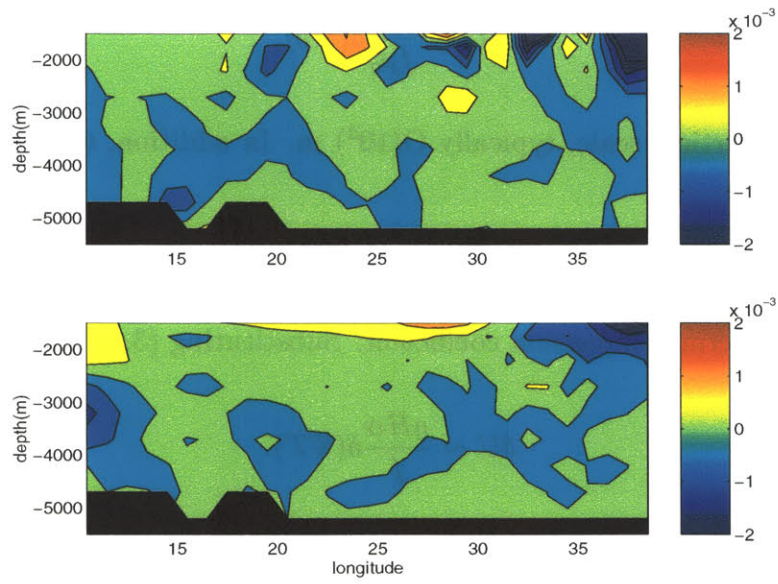
Figure 3-15: Observed (upper) and modeled (lower) $\partial T/\partial y$ (^{o}C/km) along WOCE A20 ($\sim 52^o$W). The contour interval is 0.5×10^{-3} ^{o}C.
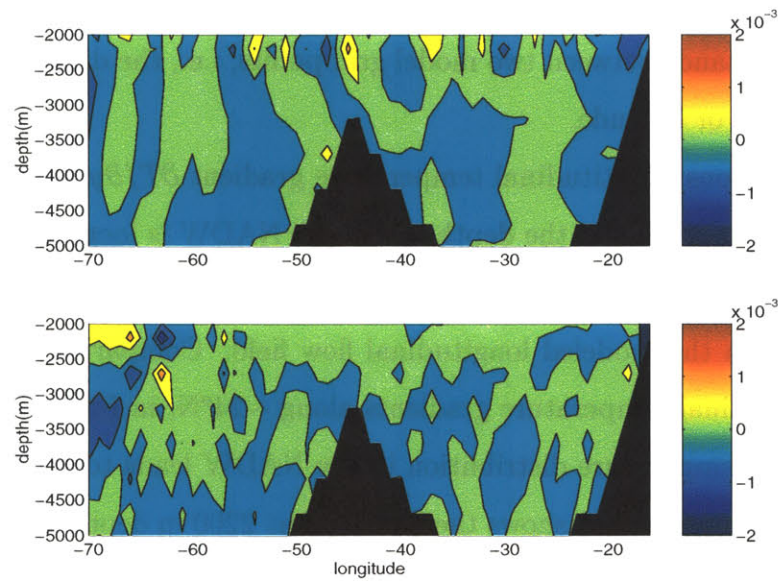
Figure 3-16: Observed (upper) and modeled (lower) $\partial T/\partial x$ (^{o}C/km) along WOCE AR01 ($\sim 24^o$N). The contour interval is 0.5×10^{-3} ^{o}C.
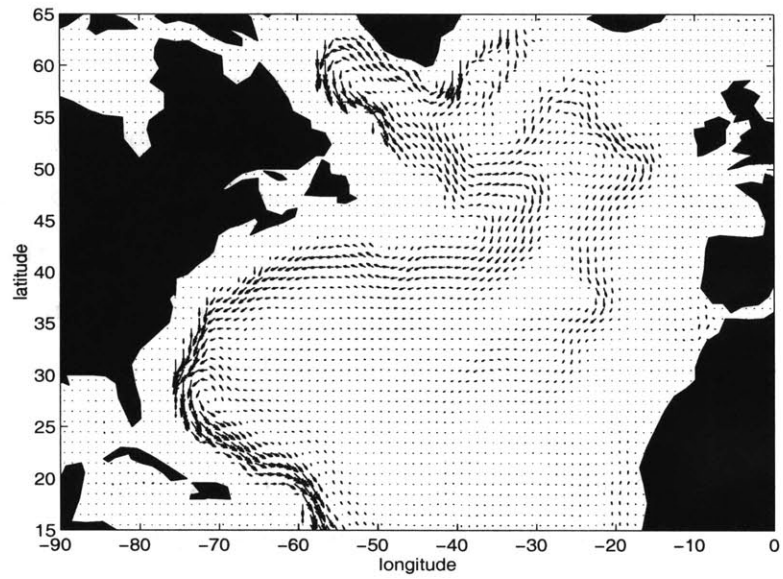
Figure 3-17: The flow field at 2200 m depth in Feb. in the offline model. The maximal velocity has a value of 5.7 cm/s.

3.5 Comparison of tritium and helium observations with model results

The modeled and observed tritium distributions along the western Atlantic GEOSECS section are shown in Fig. 3-18. Model-data discrepancies are very obvious in the high latitudes, where vigorous convection homogenizes the entire water column in the model. Observations show, however, that the tritium-enriched upper NADW at about 1500 m depth is separated from the bottom local maximum along the topographic slope by low tritium water.

Comparison along other sections (Fig. 3-19) shows that most model-data differences of tritium are similar to those of CFC-11. In the model, vertical penetration of surface values in the high latitudes is too deep, as shown by tritium distributions along 20^oW. Modeled tritium concentration near the western boundary, especially in the high latitudes, is too high. In the subtropical gyre, unlike in the CFC-11 distributions, the two deep maxima indicating the LSW and OW are not obvious in the tritium observations, owing to the radioactive decay which weakens the tritium signals.

Discrepancies between the modeled and observed ^3He values are large. These model-data misfits come from both the poorly simulated tritium distribution and the large amount of terrigenic ^3He in some regions. For example, along the section nominally at 46^oN (Fig. 3-20), modeled ^3He concentration between depth 1500 - 3000 m is too high due to the excessive tritium in this depth range. Near the ocean floor, there is a maximum in the observations, indicating a significant contribution from mantle outgassing. For the future use of ^3He data, a good simulation of tritium concentrations and accurate estimate of mantle ^3He distribution are required. This does not belong to the scope of this study. We will not use ^3He data in the assimilation study.
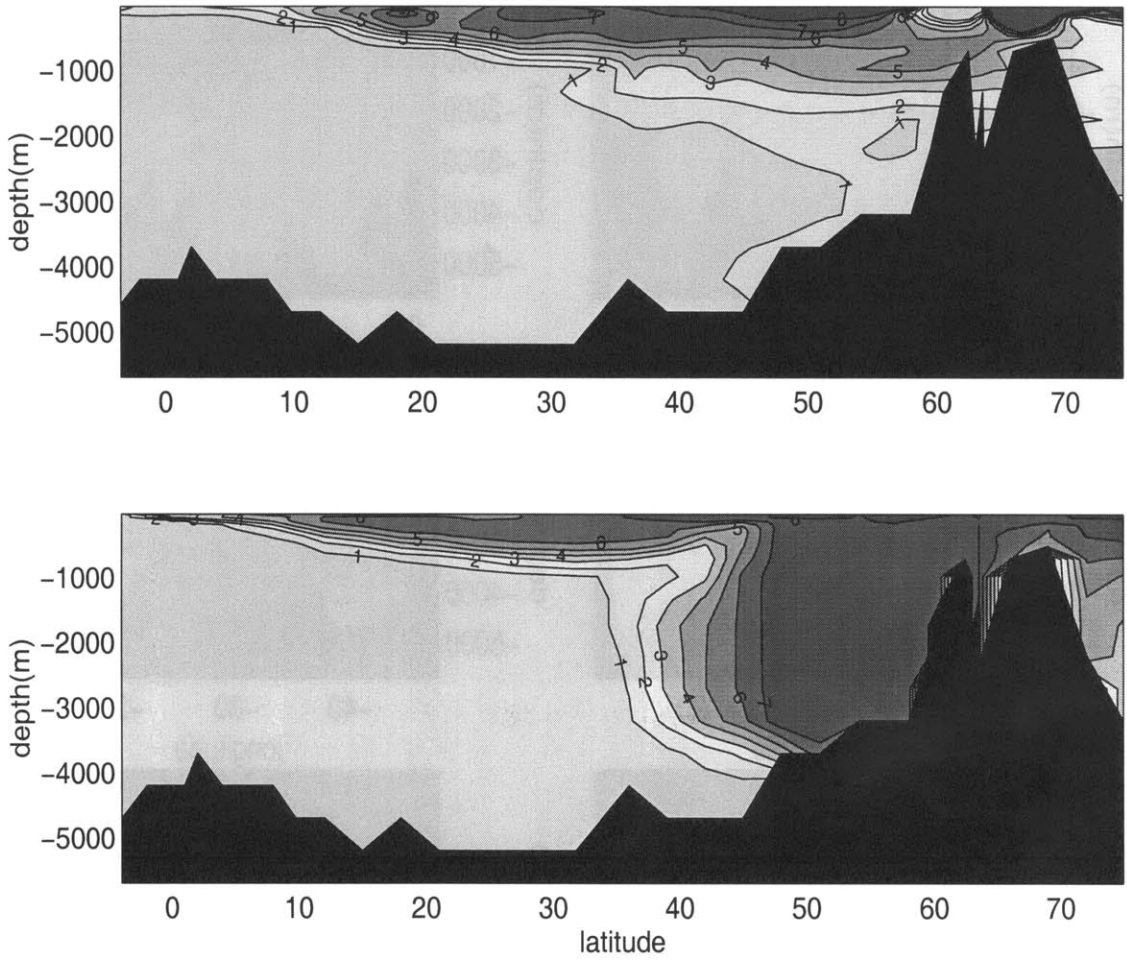
Figure 3-18: Observed (upper) and modeled (lower) tritium distributions (TU) along the western Atlantic GEOSECS section, 1972.
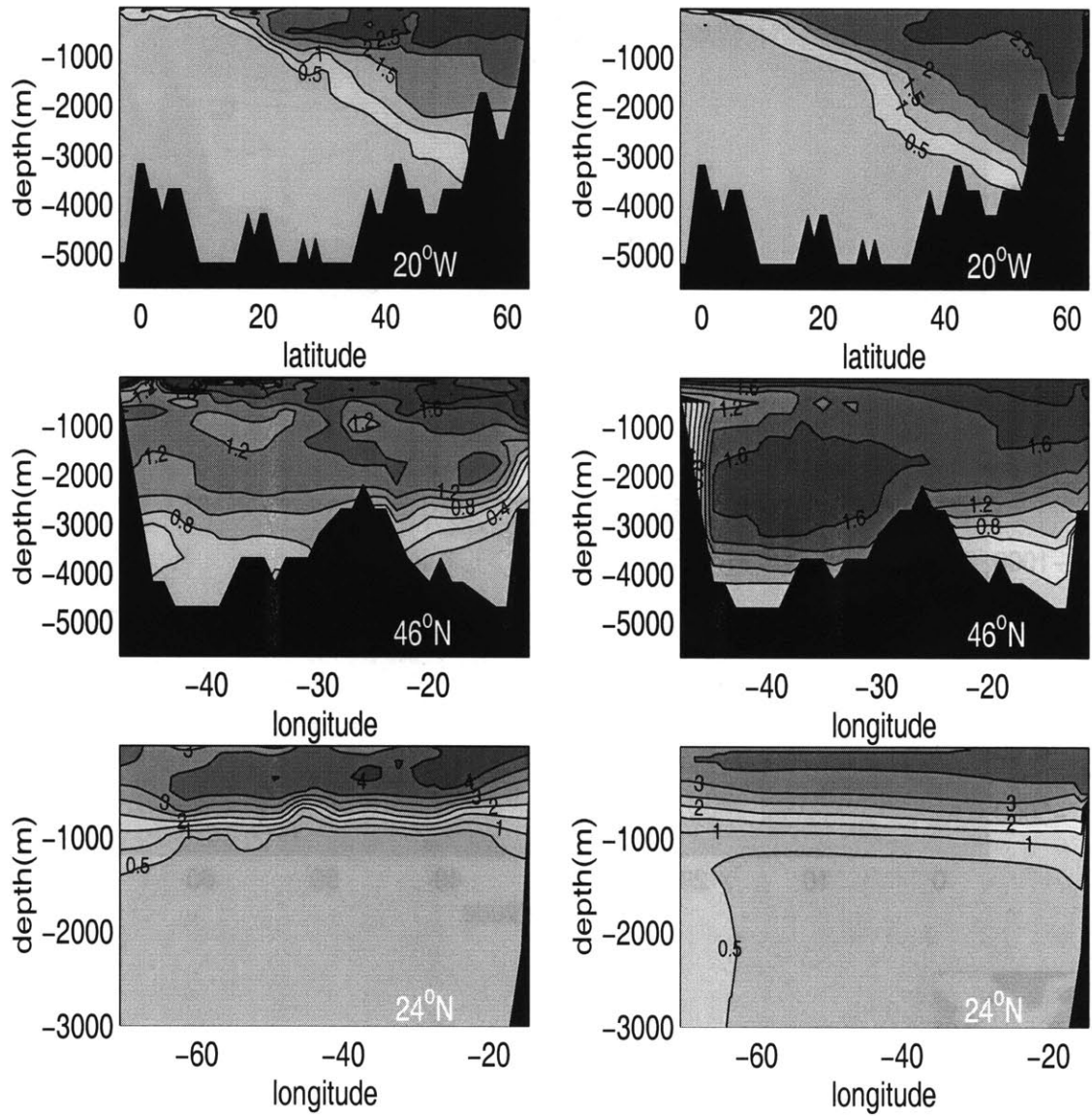
Figure 3-19: Observed (left) and modeled (right) tritium distributions (TU) along sections nominally 20°W (Jul. - Aug., 1988), 46°N (Nov., 1994), and 24°N (Aug., 1981).
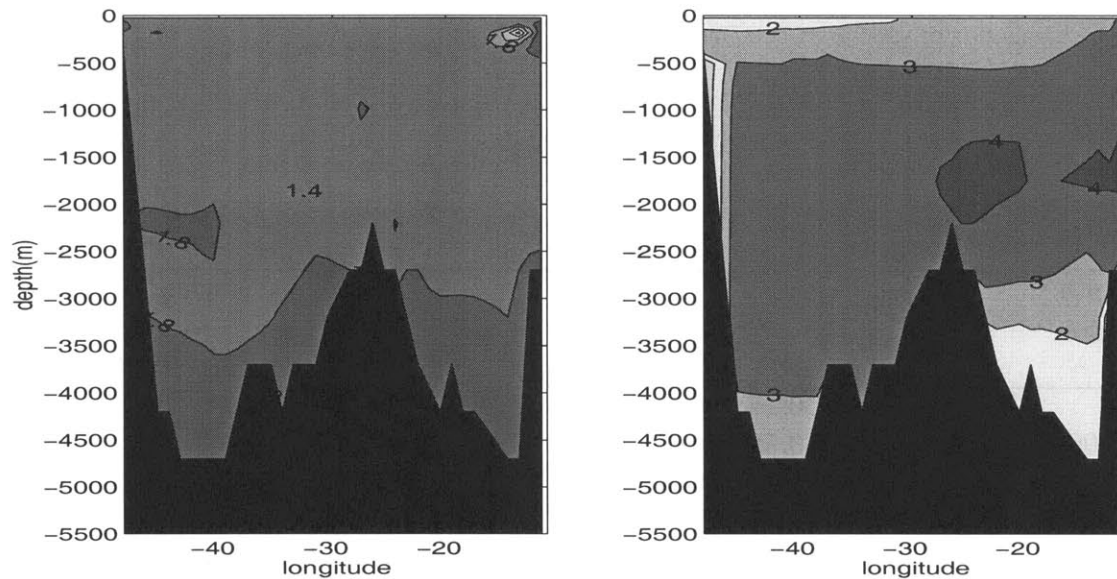
Figure 3-20: Observed (left) and modeled (right) ^{3}He distributions (TU) along the section nominally 46°N, Nov., 1994.

3.6 Quantitative calculation of the model-data differences

Root-mean-square (RMS) model-data differences at the observational sections are computed to provide quantitative information. The ocean is divided into five vertical layers: surface ($\leq$100 m), upper (100 - 500 m), thermocline (500 - 1500 m), deep (1500 - 3500 m), and bottom ($\geq$3500 m) layers. Since the unit and magnitude of each tracer are different, values of these RMS differences normalized by the observational variances of a corresponding tracer at cruise sections are also calculated. We call them normalized RMS differences. These normalized RMS differences provide us a numerical measure of goodness of fit. The non-normalized RMS values tell us the absolute magnitudes of model-data misfits.

Table 3.3 shows the model-data misfits along the observational sections. Some details are noteworthy and help to identify the model predictions. (1) The normalized RMS differences of CFC-11 and CFC-12 are similar due to similar source functions. (2) Model-data misfits of all tracers in the upper 100 m are large in the high lat-

101

Table 3.3: Model-data misfits along WOCE sections.

Depth (m)	Section	RMS					Normalized RMS				
		F11	F12	HTO	T	S	F11	F12	HTO	T	S
≤100	AR01	0.16	0.06	0.36	1.56	0.60	0.15	0.11	0.36	0.18	0.61
	A02A	0.58	0.27	0.44	2.92	0.59	0.58	0.51	0.96	0.53	1.28
	AR07WD	1.31	0.48	0.68	1.63	0.36	1.43	1.06	0.85	1.91	0.70
	A20	0.10	0.40	NA	1.55	0.42	0.11	0.10	NA	0.17	0.49
	A16N	0.25	0.11	0.53	2.01	0.17	0.21	0.20	0.88	0.29	0.28
100-500	AR01	0.17	0.08	0.36	0.98	0.30	0.18	0.16	0.37	0.11	0.31
	A02A	0.54	0.26	0.26	3.21	0.47	0.53	0.49	0.56	0.58	1.01
	AR07WD	1.96	0.73	0.29	1.06	0.16	2.15	1.62	0.36	1.24	0.30
	A20	0.19	0.09	NA	1.61	0.28	0.20	0.19	NA	0.18	0.32
	A16N	0.22	0.15	0.27	1.30	0.20	0.19	0.28	0.46	0.19	0.34
500-1500	AR01	0.29	0.14	0.51	0.58	0.11	0.29	0.28	0.52	0.07	0.12
	A02A	0.99	0.48	0.24	2.25	0.22	0.98	0.90	0.53	0.41	0.48
	AR07WD	2.25	0.83	0.24	0.78	0.09	2.46	1.83	0.30	0.92	0.18
	A20	0.33	0.15	NA	0.99	0.14	0.34	0.31	NA	0.11	0.16
	A16N	0.54	0.30	0.36	0.87	0.14	0.45	0.56	0.59	0.12	0.24
1500-3500	AR01	0.14	0.07	0.24	0.20	0.03	0.13	0.14	0.24	0.02	0.03
	A02A	1.52	0.70	0.47	0.26	0.03	1.51	1.31	0.96	0.05	0.06
	AR07WD	1.78	0.70	0.27	0.47	0.06	1.95	1.56	0.34	0.56	0.11
	A20	0.45	0.22	NA	0.21	0.02	0.47	0.44	NA	0.02	0.02
	A16N	0.38	0.20	0.31	0.38	0.04	0.32	0.36	0.52	0.06	0.07
≥ 3500	AR01	0.02	0.01	0.03	0.21	0.01	0.02	0.03	0.03	0.02	0.01
	A02A	0.02	0.02	0.04	0.07	0.00	0.02	0.03	0.10	0.01	0.00
	AR07WD	NA	NA	NA	NA	NA	NA	NA	NA	NA	NA
	A20	0.05	0.02	NA	0.2	0.01	0.05	0.04	NA	0.02	0.01
	A16N	0.01	0.01	0.01	0.15	0.00	0.01	0.01	0.02	0.02	0.01

Note: F11, F12, and HTO represent CFC-11, CFC-12, and tritium respectively.
The HTO observations at ar01 ($\sim$24°N) are measured in Sept., 1981.

itudes, where the surface values invade the interior. This leads to the model-data inconsistency at depth along the western boundary. (3) In the deep ocean, below 1500 m, normalized model-data misfits of all tracers in the subtropical area (WOCE AR01) and eastern basin (WOCE A16N) are smaller than those in high latitudes (WOCE AR07WD and A02A). The largest model-data discrepancies of CFCs and temperature appear in the Labrador Sea. (4) The normalized RMS differences of T-S are similar to those of the transient tracers in the upper ocean. At places such as the Labrador Sea (WOCE AR07WD), where the model-data differences of the CFC concentrations are large, model-data misfits of T-S are large as well.

We have compared the model predictions with observations at individual cruise tracks. For a whole domain picture on an average, an index is calculated. This index is a measurement of model-data mismatch,

$$I = \sqrt{\frac{1}{n}\sum_{i=1}^{n}(C_i^{model} - C_i^{obs})^2/(C_i^{obs})^2}. \qquad (3.11)$$

Offline model predictions of transient tracers C_i^{model} are compared with observations C_i^{obs} wherever measurements are available. In this comparison, the data are binned meridionally, zonally and vertically into model grid cells. An average is calculated if more than one sample is within a box. Measurements made within a month are assumed to be synoptic and compared with the monthly mean tracer fields in the model.

The values of the index are:

$$I_{CFC-11} = 20, \ I_{CFC-12} = 10, \ I_{tritium} = 25, \ I_{helium} = 57.$$

The index for tritium is larger than those of CFCs. Tritiogenic ^{3}He is the radioactive decay product of tritium. We cannot expect the model to reproduce the ^{3}He distribution well if the tritium distribution is not well simulated, not to mention the large uncertainty in the estimate of the mantle outgassing component. Therefore, model-data misfit of ^{3}He is the largest.

The values of the index demonstrate that the estimates of CFC boundary conditions are better than that of tritium. This is a major reason for the apparent lack of studies to simulate tritium in OGCMs, while simulations of CFCs are more common [England et al., 2001]. Therefore, sensitivities of CFC properties are compared with those of a steady tracer quantity in the next chapter. Yet to make full use of the existing data, both CFC and tritium observations are assimilated in the model.

3.7 Discussion

Severals sources of errors contribute to the model-data misfits shown above. Besides errors in the boundary conditions of transient tracers and of T-S, there are errors in both the data and model, as no data or model is perfect. The imperfect parameterization of sub-grid scale physics, numerical schemes, and simplifications made in the model all lead to the model-data misfits. Discerning the components of model-data misfits contributed by different sources is not trivial. Here we discuss the possible implications for our results.

The modeled transient tracer distributions are simulated in the offline model, which uses the monthly climatological mean velocities and T-S fields, in which internal model dynamics such as inter-annual variabilities in circulation fields are absent. Some errors are thus introduced into the offline model predictions. The steady state assumption is a good approximation for large-scale open ocean dynamics. Convective activities, however, have strong interannual to decadal variability [e.g., Dickson et al., 1996]. The interannual variability in the ocean, especially that of deep convection, will have signatures in the tracer fields [e.g., Doney et al., 1998]. Using tracer fields to study the variability in the ocean is not discussed in this study and deserves further research. In addition, the offline model uses the monthly mean convective fields, while the convection itself is a process whose time scale is usually less than a month. Whether it is adequate to represent the convective fields in their monthly means needs more exploration. Resolving the deep convective process in the model remains a challenge and is a direction of future research.

Even though there are many sources that contribute to the model-data misfits, the main conclusion that model-data discrepancies of transient tracer fields appear in regions where the modeled and observed water mass structures are different is obvious and reasonable. It is unlikely that the consistent structures of model-data misfits in all the tracer fields are totally due to the errors in the boundary conditions and simplifications in the offline model. Those large-scale model-data disagreements reflect problems in the modeled water masses, which are identifiable in both transient and T-S fields. Our attention here is restricted to a descriptive and semi-quantitative comparison of the model and data. Whether those problems in the model can be quantitatively improved by the transient tracer data will be investigated last.

3.8 Summary

Comparisons of model predictions with observations in the North Atlantic show that large model-data discrepancies exist in the high latitudes and deep western basin. The model-data disagreements of transient tracer fields appear in regions where the modeled and observed water mass structures are different. Model-data misfits of CFCs are smaller than those of tritium and ^{3}He.

The modeled transient tracer and T-S fields show too much vertical penetration of surface values in the high latitudes. In the deep convective regions, the modeled temperature/isopycnal surfaces are very steep, in contrast to observations. This permits a quick vertical invasion of the surface water properties along those steep isopycnals. Associated with this, the NADW in the model is poorly simulated. The model produces a very thick and relatively uniform NADW originating from the Labrador Sea. Along its pathway through the Western Atlantic Boundary, this voluminous water mass occupies depths from 1500 m down to about 4000 m. In addition, due to the model resolution and topography, the lower limb of the NADW, i.e., the OW, is not resolved by the model. The excessive uptake of the surface values in the deep convective regions yields transient tracer concentrations in the deep western North Atlantic that far exceed the observations.

The extensive vertical penetration of the convective adjustments, problematic production and outflow of the NADW can be monitored by both transient tracer and T-S fields. All tracers, steady or transient, undergo the same dynamics controlled by flow fields and mixing rates. Both T-S and transient tracers can be used to locate rapid mixing processes where vertical homogeneity is present. In the model, CFC-11 and salinity fields exhibit a strikingly similar pattern of the ventilation pathway of the LSW. All characteristic properties of a water mass will be tagged along the trajectory of that water mass. Steady tracers, for instance salinity, can help us evaluate the ventilation pathways in the model as well.

Qualitatively, this comparison study shows that major problems in the model, i.e., too much vertical penetration of surface values in the high latitudes, too thick and voluminous LSW along the western boundary, and the absence of OW, can be identified in all the tracer fields. Quantitatively, whether the transient tracer data can be used to improve the model performance depends on the extent to which the data can constrain the model circulation properties. The one-dimensional idealized tracer study in Chapter 2 has shown that the steady state observations can effectively constrain the mixing rate because of the simplicity of the steady boundary conditions; the transient state observations, on the other hand, cannot accurately constrain the mixing rate due to the large degree of uncertainties in its time-varying boundary conditions. In a comprehensive model of the real ocean, a sensitivity study can help us evaluate the potential capabilities of steady and transient tracers to constrain the circulation properties, which will be presented in the next chapter. The extent to which the currently available transient tracer data can constrain the ocean circulation in the model will be answered more directly by a data-assimilation study.

Chapter 4

An Adjoint Sensitivity Study: Transient and Steady Tracers

4.1 Introduction

The objective of this chapter is to investigate the potential capabilities of transient and steady tracers to constrain the ocean circulation in a general circulation model (GCM) in the North Atlantic, according to their adjoint sensitivities. Propagation pathways and timescales of the sensitivities in the model are analyzed. The sensitivities are compared quantitatively.

In the literature of tracer oceanography, our understanding of the information content of the transient tracers mostly comes from the direct observational pictures [e.g., Smethie et al., 2000], comparisons of model results with data [e.g., England and Maier-Reimer, 2001], and inferences under simple assumptions [e.g., Jenkins, 1991; Kelley et al., 1999]. With the advances in dynamic theories, oceanic observations (e.g., altimetry, current meters, floats, and traditional tracers), and numerical models, our estimation of the ocean state becomes more and more realistic [e.g., Stammer et al., 2002]. The integrated tracer transport rates and pathways can be calculated directly from the estimated advective and mixing rates. As the transient tracer observations have been and will always be sparse, direct combination of a numerical model with the observations is one of the major techniques for us to obtain quantitative information.

In Chapter 3, the forward model predictions show that the extensive vertical penetration of the convective adjustments, problematic production and outflow of the North Atlantic Deep Water (NADW) in the model are indicated by transient tracer, temperature and salinity (T-S) fields. In an inverse aspect, a sensitivity study can reveal the timescales and pathways of important physical processes that govern the tracer distributions. Or to put it another way, the sensitivity study can exhibit how the observational information of transient and steady tracers will propagate in the model and thereby constrain the model physics.

The sensitivities will help us to evaluate the potential capabilities of steady and transient tracers to constrain the ocean circulation properties, which are treated as a set of control variables. The more sensitive an observation is to a control variable, the more rigorously the observation can constrain the control variable. The adjoint method provides the sensitivities to all control variables in one integration. These sensitivities thus allow us to determine which of the competing tracers, transient or steady, can be most effectively used to constrain the ocean circulation.

Adjoint sensitivity analysis in meteorology can be dated back to the early 1980s. Hall [1986] successfully estimated the first order sensitivities in an atmospheric GCM with the adjoint method. This method had not been widely applied in oceanography until the innovation of the Tangent Linear and Adjoint Model Compiler (TAMC), which produces the adjoint model in a semi-automatic way and helps us overcome the daunting burden of writing the adjoint code [Giering, 1998]. Marotzke et al. [1999] calculated the Atlantic heat transport sensitivity using the adjoint MIT GCM constructed by the TAMC. In this study, the sensitivities are computed by the offline version of the MIT GCM and its adjoint, which is generated by the TAMC.

CFC-11 and CFC-12 are perhaps the simplest transient tracers to be incorporated in a model, as they have relatively well known source functions. Robbins [2000] argued that a single tracer property was not sensitive to discerning the effects of diffusive versus advective ventilation; the use of coupled transient tracers, such as tracer age, might provide greater sensitivity to diffusive effects. Therefore, sensitivities of both CFC-11 concentration and CFC-11/CFC-12 ratio age are computed.

The most commonly observed steady tracers in oceanography are T-S and nutrients (e.g., oxygen and silica). Simulation of natural tracers such as nutrients requires proper modeling of bio-chemical processes, about which our knowledge is limited and large uncertainty potentially exists. T-S are dynamically active tracers. In the offline model, the flow fields are treated as parameters that are independent of the tracer distributions. This is true only for passive tracers. Dynamically active tracers, on the other hand, give feedbacks on the flow fields via their impacts on the sea water density. The density can be represented approximately as

$$\rho = \rho_o[1 - \alpha(T - T_o) + \beta(S - S_o)]. \tag{4.1}$$

Here α and β are thermal and haline expansion coefficients, respectively; ρ_o, T_o and S_o are constants. The quantity $\alpha T - \beta S$, called "spiciness" and symbolized by π [e.g., Veronis et al, 1972; Munk, 1981], has little influence on the density and thus flow fields. In this study, I define τ as

$$\tau = T - (\beta/\alpha)S. \tag{4.2}$$

If the mean surface values of temperature is 15 ^oC and salinity is 35.5 in the North Atlantic, τ is O (-100). In this region, the largest interannual variability of temperature is about O (1) ^oC, and that of salinity is about O (0.1) [e.g., Levitus et al., 1994, 1995]. According to Eq. (4.2), the largest interannual variability of τ is O (1), two orders less than its absolute mean value. Therefore, τ can be treated as a steady passive tracer. The sensitivities of this steady tracer quantity τ will be analyzed and compared with those of CFC-11 concentration and CFC-11/CFC-12 ratio age.

The distributions of CFC-11 and CFC-12 are calculated as described in Chapter 3. The CFC-11/CFC-12 ratio age is computed from the modeled CFC-11 and CFC-12 concentrations. The monthly climatological T-S fields described in Chapter 3 are used for initializing τ fields. At the ocean surface and lateral boundaries, τ are restored toward the same climatologies.

After 1980, the atmospheric CFC-11/CFC-12 ratio was no longer a monotonic
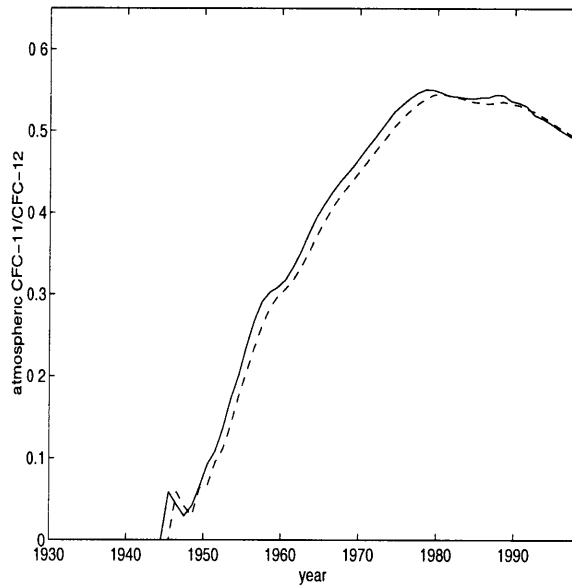
Figure 4-1: Estimate of the atmospheric CFC-11/CFC-12 ratio as a function of time and hemisphere, following Walker et al., [2000]. Values in the southern hemisphere are dashed.

increasing function of time (Fig. 4-1). Estimation of the CFC-11/CFC-12 ratio age in the sea water is thus limited to the time before 1980 in this study. In addition, the atmospheric CFC-11 content is small (Fig. 3-2) before 1950. The forward model predictions at the end of 1950 are used to initialize the CFC distributions. A time period over June 1980 to December 1950 is chosen for the backward adjoint integration.

In the North Atlantic, the transient tracers are commonly used to study the ventilation processes, notably those of the NADW and the lower subtropical thermocline. In Chapter 3, the comparison of modeled and observed tracer distributions shows that a major deficiency of the model is the problematic representation of the NADW, while model-data misfit in the upper ocean is relatively small. It would be interesting to see both transient and steady tracers can provide information about ocean ventilation, in an inverse study. The sensitivities of CFC-11 concentration, CFC-11/CFC-12 ratio age and τ in the NADW and lower thermocline will be presented.

In this chapter, the tangential linearization and the adjoint operator are interpreted first. Analysis of the sensitivities of the tracer properties in the NADW follows. The sensitivities of the tracer properties in the lower subtropical thermocline

are presented last.

4.2 Tangential linearization and interpretation of the adjoint operator

The basics of adjoint models have been documented by numerous papers [e.g., Giering, 1998; Errico et al., 1992]. Consider a physical system that can be represented by a set of state variables **X**. Its evolution is governed by

$$\frac{d\mathbf{X}}{dt} = F(\mathbf{X}, \mathbf{U}). \tag{4.3}$$

Here **U** is a vector containing a set of parameters (control variables); F is a (linear or nonlinear) function. A prognostic numerical model necessarily has a discrete representation

$$\mathbf{X}^{n+1} = \mathbf{A}(\mathbf{X}^n, \mathbf{U}), \tag{4.4}$$

with the time being replaced by time step n. Now consider a scalar function, i.e., the cost function, which is used to quantify a forecast aspect. In data-assimilation problems, J is typically a measure of model-data misfit, and can be expressed as

$$J(\mathbf{X}, \mathbf{U}) = (\mathbf{X} - \mathbf{X}_{obs})^T \mathbf{R}^{-1} (\mathbf{X} - \mathbf{X}_{obs}) + (\mathbf{U} - \mathbf{U}')^T \mathbf{Q}^{-1} (\mathbf{U} - \mathbf{U}'), \tag{4.5}$$

where **R** and **Q** are error covariances of observation and controls, respectively, as also described in Appendix A. In some sensitivity studies, J is simply a scalar function of the components of **X**, for example,

$$J = \sum_i x_i^m. \tag{4.6}$$

Let $\bar{\mathbf{X}}$ denote some basic state, which is time dependent. $\bar{\mathbf{U}}$ is the control variable vector the model used to produce the basic state. A small perturbation from this basic state will lead to a perturbation of J. In a linear case, the perturbation of J will

be small also and a first order Taylor series approximation can be applied,

$$\delta J = \sum_i \frac{\partial J}{\partial x_i^m} \delta x_i^m. \tag{4.7}$$

At any time step n, the perturbation of $\mathbf{X}$ follows the governing equation

$$\delta \mathbf{X}^{n+1} = [\frac{\partial \mathbf{A}(\mathbf{X}^n, \mathbf{U})}{\partial \mathbf{X}^n}|_{\mathbf{X}^n = \bar{\mathbf{X}}^n} \delta \mathbf{X}^n] + [\frac{\partial \mathbf{A}(\mathbf{X}^n, \mathbf{U})}{\partial \mathbf{U}}|_{\mathbf{U} = \bar{\mathbf{U}}} \delta U], \tag{4.8}$$

where $\delta \mathbf{X}^n = \mathbf{X}^n - \bar{\mathbf{X}}^n$. Here the first order Taylor series has been applied again. Equation (4.8) represents a linear model whose coefficients are determined by slopes tangential to the trajectories of the state variables and control variables in the forward model, and hence it is called a tangent linear model. This linear approximation depends on the assumption that perturbation $\delta \mathbf{X}^n$ at every time step n of the integration is small. Regarding the initial state $\mathbf{X}^0$ as the control variables, by successive replacement of (4.8), one obtains the final perturbation at time step m

$$\delta \mathbf{X}^m = \mathbf{M} \cdot \delta \mathbf{U}. \tag{4.9}$$

Here M is a matrix composed of successive sums of iterations of the partial derivatives of the forward model $\mathbf{A}$ to $\mathbf{X}$ and $\mathbf{U}$. Substituting (4.9) into (4.7), we get

$$\delta J = \frac{\partial J}{\partial \mathbf{X}^m} \mathbf{M} \cdot \delta \mathbf{U}. \tag{4.10}$$

For a more general case, we can regard J as any function of $\mathbf{X}$ (provided $\frac{\partial J}{\partial \mathbf{X}}$ exists). The above equation can also be written as

$$\delta J = \left\langle \mathbf{M}^* \frac{\partial J}{\partial \mathbf{X}}^*, \delta \mathbf{U} \right\rangle. \tag{4.11}$$

The sensitivity $\mathbf{M}^* \frac{\partial J}{\partial \mathbf{X}}^*$ can be found numerically by integrating backward the adjoint equations of the forward model. Let

$$\delta^* \mathbf{X}^m = 1 \tag{4.12}$$

112

$$\delta^* \mathbf{X}^{m-1} = (\frac{\partial J}{\partial \mathbf{X}})\delta^* \mathbf{X}^m \tag{4.13}$$

$$\delta^* \mathbf{X}^{n-1} = [\frac{\partial \mathbf{A}(\mathbf{X}^{n-1}, \mathbf{U})}{\partial \mathbf{X}}]\delta^* \mathbf{X}^n \tag{4.14}$$

$$\delta^* \mathbf{U}^m = 0 \tag{4.15}$$

$$\delta^* \mathbf{U}^{n-1} = \delta^* \mathbf{U}^n + [\frac{\partial \mathbf{A}(\mathbf{X}^{n-1}, \mathbf{U})}{\partial \mathbf{U}}]\delta^* \mathbf{X}^n. \tag{4.16}$$

Therefore, the sensitivity information propagates backward by the backward integration of the adjoint equations. The sensitivity of J to the control vector is given by the final condition $\delta^* \mathbf{U}^0$.

4.3 Sensitivities of tracer properties in the NADW

This section presents the adjoint sensitivities of the CFC-11 concentration, CFC-11/CFC-12 ratio age, and τ in the NADW. Propagation of the sensitivities is analyzed to explore the abilities of CFCs and τ in providing the information about the transport pathway of the NADW and its timescale. Sensitivities, notably those to the mixing rates, which are considered to be well constrained by the transient tracers, are quantitatively compared.

The cost function is

$$J = \frac{1}{n} \sum_i^n C_i. \tag{4.17}$$

Here C denotes CFC-11 concentration, CFC-11/CFC-12 ratio age, or τ; i represents tracer property samples in June 1980 at 30.5°N, within depths 1335 - 2700 m and longitudes 80.5 - 60.5 °W. These samples are summed horizontally and vertically at each time step in June 1980. The summation is then divided by n, the number of total samples of each tracer property. This cost function represents roughly the mean tracer property in the NADW at 30.5°N in June 1980. The values of the cost function are slightly high weighted toward the core values in the NADW, as compared to the volume weighted means, because the volume of the core is less than that of the ambient NADW. Therefore, the sensitivities revealing the pathway and timescale of the NADW core in the model stand out.

4.3.1 The modeled tracer distributions in the NADW

Figure 4-2 shows that the distributions of the tracer properties at 2200 m, approximately the central depth of the modeled NADW, have a similar pattern. Formed in the deep convective region in the Labrador Sea, the modeled NADW spreads southeast-ward with the Labrador Sea Current. After it passes the Grand Banks of Newfoundland, a large part of it turns southward with the Deep Western Boundary Current (DWBC) along the American coast. The rest enters the eastern basin via the Charlie-Gibbs Fracture Zone. After intruding into the eastern basin, the NADW is advected southward by the DWBC along the Mid-Atlantic ridge, then it re-enters the western basin between 35°N - 25°N and joins the other branch (also see Fig. 3-17).

4.3.2 Normalized sensitivity

Sensitivities of different tracers are normalized for comparison. The normalized sensitivity is represented as

$$s = \frac{1}{\delta J_o} \frac{\partial J}{\partial u}. \tag{4.18}$$

Here $\partial J / \partial u$ is the adjoint model result, with u the control variable, such as the boundary condition, flow field or mixing coefficient. In this sensitivity study, J is the mean tracer property at a specific location. The amplitudes of δJ_o correspond to modeled tracer perturbations of the order of J. For example, in Fig. 4-2, the perturbations of tracer properties in the NADW at 30.5°N in June 1980 are $|\delta J_o| = O(0.1)$ pmol/kg for CFC-11 concentration, $|\delta J_o| = O(10)$ years for the CFC-11/CFC-12 ratio age, and $|\delta J_o| = O(1)$ °C for τ. For CFC-11 concentration or τ, δJ_o is positive. Unlike the CFC-11 concentration and τ, low values of CFC age (young water) are carried by the NADW. δJ_o is taken to be -10 years for the CFC age. Therefore, the normalized sensitivity of the CFC age takes on the opposite sign of $\partial J / \partial u$.

The sensitivity to a model parameter can be interpreted as either the response of the cost function to a perturbation of the parameter or the extent to which a value of the cost function (e.g., a model-data misfit) can constrain the parameter. The larger the sensitivity, the more rigorously the parameter can be constrained.
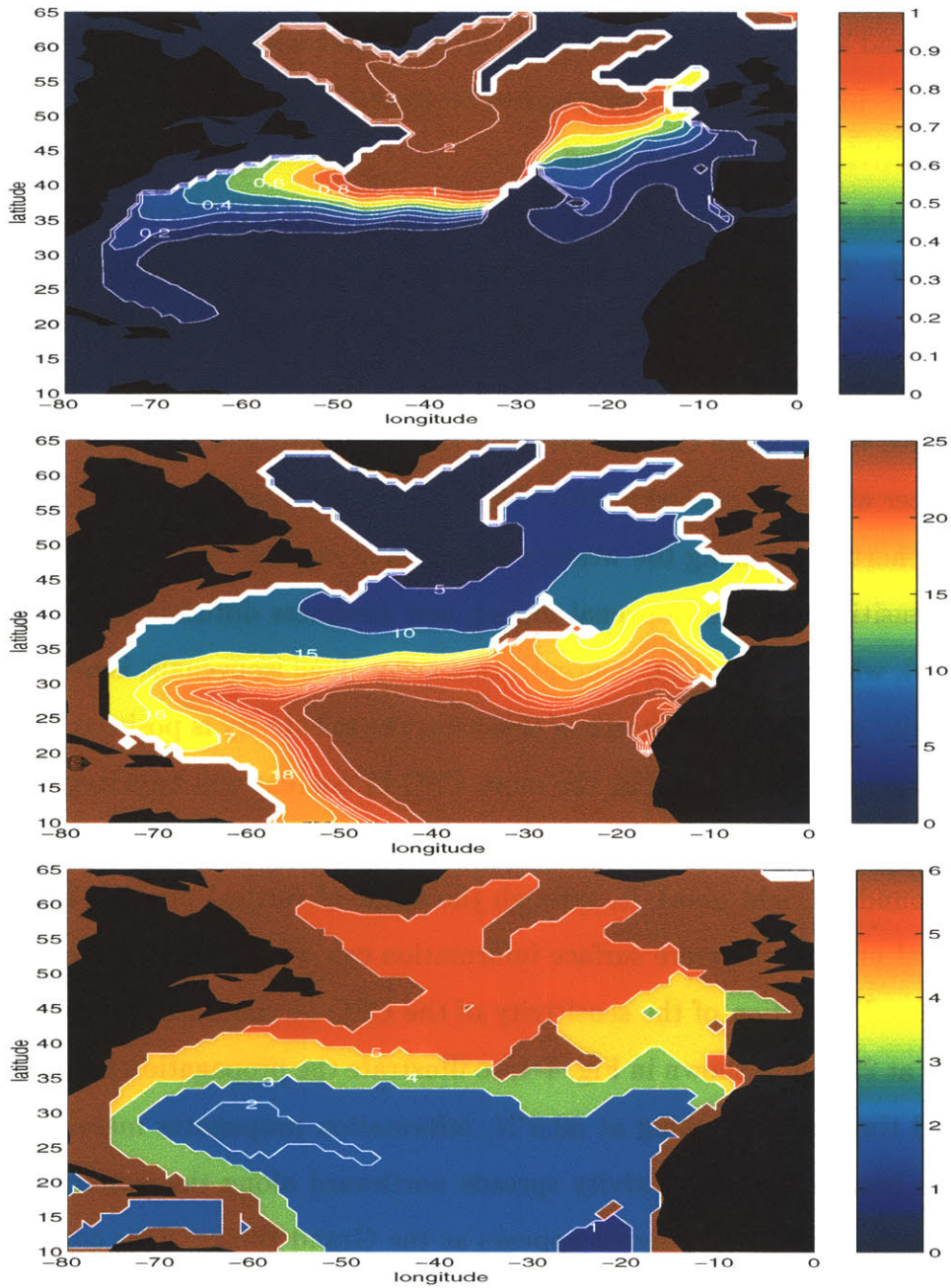
Figure 4-2: Distributions of the modeled CFC-11 concentration(upper, pmol/kg), CFC-11/CFC-12 ratio age (middle, year) and $\tau+120$ (lower, ^{o}C) at 2200 m, June 1980. The scales of the colorbars are chosen to let the southward spreading tongue near 30.5^{o}N stand out.

4.3.3 Propagation pathway and the associated timescale

The adjoint model is forced by tracer perturbations at 30.5°N, between depths 1335 ~ 2700 m and longitudes 80.5 ~ 60.5 °W, in June 1980, within which the cost function is evaluated. Information then propagates backward in time. In this section, evolution of the sensitivities will be presented.

Figure 4-3 shows the normalized sensitivities of the CFC-11 concentration at the end of 1977. The sensitivity to the meridional flow is positive south of 30.5°N and negative north of 30.5°N. This indicates the advective effect: more CFC-11 will converge to this section if the velocity toward this section becomes larger. For instance, the negative values mean that the stronger the southward flow, the more CFC-11 enriched water will be be carried to 30.5°N from the high latitudes. Advective sensitivity spreading northward along the western boundary is clearly visible.

The sensitivity to the isopycnal mixing and thickness diffusion (see Appendix B for details), which diffuse CFC concentration away along isopycnals, is negative in the close vicinity of 30.5°N. Just north of this area, the sensitivity is positive, because the stronger the isopycnal mixing is, the more CFC-11 content will be conveyed towards 30.5°N from the high latitudes. Vertically, the deep ocean feels the influence of the surface boundary right above it, through the agent of vertical mixing. The stronger the vertical mixing, the more surface information can be carried downward.

Continued evolution of the sensitivity of the CFC-11 concentration to the meridional flow at 2200 m is shown in Fig. 4-4, to illustrate the propagation pathway and its associated timescale. Starting at 30.5°N, information propagates mainly upstream. The main branch of the sensitivity spreads northward along the western boundary. After 6 years, a substantial signal appears at the Grand Banks. This corresponds to a mean transport speed about 2 cm/s. It requires about 15 years (from 1980 to 1965) for the information to reach the Labrador Sea, where the modeled NADW originates. This is consistent with the forward run. As the time of the adjoint integration increases, the sensitivity in the Labrador Sea grows stronger and stronger. The other branch, extending eastward, propagates slowly. During the 30 years integration, it is

Figure 4-3: Normalized sensitivities of the CFC-11 concentration in the NADW between depths 1335 - 2700 m and longitudes 80.5 - 60.5 ^{o}W at 30.5^{o}N, June 1980 to the meridional flow at depth 2200 m in February (a, $(10^{-2}$ m/s$)^{-1}$), isopycnal mixing and thickness diffusion at depth 2200 m (b, $(100$ m^2/s$)^{-1}$), surface piston velocity (c, $(10^{-4}$ m/s$)^{-1}$), and background vertical mixing at depth 360 m (d, $(10^{-5}$ m^2/s$)^{-1}$) at the end of 1977.

confined to the western basin.

The deep ocean information is carried up via vertical mixing. Once a substantial signal arrives at the Labrador Sea in 1965, it is quickly brought up by the convective mixing. Consequently, the sensitivity to the surface forcing increases by an order of magnitude and is maximized at the Labrador Sea (Fig. 4-5).

Figure 4-4: Normalized sensitivities of the CFC-11 concentration in the NADW between depths 1335 - 2700 m and longitudes 80.5 - 60.5 ^{o}W at 30.5^{o}N, June 1980 to the meridional flow $((10^{-2} \text{ m/s})^{-1})$ at 2200 m depth in February at the end of year 1977 (a), 1973 (b), 1965 (c), and 1950 (d).

The normalized sensitivities of the CFC-11/CFC-12 ratio age and τ, in Fig. 4-6, exhibit a similar advective pathway and timescale. Mainly along the western boundary, information is carried northward. It takes about 6 years for a signal of
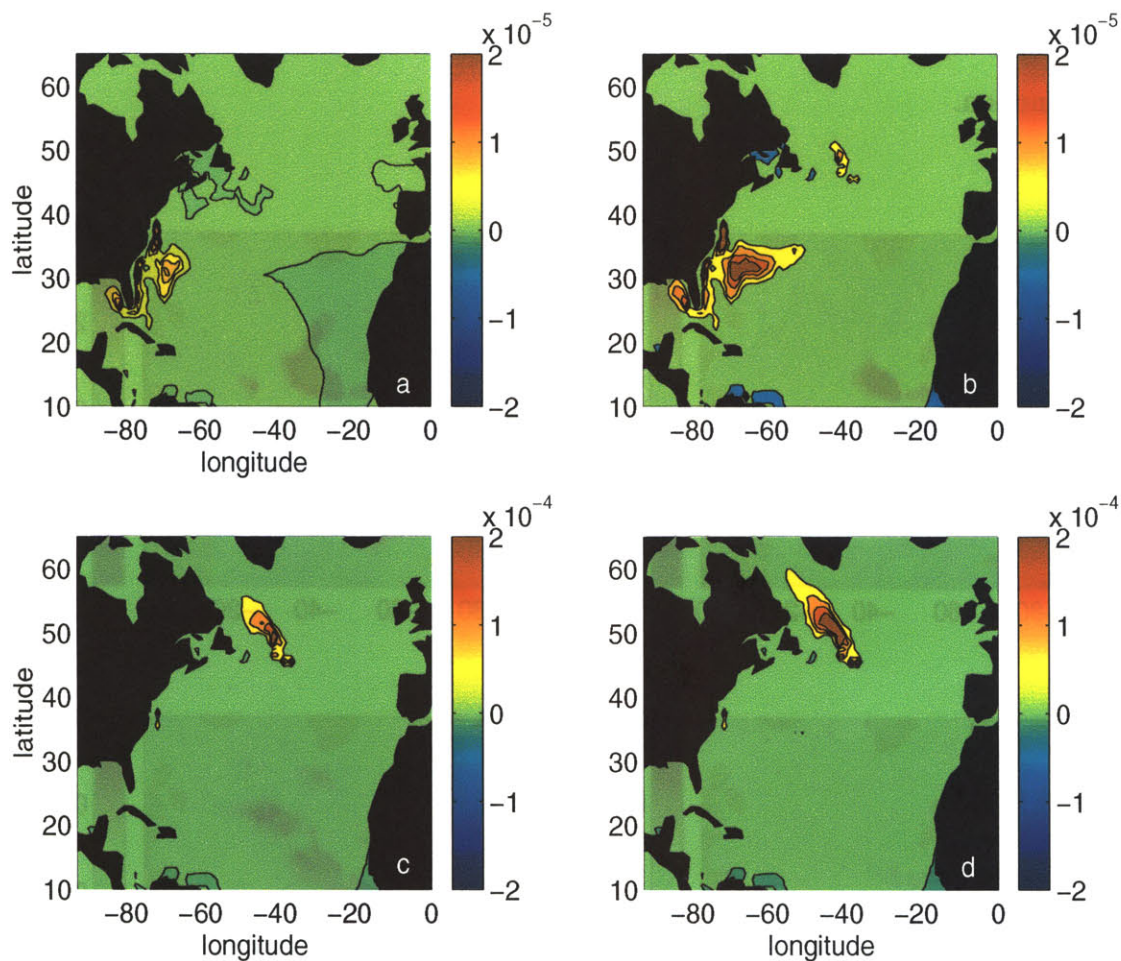
Figure 4-5: Normalized sensitivities of the CFC-11 concentration in the NADW between depths 1335 - 2700 m and longitudes 80.5 - 60.5 ^{o}W at 30.5^{o}N, June 1980 to the surface piston velocity in February $((10^{-4} \text{ m}^2/\text{s})^{-1})$ at the end of year 1977 (a), 1973 (b), 1965 (c), and 1950 (d). Note that values in the lower panels are an order of magnitude larger than those in the upper ones.

either a transient or steady tracer property at 30.5°N in the NADW to reach the Grand Banks, and 15 years to reach the Labrador Sea. The negative values of the normalized sensitivity of the CFC age, presented in the opposite sign of $\partial J/\partial u$ (Eq. (4.18)), can be explained by the advective effect. A decrease of the southward flow in the region north of 30.5°N (carrying young water), or an increase of the northward flow in the region south of 30.5°N (carrying old water), leads to an increase of the cost function.
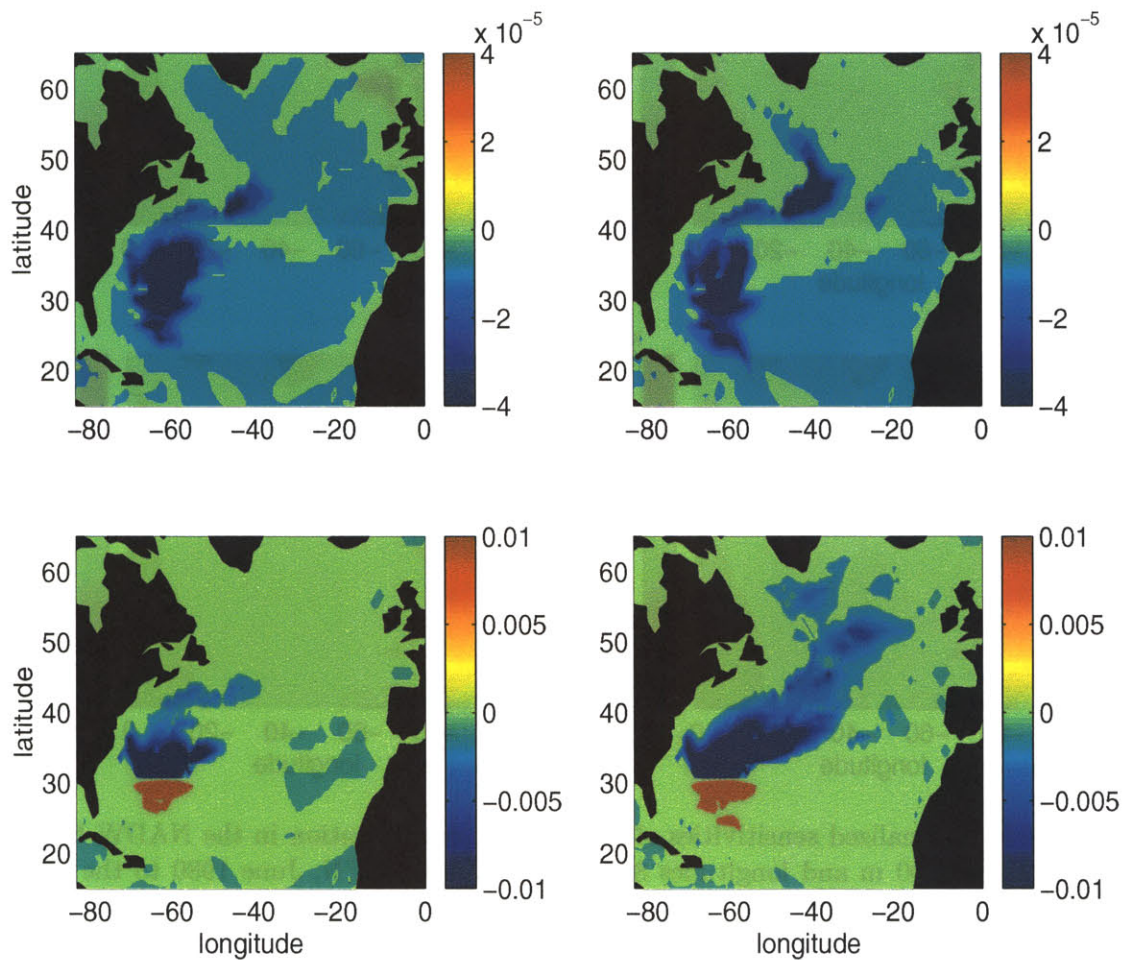
Figure 4-6: Normalized sensitivities of the CFC-11/CFC-12 ratio age (upper) and τ (lower) in the NADW between depths 1335 - 2700 m and longitudes 80.5 - 60.5 °W at 30.5°N, June 1980 to meridional flow $((10^{-2} \text{ m/s})^{-1})$ in February at 2200 m depth at the end of year 1973 (left) and 1950 (right). Note that values in the lower panels are much larger than those in the upper ones.

The steady tracer quantity τ provides the strongest sensitivity to the flow field, suggesting that the flow field will be more rigorously constrained by τ than by CFCs. This result depends on the modeled flow field. As the modeled flow field is marginally consistent with observations, we regard the adjoint sensitivities in the model as first order approximations. In an online GCM, the flow field is calculated from the distributions of T-S, according to model dynamics. If the transient tracer data are used to constrain the flow field in the online model, the optimization has to be carried out via adjustments of the model parameters, such as the boundary conditions of T-S, that govern the modeled T-S fields. Using the T-S data to constrain the flow field directly in an OGCM will be more efficient than using the transient tracer data.

After the signal arrives at the Labrador Sea, it is quickly conveyed vertically to the surface by convective mixing. Therefore, the sensitivities to the surface forcing (Fig. 4-7) demonstrate that all tracer properties in the NADW are mainly controlled by the surface values in the Labrador Sea, where the modeled NADW forms.

These adjoint sensitivities are used to infer likely errors in the modeled tracer distributions, owing to uncertainties of the surface boundary conditions. Let

$$
\begin{aligned}
e &= s \cdot \delta u \\
&= \frac{1}{\delta J_o} \frac{\partial J}{\partial u} \delta u \\
&= \frac{\delta J}{\delta J_o}.
\end{aligned}
\tag{4.19}
$$

Here δu is the uncertainty of the surface boundary condition; s and δJ_o are the same as in Eq. (4.18). Therefore, e is the relative error of J, the mean tracer property in the NADW between depths 1335 - 2700 m and longitudes 80.5 - 60.5 °W at 30.5°N, June 1980. If the uncertainties of the surface values in the Labrador Sea are 1 °C for temperature, 0.1 for salinity, and 5×10^{-5} m/s for surface piston velocity, according to the sensitivities, these uncertainties will lead to relative errors of 10^{-4} % in τ, 10^{-2} % in the CFC-11 concentration, and (5×10^{-3})% in the CFC ratio age, in the NADW at 30.5°N. The uncertainty of the surface piston velocity in the Labrador Sea leads to larger relative errors in the CFC fields in the NADW, compared with the

corresponding error in τ due to the uncertainties in surface T-S.
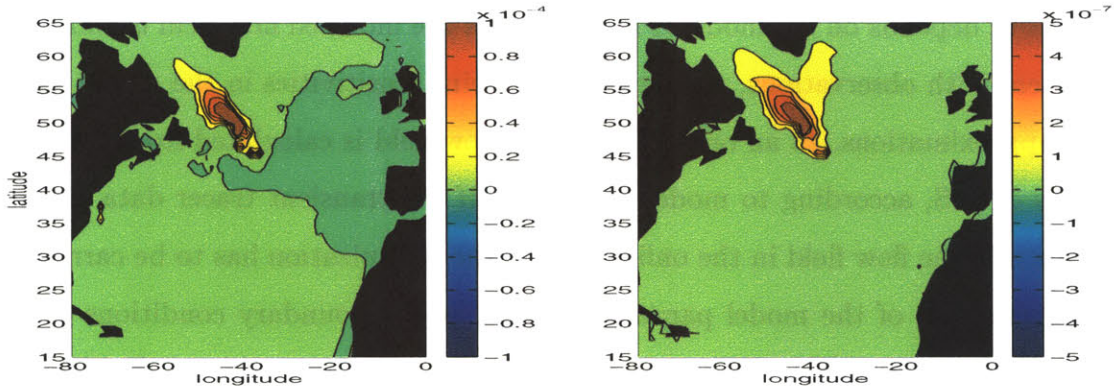
Figure 4-7: Normalized sensitivities of the CFC-11/CFC-12 ratio age in the NADW between depths 1335 - 2700 m and longitudes 80.5 - 60.5 ^{o}W at 30.5^{o}N, June 1980 to the surface piston velocity in February (left, $(10^{-4}$ m^2/s$)^{-1}$) and τ in the NADW to the surface value of τ in February (right, $(^oC)^{-1}$) at the end of 1950.

In spite of different surface boundary conditions and oceanic distributions, the sensitivities of both steady and transient tracer properties successfully exhibit the ventilation pathway of the NADW and the associated transport timescale in the model. Observational information of either steady or transient tracers, once it enters a model, will propagate under the same dynamic rules. The corresponding sensitivity, such as that of a model-data misfit, then provides information about problematic transport pathways and timescales mainly upstream, and serves as a guide for the adjoint model to optimize its parameters.

4.3.4 Quantitative comparison: normalized sensitivities to the isopycnal mixing and thickness diffusion

Mixing rates are the most common quantities that are inferred from the transient tracers. After being brought down by the deep convection, the tracer properties spread southward approximately along isopycnals. Therefore, it is sensible to analyze their sensitivities to the isopycnal mixing rate. In the model, the isopycnal mixing and thickness diffusion are represented by the same parameter. The normalized sen-

sitivities to the isopycnal and thickness diffusion are presented and compared in this section.

The normalized sensitivity of a sample column at 60.5^oW, as shown in Fig. 4-8, tells us that a tracer property in the NADW at 30.5^oN responds most actively to the mixing rate between 1500 - 3000 m depth, with a dipole centered at about 2000 m near 30.5^oN. North of 30.5^oN mixing conveys the CFC-enriched water, while south of 30.5^oN mixing conveys the CFC-deficient water. This explains the opposite sign of the sensitivity adjacent to 30.5^oN.

The horizontal distributions of normalized sensitivities of all tracer properties at 2200 m depth show that maximum values are concentrated to the north of 30.5^oN. There are weak minima just south of this section. The strongest sensitivities are localized near 30.5^oN. The sensitivity pattern of each tracer exhibits a pathway similar to that of the advective sensitivity: a clear band of large values along the western boundary. The amplitudes of the normalized sensitivities have the same order. No obvious advantage of the transient tracer properties in constraining the mixing rates in the deep ocean has been found.
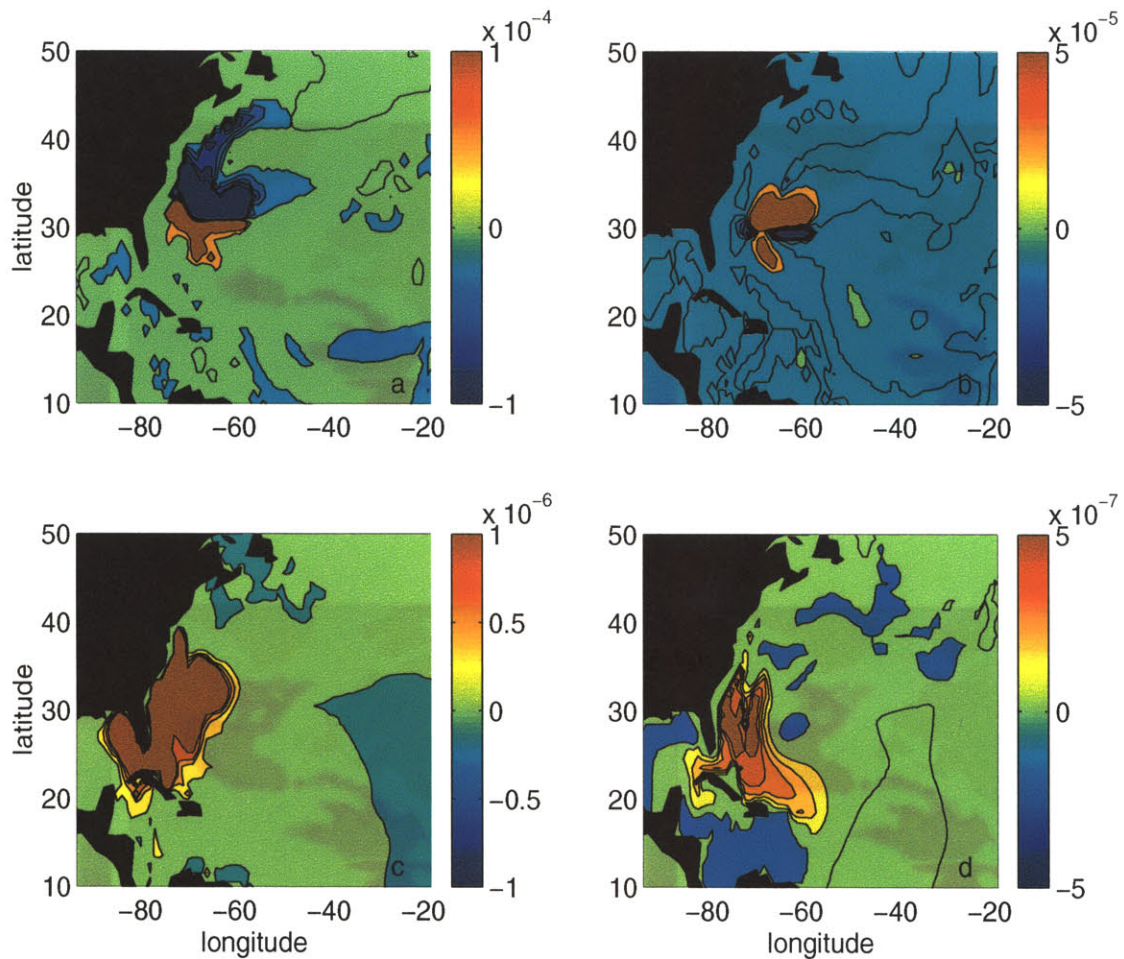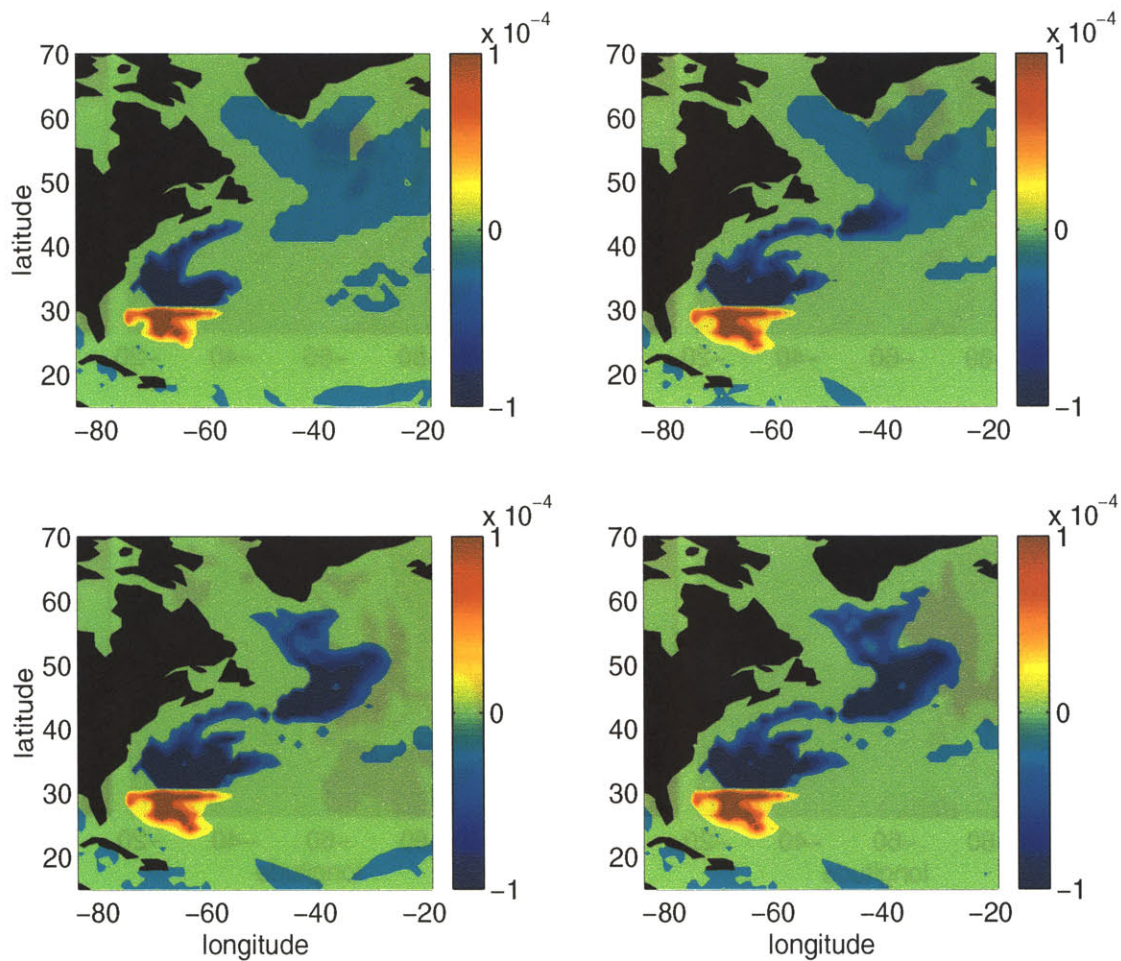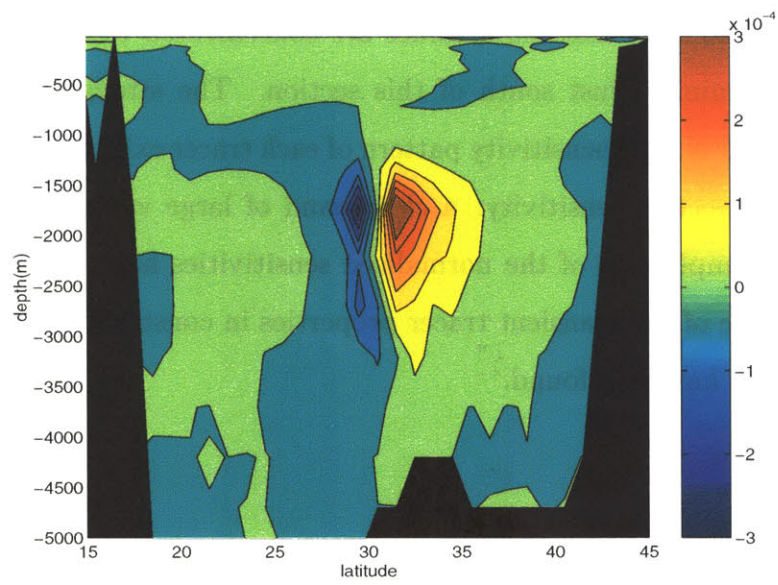
Figure 4-8: Normalized sensitivity of the CFC-11 concentration in the NADW between depths 1335 - 2700 m and longitudes 80.5 - 60.5 ^{o}W at 30.5^{o}N, June 1980 to the isopycnal mixing and thickness diffusion $((100 \text{ m}^2/\text{s})^{-1})$ at 60.5^{o}W at the end of year 1950.

Figure 4-9: Normalized sensitivities of the CFC-11 concentration (upper), CFC-11/CFC-12 ratio age (middle), and τ (lower) in the NADW between depths 1335 - 2700 m and longitudes 80.5 - 60.5 ^{o}W at 30.5^{o}N, June 1980 to the isopycnal mixing and thickness diffusion ((100 m^2/s)$^{-1}$) at 2200 m depth at the end of year 1950. The left panels show the maximum values.

4.4 Sensitivities of tracer properties in the lower subtropical thermocline

There are several studies about the mechanisms contributing to the ventilation of the lower subtropical thermocline in the North Atlantic, using tracer data [e.g., Robbins et al., 2000; Roether et al., 1988]. To my knowledge, however, comparison of the quantitative information extracted from different tracers, with the same methodology, does not exist. It is not clear whether a transient tracer measurement (or derived tracer age) can provide more information about mix layer-thermocline exchange than a steady tracer measurement. This will be investigated in this section.

The cost function is still represented as

$$J = \frac{1}{n} \sum_{i}^{n} C_i. \tag{4.20}$$

Here C denotes CFC-11 concentration, CFC-11/CFC-12 ratio age, or τ; i represents samples in the lower subtropical thermocline between depths 510 m and 710 m and longitudes 60.5 - 20.5 ^{o}W at 30.5^{o}N, in June 1980; n is the number of the total samples of each tracer property. The value of the cost function is roughly the mean tracer property in the lower subtropical thermocline. The vertical layer thickness at 510 m in the model is 75% of the layer thickness at 710 m. Therefore, the mean tracer properties represented by the cost function are slightly weighted toward values at 510 m.

The modeled tracer distributions at 510 m are shown in Fig. 4-10. The distribution patterns of CFC-11 concentration and the CFC age are similar: the surface values invade the subtropical area from its northeast corner and penetrate southwestward across the gyre. The distribution of the steady tracer is different. Its isolines are consistent with stream lines. The recirculation of the subtropical gyre is evident in the closed isolines of high values. The western boundary current and its extension are demonstrated by the compression of isolines.

There are three basic mechanisms that can ventilate the subtropical thermocline:
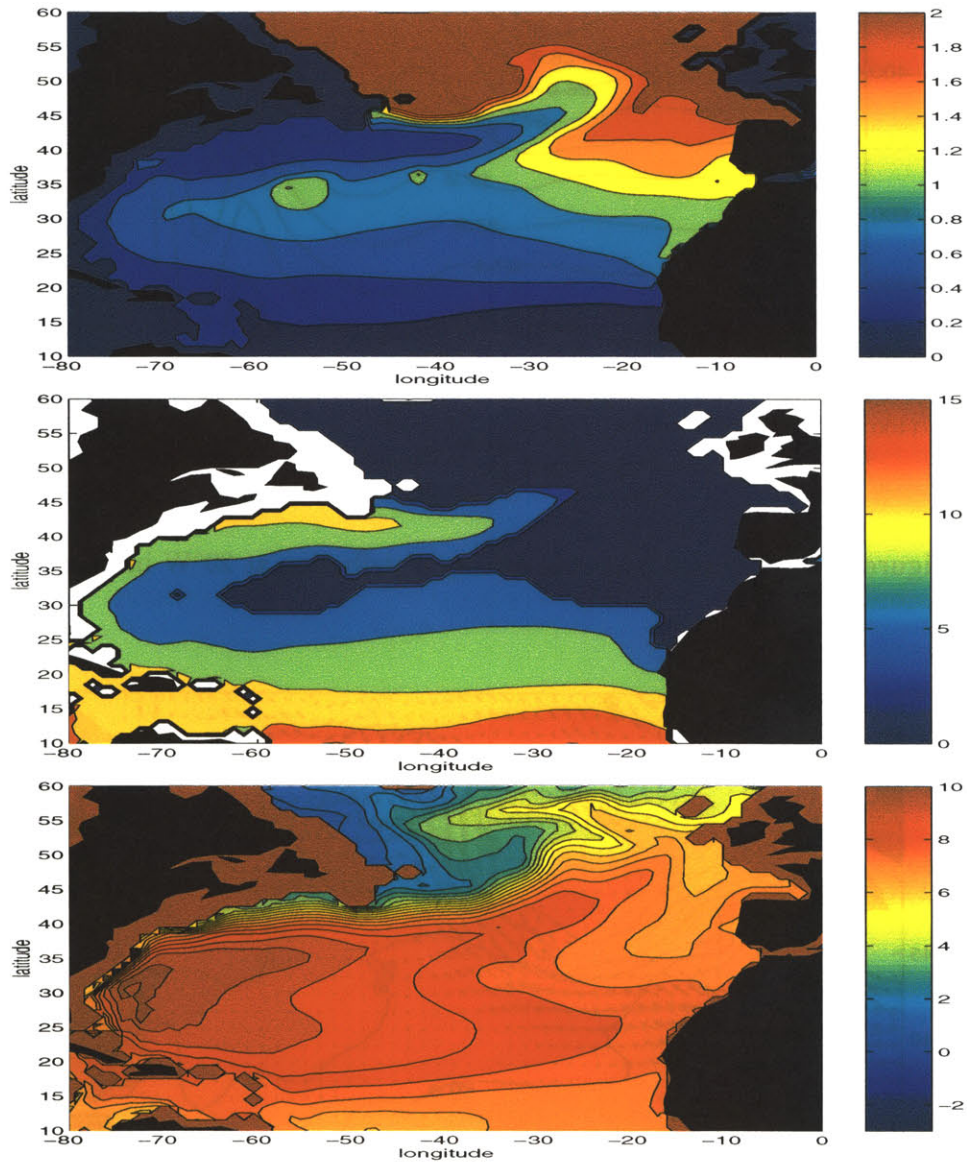
Figure 4-10: Distributions of the modeled CFC-11 concentration (upper, pmol/kg), CFC-11/CFC-12 ratio age (middle, year), and $\tau + 120$ (lower, ^oC) at 510 m depth, June 1980.
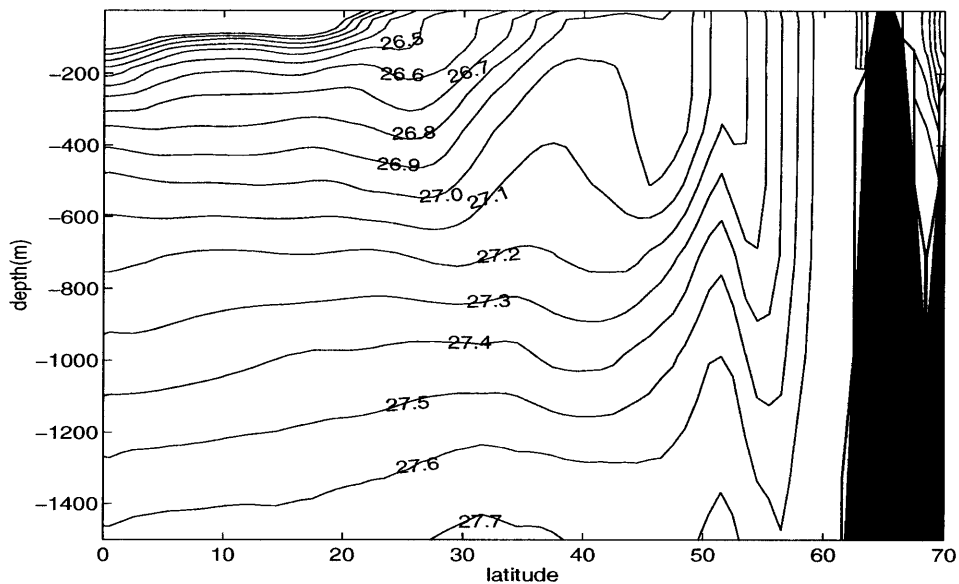
Figure 4-11: Modeled potential density distribution at 20°W in March.
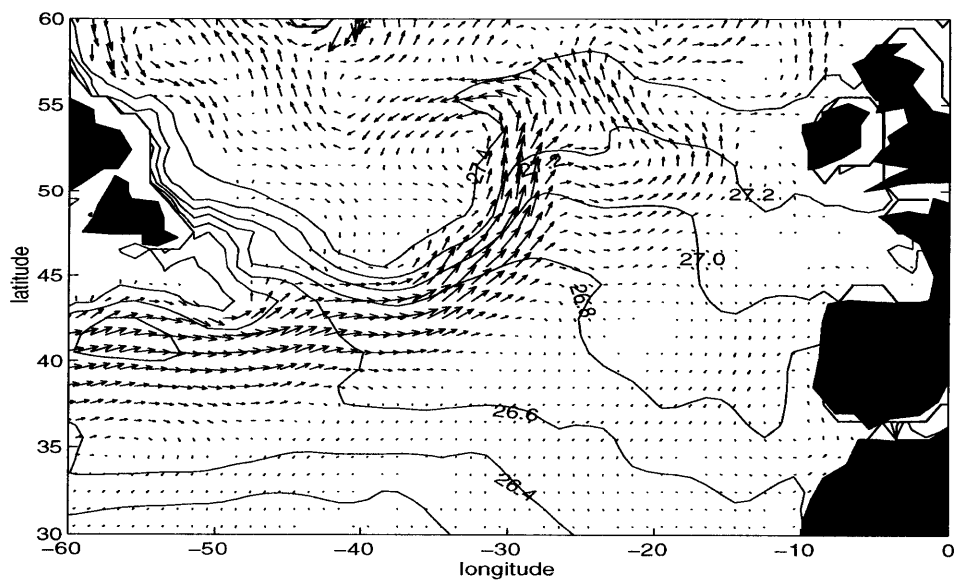
Figure 4-12: Modeled potential density distribution at the surface and the flow field at 510 m depth in March.

direct ventilation due to Ekman pumping, passage of recirculating waters through areas of deep winter convection, and diffusive ventilation due to isopycnal mixing near the outcrops. The modeled potential density distribution shows that the lower thermocline in the depth range 510 - 710 m at 20°W is ventilated by isopycnals between 27.0 - 27.2 (Fig. 4-11). These isopycnals outcrop at the surface within latitude range 43 - 55 °N in the eastern basin (Fig. 4-12). Originating from the region of the winter outcrop, a weak southward flow at 510 m depth feeds the subtropical gyre near the eastern boundary. The flow path, however, is not consistent with the axis of tracer penetration in Fig. 4-10. The Azores Current, which blocks the direct advective ventilation of lower subtropical thermocline in Robbins et al. [2000], is absent in the $1^o \times 1^o$ model.

Again, in order to compare the sensitivities of different tracers, the sensitivities are normalized. The perturbation δJ_o in Eq. (4.18) is taken to be 1 pmol/kg for CFC-11 concentration, -1 year for CFC-11/CFC-12 ratio age, or -10 °C for τ. The amplitudes of δJ_o correspond to tracer perturbations of O(100%) uncertainty, between longitudes 60.5 - 20.5 °W at 30.5°N and 510 depth, June 1980 (Fig. 4-10). δJ_o is taken to be negative for the CFC age and τ because low values are carried by the ventilated water from the northeast corner of the subtropical gyre.

The sensitivities are forced by the monthly mean tracer perturbations in June 1980, between depths 510 - 710 m at 30.5°N. Information then propagates, mainly upstream in the backward integration of the adjoint model. Figure 4-13 shows the normalized sensitivities of the tracer properties to the isopycnal mixing and thickness diffusion at 40.5°W. Positive values spread northward approximately along isopycnals, demonstrating the ventilation pathway. During the 30 years integration, no appreciable sensitivity has appeared in the outcrop region. Sensitivities to the surface values are thus weak. The normalized sensitivity of the CFC age is stronger than that of the CFC-11 concentration. This is consistent with the result of Robbins et al. [2000]. The steady quantity τ shows a weaker sensitivity to the isopycnal and thickness diffusion than the CFC properties, in the lower subtropical gyre. A practical problem of the assimilation of sparse transient tracer data, however, has to take the

large uncertainties in the time-varying boundary conditions into account. This will be discussed in the next chapter.

In the backward integration of the adjoint model, the sensitivities propagate upstream/upward. As shown in Fig. 4-13, no substantial signal in the lower thermocline at 30.5 °N has arrived the surface outcrop region during the 30 years integration. Sensitivities to the surface values are thus weak. Therefore, we present horizontal distribution of the normalized sensitivity to the meridional flow field at 710 m, to show the propagation pathways. After 30 years integration, the sensitivity patches (Fig. 4-14 - 4-17) are confined to the south of the Gulf Stream extension, where the potential density gradient is very large. Axes of sensitivity tongues are approximately proportional to isopycnals. The axis of the strongest tongue does not totally agree with the advective pathway of the southward flow near the eastern boundary (Fig. 4-15), but is approximately along the 27.2 isopycnal. As also shown in Fig. 4-13, the sensitivity information in the lower subtropical thermocline propagates approximately along isopycnals. Isopycnal processes, including isopycnal mixing, play a very important role in ventilating the lower subtropical thermocline.

The advective sensitivity of the CFC age in the lower subtropical thermocline has the same amplitude as that of CFC-11 concentration (Fig. 4-16). The horizontal distributions of the normalized sensitivities of CFC-11 concentration and τ to the meridional flow field at 710 m exhibit a similar distribution pattern (Fig. 4-14 and 4-17). A ventilation trajectory approximately along the 27.2 isopycnal is visible. The amplitude of the advective sensitivity of τ is about an order of magnitude larger (Fig. 4-17) than those of the CFC properties. The steady tracer shows a greater potential capability in constraining the flow field.

The normalized sensitivities of both steady and transient tracer properties in the lower subtropical thermocline exhibit the ventilation pathways along isopycnals. Ventilation is very slow in the model. Over 30 years integration, no substantial signal from 30.5°N in the lower thermocline has arrived at the surface winter outcrop region.
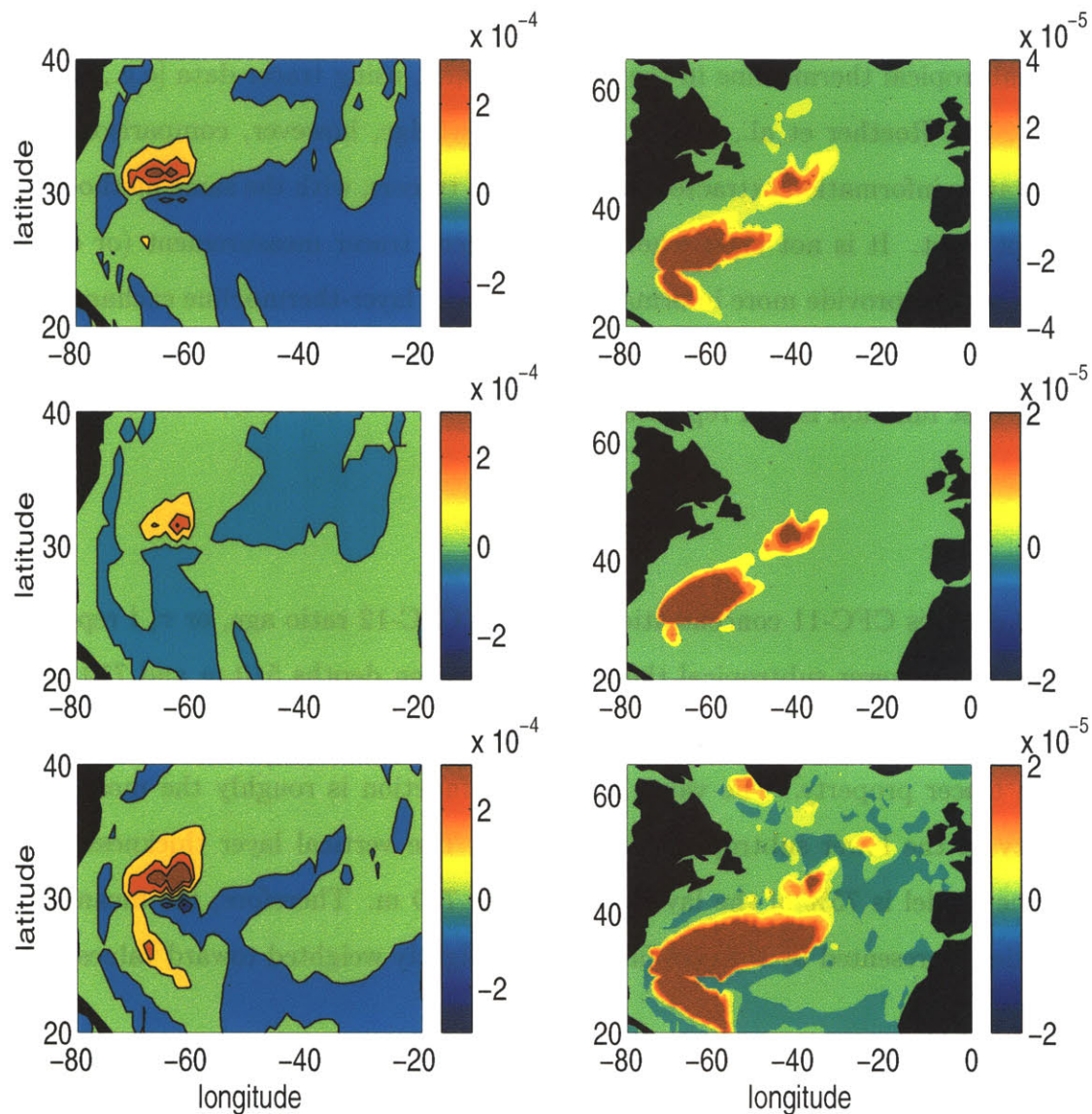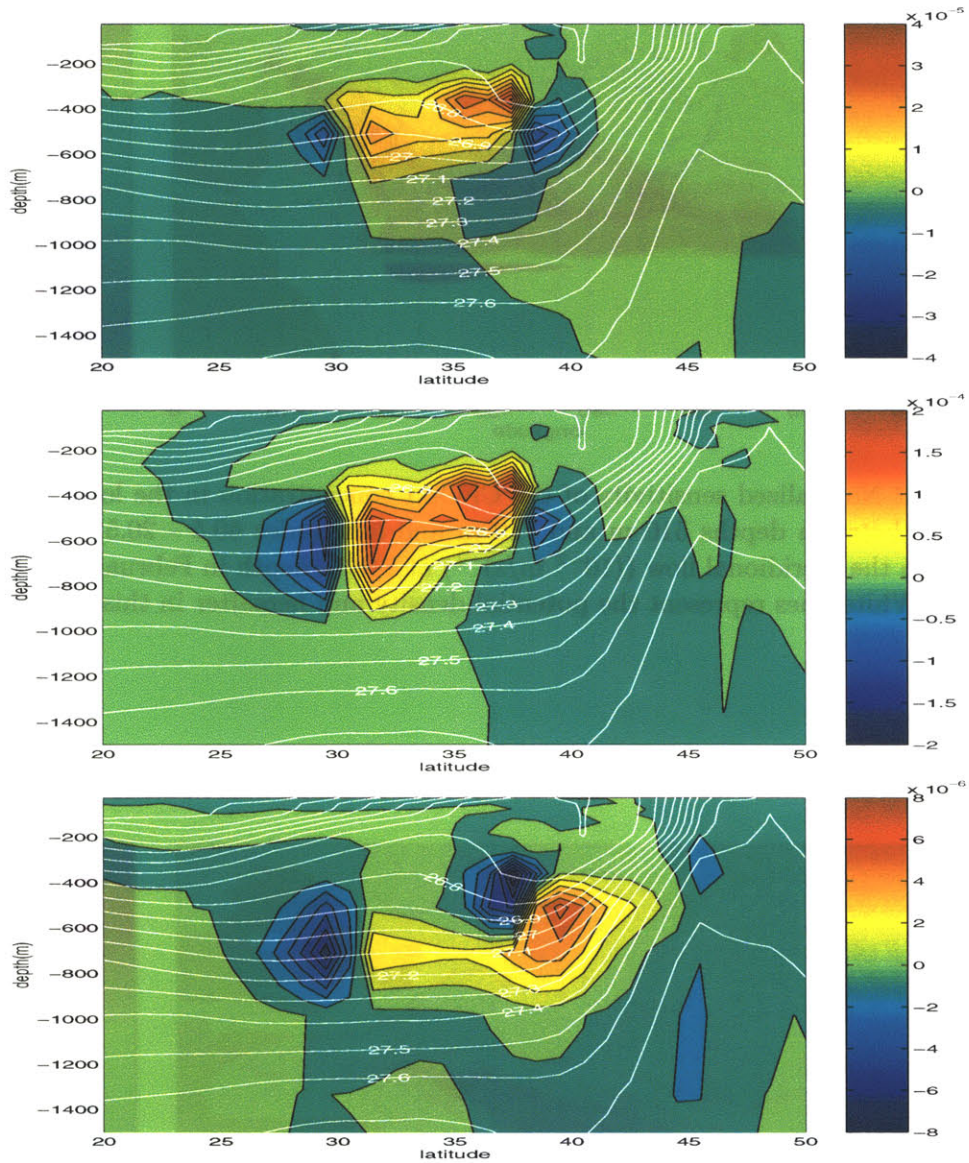
Figure 4-13: Normalized sensitivity of the CFC-11 concentration (upper), CFC-11/CFC-12 ratio age (middle), and τ (lower) in the lower subtropical thermocline between depths 510 m and 710 m and longitudes 60.5 - 20.5 ^{o}W at 30.5^{o}N, June 1980 to the isopycnal mixing and thickness diffusion ((100 m^2/s)$^{-1}$) at 40.5^{o}W at the end of year 1950.
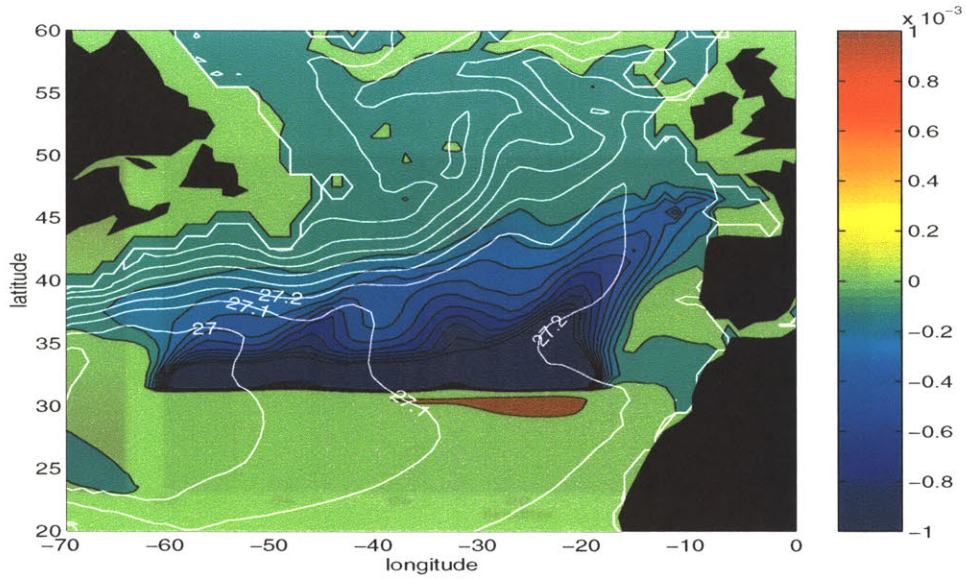
Figure 4-14: Normalized sensitivity of the CFC-11 concentration in the lower subtropical thermocline between depths 510 m and 710 m and longitudes 60.5 - 20.5 ^{o}W at 30.5^{o}N, June 1980 to the meridional flow $((10^{-2} \text{ m/s})^{-1})$ at 710 m depth in February at the end of year 1950. White lines represent the potential density and hereafter in this section.
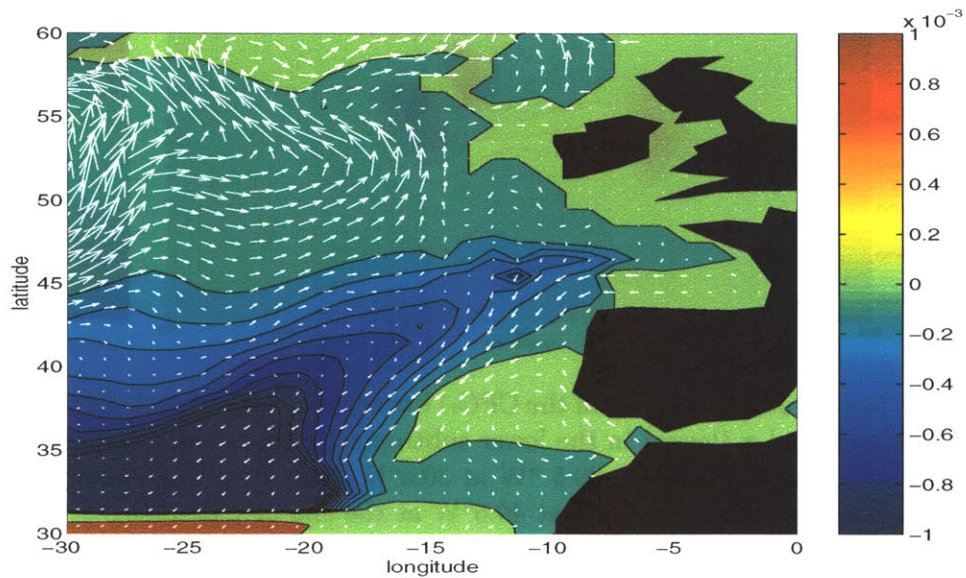
Figure 4-15: Same as Fig. 4-14 with the eastern basin expanded. The white arrows are the modeled flow field at 710 m depth in February.

132
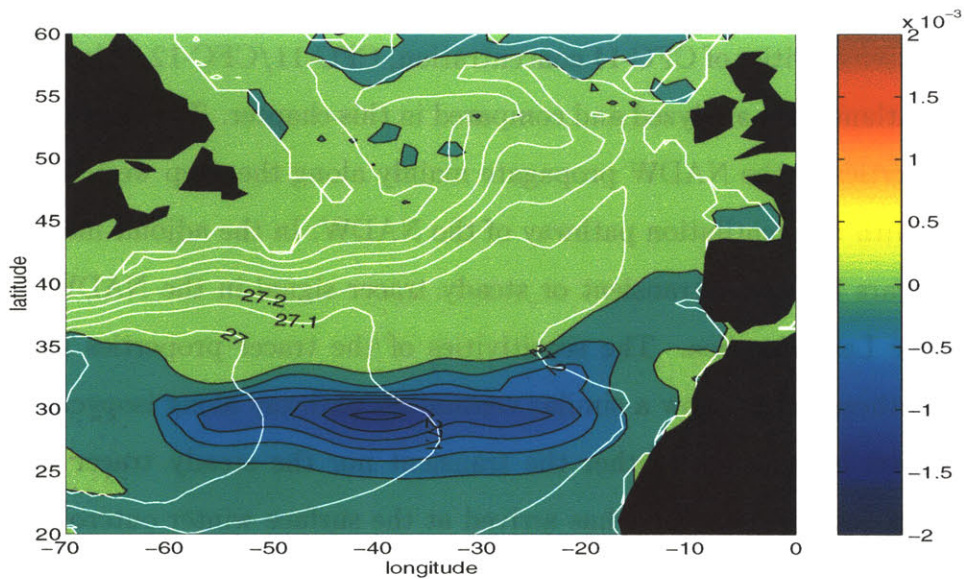
Figure 4-16: Normalized sensitivity of the CFC-11/CFC-12 ratio age in the lower subtropical thermocline between depths 510 m and 710 m and longitudes 60.5 - 20.5 ^{o}W at 30.5^{o}N to the meridional flow $((10^{-2} \text{ m/s})^{-1})$ at 710 m depth in February at the end of year 1950.
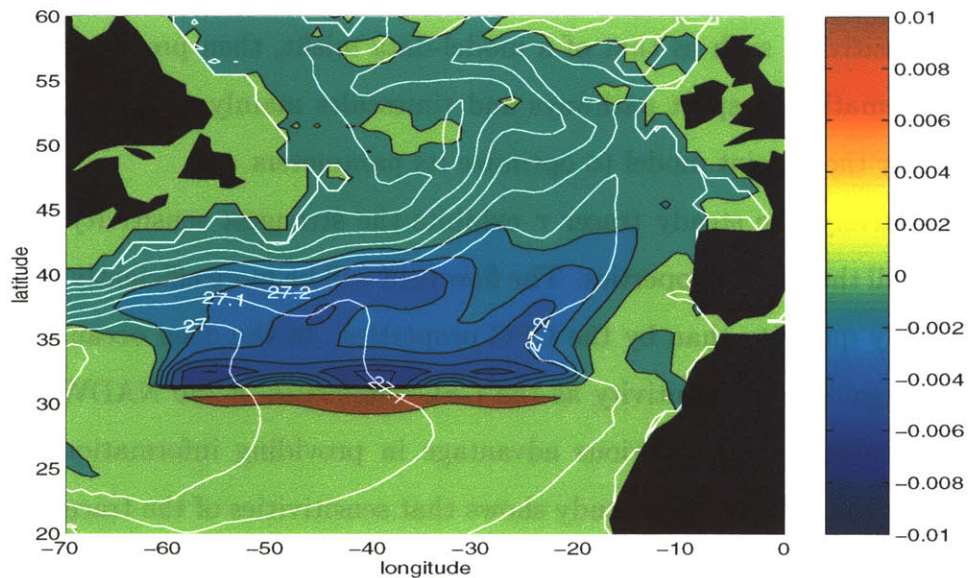
Figure 4-17: Normalized sensitivity of τ in the lower subtropical thermocline between depths 510 m and 710 m and longitudes 60.5 - 20.5 ^{o}W at 30.5^{o}N to the meridional flow $((10^{-2} \text{ m/s})^{-1})$ at 710 m depth in February at the end of year 1950.

133

4.5 Summary

The adjoint sensitivities of CFC-11 concentration, CFC-11/CFC-12 ratio age, and τ in the North Atlantic are analyzed and compared in this chapter. The sensitivities of the tracer properties in the NADW propagate mainly along the deep western boundary, consistent with the ventilation pathway of the NADW. In the adjoint model, it takes about 15 years for either transient or steady tracer signal in the NADW at 30.5°N to reach the Labrador Sea. The sensitivities of the tracer properties in the lower subtropical thermocline show a similar ventilation pathway along isopycnal surfaces. Over 30 years integration, neither the transient nor the steady tracer signal from 30.5°N in the lower thermocline has arrived at the surface winter outcrop region.

In spite of different surface boundary conditions and oceanic distributions, the sensitivities of both steady and transient tracer properties successfully exhibit the ventilation pathways and the associated timescales in the model, and thereby can provide information to constrain the corresponding model physics. In a real data assimilation process, observational information of either steady or transient tracers, once it enters a model, will propagate under the same dynamic rules. The corresponding sensitivity, such as that of a model-data misfit, then provides information about problematic transport pathways and timescales mainly upstream, and serves as a guide for the adjoint model to optimize its parameters.

Quantitatively, the steady tracer τ exhibits the strongest sensitivity to the flow field among all the tracer properties. The flow field will be more efficiently constrained by this steady quantity than by the CFC properties. In the deep ocean, τ provides the same magnitude of sensitivity as the CFC properties in the NADW. The CFC properties demonstrate no obvious advantage in providing information about the ventilation of the NADW. This study shows that sensitivities of the tracer properties are dissimilar in different regions. It is worthwhile to investigate why the amplitudes of the sensitivities of steady tracers are different from those of transients and how the differences vary with ocean regions. This investigation will not be carried out in this study and will be left for future research.

Observations of steady tracers have been successfully assimilated in numerical models to improve the model circulation quantitatively [e.g., Schlitzer, 1993; Yu et al., 1996; Stammer et al, 2002]. Yet there exists no published paper about successfully constraining the circulation with the transient tracer data, in a model of the real ocean. Therefore, it is important to evaluate the extent to which the transient tracer observations can constrain the ocean circulation. This will be done by real data-assimilation experiments presented in the next chapter.

Chapter 5

Constraining the North Atlantic Circulation with the Transient Tracer Observations

Comparison of model predictions with observations described in Chapter 3 shows that major model-data misfits of tracers appear in the formation regions of the North Atlantic Deep Water (NADW) and along its pathways downstream, especially in the deep western basin in the high latitudes. In this chapter, we incorporate the currently available CFC-11, CFC-12, and tritium data into the offline model of the North Atlantic, to evaluate the extent to which the transient tracer data can constrain the model circulation.

There are many published papers about assimilation of temperature and salinity (T-S) observations in ocean general circulation models (OGCMs). Traditional hydrographic data of steady tracers have been successfully used to constrain the large-scale mean ocean circulation [e.g., Schlitzer, 1993; Yu et al., 1996] and time-varying ocean state [Stammer et al, 2002] in OGCMs. On the other hand, published papers about the direct combination of transient tracer observations and a dynamic model are few. The pioneer work of Mémery and Wunsch (hereafter referred to as MW) [1990], using a geostrophic coarse box model and a Green function approach, showed that uncertainty in the tritium boundary conditions and sparse data coverage greatly weakened

the ability of tritium to constrain the model. Almost 10 years later, Gray and Haine (hereafter GH) [2001] recently combined a North Atlantic OGCM with chlorofluoro-carbon observations, using the Green function method. In their work, the model-data misfit was minimized by the improved estimates of gas transfer rates at the air-sea interface in the high latitudes. They concluded that after the optimization of the surface fluxes, the model and data were marginally consistent. As recommended by the paper of MW [1990], this study continues to explore the capability of the present transient tracer observations to constrain ocean circulation properties, using a comprehensive OGCM (MIT GCM) and its adjoint. The following table lists the similarities and differences of the three studies about constraining the North Atlantic ocean circulation with the transient tracer data.

Table 5.1: Comparison of the studies about constraining the North Atlantic ocean circulation with the transient tracer data.

	MW [1990]	GH [2001]	this study
model	box model	OGCM	OGCM
horizontal resolution	8 surface boxes	$4/3^o \times 4/3^o$	$1^o \times 1^o$
vertical layers	10	20	21
data	tritium	CFCs	CFCs and tritium
method	Green function	Green function	adjoint method
surface boundary condition	tritium flux at outcropping boxes	CFC fluxes in 23 impulsive source regions	CFC flux and tritium concentration at each surface grid
open boundary condition	non-zero tritium flux	no CFC flux	non-zero tritium and CFC concentrations
model circulation	steady	steady	climatological monthly means
control variables	surface and lateral tritium flux	surface CFC flux	surface and lateral boundary conditions of CFC and tritium

Some issues arise in the above applications of the Green function theory in the numerical modeling of the transient tracers. The advection-diffusion equation for a tracer is

$$\frac{\partial C}{\partial t} = -\nabla \cdot (\vec{u}C) + \nabla \cdot (\mathbf{K}\nabla C) + S. \tag{5.1}$$

137

Here C is the tracer concentration; $\mathbf{K}$ represents mixing processes; S is sources/sinks. A boundary Green function component can be obtained from

$$\frac{\partial G}{\partial t} + \vec{u} \cdot \nabla G - \nabla \cdot (\mathbf{K}\nabla G) = 0, \tag{5.2}$$

with the concentration boundary $G = \delta(t - t')$ defined in a region of the boundaries. If the initial condition of a passive tracer is zero and a flux boundary condition is imposed,

$$\kappa \nabla C \cdot \mathbf{n} = B_N, \tag{5.3}$$

with κ a constant and $\mathbf{n}$ a unit vector normal to the boundary. The tracer concentration at location $\mathbf{r}$ and time t can be represented as [e.g., GH, 2001]

$$C(\mathbf{r},t) = \int_o^t \int_R G(\mathbf{r},t;\mathbf{r_0},t_0)dt_0 dV_0 + \int_o^t \int_S G(\mathbf{r},t;\mathbf{r_S},t_0)B_N(\mathbf{r_S},t_0)dt_0 dS_0. \tag{5.4}$$

Here R is the three-dimensional domain where the tracer evolutes and is bounded by the surface S. The above solution shows that when a tracer distribution is represented in terms of Green function components, the Green function components should include all components due to impulse sources at all points and all times. In GH [2001], 23 smeared impulsive surface sources are used to obtain the Green function components. Therefore, in MW [1990] with a coarse box model and in GH [2001], the impulses are discretized and summed over large steps, in both space and time (the Green function components are stored annually). Uncertainties are introduced. Within the surface region of each discretized impulse, the tracer flux has to be constant in space. Because the gas-exchange rates of CFCs depend on wind speed, for which the spatial variabilities are large, the assumption of constant CFC flux in space within a large-scale region certainly introduces errors. As the sources are all located on the ocean surface in GH [2001], lateral fluxes of CFCs are totally ignored. An inverse study that allows more realistic transient tracer boundary conditions is needed.

Compared to the above two published studies, the model used in this study has a

higher resolution. At the ocean surface, the CFC fluxes and tritium concentration at every model-grid point are imposed. Unlike GH [2001], in which the CFC saturation and the piston velocity at the ocean surface are assumed to be constant inter-annually to separate the surface CFC fluxes into temporal and spatial components, the surface CFC saturation and piston velocity in this study vary every month at each surface grid independently. At open boundaries, non-zero transient tracer fluxes are allowed.

The assimilation technique makes use of the same offline model and its adjoint, as already described in Chapter 4. From the governing equation (5.1), we can see that several elements are responsible for tracer distributions in the ocean. They are the time-evolving tracer boundary conditions, the mixing rates and the flow fields. The main goal of this chapter is to evaluate the extent to which the transient tracers can constrain the ocean circulation properties. If the model parameters, such as the mixing rates, cannot be effectively constrained by the transient tracer data in the offline model, then they will not be well constrained in the online OGCM. The offline model uses the monthly climatological flow fields and mixing rates in the ocean. The short-time fluctuations on which the tracer data acts to integrate are not resolved. Possible inter-decadal variabilities of the oceanic circulation are ignored in this study.

The extent to which the transient tracer data can constrain the ocean circulation depends on a number of factors. They include the accuracy of the forecast model, the initial-boundary conditions used to drive it, the spatial and temporal coverage of the data. Given the dearth of the transient tracer observations, the large number of degrees of freedom in the parameters emerges as a central issue in the study of constraining a numerical model with the transient tracer data. The boundary conditions, for instance, comprise the number of time steps during the integration period multiplied by the number of grid points at the surface and lateral boundaries. If they are allowed to vary independently, for a North Atlantic model with $1^o \times 1^o$ horizontal resolution and an integration period of 10 years with a model time step of 24 hours, the number of control variables concerning the surface boundary conditions will be 37,332,000. Interpreting the transient tracer distributions with uncertain input histories and sparse data coverage is the focus of this study.

5.1 Data error

The error covariance matrix R in Eq. (4.5) determines the extent to which we expect the model and data to match each other. It depends on the accuracies of both data and model. If model-data differences fall within their accuracies, we will conclude that the model is consistent with data. Unfortunately, the error information, especially that of the model, is unavailable and a statistically empirical estimate is often used.

Generally, the tracer distribution at a cruise section is regarded as synoptic: measurements of a cruise are regarded as a representation of a snapshot at one instant. Therefore, a sample at single time $C(t_o)$ is supposed to represent a time average $< C >$ over the cruise period, with some error n,

$$< C >= C(t_o) + n, \qquad (5.5)$$

Here $<>$ denotes a time average. The temporal variability during the cruise period becomes a part of the data error. Because the spatial resolutions of both model and observations are limited, small scale variability also contributes to the error budget. If we treat the subgrid scale variability that cannot be reproduced by the model as the data error, the total data error has two parts: measurement error and the variability that the data or the model cannot catch

$$n = n_{measurement} + n_{variability}. \qquad (5.6)$$

The measurement error includes the instrumental and navigation error. The analytical precisions of CFC-11, CFC-12, and tritium are around 0.005 pmol/kg, 0.005 pmol/kg, and 0.02 TU, respectively. Navigation error is minor, compared to the subgrid (about 100 km in our model) variability that the model cannot resolve.

The variabilities that contribute to the data error include both temporal and spatial parts. The temporal variabilities over cruise time (around a month) are calculated with the help of the GCM. The spatial part has several sources: small scale turbulence, internal waves and meso-scale eddies. The spatial variances of the modeled

140

tracer distributions are calculated as a function of depth and time. The variance contributed by the subgrid scale is taken to be 1/9 of the variance obtained from the model [Stammer et al., 2002]. This fraction of 1/9 is consistent with the passive tracer power spectrum obtained by [Haine et al., 2001]. The study of Haine et al. [2001] showed that it was the subgrid spatial variability that dominated the error budget, which is well over an order of magnitude greater than the temporal and instrumental errors. This is also confirmed by our model result.

Figure 5-1 shows the vertical profiles of the data errors in area 4.5°S-39.5°N, 99.5°W-21.5°E, 1990. They decrease with depth. Large uncertainties appear above 4500 m, due to the variabilities of the upper and intermediate water masses, and the NADW. Below 4500 m depth, the uncertainties are very small. This is consistent with the fact that both transient tracer concentrations and their variabilities in this part of the ocean are small. Since the CFC-11 content in the ocean in 1990 is large, the amplitudes of CFC-11 variabilities are relatively large. Therefore, the uncertainty prescribed for CFC-11 concentration in 1990 is larger than those of CFC-12 and tritium.

In our model-data comparison, the data is binned meridionally, zonally and vertically into model grid cells. A box average is calculated if more than one sample is within a box. Tracer measurements made within a month are compared with their monthly means in the model.
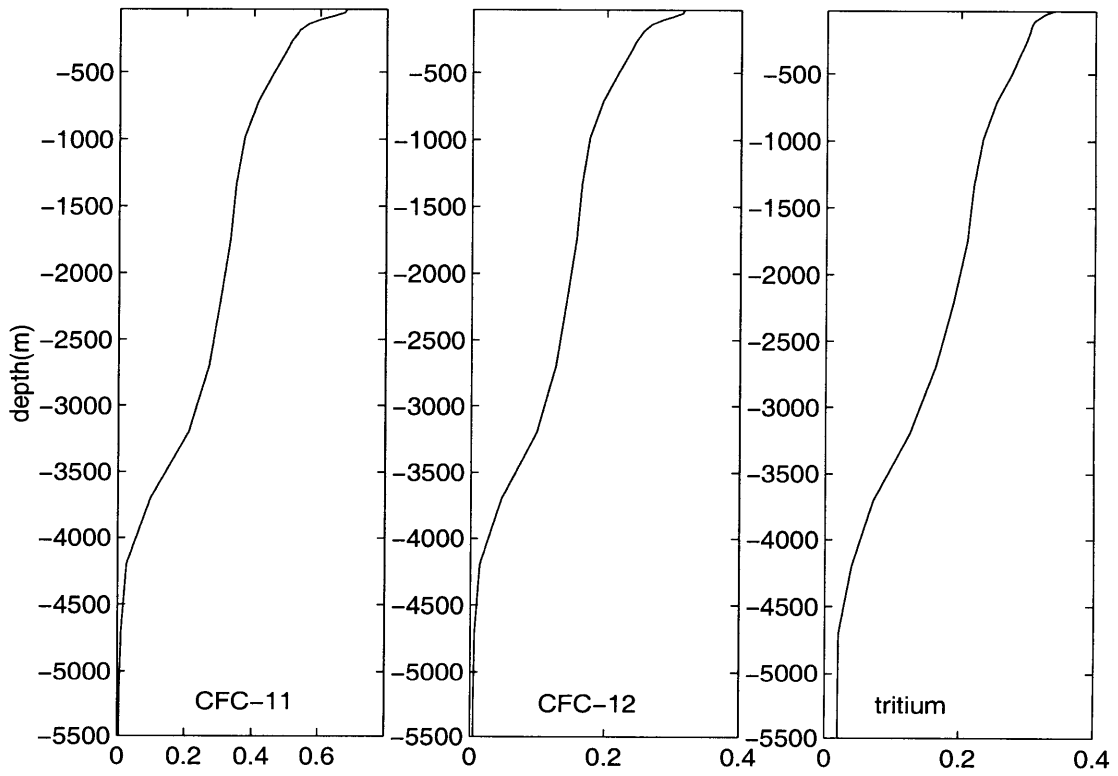
Figure 5-1: Uncertainty profiles prescribed for different tracers in area 4.5°S-39.5°N, 99.5°W-21.5°E, 1990. Units of CFC and tritium are pmol/kg and TU, respectively.

5.2 Optimization of the CFC boundary conditions

One of the difficulties of extracting ocean circulation information from the transient tracer data lies in the uncertainties of the boundary conditions. A transient tracer distribution at one time is governed by its previous boundary histories. This section will give a perspective of whether the inherent temporal variabilities of the transient tracers are able to provide unique information about ocean circulation, or on the contrary, whether the complexity of the temporal variabilities practically undermines our systematic and quantitative inferences. The large number of degrees of freedom concerning the time history of the transient tracer boundary conditions is the focus of this section.

Following the same ideas described by MW [1990], we treat the boundary conditions as control variables. If the existing circulation in the model can be brought into accord with the transient tracer observations by physically acceptable adjustments of the boundary conditions, the observations cannot provide additional information to the model. If, on the other hand, no physically acceptable boundary conditions can be found, then we can further explore how effectively the observations can constrain the circulation properties.

For the surface fluxes, we regard the atmospheric history and solubility properties of CFCs as relatively well known. The uncertainties of the CFC surface flux estimates mainly come from the uncertainties of the piston velocities, which are described in Chapter 3. The uncertain relationship between the piston velocity and the Schmidt number, the poorly understood effects of bubbles, turbulence and boundary layer stability in the air-sea tracer exchange, and the deviation of the climatological wind speeds from in situ conditions contribute to the errors in the piston velocity estimate [Wanninkhof, 1992]. Overall, a fractional uncertainty of 30% [GH, 2001] is taken for the piston velocity estimate in this study.

The relative uncertainties of initial and open boundary tracer concentrations, which come from the forward model run, are assumed to be 100%. However, the errors are replaced by a constant whenever they are judged to be too small relative

to the systematic errors. The threshold value of the uncertainties is 0.005 pmol/kg for CFC concentrations.

The general form of the cost function is described in Appendix A. Since each observation and control variable is regarded as independent, the off-diagonal terms of the covariance matrix $\mathbf{R}$ and $\mathbf{Q}$ are zero. Here the cost function can be represented more specifically as

$$J = \sum_i \frac{(C_i - C_{obs})^2}{r_i^2} + \sum_j \frac{(U_j - U_j')^2}{q_j^2}, \tag{5.7}$$

where r and q denote the uncertainties of data and control variables, respectively. The number of elements of the model-data misfit term in Eq. (5.7) is the number of the bins ($1^o \times 1^o \times$ model layer thickness $\times$ 30 days) within which the observations are available.

5.2.1 Failed optimization over the entire North Atlantic

First, the optimization is carried over area 99.5^oW - 21.5^oE, 4.5^o - 78.5^oN in the North Atlantic, with monthly climatological piston velocities (see Chapter 3 for details) as control variables. The integration period is over the years 1960 - 1999, so that impacts of the uncertainties in the initial CFC conditions are minor.

In Chapter 3, the forward model results show that major model-data misfits appear in the deep western basin, especially in the high latitudes. The misfits come from the excessive vertical penetration of surface values in the deep convective regions. To reduce the model-data misfits, the optimization quickly reduces the CFC fluxes in the deep convective regions in the Labrador Sea. During the first four iterations, the winter piston velocities in the Labrador Sea are decreased by almost 70% (Fig. 5-2). This decrease of the surface piston velocity leads to a decrease of the model-data misfit term in the cost function (Eq. (5.7)) of about 20%. As shown in Fig. 5-2, in some places in the Labrador Sea, the piston velocity in February drops to almost zero. The Labrador Sea endures severe weather during the winter; the winter piston velocity should be high in this region. The optimized values deviate far from the real-

ity and are not consistent with our a priori statistical assumption of 30% uncertainty. Therefore, the optimization is manually stopped.
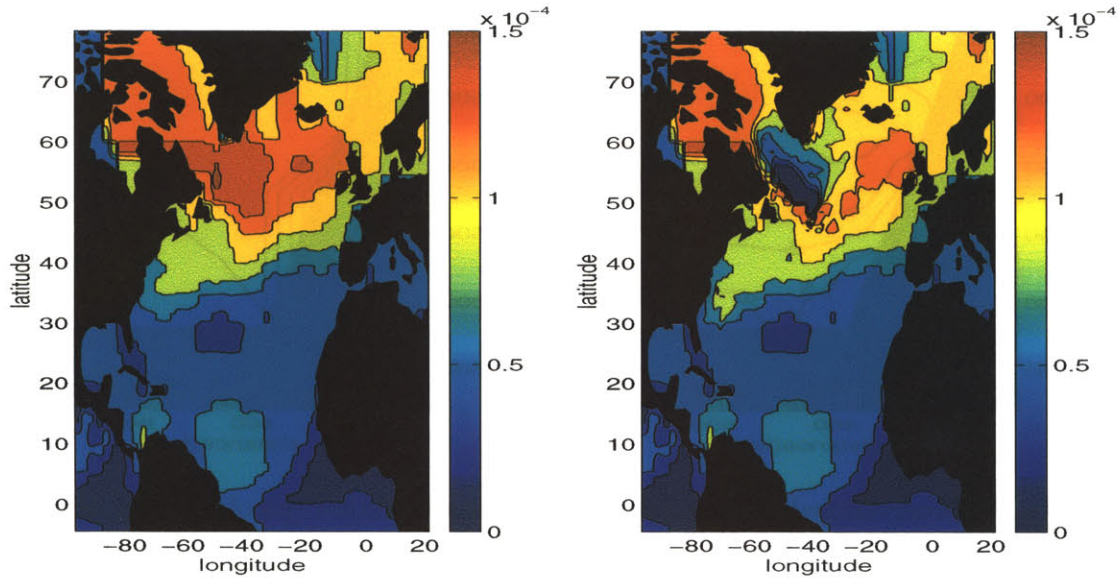
Figure 5-2: Distributions of the surface piston velocity in February at iterations 1 (left) and 4 (right).

The poorly resolved deep convection in the model results in the spurious decrease of the surface piston velocity during the optimization. As an alternative, the convective mixing rates are allowed to change instead. The convective mixing rates are reduced manually, with the piston velocities fixed. The model-data misfit drops monotonically with the decrease of the convective mixing. Figure 5-3 shows the observational and modeled CFC-11 concentrations along a section in the Labrador Sea, when the convective mixing in high latitudes is totally shut off. A significant amount of CFC content still appears in the deep western basin. Between depths 710 - 2500 m, the modeled CFC concentration in the Labrador Sea basin is 3.0 - 3.5 pmol/kg and higher than observations, which have values between 2.5 - 3.0 pmol/kg. As presented in Chapter 3, the modeled isopycnal surfaces in this area are very steep. Tracer properties can be carried downward by isopycnal mixing. This erroneous downward mixing along steep isopycnals leads to the high CFC concentration in the deep Labrador Sea basin.
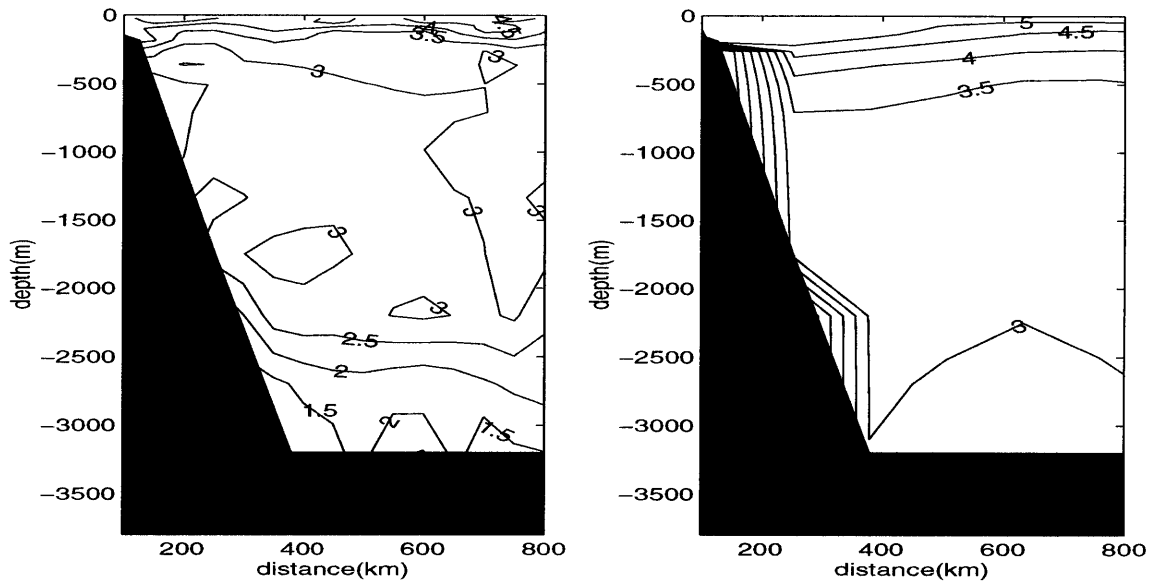
Figure 5-3: Observational and modeled CFC-11 concentration (pmol/kg, and hearafter) along a section in the Labrador Sea (WOCE AR07W), June, 1993. The modeled convective mixing in the high latitudes is totally shut off.

The underlying model physics in the high latitudes are poorly resolved. Without the substantial enhancement of the modeled T-S fields in the high latitudes, the deep convection and the surface gas exchange rates cannot be reasonably optimized. Resolving the deep convective process is still a challenge to numerical modeling and is not within the scope of this study. The first step to improve the model performance in the high latitudes is to use T-S data to improve modeled T-S fields. Work about assimilating T-S data in a high resolution model towards understanding Labrador Sea synthesis is going on (Geoffrey Gebbie, personal communication). Our objective here is to evaluate the extent to which the transient tracer data can constrain an ocean model. A regional model over a smaller area can still achieve this goal.

5.2.2 Optimization over the Atlantic between 4.5°S and 39.5°N

We move the northern boundary southward to 39.5°N (Fig. 5-4). This location has been chosen to be sufficiently far from the convective region, but well within the domain in which the CFCs penetrate to great depth. Also at this location, the ocean

146

basin is very deep; fluxes of deep overflows can enter from the northern boundary. In this model domain, there are 23,250 model bins within which the CFC observations are available.
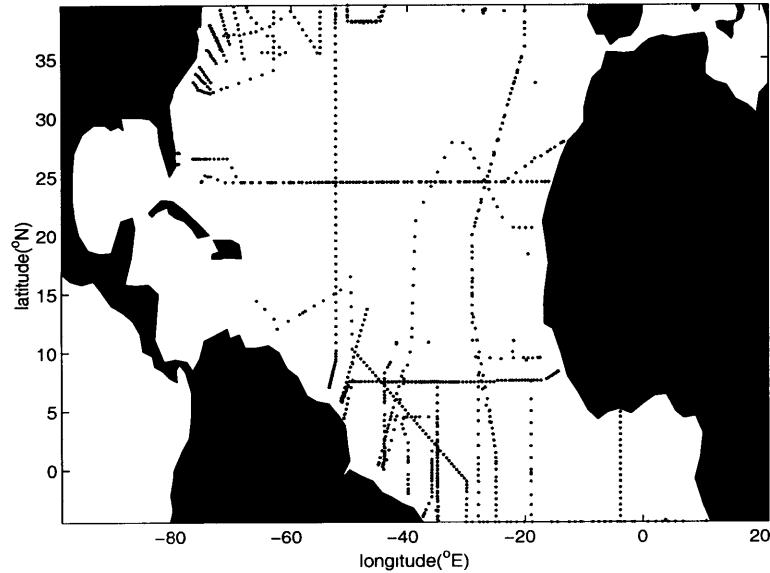
Figure 5-4: The new model domain. Black dots represent CFC data stations.

The control vector comprises the yearly average open boundary CFC concentrations, initial CFC states and monthly climatological piston velocities. Their first estimates are taken from the forward run. At the open boundaries, CFC concentrations are prescribed and permitted to vary independently each year at each model grid cell. An integration period over the years 1981 - 1999, within which all CFC data available falls, is chosen to minimize the number of control variables concerning the open boundary conditions.

The observations enter the model at various times and locations. Some of them are located at the open boundaries; some of them are in the interior. Whenever an observation which differs from the corresponding model value is available, the adjoint model is forced at the same time and location. The misfit information then propagates, governed by the model dynamics. Those observations at the open boundaries strongly constrain the open boundary concentrations at the observational locations in the corresponding years, but cannot constrain the boundary CFC concentrations at

other locations or years, because the yearly mean CFC boundary concentrations are prescribed and vary independently. In years or at places in which there is no observation available at the open boundaries, the corresponding boundary conditions are adjusted by the interior observations. Since the adjoint model is integrated backward in time, the observations can only constrain the earlier boundary values.

Mainly by adjusting the CFC concentrations at the northern boundary, the cost function is minimized. Figure 5-5 and Figure 5-6 show the initial and optimal CFC-11 distributions at the northern boundary in 1994, a year when CFC observations at the open boundary are available. Before the optimization, there is a large volume of water with CFC-11 concentration about 2.5 pmol/kg located in the deep western basin. This is the CFC-enriched NADW in the unconstrained model. The CFC-11 concentration in the NADW at this location increases from 1 pmol/kg to more than 3 pmol/kg during 1981 - 1999 before the optimization. The initial estimates of the northern boundary CFC concentrations are too high in the deep western basin, owing to the excessive CFC uptake in the high latitudes,.

After optimization, the CFC-11 concentration in the western basin between 2000 - 4000 m is greatly reduced (Fig. 5-6). Large adjustments appear at observational locations. Comparison of the optimal boundary values with observations, in Fig. 5-7, shows that the optimal boundary values are very close to the observations. At 43.5°W, the vertical profile of the observations has some scatter. The model produces a CFC-11 profile that is roughly the mean profile of observations. The model-data misfits fall within the errorbars we prescribed. About 7 degrees apart, at 50.5°W, the modeled values at depth are slightly higher than the observations, because the initial guess of the modeled values are high. The modeled CFC-11 values at 50.5°W are similar to those at 43.5°W, which is consistent with the large-scale feature of the model physics. We regard this optimal estimate of the boundary values as physically reasonable and is consistent with the present observations and knowledge.

The amplitudes of the boundary condition adjustments vary with different years and locations. The adjustments are large in years and places within which observations are available at the open boundary. The adjustments forced by the interior

148
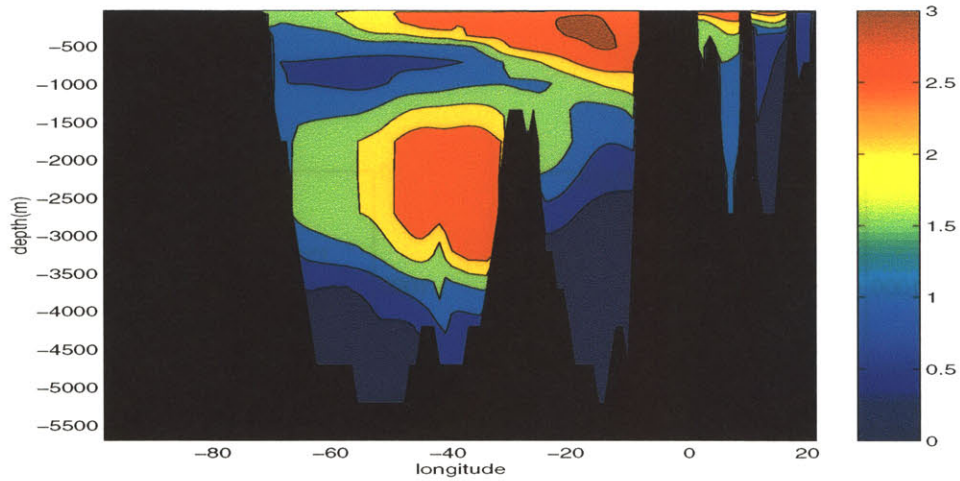
Figure 5-5: The first estimate of the CFC-11 distribution at the northern boundary (39.5°N) in 1994.
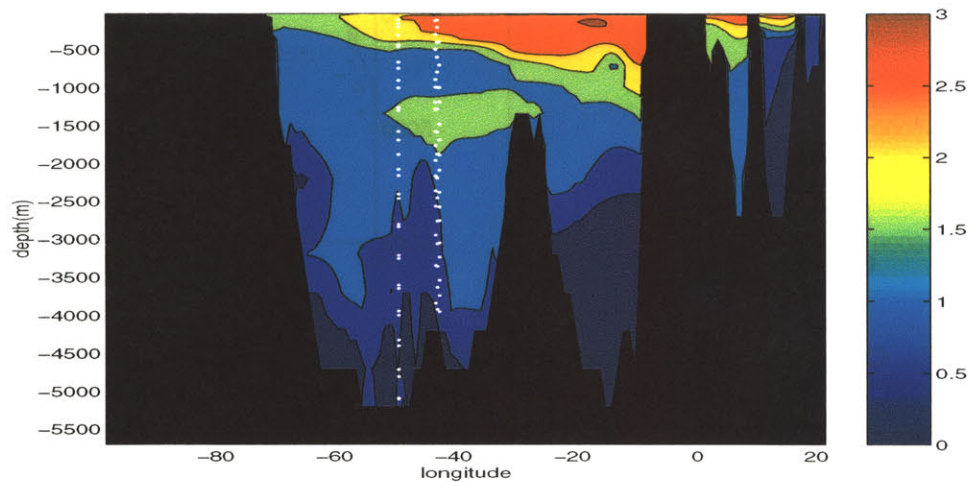
Figure 5-6: The optimal CFC-11 distribution at the northern boundary in 1994. White dots represent observational locations.
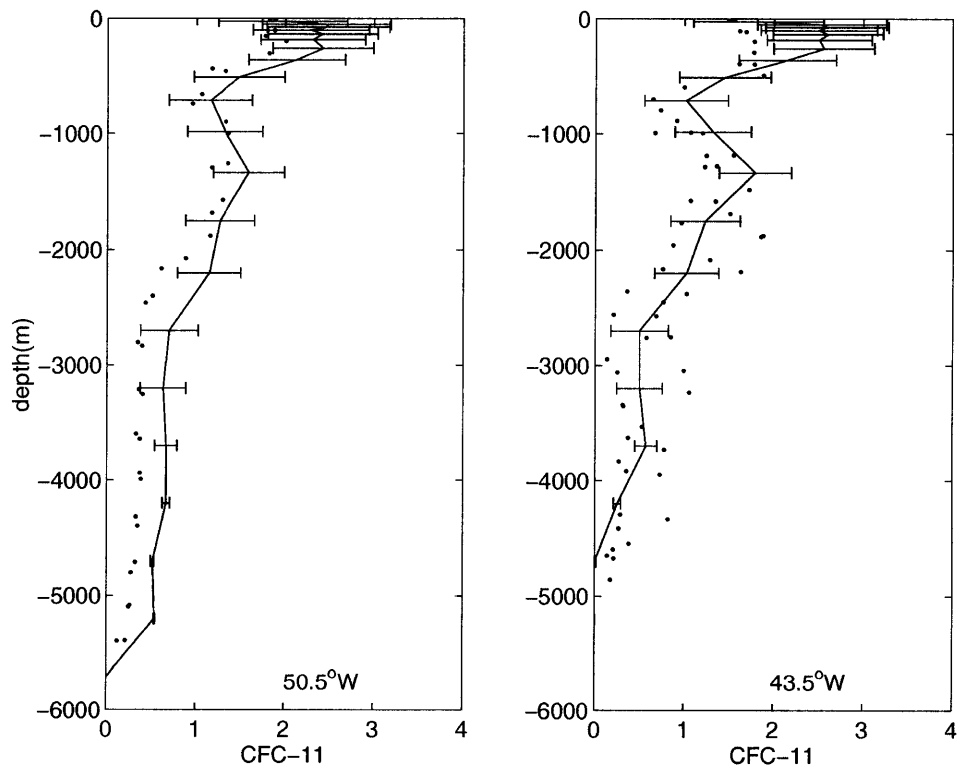
Figure 5-7: Comparison of the optimal (solid lines) and observational (dots) northern boundary CFC-11 concentrations in 1994. Errorbars represent the CFC-11 data error, dominated by the subgrid variability the model cannot resolve (See section 5.1 for details).

150

observations are much smaller. In years and places within which no observation is available at the northern boundary, the boundary CFC concentrations in the deep western basin are manually reduced, because the first estimates of CFC values there are too high. After the manual adjustments are made, the optimization is restarted. Figure 5-8 and 5-9 show the optimized northern boundary conditions between 1981 - 1998. CFC concentrations in the deep western basin are greatly reduced after optimization. The optimal CFC boundary values at depth are far less than the surface values. In years such as 1993, 1994, 1995, 1997, where deep observations are available at the boundary, the CFC concentrations at the observational locations are reduced strongly, leading to the low CFC values at these locations.

At the ocean surface, the adjustment of the piston velocity, the air-sea gas exchange rate, is minor. Figure 5-10 shows the first guess of the piston velocity in February and the corresponding difference between the constrained and unconstrained values. The largest adjustment is about 1% of the first estimate. The CFC data only weakly constrain the surface-gas change rates in the assimilated model domain. The adjustments of the initial CFC concentrations are small too. The largest adjustment of the initial values appears at depth 3700 m. As shown in Figure 5-11, the assimilation reduces the initial CFC-11 concentration in the western basin near the northern boundary, notably the vicinity of the 1983 observations. As CFC surface fluxes increase with time, the model-data misfits after 1988, when most CFC observations are available, are not sensitive to the initial conditions about a decade before.

At iteration 85, the cost function no longer drops significantly and is about 10% of its first value (Fig.5-12). The obvious drop of the cost function at iteration 60 is due to the manual adjustment of the boundary conditions. After the optimization, the root-mean-square value of the model-data misfit terms in Eq. (5.7) is 0.9, almost of unity. On an average, the model-data differences fall within the errorbars prescribed.

Figure 5-13 shows the observational and modeled CFC-11 distributions before and after the optimization, along a meridional section 52^oW in the western basin where the model-data misfit is the largest. Even though the unconstrained model successfully produces some typical features of the observations, as described in Chapter 3, the
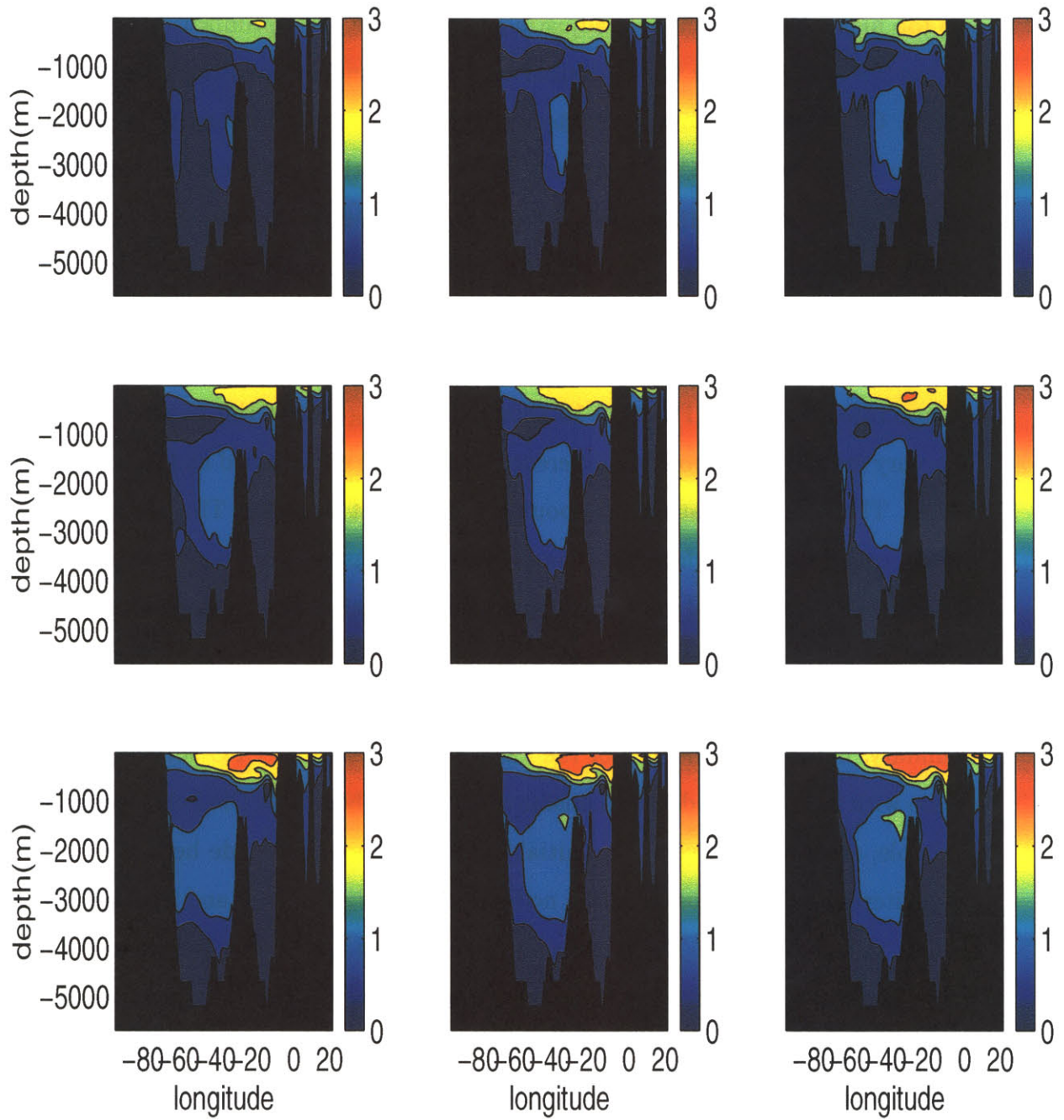
Figure 5-8: The constrained northern boundary CFC-11 concentrations (pmol/kg and hereafter) in years 1981, 1982, ..., 1989 (left to right first).
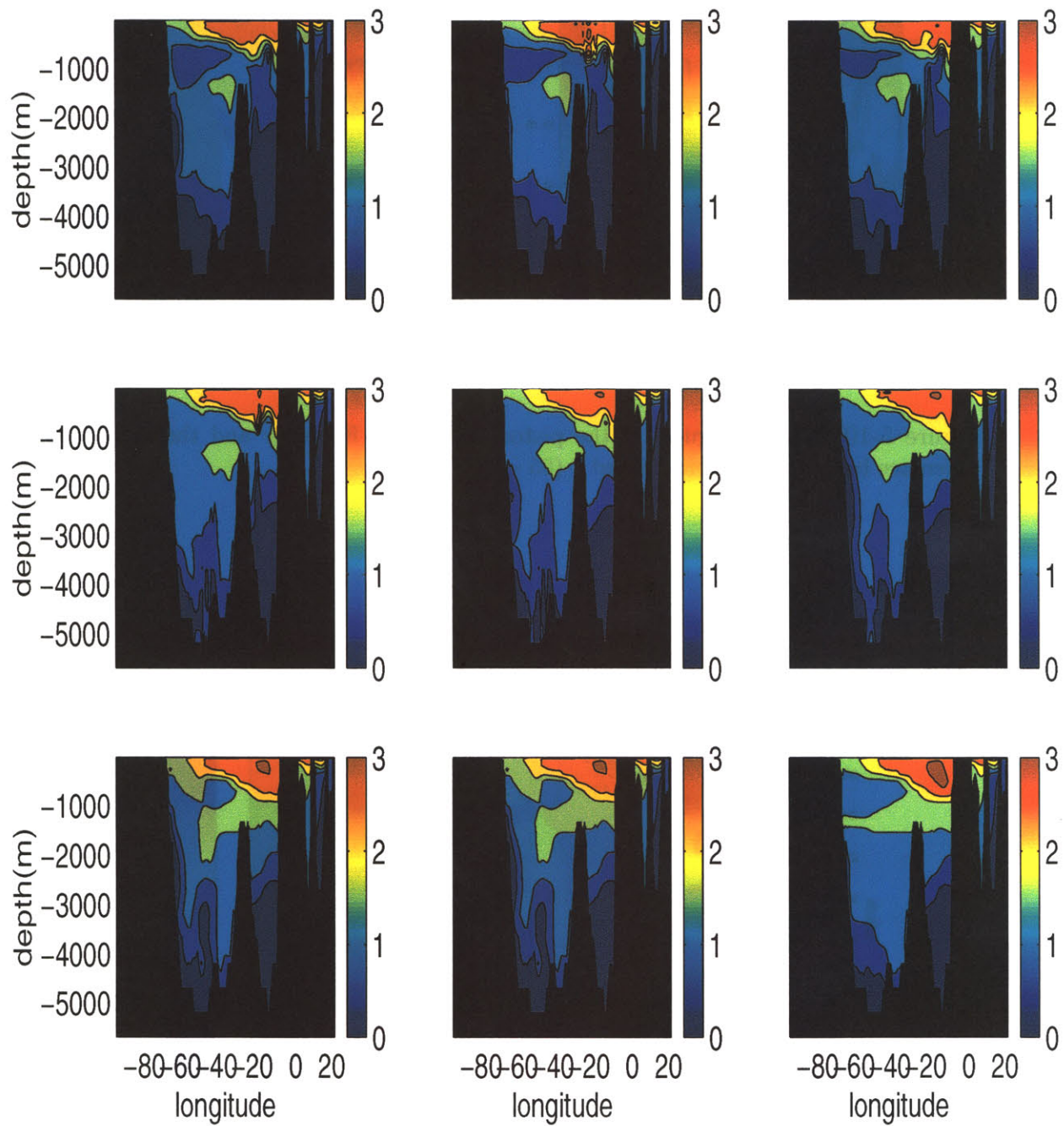
Figure 5-9: The constrained northern boundary CFC-11 concentrations in years 1990, 1991, ..., 1998 (left to right first).
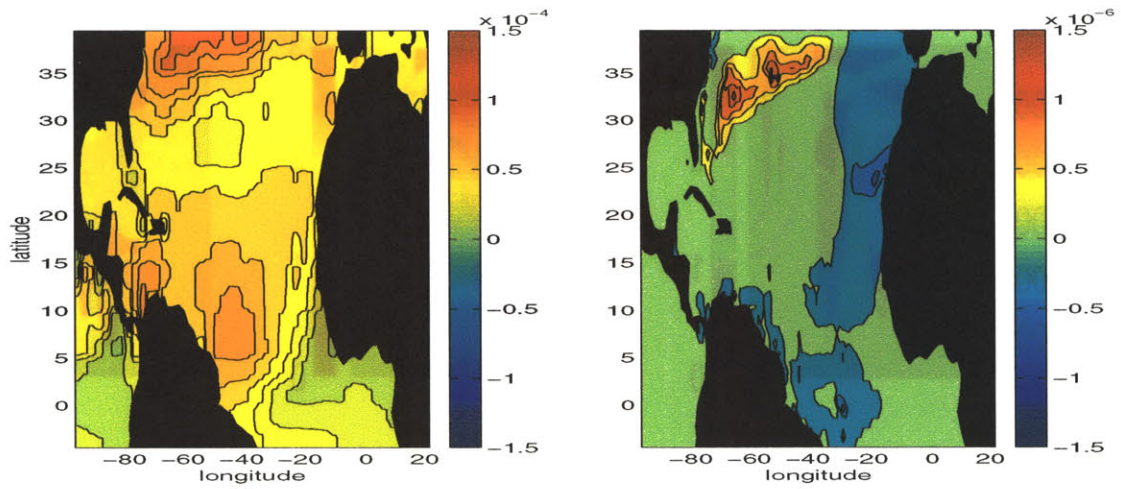
Figure 5-10: The first guess of the piston velocity in February and the corresponding difference between iterations 85 and 1 (85 - 1).
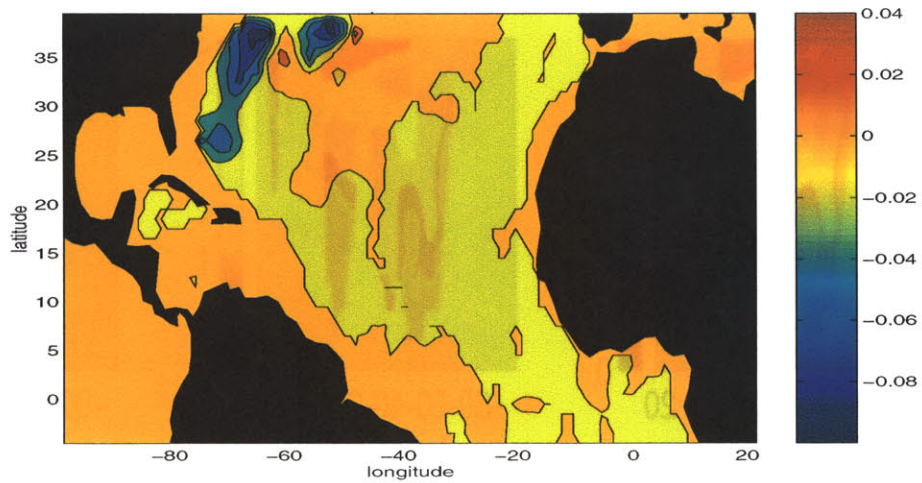
Figure 5-11: Differences of the initial CFC-11 concentrations at depth 3700 m between iterations 85 and 1 (85 - 1).
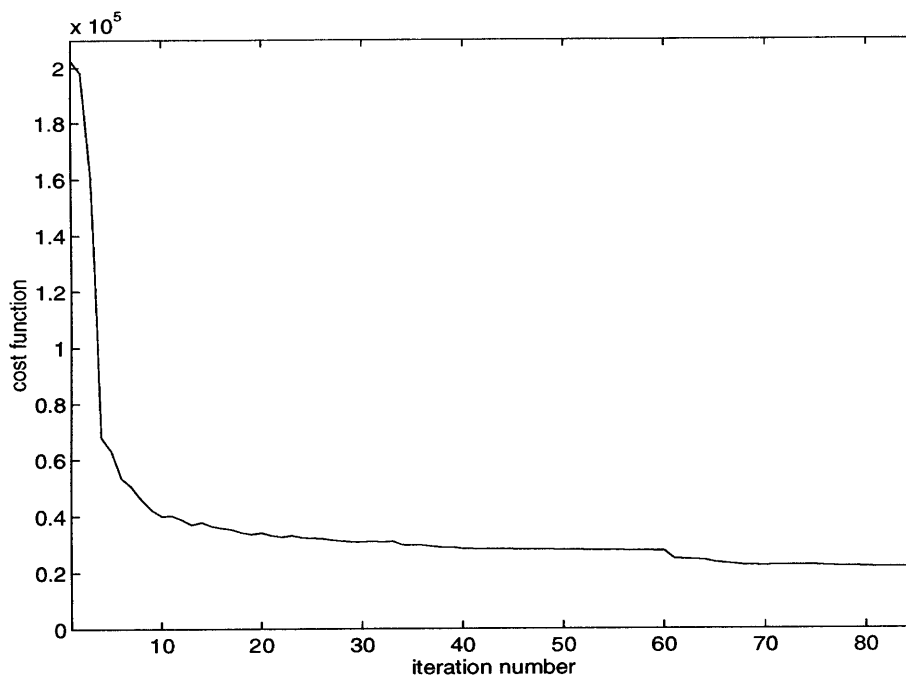
Figure 5-12: Value of the cost function during the optimization.

modeled CFC-11 concentration in the NADW is by far too high. The observed two separate deep maxima from two different water sources are not reproduced by the model. After 85 iterations, the modeled CFC-11 concentration in the NADW has been significantly modified. The CFC-enriched tongue of the upper NADW is now modeled more realistically. Both modeled and observed CFC-11 concentrations in the upper NADW have the highest value of 1.5 pmol/kg centered at about 1500 m depth. The tongue of the upper NADW with CFC-11 concentration higher than 0.75 pmol/kg ends at 33°N, in both model and data. At about 4500 m depth, relatively high CFC-11 concentrations appear in the model at iteration 85. The deep maximum at about 4500 m, indicating the signature of the Overflow Water (OW), is visible near the northern boundary. It is, however, quickly dissipated away from the northern boundary in the model. This is a general feature of a coarse-resolution model [e.g., England et al., 1998]. To model the signature of the OW more realistically, substantially higher horizontal and vertical resolution are required. Nevertheless, only by adjusting the boundary conditions does the model successfully reproduce the basic large-scale
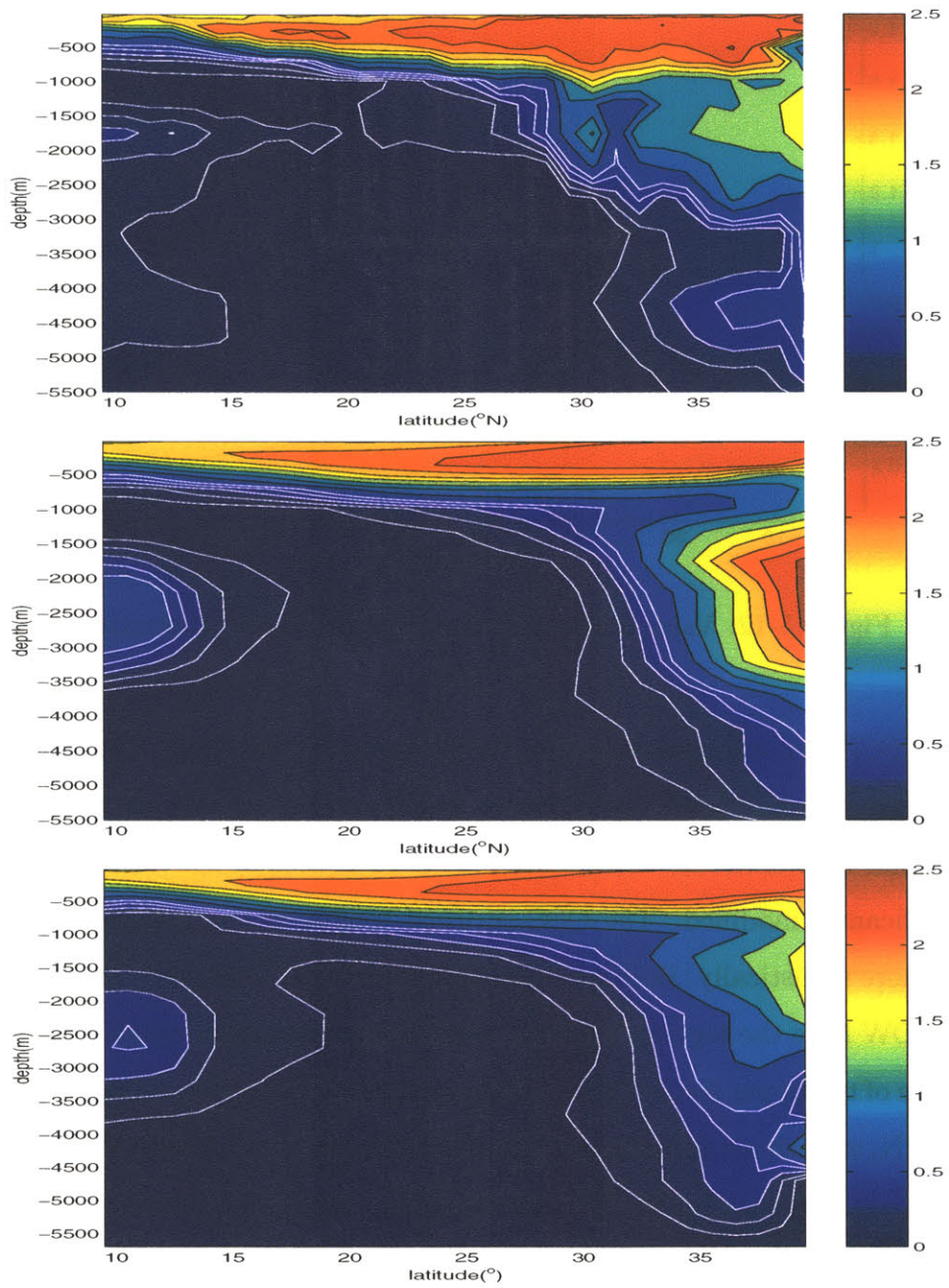
Figure 5-13: Distributions of observational (upper) and modeled CFC-11 concentrations at iterations 1 (middle) and 85 (lower) along WOCE A20 (52°W), July - August, 1997. The contour intervals of white (below 0.5) and black lines (above 0.5) are 0.1 and 0.25, respectively.

features of the observations.

On an average, after optimization, model-data differences fall within the error profiles we have prescribed. Discrepancies, however, exist inevitably. Figure 5-14 shows the differences between the optimal and observational CFC-11 concentrations along the same meridional section (52^oW) in the western basin. There are both negative and positive values. Major differences appear below the ocean surface. Modeled CFC-11 concentrations are too high between 10^oN and 15^oN at about 300 m depth and too low between 25^oN and 39^oN (also see Fig. 5-13) at depths 600 - 900 m. These model-data differences are due to the coarse vertical resolution of the model. It is common that in a coarse-resolution model, sharp gradients tend to be smeared out [e.g., Land et al., 2001]. Therefore, the modeled vertical gradient of CFC-11 in the thermocline is weak. This weak vertical gradient leads to the model-data differences in the thermocline. At about 33^oN, the negative values centered about 2000 m depth are due to the weak front of the Labrador Sea Water (LSW) in the model. Again we can attribute this weak front to the coarse horizontal resolution of the model [e.g., Redler et al., 1999]. The negative values at about 30^oN between 1500 m and 2200 m depth are due to the highly coherent meso-scale structure that exists in the observations, but are regarded as the data error by the model. Down deep at about 3000 m depth, the positive values indicate that modeled CFC-11 concentrations are slightly higher than observations, because our initial estimate is too high. In addition, the steady state simplification of the surface piston velocities and ocean circulation certainly contributes to the model-data misfits to some degree. Nevertheless, with this model resolution of $1^o \times 1^o$, we regard that the model predictions and the data are marginally consistent after the optimization of the CFC boundary conditions.

Comparisons of the modeled CFC distributions with observations along other sections show similar characteristics. The CFC-11 concentration in the NADW is largely reduced. Modifications of CFC concentrations in the upper ocean and near the bottom, as well as in the eastern basin are relatively small. Figure 5-15 shows the observational and modeled CFC-11 concentrations nominally along 20^oW, July - August, 1993, when sufficient CFC has arrived in the deep eastern basin between 30

structure
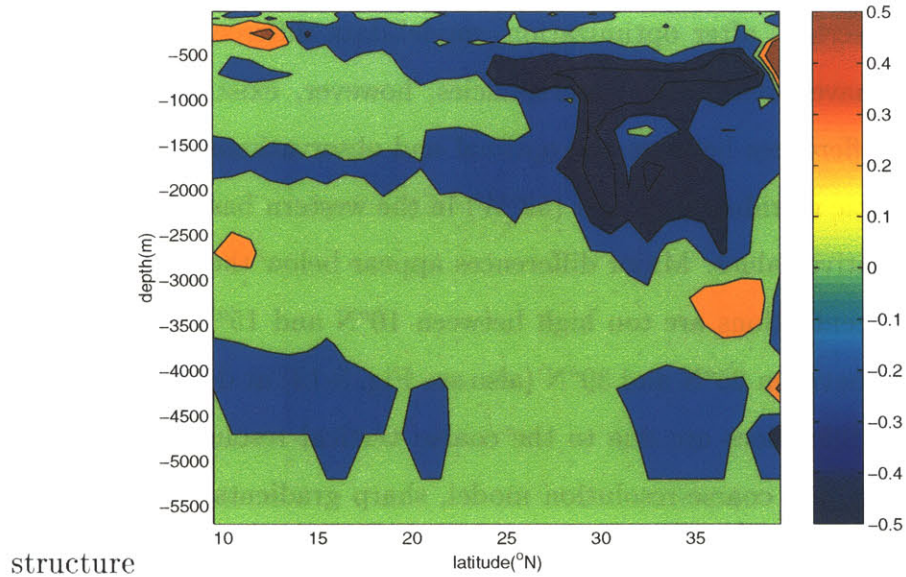
Figure 5-14: Differences between the constrained and observational CFC-11 concentrations (model - data) along $\sim 52^o$W, WOCE A20.

- 40 ^{o}N. The optimization reduces the CFC-11 concentration in the modeled NADW centered at 2000 m depth. After optimization, modeled and observational CFC-11 concentrations at depth are similar: CFC-11 concentration is about 1 pmol/kg at the northern boundary and gradually decreases with depth and latitude; below 2500 m or south of 25°N, the CFC-11 concentration is smaller than 0.1 pmol/kg. In the upper ocean, the large-scale distribution patterns of modeled and observational CFC-11 concentrations agree with each other: high CFC-11 concentration about 2.75 pmol/kg appears at the northern boundary, occupying upper 500 m; the concentration gradually decreases and the CFC isolines shoal toward surface with latitude. South of 15°N, the CFC content is confined to the near surface. There are, however, obvious model-data differences. The observed small-scale structures in the upper ocean and the meso-scale structure at 1500 m are not reproduced by the model, but is regarded as data error. Therefore, along this section of the eastern basin, the modeled and observed CFC-11 distributions are consistent, given the data error prescribed in section 5.1 and the model resolution of $1^o \times 1^o$.

158
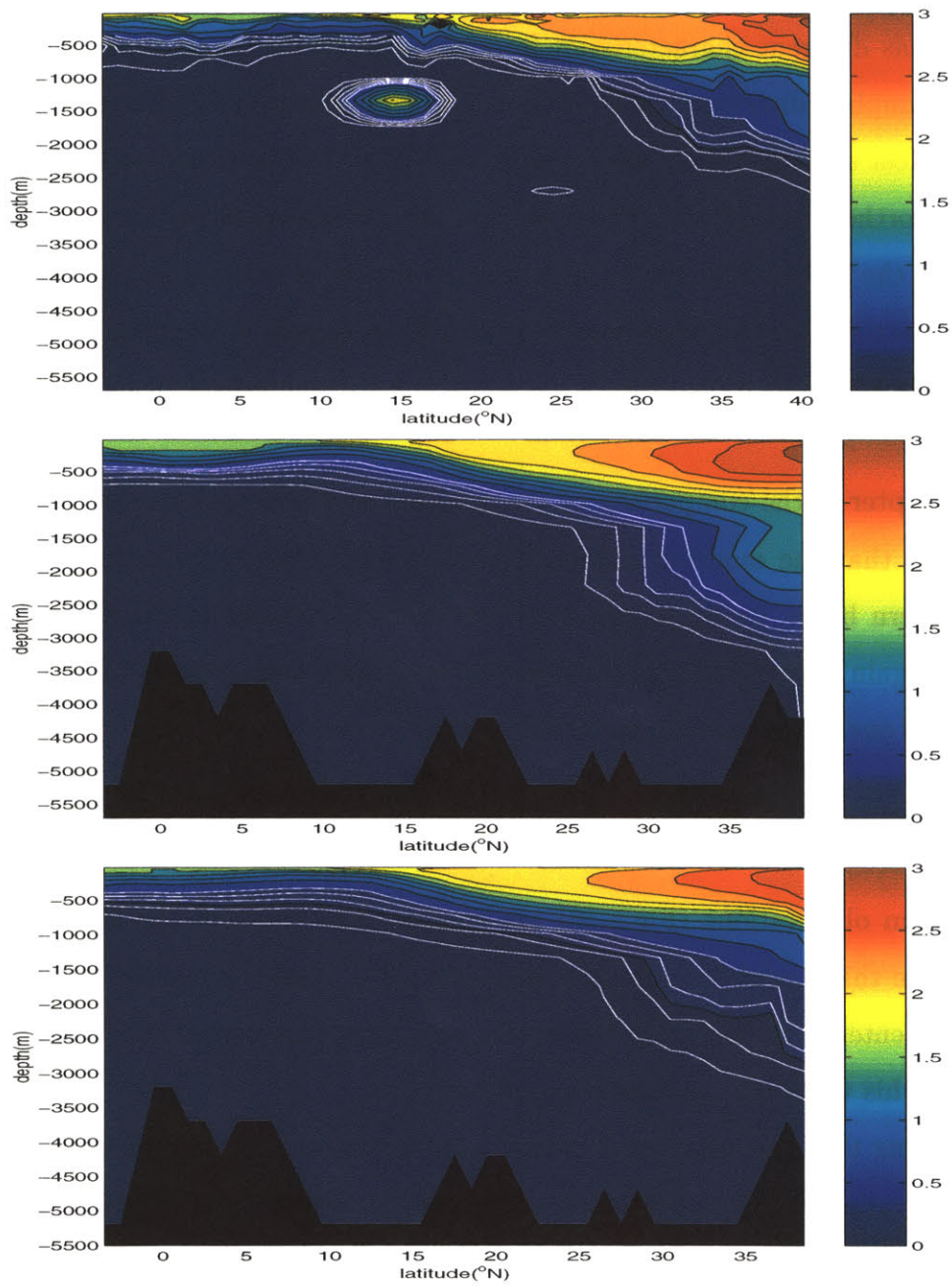
Figure 5-15: Same as Figure 5-13 but for WOCE AR21 (Repeated track of Oceanus Cruise No. 202, ~20^oW), July - August, 1993.

5.3 Optimization of the tritium boundary conditions

Tritium has different characteristics from those of CFCs: their input histories and oceanic sampling distributions are different; tritium decays radioactively while CFCs do not. Most tritium entered the ocean in the 1960s via the ocean surface in the high-latitude northern hemisphere, where the uptake of surface values is poorly simulated. Not until the 1970s were the earliest measurements of tritium in the ocean made. The radioactive decay strongly weakens the tritium signals in the deep ocean interior. These facts add more difficulties in the use of the tritium data to constrain the model circulation.

In Chapter 3, the comparison of the modeled and observed tritium distributions has shown that the modeled tritium concentration is too high in the high-latitude deep western basin, owing to the overly vertical penetration in the deep convective regions. Again to avoid resolving the poorly simulated deep convection in the model, we restrict our model domain to 39.5°N south.

5.3.1 Optimization over the Atlantic between 4.5°S and 39.5°N

The tritium observations (Fig.5-16) are sparser than those of the CFCs. Tritium data within this model domain span the years 1972 - 1993. Since the major amount of tritium entered the ocean in the 1960s, an integration period over 1960 - 1993 is chosen in this tritium assimilation experiment.

Following the same approach, we treat the initial-boundary conditions of tritium as control variables. The uncertainty of the temporally and spatially varying tritium surface concentration (see Chapter 3 for details) is supposed to be 50%. The relative uncertainties of initial and open boundary tracer concentrations, which come from the forward run, are assumed to be 100%. The errors are replaced by a constant, 0.02 TU, whenever the uncertainties are smaller than this value.

The cost function is formulated in the same way as in Eq. (5.7). The yearly
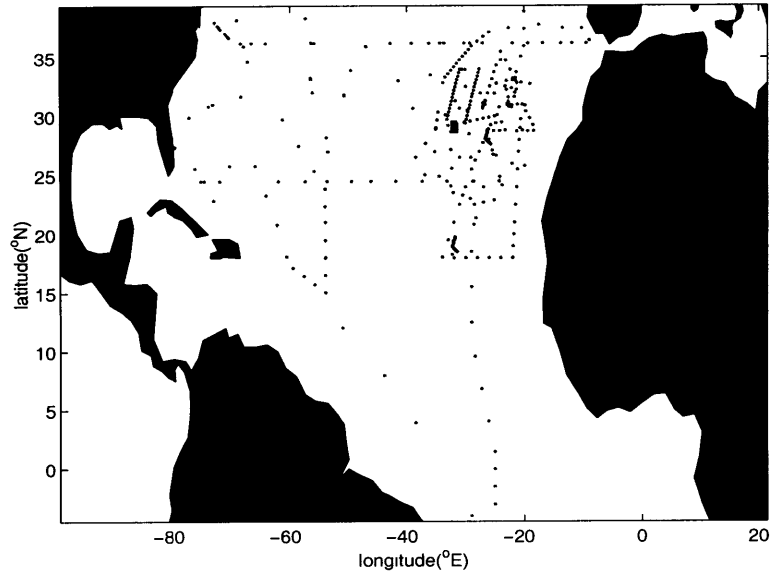
Figure 5-16: Stations (black dots) of the tritium data assimilated.

mean surface and open boundary tritium concentrations are prescribed and vary independently each year at each boundary grid in the model. The number of model bins within which the tritium observations are available is 3,787. This number is much smaller than that of CFCs.

After 60 iterations, the root-mean-square value of the tritium model-data misfits in Eq. (5.7) drops to 1.1. On an average, the model-data differences fall almost within the error-profiles prescribed. The optimization of the tritium boundary conditions brings the modeled and observed tritium concentrations into near-consistency.

Figure 5-17 shows the observational and modeled tritium distributions along the western Atlantic GEOSECS section, 1972. Before the optimization, the tritium-enriched tongue of the NADW is centered at about 2000 m depth in the model, with values too high near the northern boundary. After the optimization, the tongue is centered about 1500 m. Modeled tritium concentration in the tongue is similar to the observations; tritium concentration at 1500 m depth is about 2 TU near the northern boundary, and decreases southward to 1 TU at about 30°N. In the upper ocean, above 500 m, both the constrained and observational tritium distributions show three maxima with values higher than 7 TU located between 15 - 20 °N, 25 - 30

161

°N, and near the northern boundary. South of 10°N, most tritium content is confined to the near surface.

The observational and modeled tritium distributions in the eastern basin, nominally along ~20°W, July - August, 1988, are shown in Fig. 5-18. After the optimization, the tongue with tritium concentration of 2.5 TU penetrates farther south in the upper ocean, which is more realistic. The constrained and observational tritium isolines of 2 TU and 1.5 TU agree with each other. Water with tritium concentration higher than 2 TU penetrates to 20°N and occupies the upper 700 m in both model and data. Down deep, about 1500 m, the optimization reduces the modeled tritium concentration. The constrained and observational tritium concentrations below 1000 m are less than 1.5 TU.

As in the case of the adjustments of the CFC boundary conditions, the model-data misfit of tritium is mainly minimized by reducing the modeled tritium concentration in the NADW at the northern boundary. Presenting the surface and lateral tritium boundary histories over 30 years is paper-consuming and tedious. Only those boundary conditions in typical years are presented. The first and optimal estimates of the tritium concentrations at the northern boundary in years 1973, 1981, and 1992, when tritium observations are available in the experimental model domain, are exhibited in Fig. 5-19. In a large scale, it is obvious that tritium concentrations between depths 1500 - 3500 m in the western basin in 1973 and 1981 are greatly reduced after the optimization. In 1992, a year before the latest observations, the adjustment of the deep tritium concentration at the northern boundary is small. This is because the latest observational information in the subtropical eastern basin in 1993 has not arrived at the deep northern boundary in 1992 and cannot adjust the tritium concentrations there effectively.

Since there is no tritium observation that is exactly within the model grid cells at the northern boundary of 39.5°N, comparison of modeled and observational tritium concentrations at the northern boundary is not presented. To show observational support for our optimal tritium boundary conditions, the advective tritium flux across the northern boundary in the constrained model is calculated. This flux is used to
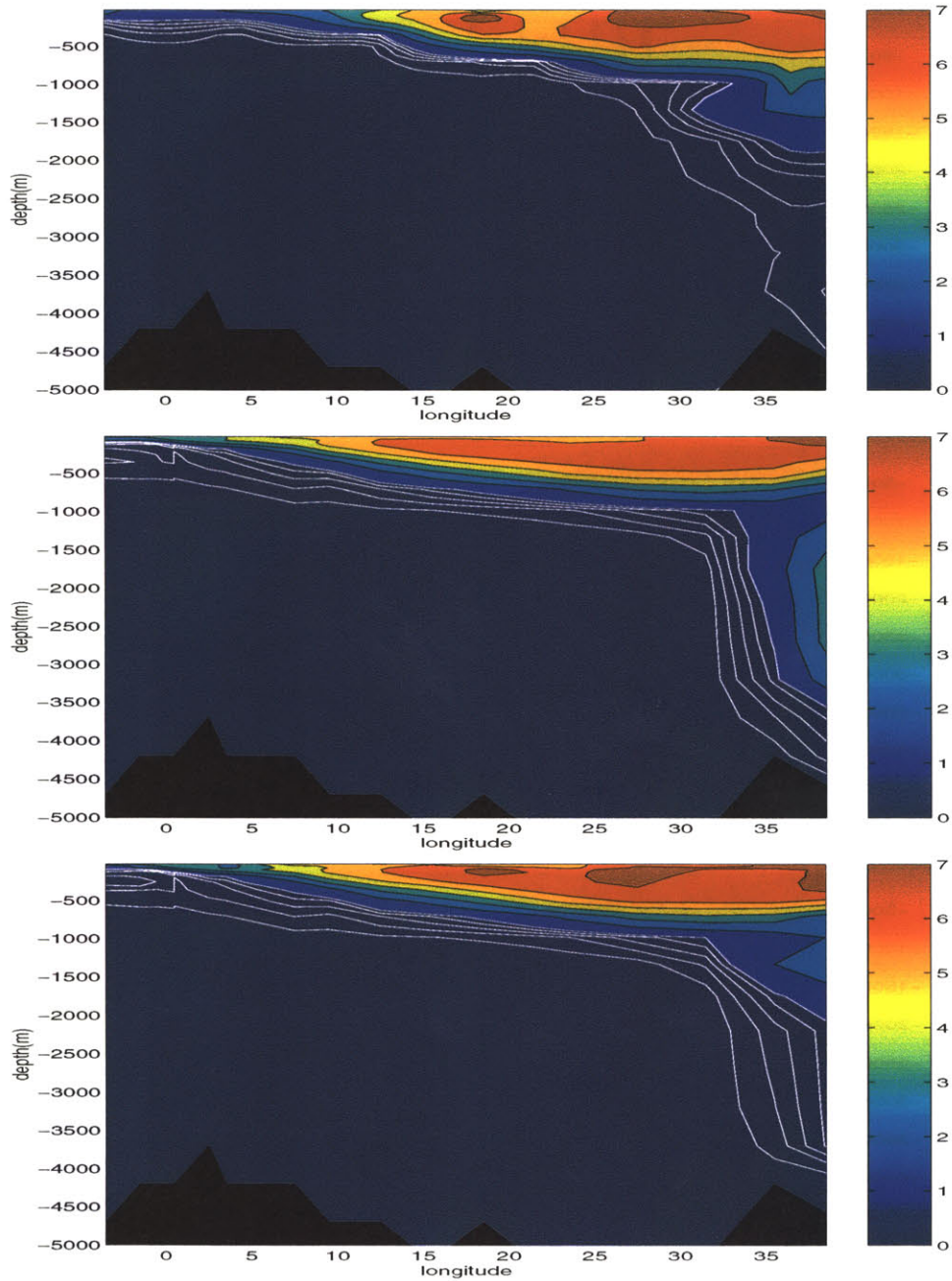
Figure 5-17: Distributions of observational (upper) and modeled tritium concentrations at iterations 1 (middle) and 60 (lower) along the western Atlantic GEOSECS section, 1972. The contour intervals of white (below 1) and black lines (above 1) are 0.2 and 1, respectively.
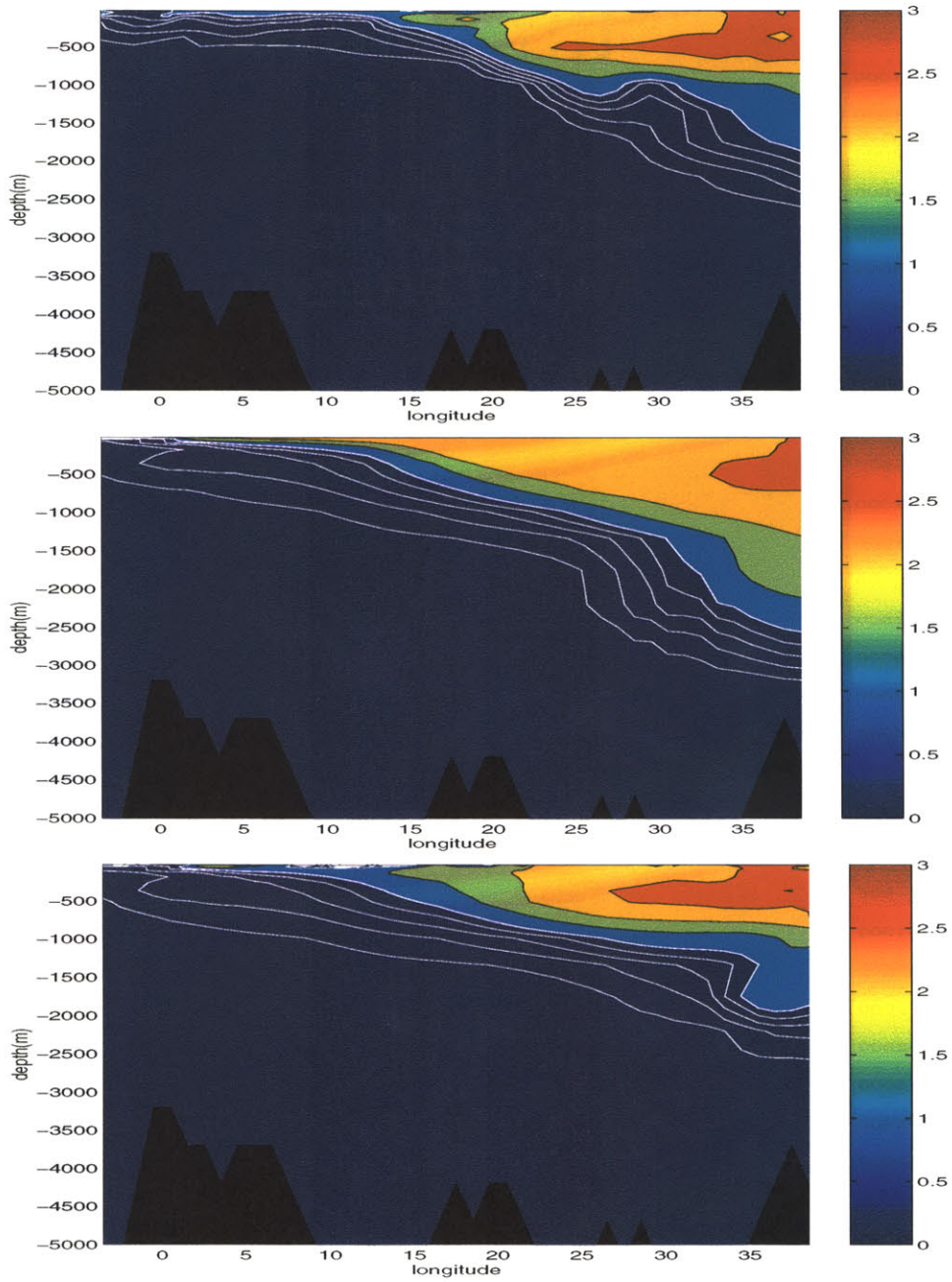
Figure 5-18: Distributions of observational (upper) and modeled tritium concentrations at iterations 1 (middle) and 60 (lower) along ∼ 20°W, July - August, 1988. The contour intervals of white (below 1) and black lines (above 1) are 0.2 and 0.5, respectively.
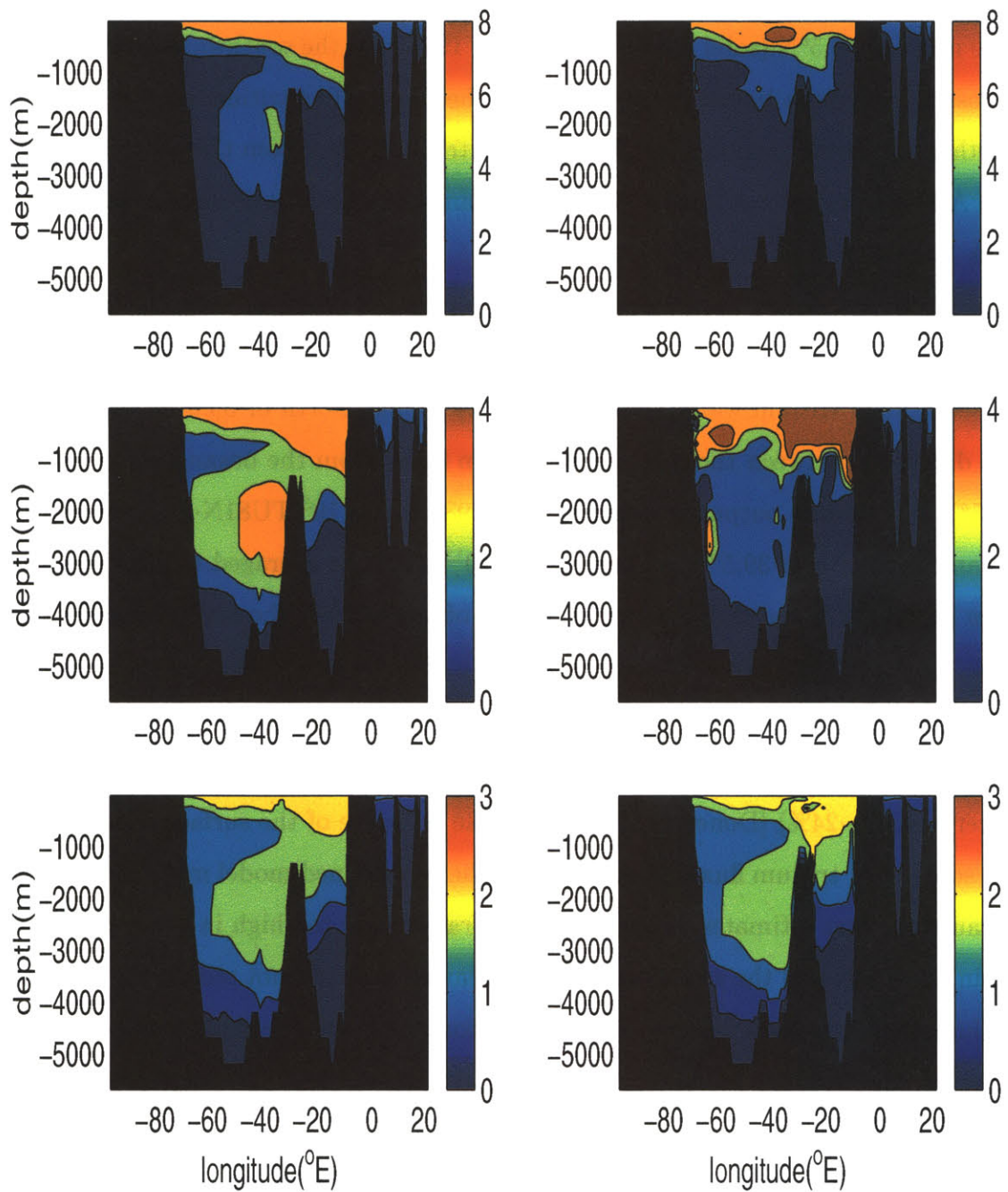
Figure 5-19: Tritium concentrations at the northern boundary (39.5°N) in 1972 (upper), 1981 (middle), and 1992 (lower) at iterations 1 (left) and 60 (right).

check whether it is consistent with the estimated tritium budget in the North Atlantic from observations [Doney et al., 1993].

Figure 5-20 shows the cumulative observational tritium input from the ocean surface north of 39.5°N (solid line) [Doney et al., 1993] and the southward tritium output across the northern boundary at 39.5°N (dashed line). The tritium output across the northern boundary is much smaller than the tritium input from the ocean surface, in the Atlantic region north of 39.5°N. Significant amounts of tritium remained in the high latitude North Atlantic before 1986.

Figure 5-21 shows the observational tritium water column inventory from Transient Tracers in the Ocean (TTO) dataset, 1981 - 1983 [Östlund and Rooth, 1990]. Observational tritium water column inventory is high north of 39.5°N. In Fig. 5-20, the difference between the cumulative tritium input from the ocean surface north of 39.5°N and tritium output across 39.5°N in 1982 is 5×10^3 TU81N·m; the horizontal ocean area north of 39.5°N is about 1.0×10^{13} m^2. The averaged tritium water column inventory in the region north of 39.5°N obtained from the observational surface input and modeled lateral boundary output at 39.5°N is 5×10^3 TU81N·m, roughly consistent with the observations (Fig. 5-21) to the first order but about 20% lower than observations. This disagreement can be caused by two major reasons: there is uncertainty ($\sim$24%) [Doney et al. 1993] in the estimate of the surface tritium input; the southward tritium flux across 39.5°N in the constrained model might be too high, because the first estimates of tritium concentrations are too high in the deep western basin at 39.5°N and the assimilation of the sparse data does not reduce the boundary tritium concentrations enough. The calculation of the tritium budget demonstrates, however, the optimal boundary conditions are better than the corresponding first estimates, and are physical reasonable.

The tritium budget in the region between 4.5°S and 39.5°N is also calculated. The total oceanic tritium content in this region is obtained from the optimal tritium distribution, which is consistent with the observations. The major inputs of tritium in this domain are from the surface and northern boundary. Tritium input from the southern boundary is negligible. The surface tritium input is from Doney et al.

166
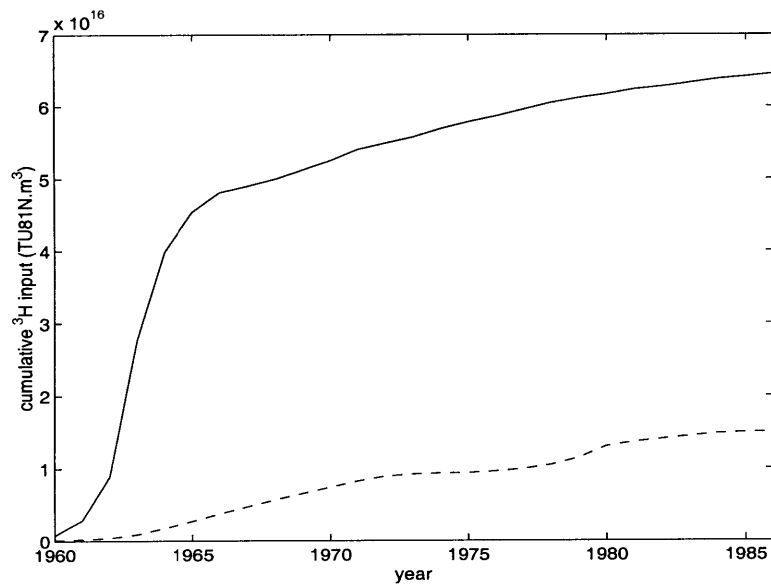
Figure 5-20: Cumulative observational tritium input from the ocean surface north of 39.5°N (solid line) [Doney et al., 1993] and the constrained southward tritium output across the northern boundary at 39.5°N (dashed line) in the North Atlantic.
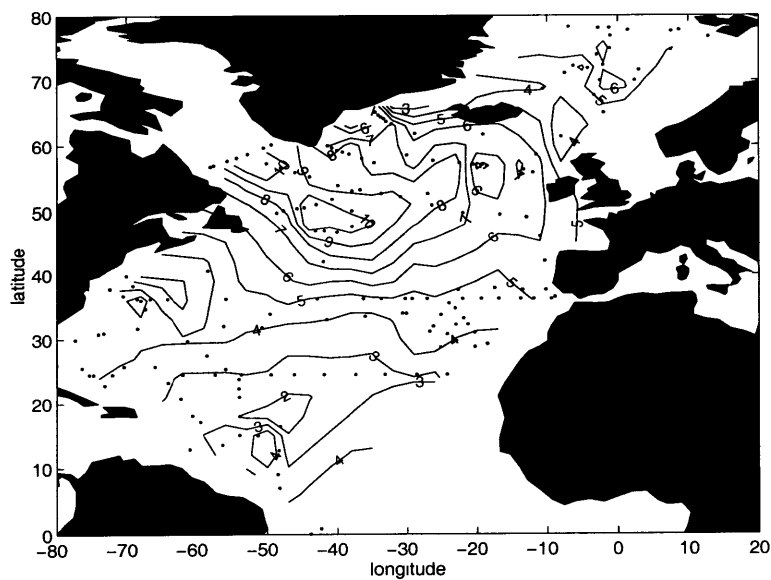
Figure 5-21: Observational tritium water column inventory ($\times 10^3$ TU81N·m) from TTO (1981 - 1983) dataset. Black dots are observational stations.

[1993]. The northern boundary input is obtained from the optimal tritium boundary conditions and the modeled flow field. Figure 5-22 shows the tritium budget in the region between 4.5°S and 39.5°N. The total tritium input from the boundaries, which has about 20% uncertainty, agrees with the total oceanic tritium content in this domain. The optimal northern boundary condition of tritium is consistent with the observed tritium budget in the North Atlantic.
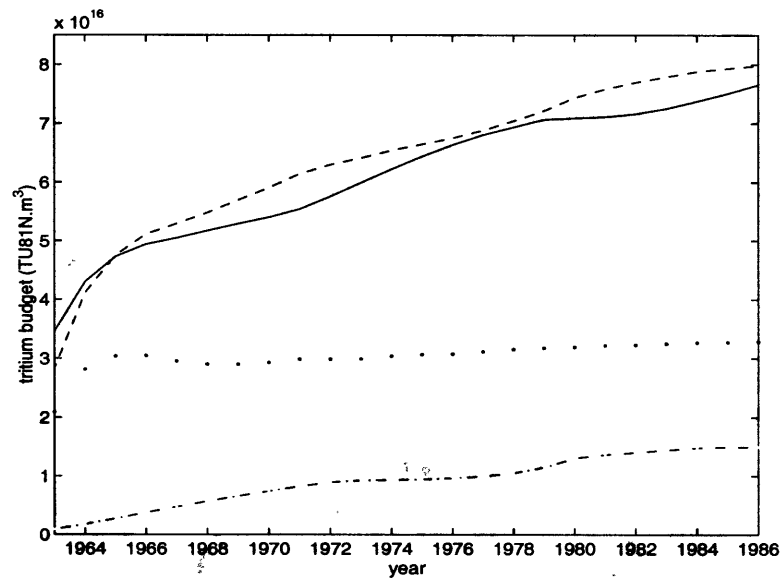
Figure 5-22: The tritium budget in the region between 4.5°S and 39.5°N in the North Atlantic: solid line, total oceanic tritium content from the constrained model; dashed line, total tritium input from the boundaries; dotted line, cumulative surface input from Doney et al. [1993]; dash-dot line, cumulative northern boundary input in the model.

As mentioned before, the tritium entered the ocean as a pulse in the 1960s. Figure 5-23 shows the optimal distribution of the surface tritium concentration in 1964, the peak of the pulse, and the corresponding differences of the surface values between iteration 60 and 1 (60 - 1). The distribution of the differences shows some large scale features: an increase of surface tritium concentration between 60°W and 40°W near

the northern boundary and a decrease in the eastern basin. The largest adjustment is about 10% of the first estimate.

In years when observations are available, adjustments of the surface tritium values are also obvious. The adjustments of the surface values in 1981, a year that has a large number of tritium observations, are shown in Figure 5-24. The largest adjustments appear at data locations. After the optimization, the modeled and observational surface tritium concentrations agree very well. Tritium concentration is higher than 4 TU near the northern boundary and in the north-eastern basin. Low tritium concentration with values of 2 TU appear in a band from 60 -70 ^{o}W, 25°N to 50 -60 ^{o}W, 15°N. Tritium concentration in the rest of the model domain is about 3 TU. The optimal boundary conditions, which bring the modeled and observed tracer distributions into consistency, are physically acceptable.

Unlike CFCs, for which the climatological surface piston velocities are regarded as controlling the oceanic CFC distributions, the yearly varying surface tritium concentrations are treated as the control variables. Therefore, the model has more freedom to adjust the tritium surface conditions. The adjustments of the surface tritium concentrations are more obvious than those of CFCs. Obvious adjustments of the surface tritium values appear in years and places within which observations are available, as well as in the years when the major amount of tritium entered the ocean.
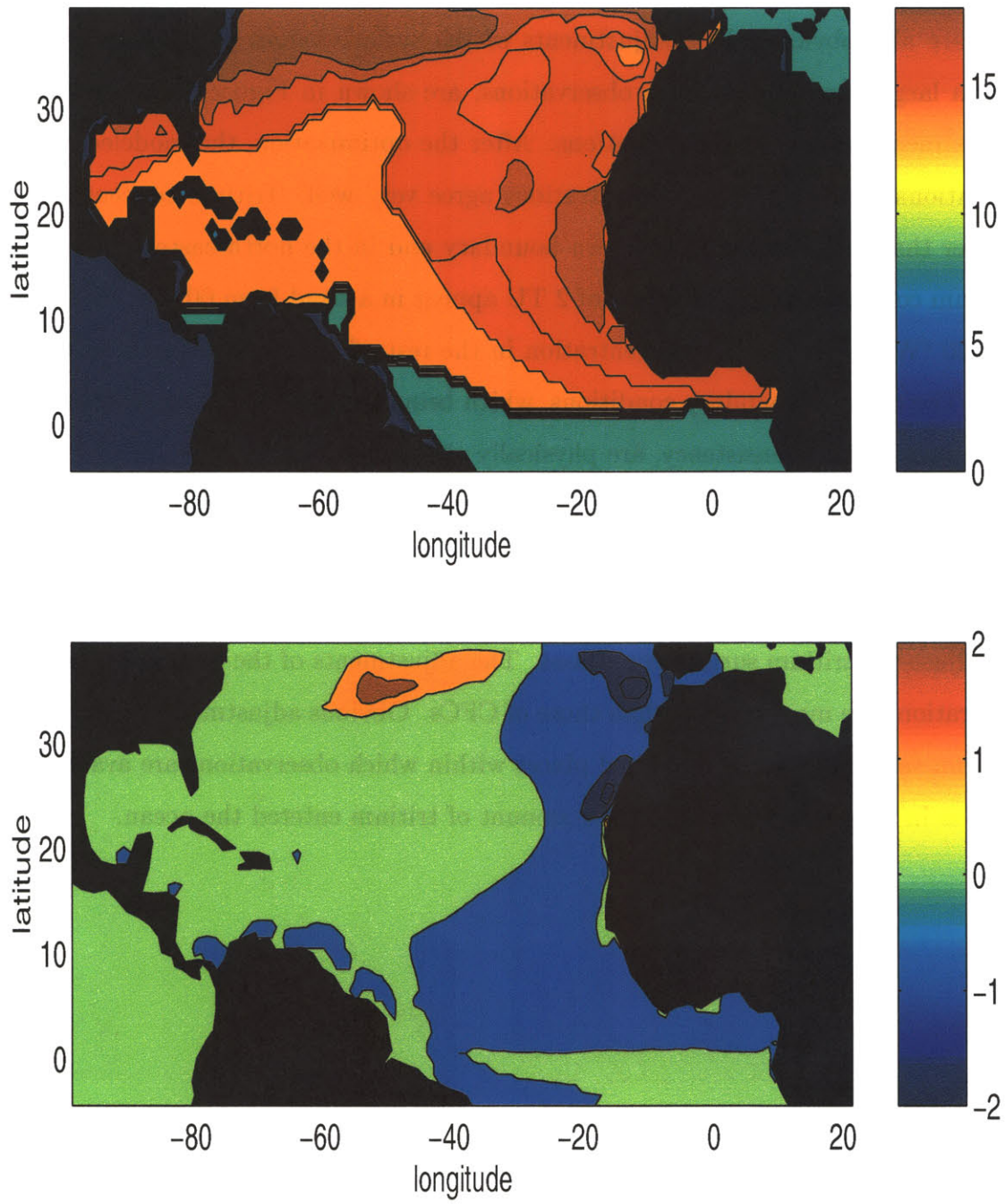
Figure 5-23: Distributions of the optimal surface tritium concentration (TU) in 1964 and the differences (TU) between iterations 60 and 1 (60 - 1).
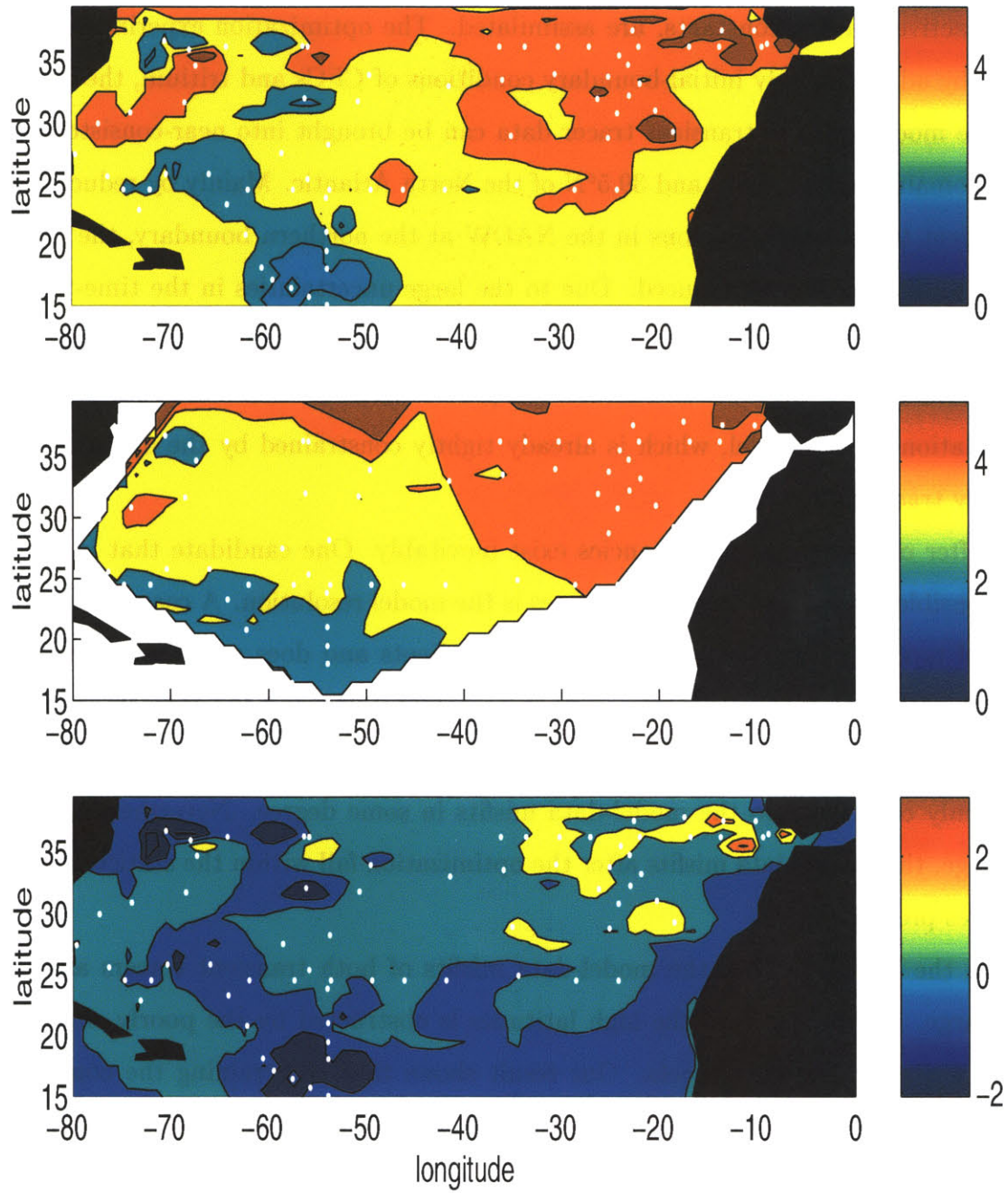
Figure 5-24: Distributions of the optimal (upper) and observational (middle) surface tritium concentrations (TU) in 1981, and the differences (lower) of the surface tritium values in 1981 between iterations 60 and 1 (60 - 1).

5.4 Summary

Both CFC and tritium data, with different input histories, sampling distributions, and radioactively decay constants, are assimilated. The optimization experiment shows that by adjusting only initial-boundary conditions of CFCs and tritium, the $1^o \times 1^o$ offline model and the transient tracer data can be brought into near-consistency, in the domain between 4.5^oS and 39.5^oN of the North Atlantic. Mainly by reducing the transient tracer concentrations in the NADW at the northern boundary, the model-data misfits are largely reduced. Due to the large uncertainties in the time-varying boundary conditions of transient tracer concentrations, and in their interior distributions, the current transient tracer data can provide little information about the ocean circulation to the model, which is already tightly constrained by the dynamics and steady tracer balances.

After optimization, discrepancies exist inevitably. One candidate that is mostly responsible for the systematic differences is the model resolution. A coarse-resolution model typically tends to smear out sharp gradients and does not resolve the OW. This leads to the large-scale differences between the model and the data. In addition, the steady state simplifications of the surface piston velocities and ocean circulation certainly contribute to the model-data misfits in some degree. Nevertheless, on an average, the model-data misfits after the optimization fall within the statistical error profiles prescribed.

In the high latitudes, the model-data misfits of both transient tracers and T-S are large. Optimization in the high latitudes is obstructed by the poorly simulated deep winter convective process. Our result shows that constraining the convective mixing rate requires proper modeling of the isopycnal mixing in the deep convective regions. Therefore, a reasonable first step to enhance the model performance in the high latitudes is to use T-S data to directly improve the modeled T-S, and hence density fields.

Chapter 6

Conclusions

6.1 Summary of the thesis

Research about transient tracers in the ocean is a multidisciplinary field. Sampling and analyzing the oceanic transient tracers depend on sophisticated chemical skills and techniques. As more and more transient tracer data have been obtained from the oceans during the last few decades, these tracer data are used to study the ocean physics, notably the exchange processes between the ocean surface and interior. One of the important objective for the investigation of the penetration of oceanic transient tracers is to study the invasion and redistribution of the anthropogenic CO_2 in the ocean.

With the advances of observational techniques, dynamic theories, and numerical modeling, our understanding of the general ocean circulation is entering into the era of quantitative oceanography (Carl Wunsch, personal communication). The utility of transient tracer observations in the ocean should reach beyond qualitatively drawing the ventilation pathways of the surface properties. Because the transient tracer data are expensive to obtain, an investigation of the efficiency of the data in providing quantitatively new information about the ocean circulation and surface gas exchange is important.

This thesis explores the capability of transient tracers to constrain ocean circulation properties and surface gas exchange rates in the North Atlantic. It compares the

roles of both steady and transient tracers under the same contexts of model evaluation and data assimilation. It is the first application of the adjoint method to constrain a comprehensive numerical ocean model with the transient tracer data, using more realistic tracer boundary conditions than those used in the previous studies (see Chapter 5 for details).

Firstly, an idealized tracer forced by a unit step surface concentration is introduced to establish a simple scenario for understanding transient tracers. Analytical study of this idealized tracer in one-dimensional (1-D) pipe flows shows that its transient distribution is a complex function of advective and mixing rates entangled with various timescales, while its steady state distribution is very simple. Interpretation of the transient distribution is difficult. The inference of the mixing rate from the steady state distribution is more accurate than that from the transient state distribution, because the boundary condition of the steady state is simple. Inferring both advective and mixing rates from the transient state distributions with uncertain boundary conditions can easily lead to erroneous solutions that are far from the true values. Three-dimensional (3-D) as well as 1-D inverse computations show that the goodness of the final optimal estimation of one control variable depends on the optimal estimations of the others. A physically acceptable estimation of the boundary conditions is a prerequisite for reasonable inferences of circulation properties from the transient tracer data.

Secondly, CFC, tritium, and temperature and salinity (T-S) observations are compared with model results in the North Atlantic. The comparison shows that major model-data misfits of tracers appear in the formation regions of the North Atlantic Deep Water (NADW) and along its pathways downstream, especially in the deep western basin in the high latitudes. The model-data disagreements of transient tracer fields appear in regions where the water mass structures are incorrectly modeled. The excessive vertical penetration of the convective adjustments, problematic production and outflow of the NADW are exhibited by both transient tracer and T-S fields. All tracers, steady or transient, undergo the same dynamics controlled by flow fields and mixing rates. Both T-S and transient tracers can be used to locate rapid mixing

processes where vertical homogeneity is present. In the model, CFC-11 and salinity fields exhibit a strikingly similar pattern of the ventilation pathway of the LSW. All characteristic properties of a water mass will be tagged along the trajectory of that water mass. Steady tracers, for instance salinity, can help us evaluate the ventilation pathways in the model as well.

Thirdly, the sensitivities of the concentration, the derived tracer age of CFCs, the simplest transient tracers with relatively well known source functions, and $T - (\beta/\alpha)S$ (α and β are thermal and haline expansion coefficients, respectively) are analyzed and compared. In spite of different surface boundary conditions and oceanic distributions, the sensitivities of both steady and transient tracer properties successfully exhibit the ventilation pathways and the associated timescales in the model, and thereby can provide information to constrain the corresponding model physics. In an inverse study, observational information of either steady or transient tracers, once it enters a model, will propagate under the same dynamic rules. The corresponding sensitivity, such as that of a model-data misfit, then provides information about problematic transport pathways and timescales mainly upstream, and serves as a guide for the adjoint model to optimize its parameters.

Lastly, the CFC and tritium observations are directly incorporated into the model to investigate the extent to which the transient tracers can constrain the model circulation. The optimization experiments show that physically acceptable adjustments of initial-boundary conditions of CFCs and tritium can bring the $1^o \times 1^o$ offline model and the data into near-consistency, in the domain between 4.5°S and 39.5°N of the North Atlantic. Due to the large uncertainties in the time-varying boundary conditions of transient tracer concentrations, and in their interior distributions, the current transient tracer data provide little information about the ocean circulation to the model, which is already tightly constrained by the dynamics and steady tracer balances.

6.2   Discussion

There are several limitations of this study. Most issues lie in the resolution of the model and simplification of the offline calculation.

The model of $1^o \times 1^o$ resolution has difficulties in resolving the high latitude physics, notably the deep winter convection. This limits our data-assimilation experiments to non-convective areas, where model-data misfits in the upper ocean are small. As a consequence, the optimizations of both CFC and tritium distributions are mainly driven by the deep northern boundary conditions, which are determined by the surface values in the high latitudes. In the local non-convective areas, adjustments of the surface CFC values, which are regarded as being controlled by the climatological surface piston velocities, are minor. There are some obvious adjustments of the surface tritium values, which vary independently each year. Those surface tritium adjustments, however, are not as strong as the adjustments of the northern boundary values. The roles of surface conditions in the assimilation sequences have not been explored thoroughly in this study. The high-latitude deep convective regions are places where the largest uncertainties of piston velocities and ice coverage exist. They are also the major places where tritium enters the ocean. An eddy-resolving high resolution model covering the convective regions is therefore important to explore the information content of the transient tracers further.

Another approach to constraining the surface gas exchange rate with the transient tracer observations is using a global GCM. This approach, however, requires adequate simulation of the ocean physics, in order to get reasonable reference of the surface gas exchange rate. This study shows that the steady tracers can enhance model physics more directly and efficiently than transients. Before constraining the surface conditions with the transient tracer data in a global model, using steady tracer data, direct current measurements, and globally covered satellite data etc., to improve the model physics would be a reasonable first step.

Due to the strong diffusivities in the relatively coarse-resolution model, the tongue of the CFC enriched overflow water in the model is quickly dissipated away from

the northern boundary and is weaker than that in the observations. In the coarse-resolution model, sharp gradients such as the vertical CFC gradients in the thermocline and the front of the CFC-enriched NADW are smeared out. These lead to some large-scale model-data differences after optimization. It is still worthwhile to run the assimilation experiments again with a high-resolution model to see whether those large-scale model-data misfits will disappear.

The offline model uses the monthly climatological mean velocities, T-S fields and convective mixing, in which internal model dynamics such as inter-annual variabilities in convection fields are absent. Errors are introduced into the model predictions. Using the transient tracers to study the variability in the ocean is totally ignored in this study and needs further quantification. In addition, the offline model uses the monthly mean convection fields, while the deep convection itself is a process whose timescale is usually less than a month. Whether it is adequate to represent the convective fields in their monthly means needs more exploration. Resolving the deep convective process in the model remains a challenge and is a direction of future research. Nevertheless, with improvements in computer technology, restoring time-varying circulation fields at a reasonable frequency, such as a week, for offline models will become possible. The offline model will continue being a powerful tool to study passive tracers.

The information content of bomb ^{14}C, one of the transient tracers in the ocean, has not been explored in this study. We could expect, however, that it will exhibit similar characteristics as CFCs, since both CFCs and ^{14}C enter the ocean through sea surface gas exchange and their atmospheric distributions are quite uniform. Constraining the ocean circulation with bomb ^{14}C needs improvement in the estimation of the natural ^{14}C component.

Given the complexity and richness of the transient tracer structure as described by Wunsch [2002], this study should be regarded as a progress toward understanding a difficult synthesis of the transient tracers in the ocean.

Appendix A

The adjoint method

The adjoint method is documented in detail in the monograph by Wunsch [1996]. The basic idea is that the model estimates the ocean state through a function of many independent variables (also called the control variables), for example, initial conditions, boundary conditions, and empirical parameters. A "performance index" or "cost function" is defined to measure how well a model solution matches observations. The optimization problem tries to estimate the independent variables such that the cost function is minimized [Marotzke, 1999]. The gradient of the cost function with respect to the control variables is calculated by what is called the "adjoint model". The Tangent-linear and Adjoint Model Compiler (TAMC) by R. Giering [1998] can generate the adjoint code automatically.

A.1 Description of the method

The forward model can be expressed as

$$\frac{\partial \mathbf{X}}{\partial t} = \mathbf{F}(\mathbf{X}, \mathbf{U}), \tag{A.1}$$

where $\mathbf{X}$ and $\mathbf{U}$ are state and control variables, respectively.

If a set of observations $\mathbf{X}_{obs}$ are available and our estimated controls are $\mathbf{U}'$, we

define the cost function as

$$J(\mathbf{X}, \mathbf{U}) = (\mathbf{X} - \mathbf{X}_{obs})^T \mathbf{R}^{-1} (\mathbf{X} - \mathbf{X}_{obs}) + (\mathbf{U} - \mathbf{U}')^T \mathbf{Q}^{-1} (\mathbf{U} - \mathbf{U}'), \qquad (A.2)$$

where $\mathbf{R}$ and $\mathbf{Q}$ are error covariance matrixes of observations and controls, respectively. Their inverses are proportional to the accuracies of the data and the model. At points where there is no observation, the corresponding elements of $\mathbf{R}$ go to infinity. The first term in Eq. (A.2) is the model-data misfits and will drive the adjoint model. The last term in Eq. (A.2) is to constrain the control vector so that they will not be too far from the initial estimate, and thereby will fall within an acceptable range [Smedstad, 1991].

The problem here is *finding* $\mathbf{U}^*$ *such that it minimizes the cost function with an acceptable value.* The gradient of J with respect to $\mathbf{U}$ will be calculated by the adjoint model. Suppose we have a series of observations at time $t = t_1, t_2, ..., t_n$. J is thus a function of $\mathbf{X}_{t_1}, \mathbf{X}_{t_2}, ..., \mathbf{X}_{t_n}$ and $\mathbf{U}$. According to the forward model (A.1), $\mathbf{X}_{t_1}, \mathbf{X}_{t_2} ..., \mathbf{X}_{t_n}$ are functions of control vector $\mathbf{U}$ (including initial conditions). Therefore the cost function is a function of $\mathbf{U}$.

Since

$$J = J(\mathbf{X}_{t_1}, \mathbf{X}_{t_2}, ..., \mathbf{X}_{t_n}, \mathbf{U})$$

$$\mathbf{X}_{t_n} = \mathbf{X}_{t_n}(\mathbf{X}_{t_{n-1}}) = \mathbf{X}_{t_n}(\mathbf{X}_{t_n-1}(...(\mathbf{X}_1(\mathbf{U})))),$$

we have

$$J = J(\mathbf{X}_{t_n}(\mathbf{X}_{t_n-1}(...(\mathbf{X}_1(\mathbf{U})))), \mathbf{X}_{t_{n-1}}(\mathbf{X}_{t_{n-1}-1}(...(\mathbf{X}_1(\mathbf{U})))), ..., \mathbf{X}_{t_1}(\mathbf{X}_{t_1-1}(...(\mathbf{X}_1(\mathbf{U})))), \mathbf{U}),$$

The gradient of J with respect to $\mathbf{U}$ is

$$\frac{dJ}{d\mathbf{U}} = \sum_{i=1}^{n} \frac{\partial J}{\partial \mathbf{X}_{t_i}} \cdot \mathbf{X}'_{t_i} \cdot \mathbf{X}'_{t_i-1} ... \mathbf{X}'_1 + \frac{\partial J}{\partial \mathbf{U}}. \qquad (A.3)$$

179

Taking the transpose of (A.3), we get

$$\left[\frac{dJ}{d\mathbf{U}}\right]^T = \sum_{i=1}^{n} (\mathbf{X}_1')^T ... (\mathbf{X}_{t_i-1}')^T \cdot (\mathbf{X}_{t_i}')^T \cdot (\frac{\partial J}{\partial \mathbf{X}_{t_i}})^T + \left[\frac{\partial J}{\partial \mathbf{U}}\right]^T, \qquad (A.4)$$

where $\mathbf{X}_{t_i}'$ is the Jacobian matrix of the model at time step t_i. The adjoint code is constructed by linearing every code assignment and executing the transposes of all linearized assignments in reverse order, initializing with the number one. Readers are referred to J. Marotzke et al. [1999] for more details. The calculation of the gradient of J with respect to $\mathbf{U}$ requires the forward model results at every time step before time t_n. We have to choose either to restore them or to calculate them again in the adjoint code [Giering, 1999].

A.2　The descent method—quasi-Newton method

Quasi-Newton method uses the change of the gradient to obtain information on the local Hessian of the objective function. It computes an approximation of the curvature of the function without actually forming the Hessian matrix. This method converges very fast, but requires a large amount of memory.

Suppose J can be approximated by its Taylor series near a point $\mathbf{U}_k$,

$$J(\mathbf{U}_k + \mathbf{p}) \approx J(\mathbf{U}_k) + \mathbf{g}_k^T \mathbf{p} + \frac{1}{2}\mathbf{p}^T \mathbf{Q}(\mathbf{U}_k)\mathbf{p}. \qquad (A.5)$$

Let $\mathbf{U}_{k+1} = \mathbf{U}_k + \alpha_k \mathbf{d}_k$, $\mathbf{B}_k \mathbf{d}_k = -\mathbf{g}_k$, where $\mathbf{B}_k$ is an approximation of the Hessian matrix. At the first iteration it is set to be an identity matrix. After each iteration, $\mathbf{B}_k$ is updated like (Smedstad et al., 1991),

$$\mathbf{B}_k = \mathbf{B}_{k-1} - \frac{\mathbf{B}_{k-1}\mathbf{s}_{k-1}\mathbf{s}_{k-1}^T\mathbf{B}_{k-1}}{\mathbf{s}_{k-1}^T\mathbf{B}_{k-1}\mathbf{s}_{k-1}} + \frac{\mathbf{y}_{k-1}\mathbf{y}_{k-1}^T}{\mathbf{y}_{k-1}^T\mathbf{s}_{k-1}}, \qquad (A.6)$$

where $\mathbf{s}_{k-1} = \mathbf{U}_k - \mathbf{U}_{k-1}$, $\mathbf{y}_{k-1} = \mathbf{g}_k - \mathbf{g}_{k-1}$.

The step length α_k is given by

$$\alpha_k = -\alpha_{k-1}\frac{(\mathbf{x}_k - \mathbf{x}_{obs})^T R^{-1}\delta\mathbf{x}_k}{\delta\mathbf{x}_k^T R^{-1}\delta\mathbf{x}_k}, \tag{A.7}$$

where $\delta\mathbf{x}_k$ is the perturbation of the model state, which is caused by the change of the control vector.

A.3 Procedure

The procedure of using observation to optimize the control variables is [Smedstad et al., 1991]:

1. From earlier studies, choose a best estimate for the control vector.

2. Integrate the model forward for the period over which the observations are assimilated.

3. Calculate the cost function J.

4. Run the adjoint code to calculate the gradient of J with respect to the control vector.

5. Choose a descent algorithm to find a new value of the control vector that makes J move toward its minimum as fast as possible

6. Check the value of J to see if it is less than a prescribed tolerance. If this is not the case, repeat from step 2 until a satisfactory solution has been achieved.

A.4 An example of TMAC code construction

Suppose we have

$$y = f(x_1, x_2, ..., x_n, y). \tag{A.8}$$

Its tangent linearization is

$$\delta y = \sum_{i=1}^{n} \frac{\partial f}{\partial x_i} \delta x_i + \frac{\partial f}{\partial y} \delta y, \qquad (A.9)$$

where δx_i and δy are small perturbations. The adjoint assignments are generated like

$$\delta^* y = \delta^* y \frac{\delta f}{\delta y}, \qquad (A.10)$$

$$\delta^* x_i = \delta^* x + \delta^* y \frac{\delta f}{\delta x_i}. \qquad (A.11)$$

For example, if we have an assignment

$z = Ax + B\,sin(y)$,

its adjoint code is

$adx = adx + adz * A$,

$ady = ady + adz * B * (-cos(y))$.

Given $\delta^* x_i = 0$, $\delta^* y = 1$ for the right hand side of (A.10)— (A.11), the assignments are equivalent to

$\delta^* y = \frac{\delta f}{\delta y}$,

$\delta^* x_i = \frac{\delta f}{\delta x_i}$.

Appendix B

The GM mixing parameterization

The GM (Gent and McWilliams) mixing parameterization scheme is to represent meso-scale eddy mixing in non-eddy resolving ocean circulation models. Gent and McWilliams [1990] argued that eddy transfer in the ocean is an adiabatic process and is related to gradients of isopycnic layer thickness. The GM parameterization mixes tracers and layer thickness along isopycnal surfaces, simulating the effects of meso-scale eddy transport that conserves density.

In large-scale ocean models the subgrid-scale eddies cannot be resolved. Therefore, the meso-scale eddy mixing must be parameterized. Decomposing the variables into large-scale Eulerian means over a time period that is long compared to an eddy life cycle, denoted by overbars, and eddy components denoted by primes, the tracer equation can be written as, in a Cartesian coordinate,

$$\frac{\partial \bar{c}}{\partial t} + \bar{\mathbf{v}} \cdot \nabla_h \bar{c} + \bar{w}\frac{\partial \bar{c}}{\partial z} = \bar{S}_0 - \nabla_h \cdot (\overline{\mathbf{v}'c'}) - \frac{\partial}{\partial z}(\overline{w'c'}). \tag{B.1}$$

Here $\mathbf{v} = (u, v)$, the horizontal velocity. The right-hand side of (B.1) is composed of source/sink and the eddy flux divergence terms due to baroclinic eddies. In a non-eddy resolving model, these flux divergences must be parameterized in terms of the averaged quantities that can be explicitly carried in the model.

The simplest parameterization is to suppose that the eddy transfer is down-gradient (Fickian diffusion),

$$\overline{\mathbf{v}'c'} = -\kappa_h \nabla_h \bar{c},$$

$$\overline{w'c'} = -\kappa_v \frac{\partial \bar{c}}{\partial z},$$

where the subscripts h and v denote horizontal and vertical directions, respectively.

In the ocean, mixing of properties occurs mostly along isopycnal surfaces. Redi [1982] introduced a mixing tensor that would mix tracers along isopycnal surfaces rather than horizontal surfaces. The mixing tensor is obtained by transforming a diagonal tensor in an isopycnal coordinate to a tensor containing off-diagonal elements in a geopotential coordinate system. In an isopycnal coordinate, the mixing tensor is represented as,

$$\mathbf{K}_I = \kappa_h \begin{pmatrix} 1 & 0 & 0 \\ 0 & 1 & 0 \\ 0 & 0 & \epsilon \end{pmatrix},$$

where $\epsilon = \frac{\kappa_h}{\kappa_v}$, a measurement of the relatively weak cross-isopycnal mixing.

Under the conditions that horizontal density gradients are much smaller than vertical gradients and there is no cross-isopycnal mixing ($\epsilon = 0$), the mixing tensor can be written as, in a Cartesian coordinate system,

$$\mathbf{K}_{redi} = \kappa_h \begin{pmatrix} 1 & 0 & \mathbf{S}_x \\ 0 & 1 & \mathbf{S}_y \\ \mathbf{S}_x & \mathbf{S}_y & \mathbf{S} \cdot \mathbf{S} \end{pmatrix}.$$

Here $\mathbf{S}$ is the slope of the density surface, $\mathbf{S} = -\nabla_{\mathbf{h}} \rho / \rho_{\mathbf{z}}$.

Gent and McWilliams [1990] added another term to the Redi tensor, so that the flux of the mean density field by the mean velocity is balanced by the divergence of a mean density flux due to meso-scale eddies (Eq. (B.3)). The GM mixing scheme includes the Redi scheme, but also represents the mixing of vertical stability gradients by meso-scale eddies, such as the flattening of density surfaces.

The mixing tensor $\mathbf{K}$ can be split in two parts in the GM mixing scheme

$$\mathbf{K} = \mathbf{K}_{redi} + \mathbf{K}_{adv}, \tag{B.2}$$

where $\mathbf{K}_{redi}$ is the symmetric tensor that represents mixing along isopycnals as in the Redi mixing scheme; $\mathbf{K}_{adv}$ is an antisymmetric tensor that represents the effect of so called "eddy-induced transport velocity" $(\mathbf{v}^*, w^*)$. Here $\mathbf{v}^*$ is defined as $\mathbf{v}^* = \frac{\overline{h'\mathbf{v}'}}{h}$, with h the physical height of a density surface (layer thickness).

The advection of $\mathbf{v}^*$ is along isopycnals in the GM scheme. This is achieved by defining the three-dimemsional effective transport velocity, such that

$$\frac{D^*}{Dt}\rho = \frac{\partial}{\partial t}\rho + \mathbf{V} \cdot \nabla_h \rho + W\rho_z, \tag{B.3}$$

where $\mathbf{V} = \bar{\mathbf{v}} + \mathbf{v}^*, W = \bar{w} + w^*$.

The transformed tracer equation (B.1) then has the form

$$\frac{\partial \bar{c}}{\partial t} + \bar{\mathbf{v}} \cdot \nabla_h \bar{c} + \bar{w}\frac{\partial \bar{c}}{\partial z} = \bar{S}_0 - R - (\mathbf{v}^* \cdot \nabla_h \bar{c} + w^* \bar{c}_z). \tag{B.4}$$

Here R denotes an isopycnal mixing process, which can be represented by the rotated diffusion tensor, $R = \nabla \cdot (\mathbf{K}_{redi}\nabla \bar{c})$.

The eddy-induced velocity satisfies both the usual continuity equation and no normal flow across the closed boundaries. That is,

$\nabla_h \cdot \mathbf{v}^* + w_z^* = 0,$

$(\mathbf{v}^* + w^*\mathbf{k}) \cdot \mathbf{n} = 0.$

In the GM mixing scheme, $(\mathbf{u}^*, w^*)$ is parameterized as

$$\mathbf{u}^* = -\frac{\partial}{\partial z}(\kappa_t \mathbf{S}), \mathbf{w}^* = \nabla_h \cdot (\kappa_t \mathbf{S}), \tag{B.5}$$

where κ_t is the thickness diffusivity. We can see it clear from this parameterization that the "eddy-induced velocity" represents the "thickness" flux; the divergence of this thickness flux tends to mix the thickness down the thickness gradient.

Let $\nabla \cdot (\mathbf{K}_{adv}\nabla c) = \nabla \cdot (\mathbf{u}^* c),$

185

then $\mathbf{K}_{adv}$ is given by

$$\mathbf{K}_{adv} = \kappa_t \begin{pmatrix} \mathbf{0} & 0 & \mathbf{S_x} \\ \mathbf{0} & 0 & \mathbf{S_y} \\ -\mathbf{S_x} & -\mathbf{S_y} & 0 \end{pmatrix}.$$

The horizontal mixing coefficient κ_h and the thickness diffusivity κ_t can vary independently in space, according to stability conditions.

Bibliography

[1] Anderson, J., D. Toohey, and W. Brune, Free radicals within the Antarctic votex: The roll of CFCs in Antaractic ozone loss, Science, 251, 39-46, 1991

[2] Anderson, L. G., E. P. Jones, and B. Rudels, Ventilation of the Arctic Ocean estimated by a plume entrainment model constrained by CFCs, *J. Geophys. Res.*, 104, 13,423-13,429, 1999

[3] Broecker, W. S., S. Sutherland, W. Smethie, T-H Peng, and G. Östlund, Oceanic radiocarbon: Separation of the natural and bomb components, *global Biogeochemical cycles*, 9, 263-288, 1995

[4] Broecker, W. S., S. L. Peacock, S. Walker, R. Weiss, E. Fahrbach, M. Schroeder, U. Mikolajewicz, C. Heinze, R. Key, T.-H., Peng, and S. Rubin, How much deep water is formed in the Southern Ocean? *J. Geophys. Res.*, 103, 15,833-15,843, 1998

[5] Bryan, F., Parameter sensitivity of primitive equation ocean general circulation models, *J. Phys. Oceanogr.*, 17, 970-985, 1987

[6] Clarke, W. B., W. J. Jenkins, and Z. Top, Determination of tritium by mass-spectrometric measurement of ^{3}He, *International Journal of Applied Radiation and Isotopes*, 27, 512-522, 1976

[7] Craig, A. P., J. L. Bullister, D. E. Harrison, R. M. Chervin, and A. J. Jr. Semtner, A comparison of temperature, salinity, and chlorofluorocarbon observations with results from a 1 degree resolution three-dimensional global ocean model, *J. Geophys. Res.*, 103, 1099-1119, 1998

[8] Dahleh, M. A., Dynamic systems, MIT lecture notes, 1999

[9] Dickson, R., J. Lazier, J. Meincke, P. Rhines, and J. Swift, Long-term coordinated changes in the convective activity of the North Atlantic, *Prog. Oceanogr.*, 38, 241-295, 1996

[10] Doney, S. C., D. M. Glover, and W. J. Jenkins, A model function of the global bomb tritium distribution in precipitation, *J. Geophys. Res.*, 97, 5481-5492, 1992.

[11] Doney, S. C. and J. L. Bullister, A chlorofluorocarbon section in the eastern North Atlantic, *Deep Sea Res.*, Part I, 39, 1857-1883, 1992

[12] Doney, S. C., W. J. Jenkins, and H. G. Östlund, A tritium budget for the North Atlantic, *J. Geophys. Res.*, 98, 18,069-18,081, 1993

[13] Doney, S. C., W. J. Jenkins, and J. L. Bullister, A comparison of ocean tracer dating techniques on a meridional section in the eastern North Atlantic, *Deep Sea Res.*, 44, 603-626, 1997

[14] Doney, S. C. and R. Wanninkof, Climatic variability in upper ocean ventilation rates diagnosed using chlorofluorocarbons, *Geophys. Res. Lett.*, 25, 1399-1402, 1998

[15] Dreisigacker, E. and W. Roether, Tritium and ^{90}Sr in North Atlantic surface water, *Earth Planet. Sci. Lett.*, 38, 301-312, 1978

[16] Duffy, P. B., D. E. Eliason, A. J. Bourgeois, and C. C. Covey, Simulation of bomb radiocarbon in two global ocean general circulation models, *J. Geophys. Res.*, 100, 22,545-22,563, 1995

[17] Dutay, J.-C., J. L. Bullister, S. C. Doney, J. C. Orr, R. Najjar, K. Caldeira, J.-M. Campin, H. Drange, M. Follows, Y. Gao, N. Gruber, M. W. Hecht, A. Ishida, F. Joos, K. Lindsay, G. Madec, E. Maier-Reimer, J. C. Marshall, R. J. Matear, P. Monfray, A. Mouchet, G.-K. Plattner, J. Sarmiento, R. Schlitzer, R. Slater, I. J. Totterdell, M.-F. Weirig, Y. Yamanaka, and A. Yool, Evaluation of ocean model

ventilation with CFC-11: comparison of 13 global ocean models, *Ocean Modelling*, 4, 89-120, 2002

[18] England, M. H. and E. Maier-Reimer, Using chemical tracers to assess ocean models, *Review of Geophysics*, 39, 29-70, 2001

[19] England, M. H. and G. Holloway, Simulation of CFC content and water mass age in the deep North Atlantic, *J. Geophys. Res.*, 103, 15,885-15,901, 1998

[20] England, M. H., V. Garcon, and J.-F Minster, Chlorofluorocarbon uptake in a world ocean model, 1. Sensitivity to the surface gas forcing, *J. Geophys. Res.*, 99, 25,215-25,233, 1994

[21] England, M. H., Using chlorofluorocarbons to assess ocean climate models, *Geophysical Research Letters*, 22, 3051-3054, 1995

[22] England, M. H. and A. C. Hirst, Chlorofluorocarbon uptake in a world ocean model, 2. Sensitivity to surface thermohaline forcing and subsurface mixing parameterizations, *J. Geophys. Res.*, 102, 15,709-15,731, 1997

[23] Errico, R. M. and T. Vukicevic, Sensitivity analysis using an adjoint of the PSU-NCAR mesoscale model, *Mon. Wea. Rev.*, 120, 1,644-1,660, 1992

[24] Ganachaud, A. and C. Wunsch, Improved estimates of global ocean circulation, heat transport and mixing from hydrographic data, *Nature*, Vol.408, No.6811, pp.453-457, 2000

[25] Gent, P. R. and J. C. McWilliams, Isopycnal mixing in the ocean circulation models, *J. Phys. Oceanogr.*, 20, 150-155, 1990

[26] Gent, P. R., J. Willebrand, T. J. McDougall, and J. C. McWilliams, Parameterizing eddy-induced tracer transports in ocean circulation models, *J. Phys. Oceanogr.*, 25, 463-474, 1995

[27] Giering, R. and T. Kaminski, Recipes for adjoint code construction, *ACM Trans. On Math. Software*, Vol.24, No.4, 437-474, 1998

[28] Gilson, J., D. Roemmich, B. Cornuelle, and L.-L. Fu, Relationship of TOPEX/POSEIDON altimetric height to steric height and circulation in the North Pacific, *J. Geophys. Res*, 103, 27,947-27,965, 1998

[29] Gordon, A. L. and R. A. Fine, Pathways of water between the Pacific and Indian Oceans in the Indonesian seas, *Nature*, 379, 146-149, 1996

[30] Gray, S. L. and T. W. N. Haine, Constraining a North Atlantic ocean general circulation model with chlorofluorocarbon observations, *J. Phys. Oceanogr.*, 31, 1157-1181, 2001

[31] Haine, T. W. N. and S. L. Gray, Quantifying mesoscale variability in ocean transient tracer fields, *J. Geophys. Res.*, 106, 15,861-13,872, 2001

[32] Haine, T. W. N. and T. M. Hall, A generalized transport theory: water-mass composition and age, *J. Phys. Oceanogr.*, In press, 2001

[33] Haine, T. W. N., A. J. Watson, M. I. Liddicoat, and R. R Dickson, The flow of Antarctic Bottom Water to the southwest Indian Ocean estimated using CFCs, *J. Geophys. Res.*, 103, 27,637-27,653, 1998

[34] Hall, T. M. and R. A. Plumb, Age as a diagnostic of stratopheric transport, *J. Geophys. Res.*, 99, 1059-1070, 1994

[35] Hall, T. M. and T. W. N. Haine, A note on ocean transport diagnostics: the idealized age tracer and the age spectrum, *J. Phys. Oceanogr.*, In press, 2001

[36] Hall, M. C., Application of adjoint sensitivity theory to an atmospheric general circulation model, *J. Atmos. Sci.*, 43, 2644-2651, 1986

[37] Heinze, C., E. Maier-Reimer, and P. Schlosser, Transient tracers in a global OGCM: source functions and simulated distributions, *J. Geophys. Res.*, 103, 15,903-15,922, 1998

[38] Holzer, M., and T. M. Hall, Transit-time and tracer-age distributions in geophysical flows, *J. Atmos. Sci.*, 57, 3539-3558, 2000

[39] Iselin, C.O'D., The influence of vertical and lateral turbulence on the characteristics of the waters at mid-depths, *Trans. Amer. Geophys. Union*, 20, 414-417, 1939

[40] Jenkins, W. J., Determination of isopycnal diffusivity in the Sargasso Sea, *J. Phys. Oceanogr.*, 21, 1058-1061, 1991

[41] Jenkins, W. J., Studying subtropical thermocline ventilation and circulation using tritium and super(3)He, *J. Geophys. Res.*, 103, 15,817-15,831, 1998

[42] Kelley, D. E. and K. A. Van Scoy, A basinwide estimate of vertical mixing in the upper pycnocline: spreading of bomb tritium in the North Pacific Ocean, *J. Phys. Oceanogr.*, 29, 1759-1771, 1999

[43] Khatiwala, S., M. Visbeck, and P. Schlosser, Age tracers in an ocean GCM, *Deep Sea Res.*, 48, 1423-1441, 2001

[44] Klinger, B. A., J. Marshall, and U. Send, Representation of convective plumes by vertical adjustment, *J. Geophys. Res.*, 101, 18,175-18,182, 1996

[45] Koster, R. D., W. S. Broecker, J. Jouzel, R. J. Souzzo, G. L. Russell, D. Rind, and J. W. C. White, The global geochemistry of bomb-produced tritium: general circulation model compared to available observations and traditional interpretations, *J. Geophys. Res.*, 94, 18,305-18,326, 1989

[46] Land, C., J. Feichter, and R. Sausen, Impact of the vertical resolution on the transport of passive tracers in the ECHAM4 model, *Max-Planck-Insititut für Meteorologie*, Report No.321, 2001

[47] Ledwell, J. R, E. T. Montgomery, K. L. Polzin, L. C. St.Laurent, R. W. Schmitt, and J. M. Toole, Evidence for enhanced mixing over rough topography in the abyssal ocean, *Nature*, Vo.403, No.6766, 179-182, 2000

[48] Ledwell, J. R., A. J. Watson, and C. S. Law, Mixing of a tracer in the pycnocline, *J. Geophys. Res.*, 103, 21,499-21,529, 1998

[49] Ledwell, J. R., A. J. Watson, and C. S. Law, Evidence for slow mixing across the pycnocline from an open-ocean tracer-release experiment, *Nature*, 364, 701-703, 1993

[50] Levine, W. S. (editor), The control handbook, CRC press, 1996

[51] Levitus, S., J.I. Antonov, and T.P. Boyer, Interannual variability of temperature at a depth of 125 meters in the North Atlantic Ocean, *Science*, 266, 96-99, 1994.

[52] Levitus, S. and Antonov, J., Observational Evidence of interannual to decadal-scale variability of the subsurface temperature-salinity structure of the world ocean, *Climatic Change*, 31, 515-544, 1995

[53] Luyten, J. R., J. Pedlosky, and H. Stommel, The ventilated thermocline, *J. Phys. Oceanogr.*, 13, 292-309, 1983

[54] Marotzke, J., R. Giering, K. Zhang, D. Stammer, C. Hill, and T. Lee, Construction of the adjoint MIT ocean general circulation model and application to Atlantic heat transport sensitivity, *J. Geophys. Res.*, 104, 29,529-29,547, 1999

[55] Mantyla, A. W., and J. L. Reid, On the origins of deep and bottom waters of the Indian Ocean, *J. Geophys. Res.*, 100, 2,417-2,439, 1995

[56] Marshall, J., C. Hill, and L. Perelman, and A. Adcroft, Hydrostatic, quasi-hydrostatic, and nonhydrostatic ocean modeling, *J. Geophys. Res.*, 102, 5733-5452, 1997a

[57] Marshall, J., A. Adcroft, C. Hill, L. Perelman, and C. Heisey, A finite-volume, incompressible Navier Stokes model for studies of the ocean parallel computers, *J. Geophys. Res.*, 102, 5753-5766, 1997b

[58] Matear, R. J. and C. S. Wong, Estimation of vertical mixing in the upper ocean at Station P from chlorofluorocarbons, *J. Mar. Res.*, 55, 507-521, 1997

[59] Mecking, S. and M. J. Warner, Ventilation of Red Sea Water with respect to chlorofluorocarbons, *J. Geophys. Res.*, 104, 11,087-11,097, 1999

[60] Mémery, L. and C. Wunsch, Constraining the North Atlantic circulation with tritium data, *J. Geophys. Res.*, 95, 5239-5256, 1990

[61] Monterey, G. and Levitus S., Seasonal variability of mixed layer depth for the World Ocean, *NOAA Atlas NESDIS 14, U.S. Gov. Printing Office, Wash., D.C.*, 1997

[62] Montgomery, R. B., A suggested method for representing gradient flow in isentropic surfaces, *Bulletin of the American Meteorology Society*, 18, 210-212, 1937

[63] Munk, W., Internal waves and small-scale processes, *Evolution of Physical Oceanography*, edited by B. A. Warren and C. Wunsch, MIT Press, Cambridge, 264-291, 1981

[64] Munk, W. and C. Wunsch, Abyssal recipes II: energetics of tidal and wind mixing, *Deep Sea Research*, 45, 1977-2010, 1998

[65] Najjar, R., Marine biogeochemistry, In K. E. Trenberth, editor, *Climate System Modeling*, 241-280, Cambridge Univ. Press, 1991.

[66] Nydal, R., and K. Lövseth, Tracing bomb ^{14}C in the atmosphere 1962-1980, *J. Geophys. Res.*, 88, 3621-3642, 1983

[67] Östlund, H. G., and G. H. Rooth, The North Atlantic tritium and radiocarbon transients 1972-1983, *J. Geophys. Res.*, 95, 20,147-20,165, 1990

[68] Pickard, G. L. and W. J. Emery, Descriptive physical oceanography, 5th Edition, *Pergamon Press, New York*, 1990

[69] K. L. Polzin, J. M. Toole, J. R. Ledwell, and R. W. Schmitt, Spatial variability of turbulent mixing in the abyssal ocean, *Science (Wash.)*, Vo.276, No.5309, 93-96, 1997

[70] Redi, M. H., Oceanic isopycnal mixing by coordinate rotation, *J. Phys. Oceanogr.*, 1154-1158, 12, 1982

[71] Redler, R. and J. Dengg, Spreading of CFCs in numerical models of differing resolution, *Int. WOCE Newsl.*, 35, 12-14, 1999

[72] Robbins, P. E., J. F. Price, W. B. Owens, and W. J. Jenkins, The importance of lateral diffusion for the ventilation of the lower thermocline in the subtropical North Atlantic, *J. Phys. Oceanogr.*, 30, 67-89, 2000

[73] Roberts, G. E. and H. Kaufman, *Tables of Laplace Transforms*, Philadelphia: Saunders, 1966

[74] Roether, W. and G. Fuchs, Water mass transport and ventilation in the northeast Atlantic derived from tracer data, *Philos. Trans. Roy. Soc. London*, A325, 63-69, 1988.

[75] Sarmiento, J . L., A simulation of bomb tritium entry into the Atlantic Ocean, *J. Phys. Oceanogr.*, 13, 1924-1939, 1983

[76] Schlitzer, R., Determining the mean, large-scale circulation of the Atlantic with the adjoint method, *J. Phys. Oceanogr.*, 23, 1,935-1,952, 1993

[77] Schlosser, P., J. L. Bullister, and R. Bayer, Studies of deep water formation and circulation in the Weddell Sea using natural and anthropogenic tracers, *Mar. Chem.*, 35, 123-136, 1991

[78] Schmitz, W. J., On the interbasin-scale thermohaline circulation, *Review of Geophysics*, 33, 151-173, 1995.

[79] Smedstad, O. M., and O'Brien, J. J., Variational data assimilation and parameter estimation in an equatorial Pacific Ocean model, *Prog. Oceanog.*, 26, 179-241, 1991

[80] Smethie, W. M. Jr., Tracing the thermohaline circulation in the western North Atlantic using chlorofluorocarbons, *Prog. Oceanogr.*, 31, 51-99, 1993

[81] Smethie, W. M. Jr., R. A. Fine, A. Putzka, and E. P. Jones, Tracing the flow of North Atlantic Deep Water using chlorofluorocarbons, *J. Geophys. Res.*, 105, 14,297-14,324, 2000

[82] Smethie, W. M. Jr., and R. A. Fine, Rates of North Atlantic Deep Water formation calculated from chlorofluorocarbon inventories, *Deep Sea Res.*, Part I, Vol.48, No.1, 189-215, 2001

[83] Stammer D., C. Wunsch, R. Giering, C. Eckert, P. Heimbach, J. Marotzke, A. Adcroft, C. N. Hill, and J. Marshall, The global ocean state during 1992-1997, estimated from ocean observations and a general circulation model, *J. Geophys. Res.*, 107(C9), doi:10.1029/2001JC000888, 2002

[84] Stommel, H., Determination of water mass properties pumped down from the Ekman layer to the geostrophic flow below, *Proceedings of the National Academy of Sciences, U.S.A.*, 76, 3051-3055, 1979

[85] Talley, L. D., and M. S. McCartney, Distribution and circulation of Labrador Sea Water, *J. Phys. Oceanogr.*, 12, 1189-1205, 1982

[86] Toggweiler, J. R., K. Dixon, and K. Bryan, Simulations of radiocarbon in a coarse-resolution world ocean model 1. Steady state prebomb distributions, *J. Geophys. Res.*, 94, 8217-8242, 1989

[87] Toggweiler, J. R., K. Dixon, and K. Bryan, Simulations of radiocarbon in a coarse-resolution world ocean model 2. Distributions of bomb-produced carbon 14, *J. Geophys. Res..* 94, 8243-8264, 1989

[88] Trumbore, S. E., S. S. Jacobs, and W. M. Jr. Smethie, Chlorofluorocarbon evidence for rapid ventilation of the Ross Sea, *Deep Sea Res.*, 38, 845-870, 1991

[89] Veronis, G. and C. C. Yang, Nonlinear source-sink flow in a rotating pie-shaped basin, *Journal of Fluid Mechanics*, 51, 513-527, 1972

[90] Visbeck, M., J. Marshall, T. Haine, and M. Spall, Specification of eddy transfer coefficients in coarse-resolution ocean circulation models, *J. Phys. Oceanogr.*, 27, 381-402, 1997

[91] Walker, S. J., R. F. Weiss and P. K. Salameh, Reconstructed histories of the annual mean atmospheric mole fractions for the halocarbons CFC-11, CFC-12, CFC-113 and carbon tetrachloride, *J. Geophys. Res.*, 105, 14,285-14,296, 2000

[92] Wanninkhof, R., Relationship between wind speed and gas exchange over the ocean, *J. Geophys. Res.*, 97, 7373-7382, 1992

[93] Warner, M. J., and R. F. Weiss, Solubilities of chlorofluorocarbons 11 and 12 in water and seawater, *Deep Sea Res.*, Part A, 32, 1485-1497, 1985

[94] Watanabe, Y. M., A. Ishida, M. Tamaki, K. Okuda, and M. Fukasawa, Water column inventories of chlorofluorocarbons and production rate of intermediate water in the North Pacific, *Deep Sea Res.*, 44, 1091-1104, 1997

[95] Weiss, W. and W. Roether, The rates of tritium input to the world oceans, *Earth Planet. Sci. Lett.*, 49, 435-446, 1980

[96] World Ocean Circulation Experiment Hydrographic Program, *http://whpo.ucsd.edu*

[97] Wunsch, C., Oceanic age and transient tracers. Analytical and numerical solutions, *J. Geophys. Res.*, 107(C6), doi:10.1029/2001JC000797, 2002

[98] Wunsch, C., Transient tracers as a problem in control theory, *J. Geophys. Res.*, 93, 8099-8110, 1988

[99] Wunsch, C., Eclectic modelling of the North Atlantic. II. Transient tracers and the ventilation of the eastern basin thermocline, *Phil. Trans. Roy. Soc., A*, 201-236, 1988

[100] Wunsch, C., Using transient tracers: the regularization problem, *Tellus*, 39B, 477-492, 1987

[101] Wunsch, C., The Ocean circulation inverse problem, *Cambridge University Press*, 1996

[102] Yu. L., and P. Malanotte-Rizzoli, Analysis of the North Atlantic climatologies using a combines OGCM/adjoint approach, *J. Mar. Res.*, 54, 867-913, 1996

[103] Zheng M., W. J. DeBruyn, and E. S. Saltzman, Measurements of the diffusion coefficients of CFC-11 and CFC-12 in pure water and seawater, *J. Geophys. Res.*, 103, 1375-1379, 1998